Core-shell InGaN/GaN wires for flexible LEDs

Akanksha Kapoor

▶ To cite this version:

Akanksha Kapoor. Core-shell InGaN/GaN wires for flexible LEDs. Materials Science [cond-mat.mtrl-sci]. Université Grenoble Alpes [2020-..], 2020. English. NNT : 2020GRALY013 . tel-03077481

HAL Id: tel-03077481
https://tel.archives-ouvertes.fr/tel-03077481

Submitted on 16 Dec 2020

THÈSE

Pour obtenir le grade de

DOCTEUR DE L'UNIVERSITE GRENOBLE ALPES

Spécialité : **NANOPHYSIQUE**

Arrêté ministériel : 25 mai 2016

Présentée par

Akanksha KAPOOR

Thèse dirigée par **Joël EYMERY**
et codirigée par **Christophe DURAND**

préparée au sein du **Labor atoire PHotonique, ELectronique et Ingéniérie Quantiques (PHELIQS)**
dans **l'École Doctorale Physique**

Core-shell InGaN/GaN wires for Flexible LEDs

Thèse soutenue publiquement le **4 June 2020**
devant le jury composé de

Prof. Peter James Parbrook
University of Cork, Ireland, Rapporteur
Prof. Jean-Paul Salvestrini
Georgia-Tech Lorrain, Rapporteur
Prof. Agnès Trassoudaine
Université Clermont Auvergne, Examinatrice
Dr. Thierry Baron
Directeur de recherché, CEA-LTM, Président du Jury
Dr. Maria Tchernycheva
Directrice de recherché, C2N Paris, Examinatrice
Dr. Benjamin Damilano
Chargé de recherché, CNRS-CRHEA, Examinateur
Dr. Joël EYMERY
Directeur de recherche, CEA/IRIG/MEM, Directeur de thèse
Dr. Christophe DURAND
Associate Professor, Université Grenoble Alpes, Co-directeur de thèse

With all due respect dedicated to my parents -

Archana & Vimal

ACKNOWLEDGEMENT

handle the PDMS polymer, Nan Guan for guiding me with device processing, Sylvain Finot for his support in cathodoluminescence measurements and Vincent Grenier for his contribution in the FIB preparation of the wires.

I consider myself fortunate to be welcomed by a lively and cheerful NPSC team. I got the opportunity to meet many other young scientists in the team and our journey of thesis together brought some of us in a strong bond of friendship: Madalina, Marion, Maria, Vincent, Saptarshi, Akhil, Alberto, Houssaine, Nathaniel, Saransh, Guillerme, Anjali, Romain, Ioanna, Alexandre, Tan, Farsane, Remy, Jane & Sergi. I received some good French learning exercises during my lunch time with Catherine, Yann and Houssaine. I would also like to give a special mention to Monika and Nitika, my Indian friends who were not less than a family in Grenoble. I will always cherish our endless talks during dinner.

I also owe gratitude to my mentor back in India – Prof. S. Annapoorni who laid a strong foundation of Physics in my career and helped me to work hard for a bright future.

Lastly, I would like to thank my mom, Archana and my dad, Vimal from the bottom of my heart for their constant love and blessings. Thank you for inspiring me and teaching me to work with dedication and honesty. Special thanks and love to my brother, Utkarsh for making me laugh during the grim of times. I am also grateful to Lakshay who stood as a pillar for me during these years.

ॐ॥ जय गुरूजी ॥ॐ

Akanksha

OUTLINE

INTRODUCTION

❖ Escalation of GaN LEDs

The first epitaxial growth of GaN by hydride vapor-phase epitaxy (HVPE) technique in 1969 at Radio Corporation of America (RCA) was indeed the beginning of a new revolution in the LED industry. Even if a high threading dislocation density and difficulties with p-type doping came across, the material seemed promising to researchers for making blue LEDs. Eventually, a Mg-doped GaN LED was reported in 1972 but showed a poor efficiency due to high contamination present in the HVPE process.[*] This slowed down the further research to realize GaN blue LEDs until Amano and Akasaki reported a significant improvement in the optical and electrical properties of GaN film in 1986.[†] The films were grown by metal organic vapor phase epitaxy (MOVPE) with use of low temperature AlN buffer layer on sapphire substrates. They also proposed a method to p-dope GaN by the activation of Mg atoms with the help of electron beam excitation.[‡] With this new demonstration (n-doping was much easier), the first GaN LED functioning as a p-n junction was reported. Unfortunately, this was practically cumbersome for the industrial production and it was still not possible to tune the emission color. The work was then fueled by the remarkable efforts of Nakamura and Mukai in 1991 who produced highly p-type Mg-doped GaN films using thermal annealing.[§] They also developed high quality InGaN layers and revealed that the luminescing can be varied in the blue-violet range by changing the indium content in the InGaN alloy.[**] Finally the first InGaN/GaN based blue and green LEDs and laser diodes were established and soon

---

[*] Maruska, H. P. et al. Violet Luminescence of Mg-Doped GaN. *Appl. Phys. Lett.* **1973**, *22* (6), 303–305.
[†] Amano, H. et al. Metalorganic Vapor Phase Epitaxial Growth of a High Quality GaN Film Using an AlN Buffer Layer. *Appl. Phys. Lett.* **1986**, *48*, 353–355.
[‡] Amano, H. et al. P-Type Conduction in Mg-Doped GaN Treated with Low-Energy Electron Beam Irradiation (LEEBI). *Jpn. J. Appl. Phys.* **1989**, *28* (12), L2112–L2114.
[§] Nakamura, S. et al. Thermal Annealing Effects on P-Type Mg-Doped GaN Films. *Jpn. J. Appl. Phys.* **1992**, *31* (2), 139–142.
[**] Nakamura, S. et al. High-Quality InGaN Films Grown on GaN Films. *Jpn. J. Appl. Phys.* **1992**, *31* (2), L1457–L1459.

commercialized.[††,‡‡] This also opened a range of other applications such as solar cells and photodiodes. The novel discoveries by Amano, Akasaki and Nakamura thus awarded them with a Nobel Prize in 2014.

The GaN blue LEDs have largely replaced the conventional light sources like incandescent bulbs and fluorescent lamps and are widely commercialized especially when combined with phosphors to emit white light. A huge development over the past few years have also led to the achievement of green and even red emission from GaN based LEDs but with a low efficiency. The standard LED design consists of a planar InGaN/GaN thin film heterostructure that has exhibited a high external quantum efficiency (EQE) of 84.3% for blue emission.[§§] Further improvement in the efficiency can be obtained from these structures if we are able to address optimization issues like light extraction, efficiency droop and in-built electric fields. The use of nanostructures such as nanowires (NWs) have the potential to overcome some of the issues faced in thin film LED. Thanks to their smaller footprint and high surface to volume ratio, NW based LEDs can be obtained with a larger lattice mismatch, lower defect density and higher light extraction. The growth of active InGaN QWs on the non-polar sidewalls in NW geometry suppresses the built-in electric fields increasing in theory the radiative efficiency of the device.

❖   Peculiarities from the Laboratory

The extensive work performed in our laboratory over the past few years has focused on the MOVPE growth of GaN wires covered by core-shell InGaN/GaN quantum wells. The approach to grow GaN wires with silane addition has been developed in our group in 2010 and facilitated the growth of ultra-long wires on full 2-inch sapphire substrates. Soon, the growth of *m*-plane InGaN QWs around the wire sidewalls allowed achieving a blue InGaN/GaN wire LED emitting at 410 nm.

[††] Zhang, M. et al. Candela-Class High-Brightness InGaN/ AlGaN Double-Heterostructure Blue-Light- Emitting Diodes. *Appl. Phys. Lett.* **1994**, *64* (13), 1687.

[‡‡] Nakamura, S. et al. InGaN-Based Multi-Quantum-Well-Structure Laser Diodes. *Jpn. J. Appl. Phys.* **1996**, *35* (2), L74–L76.

[§§] Narukawa, Y. et al. White Light Emitting Diodes with Super-High Luminous Efficacy. *J. Phys. D. Appl. Phys.* **2010**, *43*, *354002.*

Simultaneously, the unique method to fabricate flexible LEDs with core-shell wires was established in collaboration with the C2N laboratory by mechanical lift-off of embedded-wire in a polymer. The first flexible blue LED was achieved in the group in 2015. A flexible white LED was also demonstrated very soon by combining the blue LED with phosphors. These achievements are a result of strong collaboration among teams working at INAC/CEA, Grenoble and C2N, Université Paris-Sud. The growth and optical studies of the wires were carried at CEA Grenoble under the supervision of Jöel Eymery and Christophe Durand. The group of Maria Tchernycheva at C2N, Paris focused their activity on the flexible device fabrication and their electrical characterization.

After these breakthroughs achieving different interesting results by the team so far, the goal of the present thesis is to gain a reproducibility control and perform further optimizations of the previous results. The work also targets to achieve longer wavelength emission than blue from core-shell geometry, which has been challenging so far due to difficulties related to In-rich QWs. A color mixing in the single core-shell wire aiming dual-color wavelength emission is also targeted. The previous work concerning the white light emission using phosphors needs further improvement. The optimization of phosphors to be combined with the blue LED in terms of phosphor particle size and composition can allow to gain higher efficiencies. In order to achieve these objectives, the overview of the Ph.D. thesis will be the following:

❖ Organization of the Manuscript

Chapter 1 will give a background of the nitride LEDs studies and realizations. The basic properties of the nitride semiconductor will be briefly summarized. The different design structure of planar LED shall be presented followed by a discussion about the typical issues of light extraction and efficiency droop reported for these LEDs. An alternative approach of using NW LEDs would be proposed explaining their various benefits compared to thin films. An approach of demonstrating flexible LEDs will also be provided, highlighting some novel achievements of the group. The chapter will finish by explaining concisely the objectives of the thesis.

The details about m-plane InGaN/GaN core-shell wire growth will be focused in **Chapter 2**. The growth of GaN wires with silane addition will be explained followed by the influence of different growth parameters to obtain m-plane radial InGaN QWs. Various heterogeneities encountered during the wire growth such as mixing of wire polarity, inhomogeneities in indium incorporation, and non-uniformity in wire length will be explained. The selective area growth (SAG) shall also be presented containing the technicalities involved in mask fabrication and to check the reproducibility control.

Chapter 3 illustrates different wavelength emission from m-plane InGaN/GaN core-shell heterostructures by tuning the indium content inside InGaN QWs. A reproducibility control will be first tested for the blue emission. A detailed study combining structural, optical as well as electrical properties will be then performed to target green emission from m-plane radial QWs in core shell geometry. A dual color wavelength emission from core-shell wires is also targeted with two different families of InGaN QWs containing different indium content.

Chapter 4 is dedicated to the improvement of efficiency for blue emission. The influence of an InGaN under layer (UL) and GaN spacer will be investigated in core-shell wires containing single InGaN QW with a detailed study using different optical measurements like photoluminescence (PL), time-resolved cathodoluminescence (CL) as well as structural characterization including STEM and EDX analyses.

Lastly, **Chapter 5** will detail the technology involved in flexible device fabrication and the electrical measurements of the fabricated devices. The different steps involved in the fabrication process carried out in clean room environment will be thoroughly explained. Different flexible devices with blue, green, multi-color and dual color wires will be focused to be measured with electroluminescence (EL). The device fabrication will also be followed by some preliminary work performed with phosphors. Optimization of phosphors slabs in terms of composition and thickness will be focused to be combined with the blue LED to improve the white light emission.

Chapter 1: Background of Nitride based visible LEDs studies

This chapter provides an overview about the studies and realizations of GaN-based LEDs. The basic properties of the nitride semiconductors are described in the first section including the crystal structure, crystal polarity, lattice mismatch with different substrates and the electronics structures. The second section presents basic designs for planar LED structures followed by the commonly reported issues like poor light extraction and efficiency droop. Different heterostructures such as the use of surface texturing to efficiently extract the light, incorporating electron blocking layer (EBL) to prevent electron leakage, integrating superlattices beneath the active QW region are discussed. The benefits of utilizing nanowires for LEDs compared to thin film LEDs are presented in the third section followed by different ways for growing GaN wires by bottom-up approach using metal organic chemical vapor deposition (MOCVD). Different NW LEDs achieved by various groups are discussed. Some details stressing on an additional functionality of flexibility in LEDs have been provided in the fourth section highlighting the previous achievements of the group. Finally, the chapter finishes by highlighting the objectives of the present thesis work.

1.1 Basics of nitride semiconductors

This section will present the brief summary of basic properties of III-N semiconductors. It includes their crystal structure, polarity, lattice mismatch, polarization fields and band gap.

1.1.1 Crystal structure

There are three possible crystal structures for group-III nitride semiconductors (GaN, InN, AlN) namely, wurtzite (α-phase), zinc-blende (β-phase) and rocksalt (γ-phase). The γ-phase can appear only at high pressure and is not stable. The other two phases can be epitaxially grown though the wurtzite structure is thermodynamically stable. It has two hexagonal compact sublattices shifted by $\frac{3}{8}$ [0001] with respect to each other, as shown in **Figure 1.1 (a)**, where the length of the hexagon and the edge length is represented by 'c' and 'a' respectively. The internal displacement parameter 'u' is defined as the anion-cation bond length that is also the nearest-neighbour distance in the crystal divided by the lattice parameter 'c'. The c/a and u/c ratios for an ideal wurtzite structure are 1.633 and 0.375 respectively, however a certain deviation occurs for the real structure. The lattice parameters of wurtzite III-nitrides at 300 K is listed in **Table 1.1**[1] while the lattice parameters for a ternary alloy like $A_xB_{(1-x)}N$ are approximated by Vegard's law:

$a_{AB} = x\ a_A + (1-x)\ a_B$; $c_{AB} = x\ c_A + (1-x)\ c_B$ ......(Eq. 1.1)
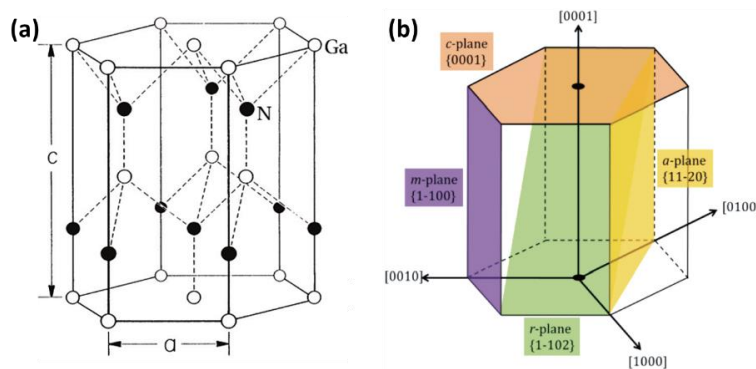
Figure 1.1: Wurtzite crystal structure of GaN in (a) and representation of some crystallographic planes in (b).

The *Miller-Bravais indices* denoted by *h, k, i* and *l* are used to identify the crystal planes in a hexagonal unit cell with the sum of first three indices necessarily zero: $i = -(h + k)$. The (0001) plane in a wurtzite crystal is along polar direction and called polar plane or *c-plane* as shown in

Figure 1.1 (b). The planes parallel to *c*-axis are called non-polar planes, such as $(1\bar{1}00)$ *m*-plane and $(11\bar{2}0)$ *a*-plane. The inclined planes with an angle between 0° and 90° with the *c*-axis are termed as semi-polar planes like the $(11\bar{2}2)$ *r*-plane.

	InN	GaN	AlN
c (Å)	5.703	5.185	4.982
a (Å)	3.545	3.189	3.112
c/a	1.608	1.626	1.600
u/c	0.377	0.377	0.382

Table 1.1: (Taken from *Ref. 1*) Lattice parameters of InN, GaN and AlN at room temperature.

1.1.2 Polarity

The wurtzite crystal is not centro-symmetric that causes the [0001] and [000$\bar{1}$] directions to be non-equivalent. These directions are determined by the association of the vector with the metal-nitrogen bond along the *c*-axis: along the [0001] direction, the vector points from the metal atom to nitrogen atom whereas the reverse is effective along the [000$\bar{1}$] direction, as depicted in **Figure 1.2**. By definition, the crystal is considered to be metal-polar if grown along [0001] direction and nitrogen-polar if grown along [000$\bar{1}$] direction. The polarity of the material is governed by the choice of substrate and growth conditions.[2] In the case of GaN growth on sapphire by MOVPE, Ga-polar phase is obtained in majority. Except for the direct growth on sapphire at high temperature (1050°C), the surface state of the substrate determines the crystal polarity: N-polar crystal is obtained in majority on nitridated sapphire contrary to dominancy by Ga-polar crystal when grown on bare sapphire substrate.[3]
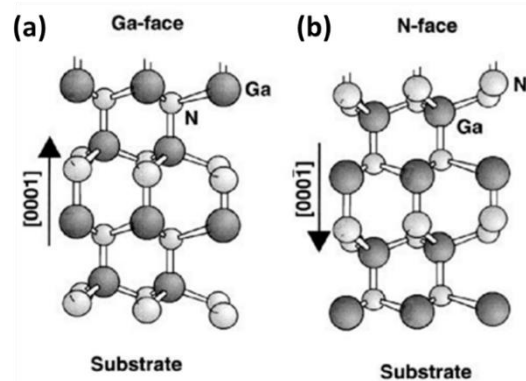
Figure 1.2: Polarity in GaN - (a) Ga-polar along [0001] and (b) N-polar along [000$\bar{1}$].

1.1.3 Lattice mismatch

During the growth of III-N heterostructures, a mechanical stress builds up in the layer due to a difference in lattice parameters with the substrate. The growing structure can be either tensile strained or compressive strained depending on the lattice mismatch as shown in **Figure 1.3**. The stained layer can either deform elastically leading to a pseudomorphic growth or plastically relax making a metamorphic growth that favors defect formation. These defects can correspond to crack propagations or dislocations. It is thus important to use a suitable growth substrate with minimum lattice mismatch to reduce the defects. The lattice mismatch parameter 'f' is defined as:

$$f = \frac{a_{sub} - a_{lay}}{a_{sub}}$$

…… (Eq. 1.2)

where, a_{sub} and a_{sub} refer to the lattice constants of the substrate and growing layer respectively. The tensile and compressive strain is governed by a positive and negative value of 'f' respectively.
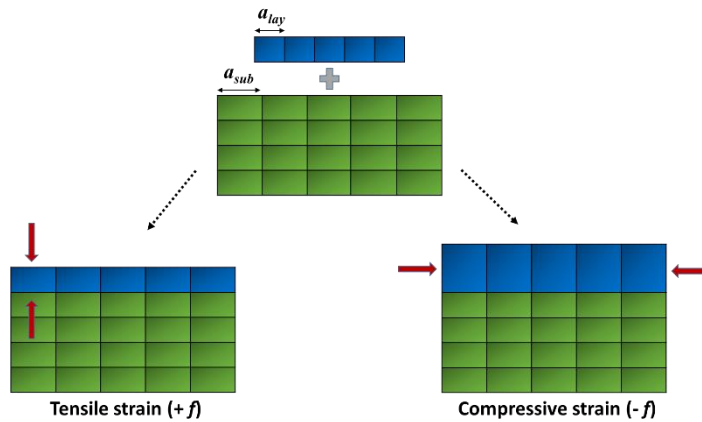
Figure 1.3: Schematics of an epitaxial growth of a lattice mismatched substrate illustrating tensile and compressive strain.

The homoepitaxy of a GaN layer can be achieved with low dislocation density, however GaN substrates are highly costly. Generally, the GaN-heteroepitaxy stacking is performed on sapphire (Al_2O_3), silicon carbide (SiC) or silicon (111) substrates. **Table 1.2** lists the lattice mismatch of GaN (0001) with these different substrates. It is worth mentioning that the estimated value of 'f' for *c*-sapphire substrate takes into consideration the in-plane 30° rotation between the *c*-plane of GaN and *c*-plane of sapphire substrate that occurs during the epitaxy. The silicon substrate has a large lattice mismatch and a large difference in thermal expansion causing cracks and a high density of dislocations in GaN layers. In addition, the melt back etching of Si by TMGa during the GaN growth by MOCVD at quite high temperature has also been reported by several groups.[4,5] Despite

these issues, Si (111) substrates present several advantages like low cost and the availability in large diameters (12''). Therefore, intensive work has been performed to develop III-N optoelectronics on Si with demonstration of efficient LED.[6,7] A high crystal quality of GaN growth has been achieved on SiC substrates[8] thanks to a small lattice mismatch, but the use of these substrates are limited by their high cost. Therefore, the most widely used substrate is *c*-sapphire as they are cheaper, even if the lattice mismatch is large.[9] The c-sapphire substrate allows growing GaN layers with limited density of threading dislocations (~10^8 cm^{-2}) by depositing low-temperature GaN prior the growth. On the contrary, the use of 3D nanostructures (wires, pyramids…) can significantly reduce the dislocation density by allowing a lateral strain relaxation on the lattice-mismatched substrates or just the bending of the dislocation to free surface and not in the active regions. This point has been further explained in the section 1.3.1.

Material	Lattice constant, a (nm)	Lattice mismatch to GaN (0001)
GaN	0.3189	0
c-Al$_2$O$_3$	0.476	-16.1 %
SiC	0.308	3.5 %
Si (111)	0.543	16.9 %

Table 1.2: (Taken from *Ref. 6*) Summary of lattice mismatch of GaN (0001) with different substrates.

1.1.4 Polarization

A strong polarization in III-N semiconductors significantly influences the optical and electrical properties of some heterostructures. The ionic nature of metal-N bond due to high electronegativity of N atom induces an electrostatic dipole. The absence of centro-symmetry along [0001] direction does not allow the compensation of non-zero dipole moment. This intrinsically creates a spontaneous polarization (P_{sp}) in the crystal, which varies for different III-V materials because the bond length between the cation and anion is different. **Table 1.3** shows that GaN has a smaller P_{sp} value while AlN has a higher value.[1]

	AlN	GaN	InN
P_{sp} (C/m^2)	-0.09	-0.034	-0.042

Table 1.3: (Taken from *Ref.1*) Spontaneous polarization for wurtzite type different III-N materials.

Another kind of polarization termed as piezoelectric polarization (P_{pz}) can be generated in the crystal structure if an external stress is applied on the lattice. A change in the charge distribution of the system occurs to accommodate the stress. The direction of P_{pz} is along the [0001] direction in case of compressive strain, while it is along [000$\bar{1}$] in the case of tensile strain. The vector sum of P_{sp} and P_{pz} provides the overall polarization 'P' in the III-V semiconductors. In case of InGaN based LEDs that uses *c*-plane GaN/InGaN/GaN heterostructures, the role of piezoelectric polarization is dominant. However, the influence of polarization on the band structure depends on the crystallographic direction of the growth orientation.
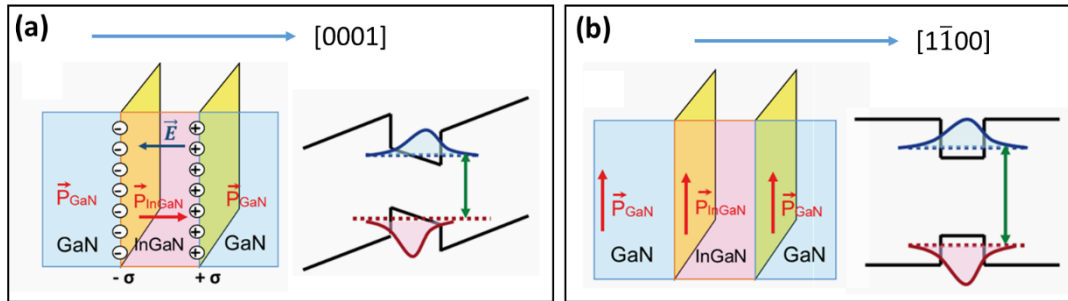
Figure 1.4: Schematics of GaN/InGaN/GaN heterostructure along with energy band structure for growth along (a) polar- [0001] and (b) non-polar [1$\bar{1}$00] direction.

If the heterostructure is grown parallel to the polar *c*-axis i.e. along the [0001] direction, an accumulation of charges with a fixed charge sheet 'σ' occurs at the heterointerfaces. This produces an internal electric field in the wells and the barriers creating a spatial separation in the electron and hole wave function. **Figure 1.4 (a)** shows a schematic of the InGaN/GaN heterostructure grown along [0001] direction illustrating the charge separation, which induces a corresponding change in the band structure. This effect is called quantum confined stark effect (QCSE)[10] and leads to a red-shift in the transition energy. Another consequence is the reduction in spatial overlap of electron and hole wave function thereby limiting the probability of carrier radiative recombination that can reduce the radiative efficiency of LED devices. Even if a red-shift in energy is achieved in these structures facilitating long wavelength emission, a compromise with the efficiency of the LED device should be considered. The presence of QCSE can be completely ruled out in the case of InGaN/GaN heterostructure grown along the non-polar *m*-plane [1$\bar{1}$00] direction. The growth direction is parallel to the total polarization and hence no accumulation of charges takes place

allowing a flat energy band as shown in **Figure 1.4 (b)**. A larger overlap of the electron and hole wave function enhances the radiative efficiency of the devices.[11]

1.1.5 Band gap
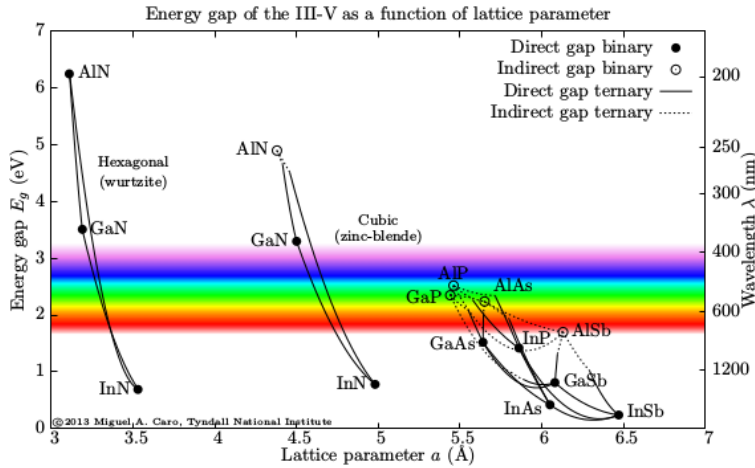
Figure 1.5: Band gap of III-N semiconductors vs lattice constant. (*Ref. 12*)

The direct band gap of III-N semiconductors at room temperature ranges from 6.03 eV (AlN) to 0.64 eV (InN) as shown by **Figure 1.5**.[12] The alloys of these materials with a given material composition cover most of the UV to IR range, explaining their extensive use in various optoelectronic devices. The energy band gap for ternary alloys depends on the composition of the alloy and can be estimated with the expression below taking the example of In$_x$Ga$_{1-x}$N alloy:

$$E_g^{(In_xGa_{1-x}N)} = (1 - x)E_g^{(InN)} + xE_g^{(GaN)} + x(1 - x)b \qquad \text{...... (Eq. 1.3)}$$

where *b*, the coefficient of the parabolic term refers to the bowing parameter accounting for the deviation from linear interpolation between the binary compounds. In addition, the strain state of the epitaxial film will also influence the value of *b*. The fundamental band gap of these materials has a temperature-dependence due to thermal expansion and electron-phonon interaction. The band gap evolution with temperature is given by the following relationship:

$$E_{g(at\ 300K)} = E_{g(at\ 0K)} - \frac{\alpha T^2}{\beta + T} \qquad \text{...... (Eq. 1.4)}$$

where, E$_g$ is the band gap, α and β are Varshni's parameters for a given temperature T. **Table 1.4** summarizes the band gap values at 0 K and 300 K as well as the Varshni's parameters for different III-N materials.

Material	Energy Gap		Varshni Parameters	
	E_g (at 0 K)	E_g (at 300 K)	α (meV/K)	β (K)
AlN (*Ref. 13*)	6.13 eV	6.03 eV	1.799	1462
GaN (*Ref. 14*)	3.51 eV	3.42 eV	0.909	830
InN (*Ref. 15*)	0.69 eV	0.64 eV	0.414	454

Table 1.4: Summary of energy gap and varshni's parameters of III-N semiconductors.

1.2 Conventional nitride based LEDs using planar structures

This section will first present the basic designs for planar LED structure for blue emission. Various alternative structures are discussed to address the issues like low light extraction, electron leakage and poor heat dissipation. The demonstration of blue emission is then extended to green emission considering the serious issues involved in targeting long wavelength emission from InGaN/GaN based LED.

1.2.1 Standard structure on sapphire

A simplified InGaN/GaN based planar LED structure consists of a GaN buffer layer, n-doped GaN layer followed by the active part composed of InGaN/GaN quantum wells (QWs) and a p-doped GaN layer. The structure is usually grown on sapphire substrates along *c*-axis. There are three basic LED chip designs that mainly differ by the substrate technology as explained below.[16]

1.   Conventional chip (CC) design: This configuration is realized by etching a part of the LED structure to access the n-GaN such that both n and p electrodes are located at the top as shown in **Figure 1.6 (a)**. A low thickness of moderately resistive p-GaN can limit the current spreading so it is typically covered by a semi-transparent conductive metallization such as Ni/Au. Generally, a transparent electrode of ITO is preferred due to high light absorption by Ni/Au. This design is popular due to its low cost and easy fabrication but it suffers from a poor light extraction and also has a major drawback of poor heat dissipation since sapphire has a low thermal conductivity.
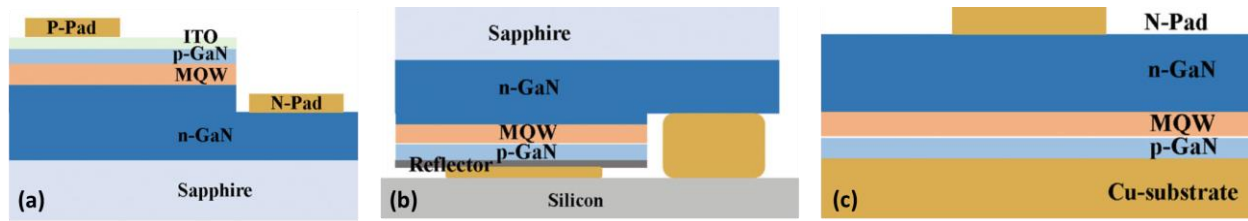
Figure 1.6: Three basic designs of an InGaN/GaN planar LED along *c*-axis: (a) conventional chip (CC), (b) Flip-chip (FC) and (c) Vertical thin film (VTF) design.

2. Flip chip (FC) design: The LED is inverted such that both n and p electrodes are bonded opposite to the sapphire substrate and the whole structure is mounted on a thermally conductive substrate acting as a heat sink for a better heat dissipation (see **Figure 1.6 (b)**). Alternatively the sapphire substrate can be removed from the top via laser lift off leading to a thin film flip chip (TFFC) design. The exposed n-GaN located at the top allows the freedom to texture or roughen the surface for a better light extraction.[17,18]

3. Vertical thin film (VTF) design: A third design of LED (see **Figure 1.6 (c)**) is a vertical structure obtained by flipping the LED structure and removing the native substrate (similar to TFFC design). As the n and p electrodes lie on the opposite side of the structure, the current is injected vertically resulting in a uniform current distribution. A reflective p-contact can be applied on the p-side of the LED chip before bonding it to a metal substrate. This enhances the thermal stability of the LED thanks to the high thermal conductivity of the metal substrate and the reflecting layer at the bottom helps to increase the light extraction.[19]

1.2.2 Ways to improve light efficiency

The LED performance is usually determined by an external quantum efficiency (EQE) which depends on three main factors as described below:

$$EQE = IQE \times \eta_{ext} \times \eta_{inj} \qquad \text{...... (Eq. (1.5))}$$

where IQE is internal quantum efficiency (IQE), η_{ext} is light extraction efficiency and η_{inj} is injection efficiency. It is thus important to consider all the above factors to achieve a high wall-plug efficiency in LED structure and different structures have been discussed below to address the same.

The IQE of an InGaN/GaN LED depends on the crystal quality and structural design of the epitaxial layers. It is generally limited by polarization charges that reduce the radiative recombination inside the structure. As said before, commercial InGaN/GaN based LEDs are commonly grown along polar *c*-axis involving a high polarization fields along *c*-axis. This phenomenon reduces the probability of radiative recombination (due to poor overlap of electron and hole wave functions) and can be overcome by the growth of LED structures on non-polar planes such as *a*-plane and *m*-plane.[11] The growth of non-polar *m*-plane InGaN/GaN LED on free standing *m*-plane GaN substrates (see **Figure 1.7**) has shown an output power of 240 µW at a driving current of 20 mA with an improved heat dissipation.[20] Another group has reported a high-power blue-LED on a free-standing ($20\bar{2}\bar{1}$) GaN substrate with a high EQE of 52% and an output power of 30.6 mW at a forward current of 20 mA.[21] However, the non-polar GaN substrates with a low defect density are limited as they are expensive, while other available substrates like *m*-plane SiC or LiAlO$_2$ results in a high density of threading dislocations and stacking faults.[22,23]
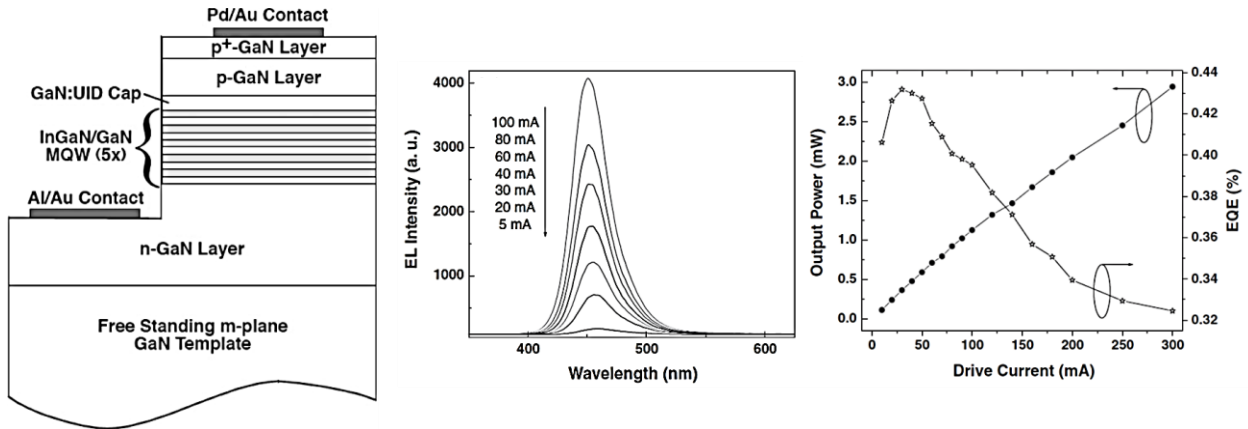
Figure 1.7: Schematic of the non-polar *m*-plane InGaN/GaN based LED grown on free standing m-plane GaN substrate (left), the EL spectra with increasing current (middle) and the output power and EQE with increasing drive current (right). (Taken from *Ref. 20*)

The crossing of high energy electrons over the active region and recombination with the holes present in p-GaN, i.e. the leakage of electrons is commonly observed in InGaN/GaN LEDs and solved by using an electron blocking layer (EBL). A study has been performed on two different structures having a Mg-doped p-type Al$_{0.15}$Ga$_{0.85}$N EBL layer: one grown for a *c*-plane LED on sapphire and other on *m*-plane GaN substrate. It is observed that with presence of EBL, the *c*-plane LED exhibit a reduction in efficiency droop by 40% up to a current density of 2250 A/cm^2 and *m*-plane LED nearly retained its efficiency.[24] Another work is performed by comparing a standard

structure containing an EBL with a constant Al-content 15% to a graded composition EBL (GEBL) with Al composition increasing along the [0001] direction from 0-15%. A reduction of only 4 % in efficiency droop is estimated for the GEBL structure in comparison to 34 % reported for EBL (see **Figure 1.8**).[25] However, later some discrepancy is observed in the use of EBL as some reports demonstrates that the LED structure shows a low EQE with EBL at high current density compared to structure without EBL.[26] The simulations performed on different LED structures containing EBL reveal that the role of EBL is actually governed by the Al composition present inside the layer, the band offset ratio and the polarization charges.[27,28]
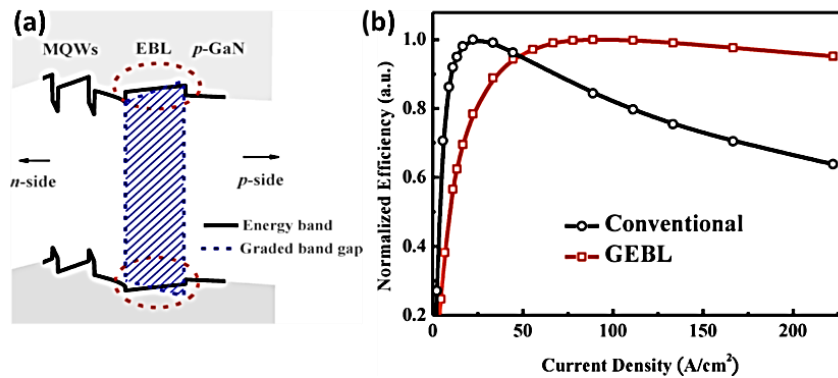
Figure 1.8: LED structure with EBL: (a) Schematic diagram of the concept of band engineering at EBL and (b) Normalized efficiency as a function of current density for conventional and GEBL LEDs. (Adapted from *Ref. 25*).

Assuming a high value of IQE for a given structure, a poor light extraction can also limit the device efficiency. Due to a high refractive index of GaN (n ≈ 2.5), the angle for the light escape cone is very small and most of the light is totally internally reflected. If we neglect the light coming out from the sides and the back side, only 4 % of light is able to escape from the top surface. In addition the emitted light can reflect onto the substrate and get absorbed by the electrodes after repeated reflections. This issue is overcome by using different methods like surface roughening or texturing techniques that can help to scatter the light outwards and avoid the total internal reflection.[19,29,30,31] This is done by different methods such as wet etching, laser bombardment or a secondary epitaxial growth. Changing the shape of the LED chip design to hemispherical, quadrilateral, spherical etc. can also help to mitigate the issue.[32] The absorption of emitted light by the electrodes and a poor current expansion in p-GaN should also be considered. The contact pads are usually coated with Ni/Au or indium titanium oxide (ITO) thin film. It is reported that Ni/Au films (5 nm/5 nm) and ITO (60 nm) show a transmittance of about 86 % and 98 % for blue light (470 nm).[33] Even if the

transparency increases with ITO contact, the forward voltage with Ni/Au is lower suggesting good ohmic contact, therefore one has to consider the compromise between light absorption and efficient current injection with the contacts.

Even if a lot of design structures of LED have been explored till date to improve the device efficiency, a decrease in EQE is observed with increasing current density. This so-called "efficiency droop" remains a significant hurdle in the LED technology and is attributed to auger recombination.[34] A way to address this issue is to increase the surface area of the LED which will reduce the current density and hence avoid the droop in efficiency. Nanostructured LEDs (such as wires, rods, pyramids…) can be a suitable candidate to serve this purpose (explained in section 1.3.1).

1.2.3 Demonstration of green LEDs

Achieving green emission from InGaN/GaN based LEDs that demands indium-rich InGaN QWs has been made possible only after an intense research work as it involves a lot of serious challenges. The lattice mismatch between GaN and InN is around 11 %. Therefore, as the indium content increases, more and more compressive strain accumulates in InGaN layers. A plastic relaxation can rapidly occur in these layers, which are strongly strained to GaN thereby favoring defect formation such as threading dislocations, stacking faults, etc.[35,36] In addition, the low growth temperature required to incorporate high indium content degrades the crystal quality of the active region especially in MOVPE. The defects act as non-radiative centers and reduce the device efficiency. The lattice mismatch also creates a piezoelectric field in the order of MV/cm at the interface of the heterostructures. This leads to the so-called QCSE which can help to red-shift the wavelength emission but the reduced overlapping of electron and hole wave functions will limit the radiative efficiency of the device.

Various types of heterostructures have been reported making use of the band engineering to overcome these issues. Recent work on lattice matched InGaN barriers (with 15 % In-content) instead of conventional GaN barriers in a green LED has shown six-fold increment in the output power with a reduction in efficiency droop.[37] The numerical design and analysis of a W-shaped QW has also been currently reported depicted in **Figure 1.9 (a)** that improved the hole confinement

owing to better localization of indium inside QWs. The authors also claim a reduction in defect related to Shockley-Read-Hall (SRH) and Auger recombination rate with the proposed design.[38] A three-layer staggered InGaN QWs LED (see **Figure 1.9 (b)**) exhibits an enhanced radiative recombination rate thanks to the improved electron-hole wave functions overlap design.[39] The output power improves by 2-3.5 times when compared to a conventional InGaN/GaN based LED. Another report on graded superlattice (GSL) of AlGaN/GaN has demonstrated a decrease in efficiency droop from 34.9 % to 19.4 % at a current density of 100 A/cm^2.[40] The GSL structure basically reduces the effective barrier height of the holes, enhancing their injection efficiency as well as polarization fields near the last well. An InGaN based LED with 12-stacked InGaN layer of the GSL is investigated as shown in **Figure 1.9 (c)** that showed 42.5 % higher output power compared to a conventional LED.[41] The report claims that the GSL insertion layer helps to release the residual stress in MQWs and also acts as an electron cooler enhancing the electron capture rate in MQWs. A pre-strained InGaN/GaN layer with 7 % of In-composition is inserted underneath the active InGaN/GaN QWs region showing a remarkable improvement in both the optical and
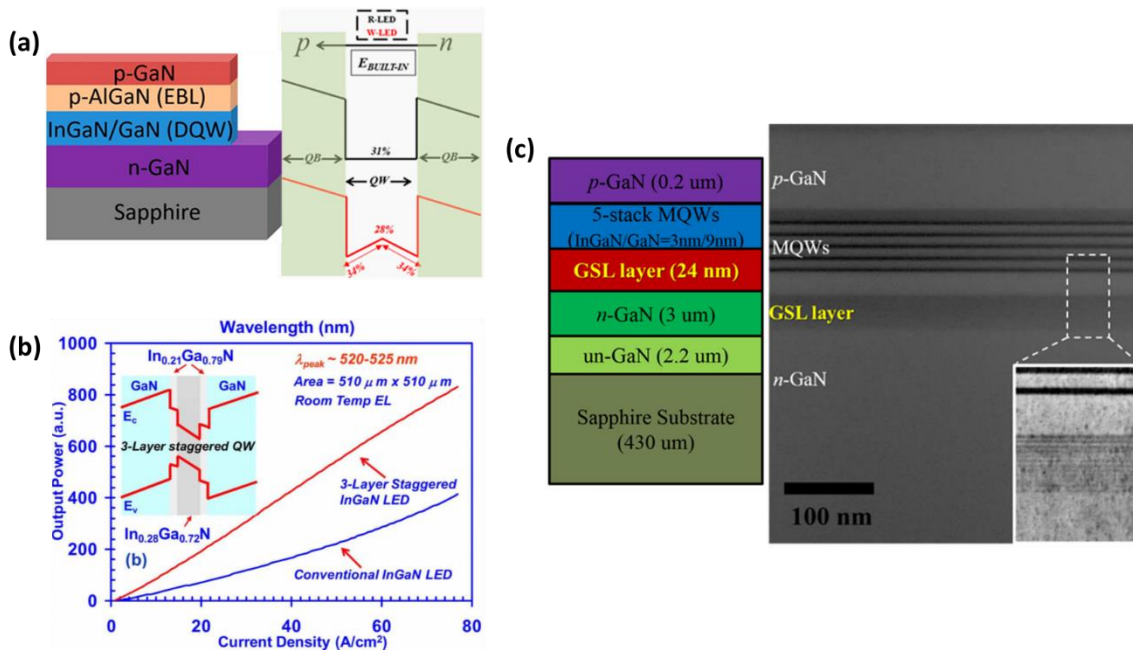
Figure 1.9: (a) Schematic of the LED structure (at left) and indium composition (on right) of standard rectangular QWs and W-shaped QWs, adapted from *Ref. 38*; (b) Output power *vs.* current density for conventional InGaN QW and three-layer staggered InGaN QW LEDs with the corresponding band energy schematic in the inset, taken from *Ref. 39*; (c) Schematic of the LED structure with a 12-stacked GSL layer (left) and TEM image of the epitaxial films in the GSL LED (on right), adapted from *Ref. 41*.

electrical properties of the LED.[42] The pre-strained layer enables the growth of active QWs at 30 °C higher growth temperature targeting the similar emission wavelength. The growth at relatively higher temperature results in a better crystal quality with improved emission efficiency. Moreover, the power-dependent photoluminescence (PL) measurements showed a reduction in QCSE effect.[42]

The use of EBL layer to overcome the issue of electron leakage is more challenging while dealing with green emission, due to several reasons: a higher Al content in EBL layer required for green emission increases the polarization mismatch between AlGaN and GaN barriers, the valence-band barrier in EBL is raised affecting the injection of holes into the active region and a high growth temperature required for AlGaN can be detrimental for the quality of the indium rich active region. A lattice-matched InAlN EBL layer has been reported to obtain a better carrier confinement, lesser thermal damage to the active QWs and improved luminous intensity.[43] The polarization fields at the interface of the heterostructures can also be addressed by an effective doping profile inside the active region to provide free electrons or holes that can screen the polarization charges at interfaces and reduce the electric field. This involves a p-type or n-type impurity doping inside QWs or barriers. A report on InGaN green LED with Mg-doped barriers has shown 12.4 % reduction in efficiency droop at high current injection.[44] Also, it is predicted that the Mg acceptors that are back diffused in the QW close to the p-layer could improve the hole injection efficiency. Similarly, Si-doped barriers in an InGaN green LED with a dopant density of the order of 10^{20} cm^{-3} screen the electric field and reduce the roughness at the InGaN/GaN heterostructure interface.[45] It also suppresses the local heating and improves the current spreading.

Facing the growth challenges to achieve green emission is also accompanied by an intrinsic difficulty related to thermodynamic instability of InGaN alloys. An uneven distribution of In-composition generally occurs within the film due to the phase separation of In-rich InGaN in its metastable state. It results in a randomness in the potential energy distribution leading to the significant localization of charge carriers.[46,47] Theoretical work has shown that the random alloy fluctuations in InGaN alloy contributes to the efficiency droop in InGaN/GaN green LEDs.[48] However, other groups have reported the dot-like In-rich InGaN clusters or quantum dots (QDs) act as localized centers that can prevent the carriers to be trapped at the dislocations, reducing the non-radiative recombination.[49,50,51] A stable electroluminescence (EL) peak has been reported from

InGaN green QDs structure emitting at 527 nm. A negligible shift in the EL peak for current density between 2 to 88 A/cm² indicates that the QCSE is reduced due to strain relaxation.[52] Another work based on coupling of InGaN QW and QD structure has been demonstrated to overcome the small carrier capture cross section provided by the QD and an IQE of 45 % was reported.[53]

1.3 Moving towards wire-based LEDs

1.3.1 Benefits of wires over planar based LEDs

The previous section has described many different issues present in the standard planar *c*-plane LEDs, such as the high lattice mismatch, the presence of QCSE effect and the high defect density. Nanostructured LEDs have been intensely studied over the past few years as an alternative of planar LEDs. They offer a number of key advantages and have the potential to overcome the limitations of planar LED. The wire growth can be performed either in a self-assembled mode (i.e. wire growth at random positions) or using a patterned mask to achieve organized wires at fixed positions. Both the methods have their own benefits and limitations, which will be described later. The wires are obtained by either a bottom-up approach or a top-down etching. The present thesis is based on radial geometry (i.e. core-shell wires) grown by bottom-up technique as depicted in **Figure 1.10 (a)**.[68] This section will be mainly focused on a rapid overview of the state-of-the-art based on this core-shell approach.

The GaN nanowires (NWs) have a high tolerance with different mismatched substrates such as sapphire[54,55,56] Si[57,58] and graphene[59]. A typical SEM image of self-assembled GaN wires grown on sapphire substrate demonstrated by our group in 2010 is shown in **Figure 1.10 (b)**.[56] The small footprint of the wires reduces the lattice mismatch with the substrate facilitating higher strain relaxation and consequently a decrease of defect density.[60,61] The dislocation formation can be avoided in NWs with nm-scaled diameter, while they can be formed for wires having larger diameter at the substrate interface. However, they are mainly found in the immediate vicinity at the wire base and bend to join the lateral free lateral surface.[62,63] A detailed study on the growth of highly uniform arrays of GaN nanocolumns with varying diameters on Si substrates is demonstrated by Kishino *et al.* The dislocations are well filtered at the base of wires and almost

terminated at the sidewall for wires with diameter D ≈ 200 nm, while they are observed for wires with D > 200 nm as shown in **Figure 1.10 (c-e)**.[62] The low density of dislocations in NW based LED has shown significant improvement in the device performance.[64] The core-shell geometry with GaN wires oriented along *c*-axis allows the QW growth on non-polar *m*-plane thereby eliminating the QCSE.[65] Also a reduction in the value of Auger coefficients by two order of magnitude has been revealed in the core-shell *m*-plane LED as compared to *c*-plane planar LED.[66]
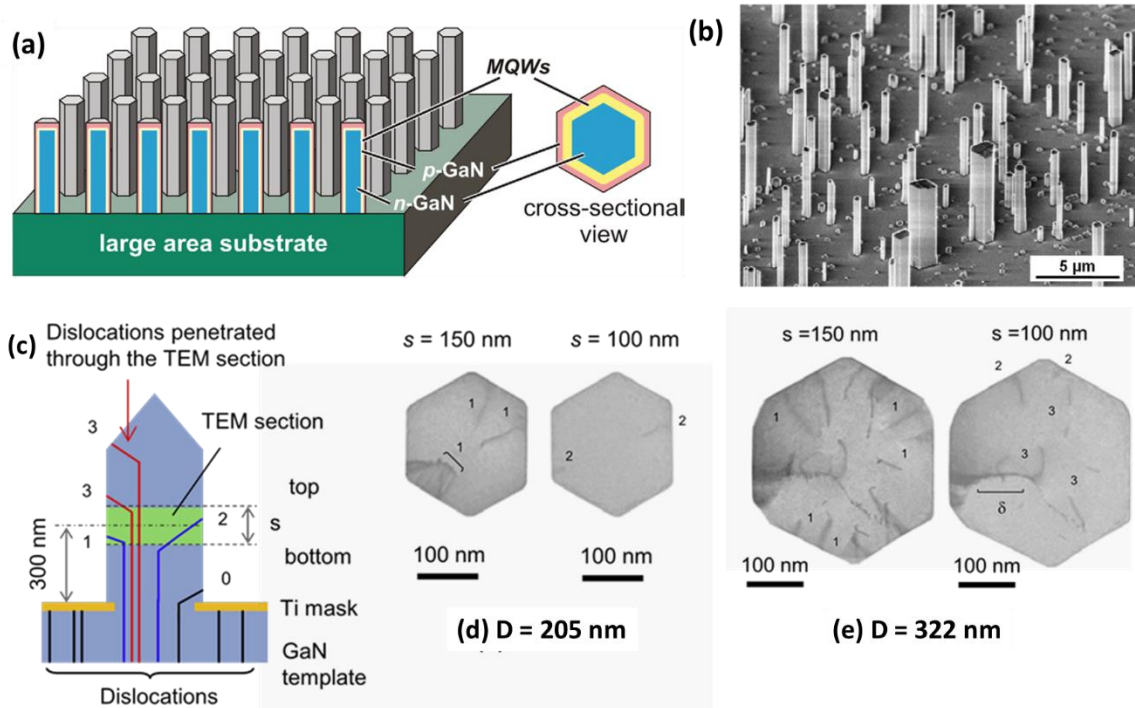
Figure 1.10: (a) Taken from *Ref. 68*: Schematics of core-shell geometry for InGaN/GaN based LED; (b) Adapted from *Ref. 56.*: SEM view of typical self-assembled GaN wires grown on *c*-plane sapphire substrate; (c-e) Taken from *Ref. 62*: Schematic diagram of dislocations propagating in a TEM section in (c), magnified plan-view TEM images of nanocolumns with diameters D= 205 nm in (d) and D= 322 nm in (e). Note the nanocolumns are sliced horizontally to a thickness of *s* at a height of ~300 nm above their bottoms.

The 3D geometry of wires offers a high surface to volume ratio with respect to the corresponding thin planar film, which significantly increases the total active area emitting light.[67] This surface increase allows to reduce the current density for a given carrier injection inside the QWs, thus mitigating the issue of efficiency droop.[68] Moreover, the increased active area improves the light extraction in the device allowing a better escape of photons.[64] However, the issue of light re-absorption should be considered, which has been commonly reported for core-shell LEDs. Apart

from the key benefits mentioned above, the wire based LED also offers a unique functionality of flexibility in a LED device. This will be described later in section 1.4.

1.3.2 Different ways to grow GaN wires

The two main growth techniques to achieve GaN wire growth are namely molecular beam epitaxy (MBE) and MOVPE. The GaN wires are spontaneously grown by MBE in nitrogen-rich conditions with a slow growth rate ($\approx$ 0.6 Å/s) and exhibit a high density ($\approx 10^{10}$ wires cm^{-2}). They are suitable to produce axial heterostructures. The wire growth by MOVPE requires a control over many growth parameters and exhibits a low wire density (10^7 wires cm^{-2}) with a faster growth rate ($\approx$ 100 Å/s) and allows growing mainly core-shell heterostructures. A detailed description of GaN wire growth is provided by Nan *et al*.[69] The four growth methods of catalyst-free GaN wires using bottom-up approach by MOVPE are explained below:

1. The vertical growth of GaN wires along *c*-axis by using a <u>pulsed growth method</u> has been first reported by Hersee *et al*. as depicted in **Figure 1.11 (a)**.[54] The precursors for Ga and N are alternatively introduced inside the reactor and wires with diameter equal to 221±7 nm are achieved on a patterned Si_3N_4 mask by selective area growth (SAG). A quite high growth temperature (> 950 °C), high V/III ratio (1500) and low pressure (100-200 mbar) under H_2 carrier gas are typically used. This work also served as a milestone for SAG growth establishing a better control over wire dimensions as well as wire density. However, the growth revealed a low growth rate (2 µm/h) and presence of structural defects mainly located at the NW base.[54] The growth technique has been later carried out by other groups reporting a high crystal quality of wires.[70,71]

2. The selective growth of ordered GaN NWs on GaN templates using an <u>ultra-low precursor</u> has been reported by Arakawa's group demonstrating wires with a diameter of 50 nm (see **Figure 1.11 (b)**).[72] This growth method uses very low TMGa and NH_3 flux as (0.1-1.0) µmol/min and (10-100) µmol/min respectively resulting in a V/III ratio between 1 and 50. The growth is performed at high temperature (950-1100 °C), low pressure (100 mbar) using N_2 carrier gas without hydrogen dilution. This approach has also been used a little bit earlier in our laboratory to grow GaN wires

on bare c-plane sapphire substrates.[73] Defect-free wires with excellent optical properties has been reported but with a quite low growth rate ($\approx$ 4 µm/h) that is mainly governed by the wire density.

3. Our group has exploited the strategy of using a <u>high silane flux</u> (200 nmol/min) compared to that for planar growths (10 nmol/min) to favor the vertical growth of very long GaN wires with a growth rate larger than 100 µm/h.[56,65] The left and right SEM images in **Figure 1.11 (c)** shows the wires grown without and with silane respectively. The high silane flux indeed imposes a high n-type doping in the order of 10^{20} cm^{-3}.[74] Other growth parameters fixed during the growth are: high growth temperature (1050 °C), low V/III ratio (<50), high pressure (800 mbar) under high flow of N_2 carrier gas. The present thesis work is based on GaN wire growth using the silane approach and more details will be described in Chapter 2.
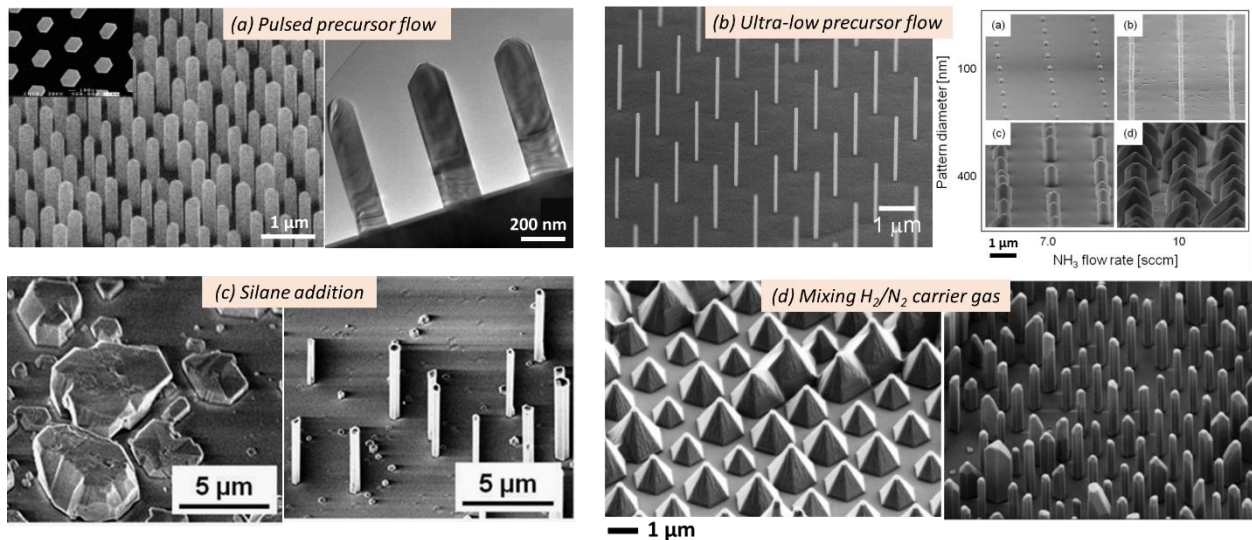
Figure 1.11: Catalyst-free MOVPE methods to grow GaN wires: (a) SEM and TEM images of ordered GaN wire arrays grown by pulsed precursor mode, adapted from *Ref. 54*; (b) SEM images of ordered GaN NW array grown by ultra-low precursor flux method as a function of the NH_3 flux and the pattern pitch, taken from *Ref. 72*; (c) SEM images of self-assembled GaN wires grown without (left) and with (right) silane addition, adapted from *Ref. 56*; (d) SEM images of ordered GaN wire arrays grown without (left) and with (right) hydrogen dilution (2:1) of N_2 carrier gas, adapted from *Ref. 75*.

4. The mixing of <u>H_2/N_2 carrier gas</u> is another method to achieve GaN wire growth as reported by the group of Waag.[75] **Figure 1.11 (d)** shows the selective growth of pyramids on *c*-sapphire under N_2 (on left) but a dilution of the carrier gas with hydrogen having H_2/N_2 ratio 2:1 allows the formation of *m*-plane facets (on right). Other growth parameters are similar to that used for the silane approach.

The present work focusses on bottom-up approach only, however some groups have also reported top-down approach to grow wires.[76,77] For example, MOCVD grown *c*-plane GaN on Si templates are etched to fabricate GaN nano rods and this can also be followed by the overgrowth of InGaN shell covering the nano rods to produce core-shell heterostructures.[76] Another recent work has reported the fabrication of GaN nanocolumns by etching GaN film on sapphire and followed by lateral overgrowth and annealing.[77] Such a hybrid top down approach has shown a reduction in threading dislocation density for the nanocolumns.

1.3.3 Demonstration of MOVPE grown wire based LEDs

NW based LEDs have seen tremendous amount of research over the past few years to gain a deep understanding about the device performance. Many groups have succeeded in fabricating wire LEDs and some companies (GLÖ, Aledia, Osram…) also focus their R&D activity on the same. Before to compete against the planar technology that exhibits highly efficient LED devices, some open issues still remain in the wire LEDs that need to be addressed. A few important works based on core-shell wire LEDs grown by MOVPE will be described in this section and various difficulties are systematically discussed.

1.3.3.1 Early achievement of blue emission

The early demonstration of core-shell NW LED grown by MOCVD has been reported by Lieber *et al.*[78,79] in 2004 using Ni particles as a catalyst to grow NWs. The catalyst free core-shell *m*-plane InGaN/GaN based LED has also been demonstrated in our laboratory by Koester *et al*. in 2011 exhibiting an emission around 410 nm.[65] The radial *m*-plane QWs are present only around the upper part of the GaN wire covered by the p-GaN shell while the wire-bottom is heavily n-doped. This unique structure can allow an efficient way to access the p-GaN (wire-top) and n-GaN (wire-bottom) for electrical contacts. This work has been further extended by fabricating a single NW LED using the core-shell InGaN/GaN wire containing five radial QWs.[80] Later, the group of Ra in 2013 has also described a wire-based LED grown with the help of Au catalyst using a pulsed-precursor flow.[81] The radial QWs are grown on the non-polar and semi-polar planes under a reduced growth pressure. An EQE of 27.9 % has been estimated for a current injection of 50 mA.[81]

The EL spectra reveals an emission at 440 nm, which is considered to originate mainly from the *m*-plane sidewall QWs.

A color shift in the EL spectra has usually been reported in NW LEDs as a function of applied voltage. It is mentioned by *Koester et al.*[65] that the QWs are present on both the lateral *m*-plane facet as well as the top *c*-plane facet with different thicknesses and In-content. A change in the EL color emission is recorded and explained by a competition between the carrier injection in the axial and the radial QWs. Similarly, a color shift has been reported for LEDs based on organized array of nanostructures.[82,83,85,86]

A work by Hong *et al.*[82] has shown a monolithic LED with GaN nanorod array grown using SiO_2 mask on GaN template on sapphire substrate with a height of about 520 nm. The indium content in $In_xGa_{(1-x)}N$ QWs present on the topmost and sidewall facets and estimated by EDX is found to be $x \approx 0.6$ and ≈ 0.15 respectively. The light emission is observed to be tunable from 690 nm to double peak (500 and 440 nm) by adjusting the voltage bias from 3 to 10 V. A field distribution model is used to explain the change in EL color. The carriers are injected preferentially in the tip due to flat
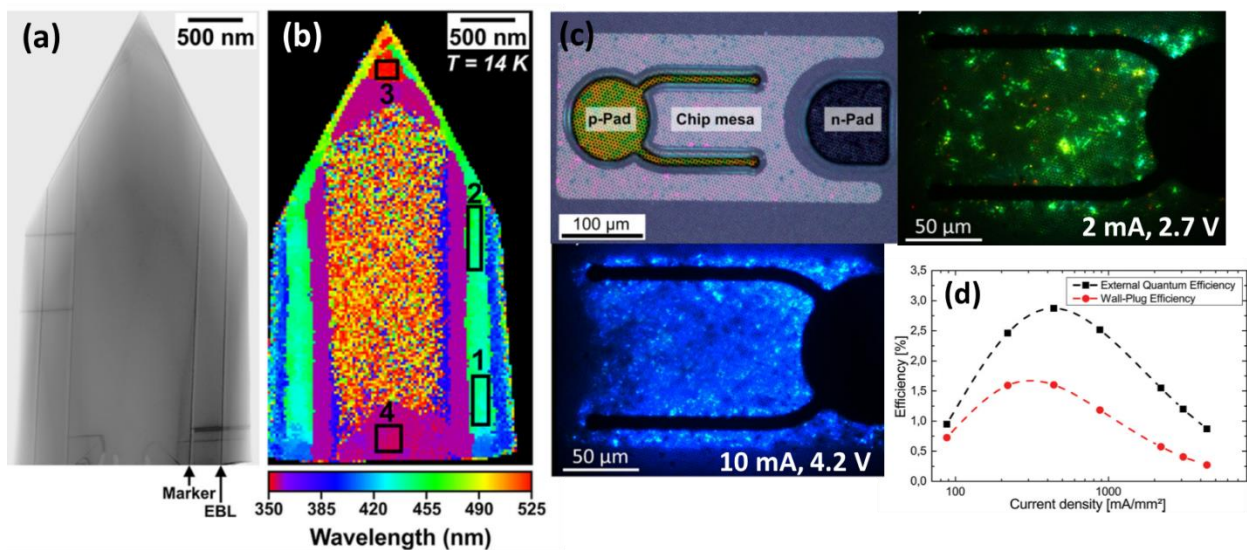
Figure 1.12: Adapted from *Ref. 83-* (a) Bright field STEM image of core-shell GaN microrod with arrows indicating the layers containing aluminum, (b) STEM-CL peak wavelength mapping of the core-shell rod, (c) Optical microscope image of the chip layout (top image), electroluminescence images from the LED chip at 2 mA (right image) & 10 mA (image below) and (d) EQE and wall-plug efficiency of the blue LED with the current density.

equipotential surface, which changed to a curved shape as the applied voltage bias increases allowing the carriers to enter though *m*-plane sidewall QWs. The temperature-dependent photoluminescence (PL) spectra reveal an IQE of 32±8 %. Another study conducted by OSRAM is based on organized array of GaN microrod (MR) LED grown on n-doped *c*-plane GaN template on sapphire wafers.[83] A SiO$_x$ mask layer fabricated by photolithography is used to grow uniform wires with a height of 3 μm. The presence of single QW on semi-polar and non-polar facets is confirmed by STEM-CL measurements (see **Figure 1.12**), while the estimated IQE from PL experiment is 10 %. A shift from green luminescence at low bias (arising from semi-polar facets) to blue luminescence for voltage > 3.0 V (coming from non-polar *m*-plane facets) is reported. The estimated EQE of the LED is 3 % at a current density of 400 mA/mm^2. Beyond the fabrication and demonstration of blue emission, white light emission has also been reported from microrod LED in this work and will be discussed in the next section.

The color switching observed in the above-mentioned reports is further investigated by the GLÖ-company.[84,85] The organized core-shell NW LEDs are fabricated with a silicon nitride mask patterned by nanoimprint on n-type GaN/sapphire substrate. The LED contains single QW located at the non-polar *m*-plane and the junction of semi-polar and *m*-plane. An electrical model is proposed to explain the color shift observed in a single NW LED. A network of diodes connected in parallel is used to represent a core-shell NW where the current distribution is calculated for different applied voltage biases and different configuration for contacts. It is concluded that the In-rich segments are injected at low bias, while the parallel and radial shell resistances dominate at higher biases allowing the current injection in the *m*-plane QW with low In content.

Recently the group of Amano has demonstrated a multi-band emission covering almost the whole visible region using core-shell InGaN/GaN nanorods grown on patterned substrates as shown in **Figure 1.13**.[86] It is explained that the incorporation kinetics for indium on the different planes of 3D nano-structures is different. So apart from the growth conditions, the size, pitch, and angle of a top cone of the NRs array also play a major role for the QW homogeneity. The PL spectra reveals the presence of different contributions arising from different parts of the NR. The NRs are then used to fabricate a LED device by filling the space between the rods by spin-on-glass (SOG) to prevent the electron leakage and ITO was used as a top contact. A thin film of Ti/Al is used as a

back contact that can be seen in the SEM image in **Figure 1.13** (labelled by 'electrode space'). The measured EL spectra is observed to strongly depend on the current density and is explained by a similar transportation mechanism of charge carriers as reported previously by other groups mentioned above.
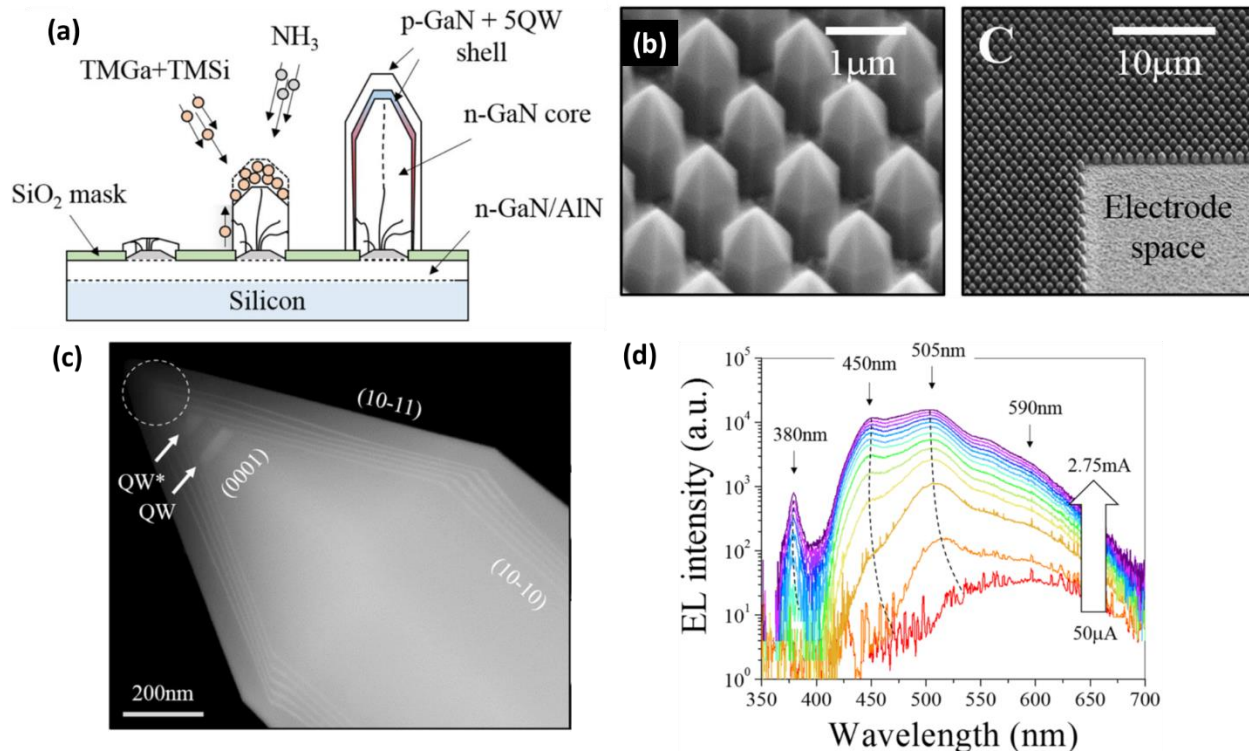
Figure 1.13: Taken from *Ref. 86-* (a) Schematics of the InGaN/GaN SAG nanorod containing n-GaN core, 5 InGaN QWs & a p-GaN shell observed with the SEM images shown in (b), (c) STEM image of the core-shell layers structure and (d) Room-temperature EL spectra recorded at different injection currents.

The multi-color emission or the color tuning with applied voltage bias in NW based LED could be used for a full color display application, however it is important to control the color emission while targeting a narrow band single color emitting device. A work by Chen *et al.*[87] has demonstrated GaN nanorod LED array grown on SiO$_2$ mask with a height of 1.3 μm with InGaN QWs located on both lateral sidewall as well the nanorod top as described in **Figure 1.14**. The TEM observation reveals a poor structural quality of the top QWs. A transparent GaZnO of low resistivity is deposited using MBE to form a coalesced layer on the nanorods to improve the current spreading over the *m*-plane QWs. A stable EL spectrum is recorded centered at 463 nm with no significant shift unlike the above mentioned reports. However, a large turn-on voltage around 6 V is recorded.

Apart from these reports, the highest IQE of 62 % has been reported till date for core-wire based LED by Nami *et al.* to the best of our knowledge.[88] The high-performance core-shell InGaN/GaN wire-based LEDs are grown on patterned SiN_x mask with an improved p-GaN growth. The EQE was measured at 8.3 % without any device packaging, although the shift of the EL emission with changing applied bias is also reported in this work.
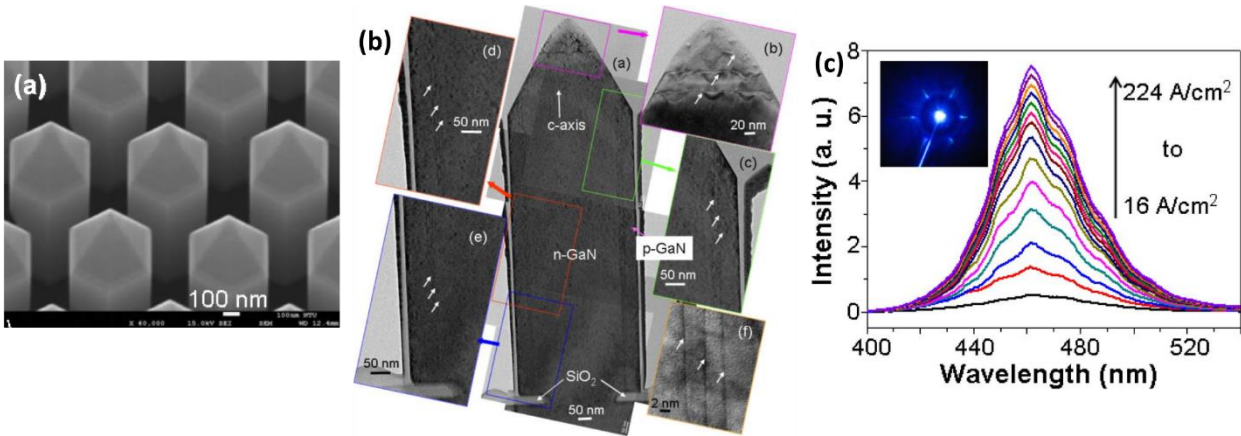
Figure 1.14: Adapted from *Ref. 87-* (a) SEM image of the nanorod LED array at large magnification, (b) TEM image of a nanorod LED NR with magnified TEM images corresponding to differernt portions of the QWs such as top face (in pink), left and right-sidewall QWs near the top (in red & green resp.) and left-sidewall QW near the bottom (in blue) with a high- resolution TEM image of the three sidewall QW and (c) EL spectra when injection current density increasing from 16 to 224 A/cm^2 with inset showing the photograph of LED at current density of 224 A/cm^2.

1.3.3.2 Achieving white LEDs using phosphors

The realization of LEDs using core-shell *m*-plane InGaN/GaN wires grown by MOCVD has been mainly demonstrated for blue emission. Longer wavelength emissions like green, yellow and red with stable color at varying bias voltage still remain a challenge for this core-shell geometry due to the difficulty to increase the In incorporation on the *m*-plane surface. This makes the RGB (red/green/blue) approach difficult to achieve white light emission from InGaN/GaN wire based LEDs. Another key solution to address this issue is to down convert the blue light from these LEDs using phosphors emitting at different colors. A phosphor is a material that absorbs light of a given energy and emits light having lower energy. Intensive research based on their synthesis optimization offers different phosphors with high efficiency (η) such as $RbLi(Li_3SiO_4)_2$:Eu^{2+} ($RLSO$:Eu^{2+}) emitting green (η≈80%)[89], Ce,Gd:$Y_3Al_5O_{12}$

(Ce,Gd:YAG) emitting yellow ($\eta\approx93\%$)[90] and $Sr[Li_2Al_2O_2N_2]:Eu^{2+}$ (SALON) emitting red emission ($\eta\approx80\%$).[91] The phosphor use is a powerful method to tune the color of the emitted light by LED devices. Actually, the mixing of yellow phosphors (Ce,Gd:YAG) with blue LED emitters to achieve highly efficient white light emission is commercialized nowadays as they are far better than the conventional incandescent bulbs and fluorescent lamps in terms of energy saving and lifetimes. The use of green-red phosphors is less common due to their lower conversion efficiency. The nitride-based white planar LEDs containing efficient yellow phosphors (Ce,Gd:YAG) is now a mature technology with current efficiency higher than 100 lm/W for commercial devices. A peak luminous efficiency of 136 lm/W has been achieved with an optimized InGaN LED chip design coated with a suitable phosphor by OSRAM in 2010.[92,93] The maximal efficiency of 303 lm/W has even been reported by CREE in 2014. For comparison, the phosphor based white organic light emitting diodes (WOLEDs) with an EQE of 34 % shows a device power efficiency of 90 lm/W.[94] In the usual planar LEDs, the blue emitters are coated with phosphor films. In the case of wire-LED devices, the air gaps between the wires/rods can be filled with phosphors leading to a better mixing of the colors as well as thermal coupling.[83] The work by OSRAM as mentioned in the earlier section also demonstrated a white LED by coupling the blue microrod LED with YAG:Ce (yellow) and nitrido-silicate (red) phosphors (e.g. $(Ca,Sr)_2Si_5N_8:Eu$).[83] A special synthesis route was adapted to produce phosphor particles with grain size diameter less than 1 µm in order to be deposited in-between wires. The particles are deposited between the MRs as shown in **Figure 1.15 (a)** using an electrophoretic technique. **Figure 1.15 (b)** shows the emission with and without light conversion and the resulting EL spectra is visible **Figure 1.15 (c)**. A coordinated color temperature (CCT) of 6600 K and a color rendering index (CRI) of 73 is measured for the white LED. This method allows
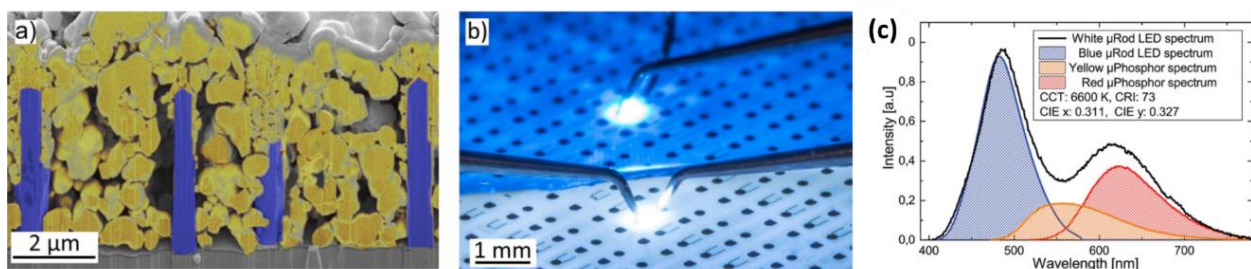
Figure 1.15: Adapted from *Ref. 83*: (a) Colored SEM image of micrograin phosphor deposited between GaN MRs by electrophoretic particle deposition, (b) Wafer with LEDs, upper half unconverted, lower half converted with micrograin phosphor; and (c) Phosphor converted white LED spectrum fitted with the contributions of the individual components.

a better phosphors cooling as they are in direct contact with the LED unlike the planar LEDs where they are dispersed in a silicone matrix.

A flexible nitride-based nanowire LED emitting white light with phosphors dispersed between the wires has also been demonstrated in our laboratory. The additional functionality of flexibility will be discussed in the next section. The device is estimated with an EQE of 13.2 % under the current density of 14.6 A/cm^2 and emission power of 10.7 mW.[95] However, a high correlated color temperature (CCT) of 6306 K (indicating cool white light) and a low color rendering index (CRI) of 54 is recorded for the device. This work was extended to further optimize the color characteristics of the LED device by investigating the source emitter as well as different phosphors. An increase in the CRI from 54 to 86 has been reported by using a blue-green LED (emitting at 439 nm and 485 nm) covered with yellow phosphors YAG:Ce^{+3} with the grain size between 5-10 μm.[96] These findings evidence the scope of achieving highly efficient white light emission from wire-based LED devices by using phosphors.

1.4 LEDs with additional functionality of flexibility

The rapidly growing electronic industry today positions a high demand for attractive applications of bendable appliances. This includes rollable displays, deformable light sources, wearable electronics, biomedical devices and many more. Nowadays, the flexible electronics are mainly fabricated using organic materials due to their lightweight and compatibility with different flexible substrates like plastic. For example, organic LEDs (OLEDs) are widely manufactured on large scale, as they are easy to process at low-cost. But issues like oxidation and degradation of organic molecules lead to a limited lifetime (5 years). On the contrary, the use of inorganic semiconductor LED can overcome this issue with possible lifetime of 50000 h. However, the standard inorganic thin film LEDs are mechanically rigid and it is challenging to instill them with flexibility. A change in the band gap also occurs due to the strain created during bending that results in shifting of the wavelength emission.[97] The high flexibility offered by nitride NWs make them a suitable candidate to be used for flexible LEDs combined with the other benefits of inorganic semiconductor material

like high efficiency and longer lifetime.[98] The NWs are able to tolerate large deformations thanks to their smaller footprint. They can be transferred on different flexible substrates avoiding the limitations imposed by growth conditions. In addition, materials having different physical and chemical properties can be combined, which is otherwise difficult for flexible thin film LEDs.

A flexible NW based LED can be obtained by a direct growth on flexible substrates. This approach has been demonstrated with ZnO wire growth on an ITO substrate at 80 °C[99] but high growth temperature required for nitride wires makes this growth approach impossible. However, GaN NWs growth have been reported on Ti metal foils by plasma assisted MBE using a preceding step of surface nitridation.[100] Another method is to perform an in-plane transfer of NWs driven by electric field, magnetic field or capillary force etc. A UV LED composed of crossed n-type GaN NWs and p-type Si NWs were sequentially dispersed on plastic substrate by orthogonal fluid-directed assembly.[101] This work showed a stable LED emission under various bending cycles but involved the complex method of positioning the single NWs.

The encapsulation of NWs in a polymer matrix and lifting-off from their native substrate is another key approach to obtain flexible LEDs. It allows the transfer of wires on almost any flexible substrate while preserving their vertical geometry.[102,103,104,95] Chung *et al.*[102] reported in 2014 the flexible GaN microrod LED using graphene. The Cu foils coated with graphene was transferred onto SiO_2/Si substrates, which were then used for the growth of InGaN/GaN nanorods (NRs) as shown in **Figure 1.16 (a)**. The NRs were embedded in an insulating polymer and the wet etching of SiO_2 was performed. The growth was followed by the transfer of the whole layer onto a Ti/Au coated flexible substrates for back contact, while Ni/Au layer was used for the top contact. The device exhibited a stable blue EL emission under a bending radius of 6 mm and 1000 bending cycles. A novel route to fabricate flexible LEDs has also been developed in our laboratory. The as-grown GaN wires on sapphire with core-shell InGaN/GaN MQWs are encapsulated in a PDMS polymer matrix, mechanically peeled off and mounted on a flexible PET sheet. The polymer layer is etched with plasma for making the electrical contacts and a thin layer of Ti/Al is used as a back contact for n-GaN. The Ag NWs are used for the flexible top p-contact and have a high transmittance, which overcomes the light absorption that is typically observed for Ni/Au contact. This method results in a semi-transparent device. A fully transparent device is fabricated by

replacing the backside metal layer using also the Ag NWs for both front and back contact. This approach was used to fabricate flexible blue and green LED as shown in **Figure 1.16 (b,c)** and **(d,e)**.[104] The blue and green LEDs showed a good flexibility under a bending curvature less than 1 cm with EL spectra peaked at 425 and 530 nm respectively. A fully transparent blue LED was stacked with a semi-transparent green LED to demonstrate a two-color flexible LED in **Figure 1.16 (f)**.
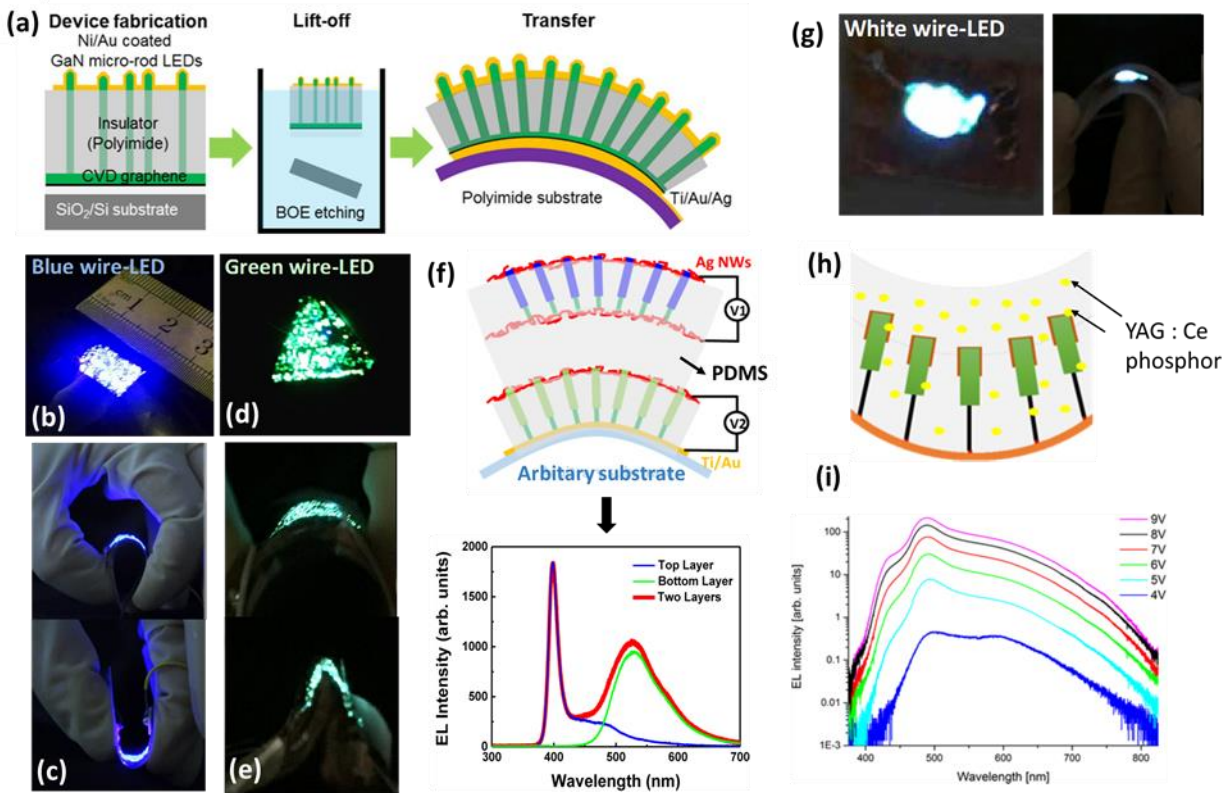
Figure 1.16: (a) Adapted from *Ref. 102-* Fabrication process of flexible GaN micro-rod LEDs grown on graphene substrate; (b-f) Taken from *Ref. 104-* Photograph of the LED emitting blue and green light in (b,c) and (d,e) resp. with bending devices at curvature radii 3.5 mm (left) and -2.5 mm (right) & (f) showing the schematic of a two-color NW flexible LED with corresponding EL spectra below; (g-i) Adapted from *Ref. 95-* (g) Photograph of the white LED with bending radii of 5 mm (right image), (h) Schematics showing phosphor dispersion between wires and corresponding EL spectra is shown in (i).

This work has also been extended by dispersing yellow phosphors (YAG:Ce) between the wires emitting blue light to fabricate a white LED as shown in **Figure 1.16 (g-i)**.[95] The EL spectrum remains stable after 10 bending cycles: no degradation was observed without any external encapsulation after 50 days storage in ambient conditions. The strategy of producing flexible LEDs

has also been applied to other devices in our group such as flexible photodiodes[105] and capacitive Piezoelectric Sensor using ultra-long GaN wires.[106]

1.5 Objective of the present thesis

The previous work in our laboratory has laid the foundation of GaN wire growth by MOCVD using silane flux addition. Further, the growth of *m*-plane InGaN/GaN based core-shell heterostructures has demonstrated the possibility to achieve visible blue LEDs in our group. The novel technique to fabricate flexible devices added a key functionality to the devices. The concept of integrating the blue LED with yellow phosphors was also used to demonstrate white light LEDs on flexible substrates.

The present thesis work is based on carrying forward the state of the art of producing core-shell heterostructures to target different wavelength emission. It is important to first validate the reproducibility and scalability of already established blue emission by the group. This is followed by aiming other long wavelength emission, such as green from the core-shell geometry while considering the well-known difficulties related to In-rich QWs. The work also targets to perform color mixing within the core-shell geometry to produce a dual-color LED. This is particularly interesting in view of producing phosphor-free white light LED by using the RGB approach. Simultaneously, the demonstration of flexible white LEDs using phosphors needs further improvement in terms of finding the best combination of phosphors integrated with the wires (phosphor size, composition). A suitable design for coupling the phosphors with blue wire LED is also important to gain maximum efficiency from the device.

The know-how to produce flexible devices requires extra-development to enhance its reproducibility. Different issues like PDMS peeling, spot-like emission and a poor current injection have been observed in the previous work. The PDMS peeling has been one of the key step involved in the fabrication and is far from being straightforward. This not only affects the overall light emission from the wires (wires falling, PDMS membrane tearing apart) but also limits the size of the flexible LED. Indeed additional work in easing this step can allow to increase the total size of

the flexible devices and one can imagine to produce a full 2-inch flexible LED. Other difficulties like poor-current injection and spot-like emission can also be addressed by optimizing the electrical contacts used in the LED.

Besides employing the self-assembled wires to fabricate homemade flexible devices, the Ph.D. work also focuses on selective area growth (SAG) using a SiN mask on sapphire substrates. Previous Ph.D. works have concluded that the SAG on sapphire indeed remains difficult and involves further optimization. Efforts have to be made in the present work to check the reproducibility control of SAG before to consider if its potential gain is worth regarding the high cost and complexities involved in the growth.

REFERENCES

[1] Vurgaftman, I.; Meyer, J. R. Band Parameters for Nitrogen-Containing Semiconductors. *J. Appl. Phys.* **2003**, *94*, 3675. https://doi.org/10.1063/1.1600519.

[2] Naresh-Kumar, G.; Bruckbauer, J.; Winkelmann, A.; Yu, X.; Hourahine, B.; Edwards, P. R.; Wang, T.; Trager-Cowan, C.; Martin, R. W. Determining GaN Nanowire Polarity and Its Influence on Light Emission in the Scanning Electron Microscope. *Nano Lett.* **2019**, *19*, 3863–3870. https://doi.org/10.1021/acs.nanolett.9b01054.

[3] Liu, F.; Collazo, R.; Mita, S.; Sitar, Z.; Duscher, G.; Pennycook, S. J. The Mechanism for Polarity Inversion of GaN via a Thin AlN Layer: Direct Experimental Evidence. *Appl. Phys. Lett.* **2007**, *91*, 203115. https://doi.org/10.1063/1.2815748.

[4] Ishikawa, H.; Yamamoto, K.; Egawa, T.; Soga, T.; Jimbo, T.; Umeno, M. Thermal Stability of GaN on (1 1 1) Si Substrate. *J. Cryst. Growth* **1998**, *189–190*, 178–182. https://doi.org/10.1016/S0022-0248(98)00223-1.

[5] Ishikawa, H.; Zhao, G. Y.; Nakada, N.; Egawa, T.; Jimbo, T.; Umeno, M. GaN on Si Substrate with AlGaN/AlN Intermediate Layer. *Jpn. J. Appl. Phys.* **1999**, *38* (5A), 492–494. https://doi.org/10.1143/jjap.38.l492.

[6] Zhu, D.; Wallis, D. J.; Humphreys, C. J. Prospects of III-Nitride Optoelectronics Grown on Si. *Reports Prog. Phys.* **2013**, *76*, 106501. https://doi.org/10.1088/0034-4885/76/10/106501.

[7] Chen, P.; Zhang, R.; Zhao, Z. M.; Xi, D. J.; Shen, B.; Chen, Z. Z.; Zhou, Y. G.; Xie, S. Y.; Lu, W. F.; Zheng, Y. D. Growth of High Quality GaN Layers with AlN Buffer on Si(111) Substrates. *J. Cryst. Growth* **2001**, *225*, 150–154. https://doi.org/10.1016/S0022-0248(01)00842-9.

[8] Xie, Z. Y.; Wei, C. H.; Chen, S. F.; Jiang, S. Y.; Edgar, J. H. Surface Etching of 6H-SiC (0001) and Surface Morphology of the Subsequently Grown GaN via MOCVD. *J. Electron. Mater.* **2000**, *29* (4), 411–417. https://doi.org/10.1007/s11664-000-0153-x.

[9] Melton, W. A.; Pankove, J. I. GaN Growth on Sapphire. *J. Cryst. Growth* **1997**, *178*, 168–173. https://doi.org/10.1016/S0022-0248(97)00082-1.

[10] Chichibu, S. F.; Abare, A. C.; Mack, M. P.; Minsky, M. S.; Deguchi, T.; Cohen, D.; Kozodoy, P.; Fleischer, S. B.; Keller, S.; Speck, J. S.; et al. Optical Properties of InGaN Quantum Wells. *Mater. Sci. Eng. B* **1999**, *59*, 298–306. https://doi.org/10.1016/S0921-5107(98)00359-6.

[11] Waltereit, P.; Brandt, O.; Trampert, A.; Grahn, H. T.; Menniger, J.; Ramsteiner, M.; Reiche, M.; Ploog, K. H. Nitride Semiconductors Free of Electrostatic Fields for Efficient White Light-Emitting Diodes. *Nature* **2000**, *406*, 865–868. https://doi.org/https://doi.org/10.1038/35022529.

[12] Caro Bayo, M. Á. 2013. Theory of elasticity and electric polarization effects in the group-III nitrides. PhD Thesis, University College Cork.

[13] Guo, Q.; Yoshida, A. Temperature Dependence of Band Gap Change in InN and AlN. *Jpn. J. Appl. Phys.* **1994**, *33*, 2453. https://doi.org/10.1143/JJAP.33.2453.

[14] Vurgaftman, I.; Meyer, J. R.; Ram-Mohan, L. R. Band Parameters for III-V Compound Semiconductors and Their Alloys. *J. Appl. Phys.* **2001**, *89*, 5815–5875. https://doi.org/10.1063/1.1368156.

[15] Walukiewicz, W.; Li, S. X.; Wu, J.; Yu, K. M.; Ager, J. W.; Haller, E. E.; Lu, H.; Schaff, W. J. Optical Properties and Electronic Structure of InN and In-Rich Group III-Nitride Alloys. *J. Cryst. Growth* **2004**, *269*, 119–127. https://doi.org/10.1016/j.jcrysgro.2004.05.041.

[16] Krames, M. R.; Shchekin, O. B.; Mueller-Mach, R.; Mueller, G. O.; Zhou, L.; Harbers, G.; Craford, M. G. Status and Future of High-Power Light-Emitting Diodes for Solid-State Lighting. *J. Disp. Technol.* **2007**, *3* (2), 160–175. https://doi.org/10.1109/JDT.2007.895339.

[17] Wong, W. S.; Sands, T.; Cheung, N. W.; Kneissl, M.; Bour, D. P.; Mei, P.; Romano, L. T.; Johnson, N. M. Fabrication of Thin-Film InGaN Light-Emitting Diode Membranes by Laser Lift-Off. *Appl. Phys. Lett.* **1999**, *75* (10), 1360–1362. https://doi.org/10.1063/1.124693.

[18] Shchekin, O. B.; Epler, J. E.; Trottier, T. A.; Margalith, T.; Steigerwald, D. A.; Holcomb, M. O.; Martin, P. S.; Krames, M. R. High Performance Thin-Film Flip-Chip InGaN-GaN Light-Emitting Diodes. *Appl. Phys. Lett.* **2006**, *89*, 071109. https://doi.org/10.1063/1.2337007.

[19] Fujii, T.; Gao, Y.; Sharma, R.; Hu, E. L.; DenBaars, S. P.; Nakamura, S. Increase in the Extraction Efficiency of GaN-Based Light-Emitting Diodes via Surface Roughening. *Appl. Phys. Lett.* **2004**, *84* (6), 855–857. https://doi.org/10.1063/1.1645992.

[20] Chakraborty, A.; Haskell, B. A.; Keller, S.; Speck, J. S.; Denbaars, S. P.; Nakamura, S.; Mishra, U. K. Demonstration of Nonpolar M-Plane InGaN/GaN Light-Emitting Diodes on Free-Standing m-Plane GaN Substrates. *Jpn. J. Appl. Phys.* **2005**, *44* (5), L173–L175. https://doi.org/10.1143/JJAP.44.L173.

[21] Zhao, Y.; Tanaka, S.; Pan, C. C.; Fujito, K.; Feezell, D.; Speck, J. S.; DenBaars, S. P.; Nakamura, S. High-Power Blue-Violet Semipolar (202̄1̄) InGaN/GaN Light-Emitting Diodes with Low Efficiency Droop at 200 A/Cm2. *Appl. Phys. Express* **2011**, *4*, 082104. https://doi.org/10.1143/APEX.4.082104.

[22] Imer, B.; Wu, F.; Craven, M. D.; Speck, J. S.; DenBaars, S. P. Stability of (1100) m-Plane GaN Films Grown by Metalorganic Chemical Vapor Deposition. *Jpn. J. Appl. Phys.* **2006**, *45* (11), 8644–8647. https://doi.org/10.1143/JJAP.45.8644.

[23] Haskell, B. A.; Chakraborty, A.; Wu, F.; Sasano, H.; Fini, P. T.; Denbaars, S. P.; Speck, J. S.; Nakamura, S. Microstructure and Enhanced Morphology of Planar Nonpolar M-Plane GaN Grown by Hydride Vapor Phase Epitaxy. *J. Electron. Mater.* **2005**, *34* (4), 357–360. https://doi.org/10.1007/s11664-005-0110-9.

[24] Lee, J.; Li, X.; Ni, X.; Özgür, Ü.; Morkoç, H.; Paskova, T.; Mulholland, G.; Evans, K. R. On Carrier Spillover in C- and m-Plane InGaN Light Emitting Diodes. *Appl. Phys. Lett.* **2009**, *95*, 201113. https://doi.org/10.1063/1.3266833.

[25] Wang, C. H.; Ke, C. C.; Lee, C. Y.; Chang, S. P.; Chang, W. T.; Li, J. C.; Li, Z. Y.; Yang, H. C.; Kuo, H. C.; Lu, T. C.; et al. Hole Injection and Efficiency Droop Improvement in InGaN / GaN Light-Emitting Diodes by Band-Engineered Electron Blocking Layer. *Appl. Phys. Lett* **2010**, *97*, 261103. https://doi.org/10.1063/1.3531753.

[26] Han, S.; Lee, D.; Lee, S.; Cho, C.; Kwon, M.; Lee, S. P.; Noh, D. Y.; Kim, D.-J.; Kim, Y. C.; Park, S.-J. Effect of Electron Blocking Layer on Efficiency Droop in InGaN / GaN Multiple Quantum Well Light-Emitting Diodes. *Appl. Phys. Lett.* **2009**, *94*, 231123. https://doi.org/10.1063/1.3153508.

[27] Xia, C. S.; Li, Z. M. S.; Sheng, Y. On the Importance of AlGaN Electron Blocking Layer Design for GaN-Based Light- Emitting Diodes. *Appl. Phys. Lett* **2013**, *103*, 233505. https://doi.org/10.1063/1.4839417.

[28] Kim, M. H.; Schubert, M. F.; Dai, Q.; Kim, J. K.; Schubert, E. F.; Piprek, J.; Park, Y. Origin of Efficiency Droop in GaN-Based Light-Emitting Diodes. *Appl. Phys. Lett.* **2007**, *91*, 183507. https://doi.org/10.1063/1.2800290.

[29] Huh, C.; Lee, K. S.; Kang, E. J.; Park, S. J. Improved Light-Output and Electrical Performance of InGaN-Based Light-Emitting Diode by Microroughening of the p-GaN Surface. *J. Appl. Phys.* **2003**, *93* (11), 9383–9385. https://doi.org/10.1063/1.1571962.

[30] Pan, J.-W.; Wang, C.-S. Light Extraction Efficiency of GaN-Based LED with Pyramid Texture by Using Ray Path Analysis. *Opt. Express* **2012**, *20* (S5), A630. https://doi.org/10.1364/oe.20.00a630.

[31] Yamada, M.; Mitani, T.; Narukawa, Y.; Shioji, S.; Niki, I.; Sonobe, S.; Deguchi, K.; Sano, M.; Mukai, T. InGaN-Based near-Ultraviolet and Blue-Light-Emitting Diodes with High External Quantum Efficiency Using a Patterned Sapphire Substrate and a Mesh Electrode. *Jpn. J. Appl. Phys.* **2002**, *41*, L1431–L1433. https://doi.org/10.1143/JJAP.41.L1431.

[32] Egalon, C. O.; Rogowski, R. S. Increased Efficiency LED. *US Pat. App. 15,705,834, Jan 6,* **1998**.

[33] Lin, Y. C.; Chang, S. J.; Su, Y. K.; Tsai, T. Y.; Chang, C. S.; Shei, S. C.; Kuo, C. W.; Chen, S. C. InGaN / GaN Light Emitting Diodes with Ni / Au , Ni / ITO and ITO P-Type Contacts. **2003**, *47*, 849–853.

[34] Iveland, J.; Martinelli, L.; Peretti, J.; Speck, J. S.; Weisbuch, C. Direct Measurement of Auger Electrons Emitted from a Semiconductor Light-Emitting Diode under Electrical Injection: Identification of the Dominant Mechanism for Efficiency Droop. *Phys. Rev. Lett.* **2013**, *110* (17), 177406. https://doi.org/10.1103/PhysRevLett.110.177406.

[35] Li, Z. L.; Lai, P. T.; Choi, H. W. A Reliability Study on Green InGaN-GaN Light-Emitting Diodes. *IEEE Photonics Technol. Lett.* **2009**, *21* (19), 1429–1431. https://doi.org/10.1109/LPT.2009.2028155.

[36] Cho, H. K.; Lee, J. Y.; Yang, G. M.; Kim, C. S. Formation Mechanism of V Defects in the InGaN/GaN Multiple Quantum Wells Grown on GaN Layers with Low Threading Dislocation Density. *Appl. Phys. Lett.* **2001**, *79*, 215–217. https://doi.org/10.1063/1.1384906.

[37] Ahmad, S.; Raushan, M. A.; Siddiqui, M. J.; Alvi, P. A.; Kattayat, S. Improvement in Efficiency Droop of Green Light Emitting Diode Using Lattice Matched Barrier. *Int. Conf. Adv. Comput. Commun. Paradig. ICACCP* **2019**, 1–5. https://doi.org/10.1109/ICACCP.2019.8882903.

[38] Usman, M.; Mushtaq, U.; Zheng, D. G.; Han, D. P.; Rafiq, M.; Muhammad, N. Enhanced Internal Quantum Efficiency of Bandgap-Engineered Green W-Shaped Quantum Well Light-Emitting Diode. *Appl. Sci.* **2019**, *9* (77), 1–10. https://doi.org/10.3390/app9010077.

[39] Zhao, H.; Liu, G.; Li, X. H.; Huang, G. S.; Poplawsky, J. D. Growths of Staggered InGaN Quantum Wells Light-Emitting Diodes Emitting at 520-525 nm Employing Graded Growth-Temperature Profile. *Appl. Phys. Lett.* **2009**, *95*, 061104. https://doi.org/10.1063/1.3204446.

[40] Kang, J.; Li, H.; Li, Z.; Liu, Z.; Ma, P.; Yi, X.; Wang, G. Enhancing the Performance of Green GaN-Based Light-Emitting Diodes with Graded Superlattice AlGaN / GaN Inserting Layer. *Appl. Phys. Lett.* **2013**, *103*, 102104. https://doi.org/10.1063/1.4819879.

[41] Park, J. Y.; Lee, J. H.; Jung, S.; Ji, T. InGaN/GaN-Based Green-Light-Emitting Diodes with an Inserted InGaN/GaN-Graded Superlattice Layer. *Phys. Status Solidi Appl. Mater. Sci.* **2016**, *213* (6), 1610–1614. https://doi.org/10.1002/pssa.201533092.

[42] Huang, C. F.; Liu, T. C.; Lu, Y. C.; Shiao, W. Y.; Chen, Y. S.; Wang, J. K.; Lu, C. F.; Yang, C. C. Enhanced Efficiency and Reduced Spectral Shift of Green Light-Emitting-Diode Epitaxial Structure with Prestrained Growth. *J. Appl. Phys.* **2008**, *104*, 123106. https://doi.org/10.1063/1.3046582.

[43] Kim, H. J.; Choi, S.; Kim, S. S.; Ryou, J. H.; Yoder, P. D.; Dupuis, R. D.; Fischer, A. M.; Sun, K.; Ponce, F. A. Improvement of Quantum Efficiency by Employing Active-Layer-Friendly Lattice-Matched InAlN Electron Blocking Layer in Green Light-Emitting Diodes. *Appl. Phys. Lett.* **2010**, *96*, 101102. https://doi.org/10.1063/1.3353995.

[44] Ning, Z.; Zhe, L.; Zhao, S.; Peng, R.; Xiao-Dong, W.; Xiang-Xu, F.; Peng, D.; Cheng-Xiao, D.; Shao-Xin, Z.; Bing-Lei, F.; et al. Reduction of Efficiency Droop and Modification of Polarization Fields of InGaN-Based Green Light-Emitting Diodes via Mg-Doping in the Barriers. *Chinese Phys. Lett.* **2013**, *30* (8), 087101. https://doi.org/10.1088/0256-307X/30/8/087101.

[45] Lin, Z.; Hao, R.; Li, G.; Zhang, S. Effect of Si Doping in Barriers of InGaN/GaN Multiple Quantum Wells on the Performance of Green Light-Emitting Diodes. *Jpn. J. Appl. Phys.* **2015**, *54*, 022102. https://doi.org/10.7567/JJAP.54.022102.

[46] Jeong, H.; Jeong, H. J.; Oh, H. M.; Hong, C. H.; Suh, E. K.; Lerondel, G.; Jeong, M. S. Carrier Localization in In-Rich InGaN/GaN Multiple Quantum Wells for Green Light-Emitting Diodes. *Sci. Rep.* **2015**, *5*, 1–7. https://doi.org/10.1038/srep09373.

[47] Park, I. K.; Kwon, M. K.; Kim, J. O.; Seo, S. B.; Kim, J. Y.; Lim, J. H.; Park, S. J.; Kim, Y. S. Green Light-Emitting Diodes with Self-Assembled In-Rich InGaN Quantum Dots. *Appl. Phys. Lett.* **2007**, *91*, 133105. https://doi.org/10.1063/1.2790783.

[48] Auf Der Maur, M.; Pecchia, A.; Penazzi, G.; Rodrigues, W.; Di Carlo, A. Efficiency Drop in Green InGaN/GaN Light Emitting Diodes: The Role of Random Alloy Fluctuations. *Phys. Rev. Lett.* **2016**, *116*, 027401. https://doi.org/10.1103/PhysRevLett.116.027401.

[49] Narukawa, Y.; Kawakami, Y.; Funato, M.; Fujita, S.; Fujita, S.; Nakamura, S. Role of Self-Formed InGaN Quantum Dots for Exciton Localization in the Purple Laser Diode Emitting at 420 nm. *Appl. Phys. Lett.* **1997**, *70*, 981–983. https://doi.org/10.1063/1.118455.

[50] O'donnell, K. P.; Martin, R. W.; Middleton, P. G. Origin of Luminescence from InGaN Diodes. *Phys. Rev. Lett.* **1999**, *82* (1), 237–240. https://doi.org/10.1103/PhysRevLett.82.237.

[51] Dong, H.; Qu, K.; Liang, J.; Zhang, A.; Jia, Z.; Jia, W.; Xu, B.; Liu, X.; Li, G.; Wu, Y. Evolution Mechanism of InGaN Quantum Dots and Their Optical Properties. *Opt. Mater.* **2019**. https://doi.org/10.1016/j.optmat.2019.109554.

[52] Lv, W.; Wang, L.; Wang, L.; Xing, Y.; Yang, D.; Hao, Z.; Luo, Y. InGaN Quantum Dot Green Light-Emitting Diodes with Negligible Blue Shift of Electroluminescence Peak Wavelength. *Appl. Phys. Express* **2014**, *7*, 025203. https://doi.org/10.7567/APEX.7.025203.

[53] Yu, J.; Wang, L.; Yang, D.; Hao, Z.; Luo, Y.; Sun, C.; Han, Y.; Xiong, B.; Wang, J.; Li, H. Improving the Internal Quantum Efficiency of Green InGaN Quantum Dots through Coupled InGaN/GaN Quantum Well and Quantum Dot Structure. *Appl. Phys. Express* **2015**, *8*, 094001. https://doi.org/10.7567/APEX.8.094001.

[54] Hersee, S. D.; Sun, X.; Wang, X. The Controlled Growth of GaN Nanowires. *Nano Lett.* **2006**, *6* (8), 1808–1811. https://doi.org/10.1021/nl060553t.

[55] Wang, G. T.; Talin, A. A.; Werder, D. J.; Creighton, J. R.; Lai, E.; Anderson, R. J.; Arslan, I. Highly Aligned , Template-Free Growth and Characterization of Vertical GaN Nanowires on Sapphire by Metal – Organic Chemical Vapour Deposition. *Nanotechnology* **2006**, *17*, 5773–5780. https://doi.org/10.1088/0957-4484/17/23/011.

[56] Koester, R.; Hwang, J. S.; Durand, C.; Dang, D. L. S.; Eymery, J. Self-Assembled Growth of Catalyst-Free GaN Wires by Metal-Organic Vapour Phase Epitaxy. *Nanotechnology* **2010**, *21*, 015602. https://doi.org/10.1088/0957-4484/21/1/015602.

[57] Salomon, D.; Dussaigne, A.; Lafossas, M.; Durand, C.; Bougerol, C.; Ferret, P.; Eymery, J. Metal Organic Vapour-Phase Epitaxy Growth of GaN Wires on Si (111) for Light-Emitting Diode Applications. *Nanoscale Res. Lett.* **2013**, *8* (61), 1–5. https://doi.org/10.1186/1556-276X-8-61

[58] Bavencove, A. L.; Salomon, D.; Lafossas, M.; Martin, B.; Dussaigne, A.; Levy, F.; André, B.; Ferret, P.; Durand, C.; Eymery, J.; et al. Light Emitting Diodes Based on GaN Core/shell Wires Grown by MOVPE on N-Type Si Substrate. *Electron. Lett.* **2011**, *47* (13), 765–767. https://doi.org/10.1049/el.2011.1242.

[59] Kumaresan, V.; Largeau, L.; Madouri, A.; Glas, F.; Zhang, H.; Oehler, F.; Cavanna, A.; Babichev, A.; Travers, L.; Gogneau, N.; et al. Epitaxy of GaN Nanowires on Graphene. *Nano Lett.* **2016**, *16*, 4895–4902. https://doi.org/10.1021/acs.nanolett.6b01453.

[60] Hersee, S. D.; Rishinaramangalam, A. K.; Fairchild, M. N. Threading Defect Elimination in GaN Nanowires. *J. Mater. Res.* **2011**, *26* (17), 2293–2298. https://doi.org/10.1557/jmr.2011.112.

[61] Qian, F.; Li, Y.; Gradecak, S.; Park, H.; Dong, Y.; Ding, Y.; Wang, Z. L.; Lieber, C. M. Multi-Quantum-Well Nanowire Heterostructures for Wavelength-Controlled Lasers. *Nat. Mater.* **2008**, *7*, 701–706. https://doi.org/10.1038/nmat2253.

[62] Kishino, K.; Ishizawa, S. Selective-Area Growth of GaN Nanocolumns on Si(111) Substrates for Application to Nanocolumn Emitters with Systematic Analysis of Dislocation Filtering Effect of Nanocolumns. *Nanotechnology* **2015**, *26*, 225602. https://doi.org/10.1088/0957-4484/26/22/225602.

[63] Coulon, P. M.; Mexis, M.; Teisseire, M.; Jublot, M.; Vennéguès, P.; Leroux, M.; Zuniga-Perez, J. Dual-Polarity GaN Micropillars Grown by Metalorganic Vapour Phase Epitaxy : Cross- Correlation between Structural and Optical Properties. *J. Appl. Phys.* **2014**, *115*, 153504. https://doi.org/10.1063/1.4870950.

[64] Kim, H. M.; Cho, Y. H.; Lee, H.; Kim, S. I. I.; Ryu, S. R.; Kim, D. Y.; Kang, T. W.; Chung, K. S. High-Brightness Light Emitting Diodes Using Dislocation-Free Indium Gallium Nitride/Gallium Nitride Multiquantum-Well Nanorod Arrays. *Nano Lett.* **2004**, *4* (6), 1059–1062. https://doi.org/10.1021/nl049615a.

[65] Koester, R.; Hwang, J.; Salomon, D.; Chen, X.; Bougerol, C.; Barnes, J.; Le Si Dang, D.; Rigutti, L.; Bugallo, A. D. L.; Jacopin, G.; et al. M-Plane Core-Shell InGaN/GaN Multiple-Quantum-Wells on GaN Wires for Electroluminescent Devices. *Nano Lett.* **2011**, *11*, 4839–4845. https://doi.org/10.1021/nl202686n.

[66] Boubanga-Tombet, S.; Wright, J. B.; Lu, P.; Williams, M. R. C.; Li, C.; Wang, G. T.; Prasankumar, R. P. Ultrafast Carrier Capture and Auger Recombination in Single GaN/InGaN Multiple Quantum Well Nanowires. *ACS Photonics* **2016**, *3* (12), 2237–2242. https://doi.org/10.1021/acsphotonics.6b00622.

[67] Waag, A.; Wang, X.; Fündling, S.; Ledig, J.; Erenburg, M.; Neumann, R.; Al Suleiman, M.; Merzsch, S.; Wei, J.; Li, S.; et al. The Nanorod Approach: GaN NanoLEDs for Solid State Lighting. *Phys. Status Solidi* **2011**, *8* (7–8), 2296–2301. https://doi.org/10.1002/pssc.201000989.

[68] Li, S.; Waag, A. GaN Based Nanorods for Solid State Lighting. *J. Appl. Phys.* **2012**, *111*, 071101. https://doi.org/10.1063/1.3694674.

[69] Li, J.; Zhang, G. Q. *Solid State Lighting Technology and Application Series*; 2018. http://www.springer.com/series/8864

[70] Qhalid Fareed, R. S.; Yang, J. W.; Zhang, J.; Adivarahan, V.; Chaturvedi, V.; Asif Khan, M. Vertically Faceted Lateral Overgrowth of GaN on SiC with Conducting Buffer Layers Using Pulsed Metalorganic Chemical Vapor Deposition. *Appl. Phys. Lett.* **2000**, *77* (15), 2343–2345. https://doi.org/10.1063/1.1316063.

[71] Tang, T. Y.; Shiao, W. Y.; Lin, C. H.; Shen, K. C.; Huang, J. J.; Ting, S. Y.; Liu, T. C.; Yang, C. C.; Yao, C. L.; Yeh, J. H.; et al. Coalescence Overgrowth of GaN Nanocolumns on Sapphire with Patterned Metal Organic Vapor Phase Epitaxy. *J. Appl. Phys.* **2009**, *105*, 023501. https://doi.org/10.1063/1.3065527.

[72] Choi, K.; Arita, M.; Arakawa, Y. Selective-Area Growth of Thin GaN Nanowires by MOCVD. *J. Cryst. Growth* **2012**, *357*, 58–61. https://doi.org/10.1016/j.jcrysgro.2012.07.025.

[73] Chen, X. J.; Gayral, B.; Sam-Giao, D.; Bougerol, C.; Durand, C.; Eymery, J. Catalyst-Free Growth of High-Optical Quality GaN Nanowires by Metal- Organic Vapor Phase Epitaxy. *Appl. Phys. Lett* **2011**, *99*, 251910. https://doi.org/10.1063/1.3671365.

[74] Tchoulfian, P.; Donatini, F.; Levy, F.; Amstatt, B.; Ferret, P.; Pernot, J. High Conductivity in Si-Doped GaN Wires. *Appl. Phys. Lett.* **2013**, *102*, 122116. https://doi.org/10.1063/1.4799167.

[75] Bergbauer, W.; Strassburg, M.; Kolper, C.; Linder, N.; Roder, C.; Lahnemann, J.; Trampert, A.; Fundling, S.; Li, S. F.; Wehmann, H.-H.; et al. Continuous-Flux MOVPE Growth of Position-Controlled N-Face GaN Nanorods and Embedded InGaN Quantum Wells. *Nanotechnology* **2010**, *21*, 305201. https://doi.org/10.1088/0957-4484/21/30/305201.

[76] Le Boulbar, E. D.; Edwards, P. R.; Vajargah, S. H.; Griffiths, I.; Gîrgel, I.; Coulon, P. M.; Cherns, D.; Martin, R. W.; Humphreys, C. J.; Bowen, C. R.; et al. Structural and Optical Emission Uniformity of M-Plane InGaN Single Quantum Wells in Core-Shell Nanorods. *Cryst. Growth Des.* **2016**, *16*, 1907–1916. https://doi.org/10.1021/acs.cgd.5b01438

[77] Zubialevich, V. Z.; McLaren, M.; Pampili, P.; Shen, J.; Arredondo-Arechavala, M.; Parbrook, P. J. Reduction of Threading Dislocation Density in Top-down Fabricated GaN Nanocolumns via Their Lateral Overgrowth by MOCVD. *J. Appl. Phys.* **2020**, *127*, 025306. https://doi.org/10.1063/1.5110602.

[78] Qian, F.; Li, Y.; Gradečak, S.; Wang, D.; Barrelet, C. J.; Lieber, C. M. Gallium Nitride-Based Nanowire Radial Heterostructures for Nanophotonics. *Nano Lett.* **2004**, *4* (10), 1975–1979. https://doi.org/10.1021/nl0487774.

[79] Qian, F.; Gradečak, S.; Li, Y.; Wen, C. Y.; Lieber, C. M. Core/Multishell Nanowire Heterostructures as Multicolor, High-Efficiency Light-Emitting Diodes. *Nano Lett.* **2005**, *5* (11), 2287–2291. https://doi.org/10.1021/nl051689e.

[80] Jacopin, G.; Bugallo, A. D. L.; Lavenus, P.; Rigutti, L.; Julien, F. H.; Zagonel, L. F.; Kociak, M.; Durand, C.; Salomon, D.; Chen, X. J.; et al. Single-Wire Light-Emitting Diodes Based on GaN Wires Containing Both Polar and Nonpolar InGaN/GaN Quantum Wells. *Appl. Phys. Express* **2012**, *5*, 014101. https://doi.org/10.1143/APEX.5.014101.

[81] Ra, Y. H.; Navamathavan, R.; Park, J. H.; Lee, C. R. Coaxial InxGa1-XN/GaN Multiple Quantum Well Nanowire Arrays on Si(111) Substrate for High-Performance Light-Emitting Diodes. *Nano Lett.* **2013**, *13* (8), 3506–3516. https://doi.org/10.1021/nl400906r.

[82] Hong, Y. J.; Lee, C.; Yoon, A.; Kim, M.; Seong, H.; Chung, H. J.; Sone, C.; Park, Y. J.; Yi, G. Visible-Color-Tunable Light-Emitting Diodes. *Adv. Mater.* **2011**, *23*, 3284–3288. https://doi.org/10.1002/adma.201100806.

[83] Schimpke, T.; Martin, M.; Stoll, I.; Pohl-Klein, B.; Bichler, D.; Franz, Z.; Strube-knyrim, J.; Huckenbeck, B.; Max, B.; Marcus, M.; et al. Phosphor-Converted White Light from Blue-Emitting InGaN Microrod LEDs. *Phys. stat. sol.* **2016**, *213* (6), 1577–1584. https://doi.org/10.1002/pssa.201532904.

[84] Tchernycheva, M.; Neplokh, V.; Zhang, H.; Lavenus, P.; Rigutti, L.; Bayle, F.; Julien, F. H.; Babichev, A.; Jacopin, G.; Largeau, L.; et al. Core-Shell InGaN/GaN Nanowire Light Emitting Diodes Analyzed by Electron Beam Induced Current Microscopy and Cathodoluminescence Mapping. *Nanoscale* **2015**, *7*, 11692–11701. https://doi.org/10.1039/c5nr00623f.

[85] Tchernycheva, M.; Lavenus, P.; Zhang, H.; Babichev, A. V.; Jacopin, G.; Shahmohammadi, M.; Julien, F. H.; Ciechonski, R.; Vescovi, G.; Kryliouk, O. InGaN/GaN Core − Shell Single Nanowire Light Emitting Diodes with Graphene-Based P - Contact. *Nano Lett.* **2014**, *14*, 2456–2465. https://doi.org/10.1021/nl5001295.

[86] Robin, Y.; Bae, S. Y.; Shubina, T. V; Pristovsek, M.; Evropeitsev, E. A.; Kirilenko, D. A.; Davydov, V. Y.; Smirnnov, A. N.; Toropov, A. A.; Jmerik, V. N.; et al. Insight into the Performance of Multi-Color InGaN / GaN Nanorod Light Emitting Diodes. *Sci. Rep.* **2018**, *8*, 7311. https://doi.org/10.1038/s41598-018-25473-x.

[87] Chen, H.-S.; Yao, Y.-F.; Liao, C.-H.; Tu, C.-G.; Su, C.-Y.; Chang, W.-M.; Kiang, Y.-W.; Yang, C. C. Light-Emitting Device with Regularly Patterned Growth of an InGaN/GaN Quantum-Well Nanorod Light-Emitting Diode Array. *Opt. Lett.* **2013**, *38* (17), 3370. https://doi.org/10.1364/ol.38.003370.

[88] Nami, M.; Stricklin, I. E.; Davico, K. M.; Mishkat-ul-masabih, S.; Rishinaramangalam, A. K.; Brueck, S. R. J.; Brener, I.; Feezell, D. F. Carrier Dynamics and Electro- Optical Characterization of High-Performance GaN / InGaN Core-Shell Nanowire Light-Emitting Diodes. *Sci. Rep.* **2018**, *8* (501), 1–11. https://doi.org/10.1038/s41598-017-18833-6.

[89] Zhao, M.; Liao, H.; Ning, L.; Zhang, Q.; Liu, Q.; Xia, Z. Next-Generation Narrow-Band Green-Emitting RbLi(Li$_3$SiO$_4$)$_2$:Eu^{2+} Phosphor for Backlight Display Application. *Adv. Mater.* **2018**, *30*, 1802489. https://doi.org/10.1002/adma.201802489.

[90] Latynina, A.; Watanabe, M.; Inomata, D.; Aoki, K.; Sugahara, Y.; García Víllora, E.; Shimamura, K. Properties of Czochralski Grown Ce,Gd:Y$_3$Al$_5$O$_{12}$ Single Crystal for White Light-Emitting Diode. *J. Alloys Compd.* **2013**, *553*, 89–92. https://doi.org/10.1016/j.jallcom.2012.11.096.

[91] Hoerder, G. J.; Seibald, M.; Baumann, D.; Schröder, T.; Peschke, S.; Schmid, P. C.; Tyborski, T.; Pust, P.; Stoll, I.; Bergler, M.; et al. Sr[Li$_2$Al$_2$O$_2$N$_2$]:Eu^{2+} — A High Performance Red Phosphor to Brighten the Future. *Nat. Commun.* **2019**, *10* (1824), 1–9. https://doi.org/10.1038/s41467-019-09632-w.

[92] Laubsch, A.; Sabathil, M.; Baur, J.; Peter, M.; Hahn, B. High-Power and High-Efficiency InGaN-Based Light Emitters. *IEEE Trans. Electron Devices* **2010**, *57 (1),* 79–87. https://doi.org/10.1109/TED.2009.2035538.

[93] Taki, T.; Strassburg, M. Review — Visible LEDs : More than Efficient Light. *ECS J. Solid State Sci. Technol.* **2020**, *9*, 015017. https://doi.org/10.1149/2.0402001JSS.

[94] Reineke, S.; Lindner, F.; Schwartz, G.; Seidler, N.; Walzer, K.; Lüssem, B.; Leo, K. White Organic Light-Emitting Diodes with Fluorescent Tube Efficiency. *Nature* **2009**, *459,* 234–239. https://doi.org/10.1038/nature08003.

[95] Guan, N.; Dai, X.; Messanvi, A.; Zhang, H.; Yan, J.; Gautier, E.; Bougerol, C.; Julien, F. H.; Durand, C.; Eymery, J.; et al. Flexible White Light Emitting Diodes Based on Nitride Nanowires and Nanophosphors. *ACS Photonics* **2016**, *3,* 597–603. https://doi.org/10.1021/acsphotonics.5b00696.

[96] Guan, N.; Amador-Mendez, N.; Wang, J.; Das, S.; Kapoor, A.; Julien, F. H.; Gogneau, N.; Foldyna, M.; Som, S.; Eymery, J.; et al. Colour Optimization of Phosphor-Converted Flexible Nitride Nanowire White Light Emitting Diodes. *J. Phys. Photonics* **2019**, *1,* 35003. https://doi.org/10.1088/2515-7647/ab2c84.

[97] Park, S. Il; Le, A. P.; Wu, J.; Huang, Y.; Li, X.; Rogers, J. A. Light Emission Characteristics and Mechanics of Foldable Inorganic Light-Emitting Diodes. *Adv. Mater.* **2010,** *22 (28),* 3062–3066. https://doi.org/10.1002/adma.201000591.

[98] Sun, H.; Li, X. Recent Advances on III-Nitride Nanowire Light Emitters on Foreign Substrates – Toward Flexible Photonics. *Phys. Status Solidi* **2019**, *216*, 1800420. https://doi.org/10.1002/pssa.201800420.

[99] Nadarajah, A.; Word, R. C.; Meiss, J.; Könenkamp, R. Flexible Inorganic Nanowire Light-Emitting Diode. *Nano Lett.* **2008**, *8* (2), 534–537. https://doi.org/10.1021/nl072784l.

[100] Calabrese, G.; Pettersen, S. V.; Pfüller, C.; Ramsteiner, M.; Grepstad, J. K.; Brandt, O.; Geelhaar, L.; Fernández-Garrido, S. Effect of Surface Roughness, Chemical Composition, and Native Oxide Crystallinity on the Orientation of Self-Assembled GaN Nanowires on Ti Foils. *Nanotechnology* **2017**, *28*, 425602. https://doi.org/10.1088/1361-6528/aa84a1.

[101] Mcalpine, M. C.; Friedman, R. S.; Jin, S.; Lin, K.; Wang, W. U.; Lieber, C. M. High-Performance Nanowire Electronics and Photonics on Glass and Plastic Substrates. *Nano Lett.* **2003**, *3* (11), 1531–1535. https://doi.org/10.1021/nl0346427.

[102] Chung, K.; Beak, H.; Tchoe, Y.; Oh, H.; Yoo, H.; Kim, M.; Yi, G. Growth and Characterizations of GaN Micro- Rods on Graphene Films for Flexible Light Emitting Diodes. *APL Mater.* **2014**, *2*, 092512. https://doi.org/10.1063/1.4894780.

[103] Lee, C.; Kim, Y.; Hong, Y. J.; Jeon, S.; Bae, S.; Hong, B. H.; Yi, G.-C. Flexible Inorganic Nanostructure Light-Emitting Diodes Fabricated on Graphene Films. *Adv. Mater.* **2011**, *23*, 4614–4619. https://doi.org/10.1002/adma.201102407.

[104] Dai, X.; Messanvi, A.; Zhang, H.; Durand, C.; Eymey, J.; Bougerol, C.; Julien, F. H.; Tchernycheva, M. Flexible Light-Emitting Diodes Based on Vertical Nitride Nanowires. *Nano Lett.* **2015**, *15*, 6958–6964. https://doi.org/10.1021/acs.nanolett.5b02900.

[105] Zhang, H.; Dai, X.; Guan, N.; Messanvi, A.; Neplokh, V.; Piazza, V.; Vallo, M.; Bougerol, C.; Julien, F. H.; Babichev, A.; et al. Flexible Photodiodes Based on Nitride Core/Shell p − n Junction Nanowires. *ACS Appl. Mater. Interfaces* **2016**, *8*, 26198–26206. https://doi.org/10.1021/acsami.6b06414.

[106] El Kacimi, A.; Pauliac-Vaujour, E.; Eymery, J. Flexible Capacitive Piezoelectric Sensor with Vertically Aligned Ultralong GaN Wires. *ACS Appl. Mater. Interfaces* **2018**, *10*, 4794–4800. https://doi.org/10.1021/acsami.7b15649.

Chapter 2: Growth of InGaN/GaN core-shell wires by MOVPE

This chapter will first present the basics of MOVPE growth technique explaining our state of the art of growing GaN wires using silane addition. The wire growth is then followed by the radial growth of m-plane InGaN/GaN core-shell heterostructures for fabrication of visible LEDs. Various heterogeneities have been observed during the wire growth considering the polarity inversion, indium fluctuations, gradients and length inhomogeneity. The selective area growth (SAG) of wires is also performed to control the wire growth in order to achieve a higher uniformity in wire length. Technical details regarding the mask fabrication for SAG have been discussed. The difficulties in SAG growth especially the reproducibility control is a key issue that needs further work and attention.

2.1 Self-assembled (SG) and catalyst-free growth of wires

2.1.1 Basics of MOVPE growth technique

Metal-organic vapor phase epitaxy (MOVPE) is a variant of the more general metal-organic chemical vapor deposition (MOCVD) growth technique that is used to perform the epitaxy of high-quality compound semiconductors.[1] It is now being widely used in industries for the production of LEDs, lasers, photodetectors, etc. since it offers the key advantage of epitaxial growth on large area substrates with high uniformity in terms of thickness, composition and doping with large production throughput. In comparison to molecular beam epitaxy (MBE) where an evaporated beam of molecules is directly deposited on the substrate, the MOCVD is based on chemical reactions at high temperature using organo-metallic precursors involving metal atoms. Then, metal-organic precursors are mixed with a carrier gas (H_2, N_2 or a mixture) to enter the MOCVD reactor. The gas mixture passes over a heated substrate that is rotated with a given speed. Different reactions may occur resulting in the breaking of molecular bonds due to pyrolytic reactions and the desired atoms are deposited on the substrate surface. The thermodynamic processes are followed by the formation of some intermediate species or byproducts that are filtered out of the equipment and purified with a scrubbing system. **Figure 2.1** shows an overview of the MOVPE process.[2] The species formed during the chemical reactions can be absorbed and diffuse along the surface before getting incorporated. The desorbed species and other undesirable products are then evacuated through the exhaust system.[2]
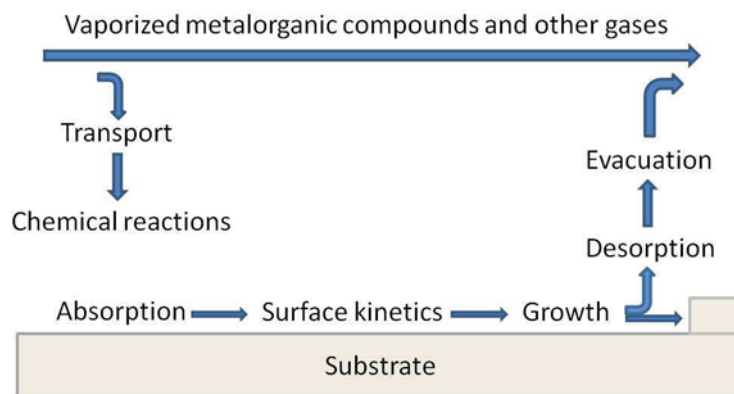
Figure 2.1: The overview of the MOVPE process. (Adapted from *Ref. 2*)

The MOCVD growth can be classified into three main regimes. During low temperature, the growth rate is governed by the reaction rates and byproduct desorption, which increase with temperature: this growth regime is kinetically limited. At higher temperature, the growth rate is then governed by the precursor flux in gas phase and becomes independent of temperature: the growth is limited by mass transport. At even higher temperatures, different reactions begin to dominate such as evaporation of the deposited materials, etching, surface desorption etc. The growth rate therefore decreases with the increase of temperature: the growth is high temperature limited. A high temperature around 1040 °C is typically chosen for GaN grown by MOCVD, which corresponds to the mass transport regime, but quite close to the high temperature one. A balance between the amount of material deposited and the etching effects (for example under H_2 carrier gas when no materials are provided) is achieved by using optimized growth pressure, temperature and carrier gas.

Figure 2.2: The Thomas Swan (Aixtron) 3x2" CCS MOVPE reactor (left). View on the susceptor with three 2" substrates (right). (*Ref. 3*)

An Aixtron 3x2'' Closed Coupled Showerhead MOVPE system has been used in the present Ph.D. work to grow nitride semiconductor materials with different types of organometallic precursors (reactor shown in **Figure 2.2**).[3] Trimethylgallium (TMGa) and triethylgallium (TEGa) are both used as group-III precursors for Ga deposition. TMGa has higher vapor pressure and has been used in the GaN wires growth. TEGa on the other hand is generally used in the growth of InGaN/GaN heterostructures since it lowers the growth rate to control accurately the thickness of the shell and also reduces the carbon incorporation. Trimethylaluminium (TMAl) and trimethylindium (TMIn) act as group-III precursors for Al and In, respectively. Highly purified ammonia (NH_3) gas is used

as group-V precursor. The precursors used for n and p-type doping are Cp_2Mg (Bis(cyclopentadienyl)magnesium for magnesium doping) and SiH_4 (for silicon doping) respectively. The reactor is based on vertical closed coupled showerhead technology that allows a homogenous distribution of the reagent gases leading to a uniform growth rate, doping and composition. The substrates are placed on a susceptor having three circular 2'' pockets. A three-zone heater is mounted below the susceptor, each of which is controlled separately to achieve a highly uniform temperature distribution across the full susceptor surface. The temperature is measured by a thermocouple placed under the susceptor. It is worth mentioning that the real value of temperature at the substrate surface is not directly provided by the thermocouple. Therefore, temperature calibration is required on regular basis. It is performed using the pyrolysis probes installed at top of the reactor that trace the substrate surface temperature in different zones during several calibration runs. This is followed by the optimization of power injected in the three zones to minimize the temperature variation (if any). It is one of the key parameter that needs to be considered, especially while growing InGaN/GaN heterostructures since the growth temperature directly influences the indium incorporation in InGaN layers. The indium variations induced by variation in growth temperature has been observed in the present work and will be discussed in section 2.2.2.

2.1.2 Catalyst-free growth of GaN wires with silane addition

The first installation of MOCVD equipment in our laboratory took place more than 10 years ago (2007). The work of former PhD students Robert Koester (2006-2010), Xiaojun Chen (2008-2011), Damien Salomon (2010-2013) and Agnès Messanvi (2013-2015) allowed the determination and optimization of GaN wire growth using silane flux and also provided some elements for the understanding of wire growth mechanism by MOVPE. Detailed analysis of wire-growth and influence of different growth parameters have been well-documented in their thesis[3,4,19,5] and in our previous report.[6,7] This section will briefly explain the growth mechanism of self-assembled GaN wires with the typical growth parameters used for the wire growth on c-sapphire substrates.

The c-sapphire substrates are firstly baked in the presence of hydrogen (H_2) at 1040 °C for 20 min to clean the surface. This is followed by nitridation step under NH_3 gas flow (2000 sccm) for 30s to form an ultra-thin AlN layer on sapphire substrates to favor the N-polarity GaN seed growth.

The resulting nitridated substrates are then exposed to simultaneous flow of NH_3 and SiH_4 with a mass flow of 4000 and 200 nmol/min respectively to form a thin SiN_x layer ($\approx$ 1.5 nm). This layer formation is probably not continuous with compositional fluctuations and can form small openings allowing GaN seed nucleations. The SiH_4 flow is then switched off, the flow of NH_3 is reduced to 1000 sccm (44.64 nmol/min) and TMGa precursor is injected in the reactor with a flow rate of 60 sccm (135 µmol/min). A short step of GaN nucleation takes place under N_2 (8000 sccm) at 1040 °C to get hexagonal nucleation discs with flat top surface. Then, the growth parameters are fixed to favor wire formation, while the carrier gas stays under N_2 flow (500 sccm)[*]. The key parameters governing the wire dimensions are growth temperature, pressure, V/III ratio, precursor flow and silane addition. With increasing growth temperature, the wire density and length decrease, while the diameter of wires increases. Therefore, an optimum temperature of 1040 °C is used for the wire growth. A low V/III ratio and high growth pressure favors the vertical growth. In our wire growth, the V-III ratio around 50 is chosen and the growth pressure is set to 800 mbar. The amount of precursor flow (despite having a low V/III ratio) also plays a key role. With increasing precursor flow, the wires tend to become thicker to compensate the amount of material present in the reactor. Therefore, a moderate TMGa precursor flow of 135 µmol/min is injected during the wire growth.

Further, the role of silane is one of the key parameter governing the wire formation in our work. The silane gas not only acts as a n-type dopant but also leads to the formation of a SiN_x layer around the wire sidewalls. Detailed investigation about the influence of SiH_4 has been performed earlier in our group.[6] Initially, the presence of silicon atoms has been detected on the wire surface by ToF-SIMS measurements. Later, I-V measurements confirmed the formation of SiN_x dielectric shell around the wire. This SiN_x layer provides passivation of wire sidewall facets that avoids any lateral growth and favors the vertical growth leading to the wire-geometry. For all other growth parameters fixed, the mechanism responsible for wire formation with the help of silane can be summarized as follows: after the nucleation step of GaN seeds mentioned above, the silane is added to the reactor in the presence of TMGa and NH_3 in the gas phase. The seeds elongate laterally with some Si atoms diffusing inside the wire core leading to n-type doping. However most of the Si atoms are accumulated on the seed lateral surface. The wire diameter keeps expanding with

---

[*] Considering silane dilution in H_2 and N_2 flow in the optical port, we can estimate to 10 % of H_2 in the reactor under standard conditions.

increasing concentration of Si on the surface. But, after reaching a threshold, the Si atoms forms with N atoms a thin SiN_x layer on lateral facets. This layer passivates the sidewall surface and inhibits the lateral growth of the wire-core. Interestingly this passivation does not occur on the wire top. Although the exact mechanism has not been understood but two probable causes can be assumed. It is possible that the formation energy of SiN_x on the $\bar{c}$-plane is different w.r.t. m-plane. Another explanation proposed by Tessarek *et al.* is that the high growth temperature under Ga-rich environment during the wire growth can lead to the formation of Ga droplets on the wire top that has a low solubility for Si.[8][†] The wire diameter thus becomes constant and all the adsorbed species will contribute to the top wire facet favoring the wire-geometry. The continuous formation of SiN_x layer on wire sidewalls due to simultaneous reactions between TMGa and NH_3 precursors allows the vertical growth of wire with n-type doped core and having a fixed diameter.

The optimized growth parameters for GaN wire formation has been summarized in **Table 2.1** and a corresponding scanning electron microscopy (SEM) image of the as-grown GaN wires is shown in **Figure 2.3**. These parameters remains similar throughout the Ph.D. work concerning the self-assembled wire growth. However, the influence of silane has been studied in the case of organized wire growth and will be discussed in section 2.3.2.1.
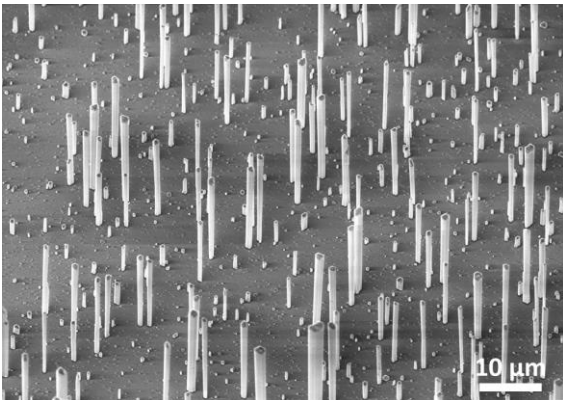
Figure 2.3: SEM images of as-grown GaN wires with the growth parameters mentioned in Table 2.1.

Growth temperature	1040 °C
Growth pressure	800 mbar
V/III ratio	15
TMGa Precursor flow	135 µmol/min
Silane flow	150 nmol/min

Table 2.1: Growth parameters for self-assembled GaN wires.

[†] Note that for thick wires, this droplet should be very large. The fact that we never observed this droplet even by decreasing quickly the temperature under N2 flow seems to be contrary to the second explanation.

2.1.3 *M*-plane InGaN/GaN MQW growth for core-shell heterostructures

The present thesis based on visible LEDs demands the growth of InGaN/GaN core-shell heterostructures. The direct growth of InGaN around the GaN wire is not possible due to SiN_x passivation layer on the sidewall surfaces. However, it has been demonstrated by Koester *et al.*[6,9] that the wires can continue to grow vertically even if the silane flux is switched off after gaining a wire length of about 5 µm. This leads to a heavily doped bottom part of the wire ($N_d \approx 10^{20}$ cm^{-3})[10,11] named as the 'n-part', while the upper part of the wire corresponds to the unintentionally doped part named as the 'u-part' that contains a residual n-type doping ($N_d \approx 10^{18}$ cm^{-3})[11]. The reason of vertical growth of the 'u-part' without the silane flux is not fully understood, but it is attributed to the residual Si species present in the reactor that forms a residual Si-rich ultra-thin layer on wire sidewalls, as observed in the Chapter 4. Nevertheless, this residual layer does not act as effective passivation layer because the shell growth can be easily performed on this 'u-part', contrary to the 'n-part'. Note that the Si also has an influence on the $\bar{c}$-plane top surface of the wire: we have a longitudinal growth with silane that is stopped without silane.

To grow core-shell InGaN/GaN heterostructure on the u-part, the precursors used for In and Ga are TMIn and triethylgallium (TEGa), respectively. For this core-shell growth, the reactor pressure is decreased to 400 mbar and the carrier gas is remains N_2 to avoid any indium etching that occurs in presence of H_2. Note that the GaN wire growth having n and u-part with fixed growth parameters explained above has been taken as a template in the present thesis work. Different structures have been grown to target a given wavelength emission by varying the growth parameters of InGaN quantum wells QWs and GaN barriers and will be described systematically later in Chapter 3. An example of growth parameters of InGaN/GaN MQWs structure targeting an indium composition around 15% for blue emission has been mentioned in **Table 2.2**.

	TMIn flow (µmol/min)	TEGa flow (µmol/min)	NH₃ flow (mmol/min)	Growth temperature	Growth time
InGaN QW	8.1	3.64	22.32	720 °C	80 s
GaN barrier	-	14.57	22.32	885 °C	150 s

Table 2.2: Growth parameters for InGaN/GaN MQW heterostructure targeting 15% In-composition for blue emission.
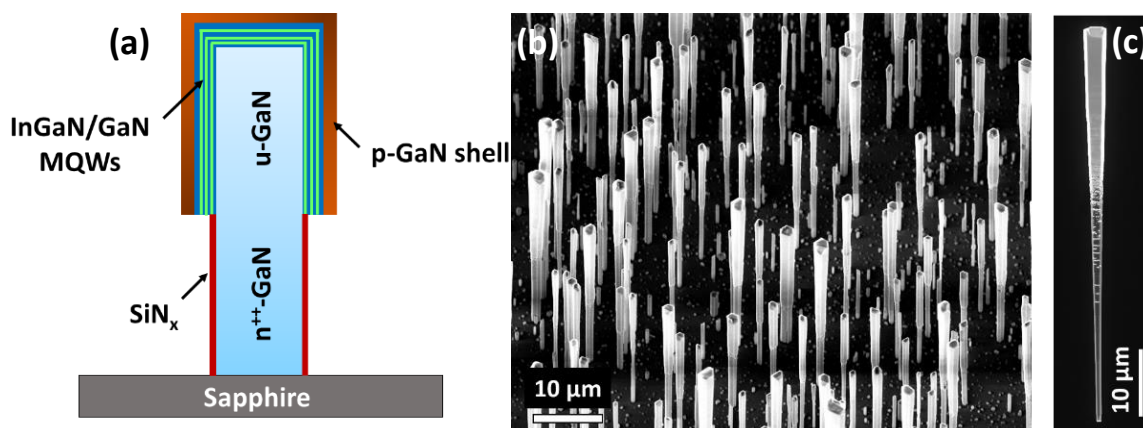
Figure 2.4: (a) Schematics of core-shell InGaN/GaN MQW structure grown on sapphire substrate, (b) 30° titled SEM image of as-grown wires (#T2512) and (c) SEM image of single wire dispersed on silicon corresponding to another sample (#T2610).

The growth of InGaN/GaN shell around the wire can be followed by the growth of a p-GaN shell at 920 °C using Cp_2Mg as a precursor for Mg incorporation and annealing at 700 °C for 20 min under N_2 to activate dopants. **Figure 2.4 (a)** shows a schematic of the final structure with core-shell InGaN/GaN MQWs located only on the upper u-part of the wire covered by a p-GaN shell, while the bottom n-part corresponds to n-GaN core without any lateral growth due to selectivity of shell growth. Such a design of the core-shell wire geometry is also beneficial for the final electrical contacts while integrating the wires in a LED device, as it allows the access to p-GaN (wire-top) and n-GaN (wire-bottom) separately. A SEM image of as-grown core-shell InGaN/GaN wires has been shown in **Figure 2.4 (b)**. The wire diameter increases at the top compared to the bottom with a difference in Z-contrast thanks to the "In-Lens" detector. A single wire SEM image of dispersed wire[‡] in **Figure 2.4 (c)** clearly shows the growth of InGaN/GaN shell around the u-part located in the upper part of wires. Some residual depositions are present in the transition region from n-GaN to u-GaN part, related to the silane gas switching off to grow u-GaN. In this case, a non-uniform thickness of SiN layer with varying composition certainly occurs with the remaining residual silane in the reactor. This might lead to a partial passivation of wire sidewalls thus allowing left over material deposition that takes place at different locations on the wire surface.

[‡] The wires depicted in Figure 2.4 (b) and (c) corresponds to two different growths. Mainly the growth time has been increased for single wire image that explains the increased wire length.

2.2 Heterogeneities encountered in the wire growth

Different scalable heterogeneities have been observed in the self-assembled wire growth covered by InGaN/GaN MQWs. The mixed wire-polarity, indium local fluctuations or gradients in the LED structure and non-uniformity in the wire length are presented in this section. The understanding of their origin and influence on the final device performance will be discussed.

2.2.1 Inversion domain of polarity
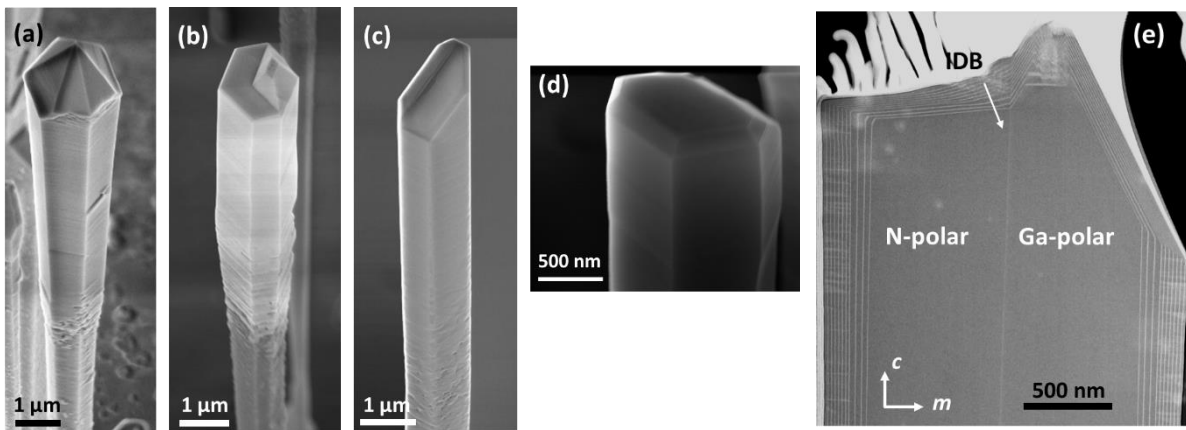
Figure 2.5: InGaN/GaN core-shell wires: (a)-(d) SEM images of single wires showing different shapes of wire-tops and (e) TEM image showing the coexistence of dual polarity in the same wire slice.

(a) #T2601 (b) #T2536, (c) #T2483, (d) #T2523 and (e) #T2612.

The shape of the wire top is governed by the crystal polarity of the wire.[12] Although the growth is mainly dominated by N-polar wires with a flat top surface, wire tops with different shapes have also been observed during the growths as shown in **Figure 2.5 (a)-(d)**. The presence of inclined surface (semi-polar crystallographic planes) on the wire top indicates the existence of Ga-polarity phase within the wire. A STEM image acquired for a core-shell InGaN/GaN wire cross-section in **Figure 2.5 (e)** clearly shows the coexistence of the two polarities present in the same wire (N-phase related to flat top surface and Ga-phase to the inclined top surface) separated by an Inversion Domain Boundary (IDB). The presence of dual polarity in GaN micropillars has also been reported by Coulon *et al.*[13] The work reported by Chen *et al.*[12] explains that the presence of opposite polarities in GaN crystals is related to the nature of the nucleating surfaces: Ga-polar crystal is preferentially formed on SiN_x mask, whereas N-polar crystal on nitridated c-sapphire surface.

Due to the different growth rate of ±*c*- and semi-polar InGaN QWs in Ga- and N-polar phase, a variation in indium composition can be expected. At high current injection, the overall emission from wires is mainly governed by *m*-plane sidewall QWs, while the current pathway is mostly dominated by the *c̄*- or semi-polar plane QWs at low injection. This has been observed during the measurements performed on final wire-LED devices and will be detailed in Chapter 5. Therefore, the issue of mixed polarity may not have a strong influence on the device emission at high applied bias voltage, but can highly affect the luminescence as low current injection.

2.2.2 Inhomogeneities in indium composition

We measured a multi-scale inhomogeneity in the indium composition in core-shell InGaN/GaN wires, which becomes more pronounced as one approaches long wavelength emission. A photoluminescence mapping performed on half-2'' sapphire wafer is shown in **Figure 2.6**.[§] The PL spectra at edges and center of the wafer in **Figure 2.6 (c)** and **Figure 2.6 (d)** show an emission around 445 and 430 nm respectively (corresponding positions are indicated **(a)** and **(b)**). The difference of 15 nm in wavelength emission is attributed to different indium content present in the core-shell wires and is related to the temperature variation across the susceptor surface. Clearly in this case, the growth temperature is higher in the center of the pocket compared to the edges. Such
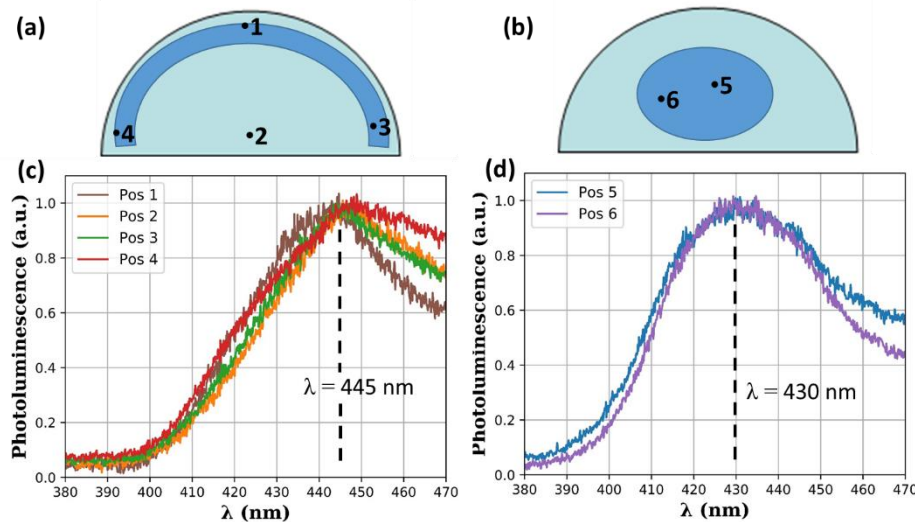
Figure 2.6: Photoluminescence measurement at room temperature scanning a half size of 2'' sapphire wafer - (a,c) and (b,d) show the measurements performed on the boundary and center of the wafer respectively.

[§] The structure consists of InGaN/GaN MQWs with QWs and barriers grown at 720 °C and 885 °C respectively.

a difference in wavelength emission may be less significant while targeting blue emission but is critical while achieving green emission as it will be explained in Chapter 3. A careful adjustment of the reactor heating zones could improve such temperature gradients, but it cannot be easily performed in our research reactor.

Apart from large scale inhomogeneous indium composition, the indium distribution also varies locally inside a single InGaN/GaN core-shell wire. A gradient of well thickness around 14% along the wire length of about 1.5 µm has been already observed along our wires[9] that can also lead to a gradient in indium composition and is also observed in this Ph.D. work and will be described in Chapter 3. At a given height, a variation in indium incorporation from well to well (in MQW) and also local fluctuations present inside a single QW can be seen in electron microscopy experiments (imaging and spectroscopy). For example, previous work in collaboration with Lorenzo Rigutti at University of Rouen has measured thin slices of core-shell InGaN wires targeting blue emission by atom probe tomography (APT) as shown in **Figure 2.7**.[14**] A non-uniform indium distribution
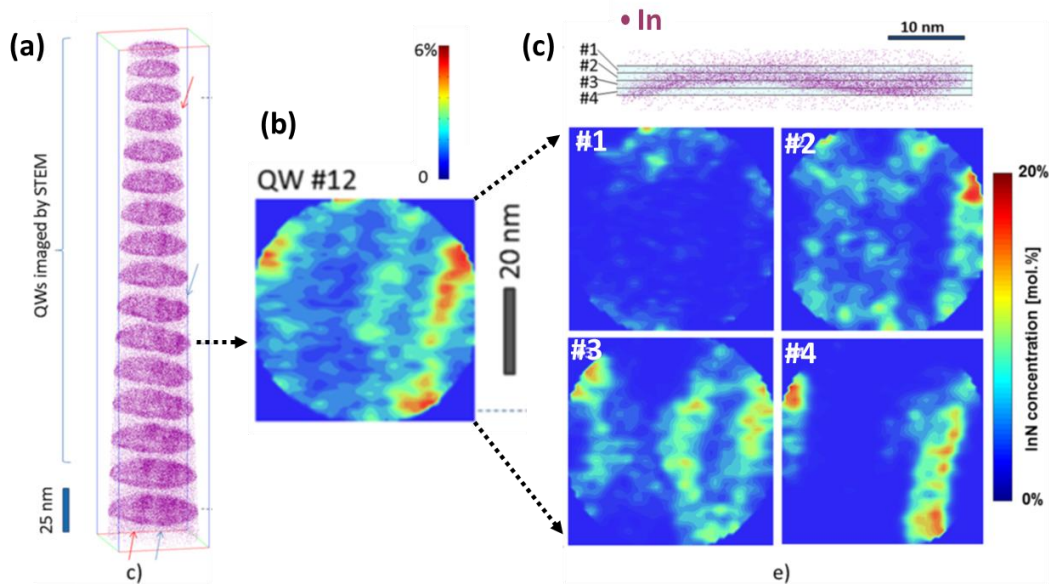
Figure 2.7: (Adapted from *Ref. 14*) Atom probe tomography measurements. (a) 3D reconstruction of the In-atom distribution in a wire slice, oriented along the [0001] zone axis but tilted to show the non-uniform In-distribution within the QW planes, (b) 2D-mapping of the in-plane fraction of InN calculated through 8 nm thick box of QW #12; and (c) InN fraction maps within 1 nm thick slices of QW #12 as shown in the upper part of the figure.

[**] The structure consists of InGaN/GaN MQWs with QWs and barriers grown at 750 °C and 870 °C respectively and the wire slice has been prepared by FIB.

can be seen in the 3D reconstructed volume (see **Figure 2.7 (a)**), oriented along [0001] zone axis but titled in another perspective. The concentration map for 8 nm thick box of QW number 12 in **Figure 2.7 (b)** shows strip-like In-rich regions approximately directed along the *a*-axis (also visible in **Figure 2.7 (a)** for other QWs) that can be attributed to the segregation at the stacking faults. We can suppose that a strain field induced by these defects will favor the clustering of In-atoms. The concentration maps of 1 nm thick slices of QW #12 volume are also measured in **Figure 2.7 (c)** showing that a maximum InN fraction of about 20 % is present in the In-rich regions contrary to the average in-plane composition of around 8 % (data not shown here). Similar APT measurements have also been performed on InGaN/GaN core shell wires targeting green emission which reveal In-rich and In-poor bands in a 2D map of In-composition for a cross-section of 2 nm thick QW slice (will be discussed in Chapter 3).

2.2.3 Length variations in wire-assembly

It is desirable to achieve a good uniformity in wire length in order to incorporate all wires efficiently in the final LED device. In electroluminescence where electrical contacts play a role, the inhomogeneity in wire length limits the total number of emitting wires.[††] Previous Ph.D. work of X.Chen[4] has investigated the length evolution for shorter wires (~ 25 μm) keeping the growth time in the range (100-400 s) for both n-GaN and u-GaN part and observed a linear dependence of wire length with time.[‡‡] The Ph.D. work of El Kacimi[15] in our group also studied wire length (for n-GaN only) at very long growth time up to 14000 s. A quasi linear dependence has been observed for growth time between (1000 and 8000 s) followed by a saturation for very long growth times (>10000 s). Further studies about the evolution of length for both n-GaN and u-GaN with higher growth times is important for the present Ph.D. work. A distribution in the wire length has also been investigated as explained hereafter.

Different growths have been performed by varying the growth time of n-GaN and u-GaN keeping identical all other growth parameters. The growth time of n-GaN is varied between (300-2500 s). A similar range of growth time is also chosen for u-GaN by keeping a fixed duration of n-GaN to

---

[††] This point will be further elaborated in Chapter 5 during the discussion about issues observed in LED devices.
[‡‡] It is worth recalling that the n-GaN and u-GaN are grown with and without silane flow, respectively.

be 1500 s. The change in length can be seen in **Figure 2.8 (a)** and **(b)**. The lengths have been estimated by measuring the average of ten wires on a given SEM image.[§§] The insets label the part of the wire measured. A growth rate of ≈ 180 μm/hr is observed for n-GaN while the trend is non-linear in the case of u-GaN. The maximum duration of 2500 s yields a length of about 120 (± 3) μm for n-GaN wires and 37(± 5) μm for u-GaN part of the wires. To check if u-GaN wire part can be further elongated vertically, additional growths at longer duration > 2500 s for u-GaN are also performed but a high density of lateral overgrowths are observed. Perhaps, the wire without silane addition i.e. the u-GaN part is able to grow till a threshold height by consuming the residual silane inside the reactor and then starts to grow laterally. This concludes that the active shell consisting of InGaN/GaN QWs covering the u-GaN part can have a maximum length of about 37 μm (for growth time of 2500 s), while the length of n-GaN wires can be elongated by simply increasing the growth time.
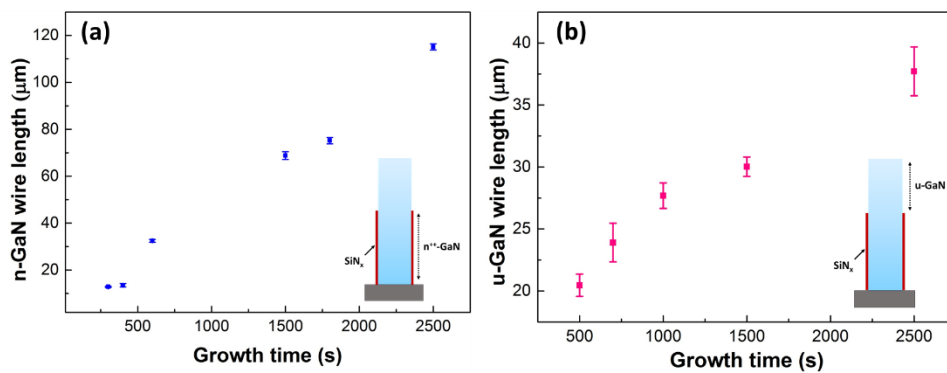
Figure 2.8: Wire length vs growth time for (a) n-GaN part and (b) u-GaN part.

Even for a fixed growth time keeping same all other growth parameters, a distribution in the total wire length has been observed. **Figure 2.9** shows the SEM images of three different growths by varying the growth time with their corresponding length distribution histograms. In **Figure 2.9 (a)** and **(b)**, a longer growth time for n-GaN part and a shorter growth time for u-GaN part shows a relatively better uniformity for the wire length. For a similar growth time of n-GaN, the distribution in length increases when a higher growth time for u-GaN is used in **Figure 2.9 (c)**. Generally, the nucleation of wires does not occur at the same time, the seeds formed first will grow into longer wires as compared to the seeds appearing later. This effect can partially lead to a non-uniformity in n-GaN wire length, which is further elevated by a longer growth time of u-GaN. Another cause

---

[§§] The SEM images are acquired with In-Lens detector to highlight the Z-contrast.
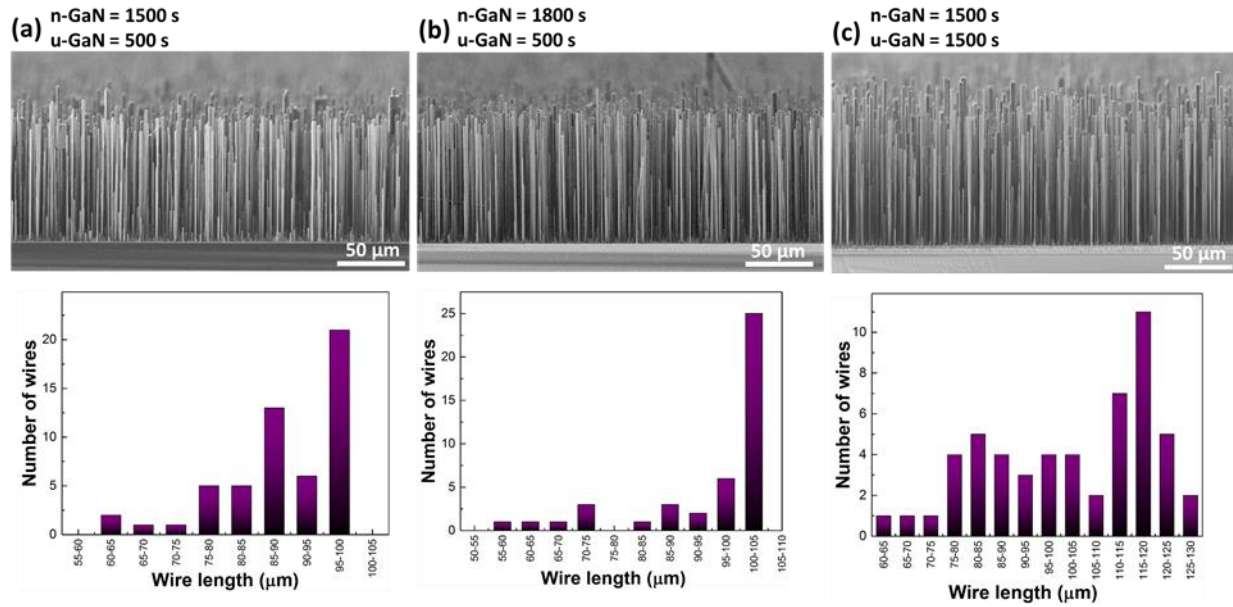
Figure 2.9: SEM images for n-GaN wires followed by u-GaN wire growth for different growth time with corresponding length distribution curves below (a) n-GaN = 1500 s, u-GaN = 500 s; (b) n-GaN = 1800 s, u-GaN = 500 s and (c) n-GaN = 1500 s, u-GaN = 1500 s. (a) #T2449, (b) #T2450, (c) #T2459
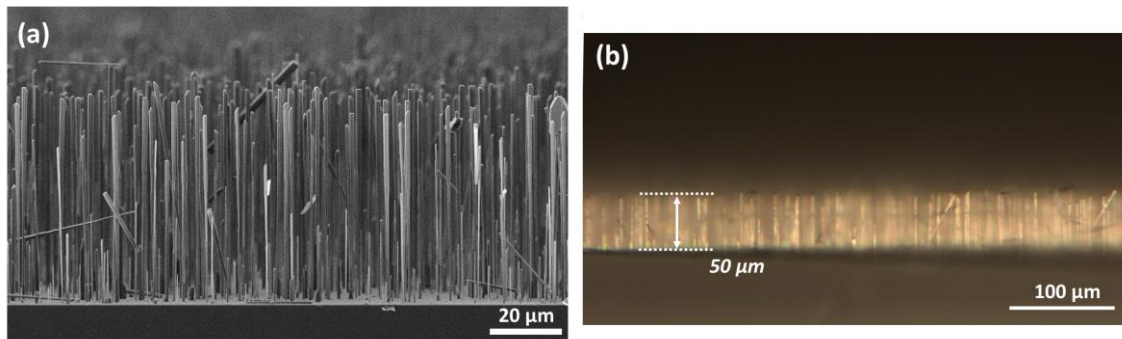
Figure 2.10: SEM image showing the cross-section of InGaN/GaN core-shell wires with growth time of n-GaN = 600 s and u-GaN = 400 s (#T2394).

of length fluctuation is also coming from polarity mixing. For example, it is often seen that the top semi-polar of the Ga-polar wire is growing slower. At least, the gas phase diffusion and the resulting non-homogeneous incorporation at the wire tip can also play an important role that has to be estimated. Nevertheless, an average of the total wire length is usually considered for integration in the final device. A typical growth time for n-GaN as 600 s and u-GaN as 400 s has been used to grow the GaN wires serving as a template for core-shell heterostructures. The average length of wires measured with the help of an optical microscope is estimated to be around 50 μm as shown in **Figure 2.10**.

2.3 Route to achieve uniformity in wire lengths: Organized wires

The growth of self-assembled wires with core-shell geometry has been well established by our group so far. However, the random position of the wires with non-uniform length affects the performances of the final wire-based LED device.[***] To tackle this problem, it has been proposed in the literature to use selective area growth (SAG) of wires to better control over wire dimensions and density.[16,17,18] The work based on organized growth in our group has been initiated in the Ph.D. work of Xiaojun Chen[4] and later continued within the framework of former Ph.D. student Agnès Messanvi.[19] Their works allowed a detailed understanding of various growth parameters to determine the growth conditions to achieve the SAG of ordered wire arrays,[20] however additional study is required to improve the quality of the wire-growth and to improve the reproducibility control. This section therefore focusses on further optimizations of the SAG growth. Section 2.3.1 will mainly give an overview of the mask fabrication involving the cleanroom processing and MOCVD growth conditions that have been previously accomplished in the group. The different difficulties observed during the SAG growth has been discussed in section 2.3.2 considering both the technicalities involved in the mask fabrication as well as MOCVD growth conditions.

2.3.1 Methodology involved in selective area growth (SAG) on sapphire

A 100 nm thick Si_3N_4 layer is firstly deposited on sapphire substrates using plasma enhanced chemical vapor deposition (PECVD).[†††] The substrates are thoroughly cleaned with acetone, isopropanol (IPA) and de-ionized (DI) water using an ultra-sonication bath for 5 minutes in each solution. A 'UV-5' photoresist is deposited on the substrates at 4000 rpm with acceleration of 2000 rpm/s for 60 s to achieve a thickness of around 500 nm. The samples are pre-baked at 130 °C for 90 s to allow the solvent evaporation. A lithography mask having circular holes with diameter of 1 µm with a pitch of 5 µm is used for deep ultra-violet (DUV) exposure during 1.3 s. Note that a study of selective growth with different opening sizes has been performed previously in the work of X. Chen and A. Messanvi. It is revealed that the opening of 1 µm is well adapted for N-polar

---

[***] This point will be further discussed in Chapter 5.
[†††] It is performed with the help of Delphin Constantin at PTA-BCAi cleanroom.

wires with our growth conditions.[‡‡‡] Following the exposition, the samples are post-baked at 130 °C for 60 s and then introduced in AF326 MIF for 60 s to develop the photoresist. They are finally washed with DI water to remove the residues of the developer if any. A reactive ion-etching (RIE) is performed to etch the Si_3N_4 layer from the holes while the remaining surface is protected by the resist. A mixture of 73 sccm of C_4F_8 and 5 sccm of O_2 gas under a pressure of 20 mTorr with 150 W of radio frequency power is used for 23 min 30 s[§§§]. The samples are cleaned to remove the resist from the surface using the similar ultra- sonication with three solutions mentioned above. **Figure 2.11** shows SEM images of a patterned sapphire substrate.
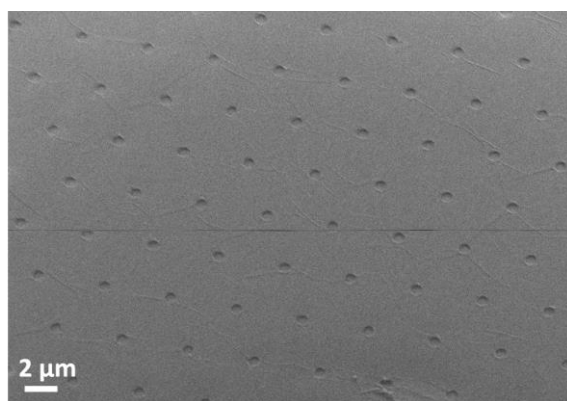
Figure 2.11: SEM image of a sapphire substrate patterned with 100 nm-thick Si_3N_4 mask.

The sapphire substrates patterned with Si_3N_4 mask are introduced inside the MOCVD reactor to perform the wire growth. The initial surface cleaning and nitridation step is similar to self-assembled wire growth explained before. The GaN nucleation takes place at 950 °C for 200 s with TMGa and NH_3 precursor flows. A high V/III ratio around 990 is preferred to allow the planar growth inside the holes. After, the TMGa source is stopped and the temperature is ramped from 950 to 1040 °C under NH_3 flow for 200 s. Finally, the TMGa supply is restarted along with silane to promote wire growth. The two-step growth with different parameters for nucleation and wire growth respectively is a critical point because filling of the openings determines the orientation and shape of the wires. The low temperature nucleation step allows a homogeneous filling of the

---

[‡‡‡] Ga-polar wires with overgrowths on the mask is observed in the selective growth for hole size < 1 µm.
[§§§] The samples are mounted on a 4 inch silicon carrier wafer by putting *Fomblin*® oil at the back side to allow a good thermal contact during etching. The etching parameters have been optimized by a former Post doc in our team named Martin Vallo.

openings with a flat seed of GaN, while a high temperature promotes the wire growth.[20] The optimized growth conditions for SAG growth with all the parameters have been listed in **Table 2.3**. The growth of GaN wire ordered array is followed by the growth of core-shell InGaN/GaN MQWs with the similar growth parameters used for self-assembled growth.

	Temperature	Pressure	NH$_3$ flow (mmol/min)	TMGa flow (µmol/min)	Silane flux (nmol/min)	V/III ratio
Nucleation	950 °C	200 mbar	44.64	45.07	-	990
Wire growth	1040 °C	300 mbar	6.69	135.22	258	50

Table 2.3: Growth conditions for SAG growth on sapphire patterned with SiN mask.

2.3.2 Difficulties related to SAG and reproducibility control
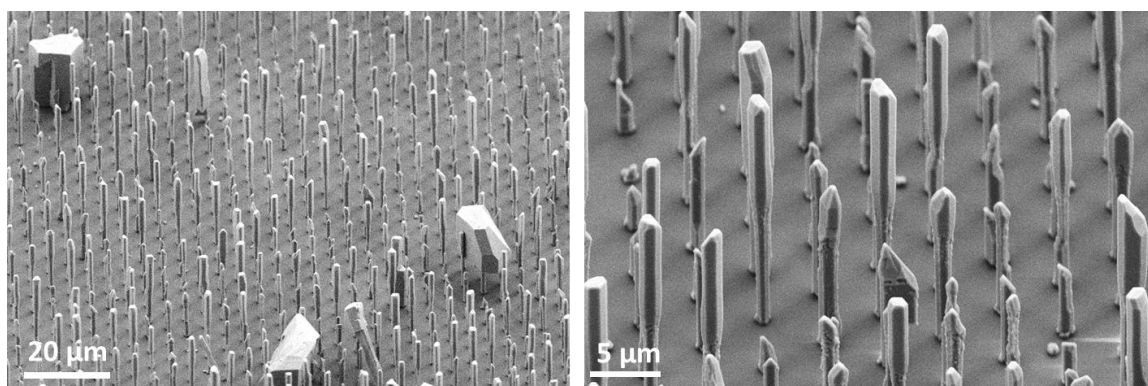
Figure 2.12: SEM images showing SAG growth of InGaN/GaN core-shell structure performed with optimized growth conditions corresponding to Table 2.3 (#T2366).

The optimized growth parameters mentioned above demonstrated the scope of achieving selective InGaN/GaN heterostructures on patterned sapphire substrates. Many growths are performed one after the other using the same optimized growth parameters, but a difference in wire growth is observed. The SEM images at different magnifications in **Figure 2.12** shows truncated wire tops sometimes with mixed polarity, non-uniform wire length and presence of overgrowths. These difficulties defeat the key advantages expected from SAG growth over self-assembled growth and hence needs further optimization.

2.3.2.1 Influence of silane flow
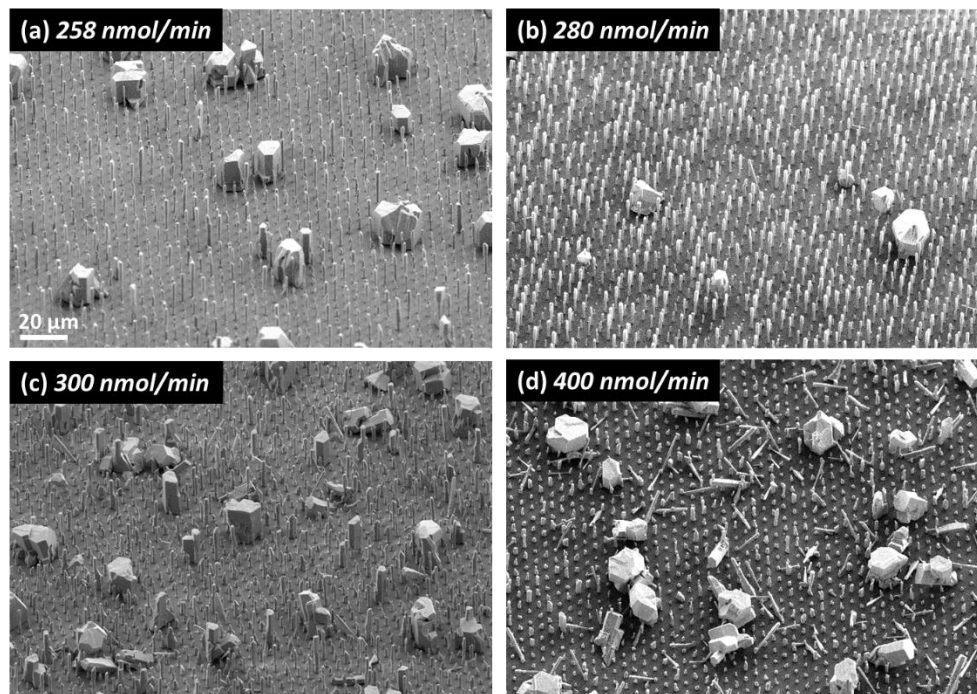
Figure 2.13: SEM images for SAG growth of InGaN/GaN core-shell wires for different silane flows: (a) 258 nmol/min, (b) 280 nmol/min, (c) 300 nmol/min and (d) 400 nmol/min. (a) #T2366 (b) #T2372 (c) #T2380 (d) #T2376.

Following the detailed investigation of different growth parameters, it is realized that perhaps the influence of silane also plays a role and can be further optimized. A series of growth experiments is performed by varying the silane flow keeping all other growth parameters fixed. **Figure 2.13** shows SEM image of SAG growths performed using silane flow of 258, 280, 300 and 400 nmol/min. It can be observed that silane indeed plays a role in the SAG growth and the effect is mainly related to the presence of large overgrowths. A high density of overgrowths with poor quality of wire growth is visible in **Figure 2.13 (c)** and **(d)**. In this case, the large silane flux certainly limits the wire-growth (due to strong passivation of wire surfaces) and the species are mainly incorporated in the big clusters/overgrowths. **Figure 2.13 (b)** shows minimum overgrowths with an appreciable density of wires. At even lower silane flow (see **Figure 2.13 (a))**, an increase of overgrowths occurs probably due to the enhanced lateral growth of wires related to an inefficient passivation of wire sidewalls, although the filling ratio of openings is improved. This result indicates that an optimum amount of silane flow is required to limit the overgrowths while promoting the wire geometry: 280 nmol/min is the optimized value for our SAG growths. Apart

from reducing the overgrowths with the help of silane, the other difficulties like lack of wire formation inside all openings and the non-uniformity in wire lengths having mixed polarity still remain.

2.3.2.2 Technological issues in fabricating the SiN$_x$ mask

After a detailed study of growth parameters during the SAG growth, we also focused our attention to the Si_3N_4 mask fabrication on sapphire substrates. The surface preparation before introducing the substrates inside the reactor is expected to play an important role in governing the quality of wire growth. The cleaning of the substrates and performing DUV lithography on sapphire, which is transparent, creates some key challenges that should also be considered. Repeated cleaning of the substrates with a longer duration of ultra-sonication is performed to prepare new patterned substrates. In addition, different modifications have been performed in the DUV lithography as well as in the etching parameters of Si_3N_4 and each time the SAG growth is systematically checked with SEM.[****] Among these changes, the growth improved remarkably when the resist is exposed for a longer duration i.e. 2.6 s (unlike the previous value of 1.3 s) and developed for lesser time i.e. 20 s (previous developing time is 60 s). A longer exposure perhaps allows the formation of openings having sharp edges with no residual resist remaining inside each hole, while a shorter developing time is beneficial to prevent the removal of resist from the remaining surface.[††††] These modifications proved beneficial and the resulting SAG growth can be seen in **Figure 2.14** at different magnifications of tilted-SEM images. The improved filling ratio of the openings, uniformity in the wire length and negligible overgrowths on a large scale area of the substrate can be observed.

The optimized SAG growth parameters along with the improved surface preparation for Si_3N_4 mask is then used to perform several growths one after the other. **Figure 2.15** shows the SEM images of organized wire growth indicated by the sample number on the top left of the images.

[****] The impact of all the changes in lithography and etching parameters has not been shown here.
[††††] Note that this resist acts as a protection for Si_3N_4 layer during etching.
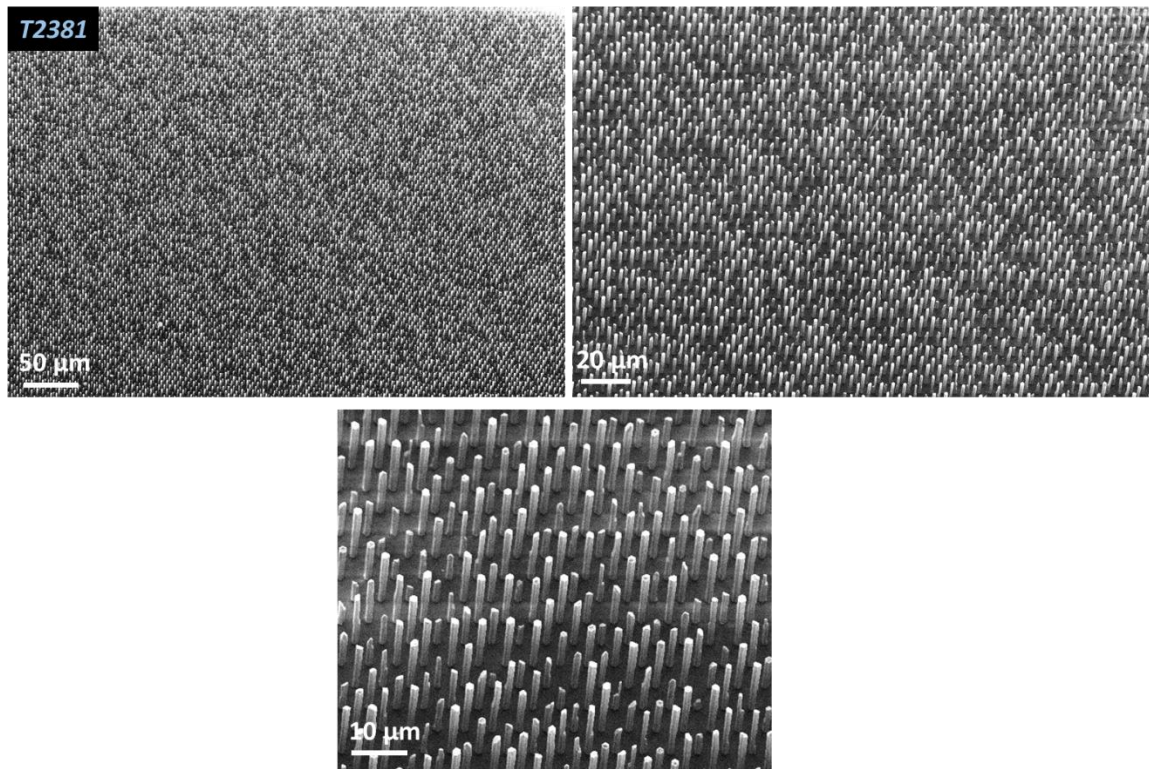
Figure 2.14: SEM images of SAG growth after improving the Si$_3$N$_4$ mask fabrication on sapphire at different magnifications.
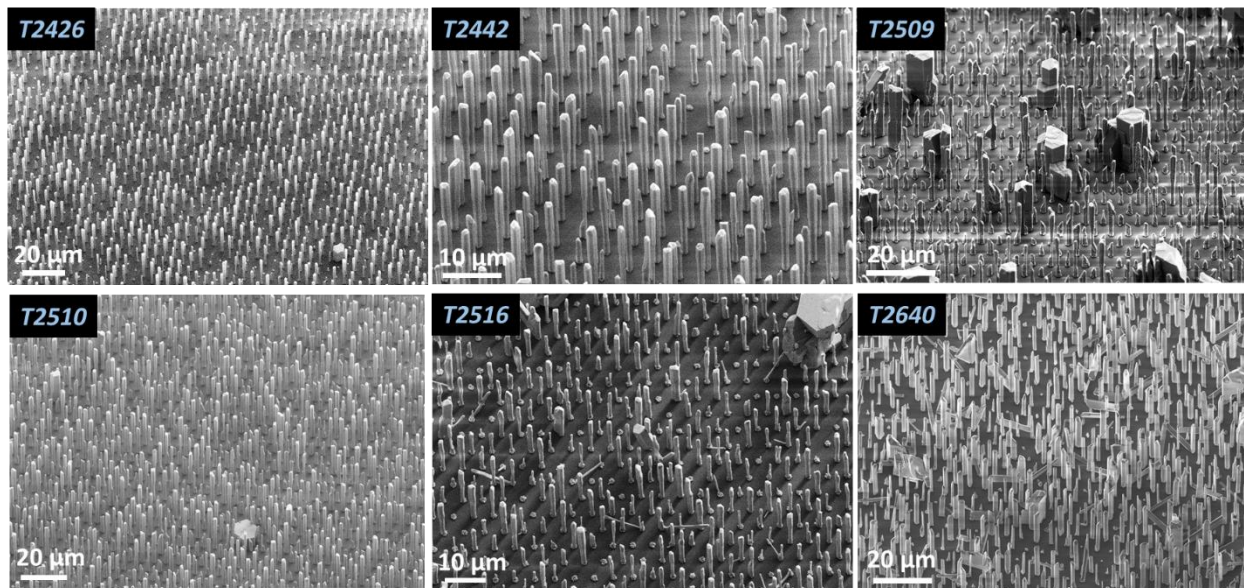
Figure 2.15: Reproducibility control - SEM images of different SAG growths indicated by the sample number at top left. The substrates are prepared together in the identical conditions and the growths are performed with the similar growth parameters, yet a difference in growth can be seen.

Despite preparing all the patterned substrates in an identical environment and using similar growth conditions, a significant difference in wire growth is observed. An appreciable wire density without overgrowths or poor hole filling is achieved for some growths but the issues appeared again for some other cases. This indicates the difficulty of reproducibility control in SAG growth. Additional growth experiments have also been performed by using a new SAG mask, however no success has been achieved to have a better controllability. Thus, we realized that approaching the organized wire growth indeed remains difficult. It requires a constant effort to be able to control the mask fabrication and optimize the growth conditions. A small size of the patterned sapphire substrates are typically used for SAG growth (atleast 10 times smaller than the pocket size) and can be more prone to the temperature gradient present across the susceptor surface inside the reactor. Nevertheless, an optimum combination of surface preparation along with the suitable growth parameters results in an improved SAG growth. This work certainly requires further attention, although the SAG development for ordered wire growths is time consuming and expensive. The group of A. Waag (Univ. Braunschweig, Germany) also reports problems of reproducibility for SAG of ordered wire growth that can disappear when the SAG is performed to grow Fin nanostructures.[21]‡‡‡‡ Therefore, we conclude that SAG of long N-polar wires remains ineffective till date in our research setup to provide the key advantages to compete against the self-assembled wire growth. The further work performed in the Ph.D. based on different wavelength emission from core-shell InGaN/GaN wires has thus been carried out by employing the self-assembled wires.

CONCLUSION

This chapter has given a brief overview of the MOVPE growth technique used to grow GaN wires. A summary of previous work from the laboratory has explained the growth conditions to achieve N-polar GaN wire growth using MOCVD with silane addition. It is then followed by the growth of InGaN/GaN core-shell MQWs. Various heterogeneities encountered in the wire growth has been discussed such as mixed polarity in the wires, variations and fluctuations in indium-incorporation and non-uniformity in the wire-length. An approach to address the issue of length

---

‡‡‡‡ It is worth mentioning that it is easier to manage the organized array of Ga-polar wires but with a shorter length as demonstrated by ALEDIA company.

inhomogeneity has been proposed based on SAG growth. The technical details involved in the mask fabrication and the optimized growth conditions for organized wire growth have been described. An improvement in wire growth is seen by changing the steps involved in Si_3N_4 mask fabrication. However, after performing several growth experiments with the optimized parameters, a lack of reproducibility control is still observed. It is concluded that presently SAG growth is far from being straightforward in our experimental conditions and many efforts have to be done to benefit from the advantages of SAG. Due to the balance between efforts and gain, self-assembled wires have been made our first choice to develop the experimental work of this Ph.D.

REFERENCES

[1] Stringfellow GB. Organometallic vapour phase epitaxy, theory and practice. San Diego (CA):Academic Press; 1989

[2] Anna Mukhtarova, InGaN/GaN Multiple Quantum Wells for Photovoltaics. *Université Grenoble Alpes*, **2015**.

[3] Robert Koester, Metal-Organic Vapour Phase Epitaxy, MOVPE, *Université Grenoble Alpes*, **2012**.

[4] Xiaojun Chen, MOVPE Growth of III-Nitride Nanostructure: From Self-Assembled Growth to Selective Area Growth, *Université Grenoble Alpes*, **2011**.

[5] Damien Salomon, Croissance, propriétés optiques et intégration d'hétérostructures radiales InGaN/GaN autour de fils auto-assemblés de GaN crûs sur saphir et silicium*, Université de Grenoble,* **2013**.

[6] Koester, R.; Hwang, J. S.; Durand, C.; Dang, D. L. S.; Eymery, J. Self-Assembled Growth of Catalyst-Free GaN Wires by Metal-Organic Vapour Phase Epitaxy. *Nanotechnology* **2010**, *21*, 015602. https://doi.org/10.1088/0957-4484/21/1/015602.

[7] Eymery, J.; Chen, X.; Durand, C.; Kolb, M.; Richter, G. Self-Organized and Self-Catalyst Growth of Semiconductor and Metal Wires by Vapour Phase Epitaxy: GaN Rods versus Cu Whiskers. *Comptes Rendus Phys.* **2013**, *14*, 221–227. https://doi.org/10.1016/j.crhy.2012.10.009.

[8] Tessarek, C.; Heilmann, M.; Butzen, E.; Haab, A.; Hardtdegen, H.; Dieker, C.; Spiecker, E.; Christiansen, S. The Role of Si during the Growth of Gan Micro- and Nanorods. *Cryst. Growth Des.* **2014**, *14*, 1486–1492. https://doi.org/10.1021/cg500054w.

[9] Koester, R.; Hwang, J.; Salomon, D.; Chen, X.; Bougerol, C.; Barnes, J.; Le Si Dang, D.; Rigutti, L.; Bugallo, A. D. L.; Jacopin, G.; et al. M-Plane Core-Shell InGaN/GaN Multiple-Quantum-Wells on GaN Wires for Electroluminescent Devices. *Nano Lett.* **2011**, *11*, 4839–4845. https://doi.org/10.1021/nl202686n.

[10] Tchoulfian, P.; Donatini, F.; Levy, F.; Amstatt, B.; Ferret, P.; Pernot, J. High Conductivity in Si-Doped GaN Wires. *Appl. Phys. Lett.* **2013***, 102,* 122116. https://doi.org/10.1063/1.4799167.

[11] Tchoulfian, P.; Donatini, F.; Levy, F.; Dussaigne, A.; Ferret, P.; Pernot, J. Direct Imaging of P-N Junction in Core-Shell GaN Wires. *Nano Lett.* **2014,** *14,* 3491–3498. https://doi.org/10.1021/nl5010493.

[12] Chen, X. J.; Perillat-Merceroz, G.; Sam-Giao, D.; Durand, C.; Eymery, J. Homoepitaxial Growth of Catalyst-Free GaN Wires on N-Polar Substrates. Appl. Phys. Lett. 2010, 97, 151909. https://doi.org/10.1063/1.3497078.

[13] Coulon, P. M.; Mexis, M.; Teisseire, M.; Jublot, M.; Vennéguès, P.; Leroux, M.; Zuniga-Perez, J. Dual-Polarity GaN Micropillars Grown by Metalorganic Vapour Phase Epitaxy : Cross- Correlation between Structural and Optical Properties. *J. Appl. Phys.* **2014**, *115*, 153504. https://doi.org/10.1063/1.4870950.

[14] Rigutti, L.; Blum, I.; Shinde, D.; Hernandez-Maldonado, D.; Lefebvre, W.; Houard, J.; Vurpillot, F.; Vella, A.; Tchernycheva, M.; Durand, C.; et al. Correlation of Microphotoluminescence Spectroscopy, Scanning Transmission Electron Microscopy, and Atom Probe Tomography on a Single Nano-Object Containing an InGaN/GaN Multiquantum Well System. *Nano Lett.* **2014**, *14*, 107–114. https://doi.org/10.1021/nl4034768.

[15] Amine El. Kacimi, Capteurs Piézoélectriques Souples À Base de Microfils de GaN En Structure Capacitive, *Université Grenoble Alpes*, 2018.

[16] Hersee, S. D.; Sun, X.; Wang, X. The Controlled Growth of GaN Nanowires. *Nano Lett.* **2006**, *6* (8), 1808–1811. https://doi.org/10.1021/nl060553t.

[17] Bergbauer, W.; Strassburg, M.; Kölper, C. H.; Linder, N.; Roder, C.; Lähnemann, J.; Trampert, A.; Fündling, S.; Li, S. F.; Wehmann, H. H.; et al. Continuous-Flux MOVPE Growth of Position-Controlled N-Face GaN Nanorods and Embedded InGaN Quantum Wells. *Nanotechnology* **2010**, *21*, 305201. https://doi.org/10.1088/0957-4484/21/30/305201.

[18] Choi, K.; Arita, M.; Arakawa, Y. Selective-Area Growth of Thin GaN Nanowires by MOCVD. *J. Cryst. Growth* **2012**, *357*, 58–61. https://doi.org/10.1016/j.jcrysgro.2012.07.025.

[19] Agnès Messanvi. Composants photoniques à base de fils de nitrures d'élément III: du fil unique aux assemblées. Matériaux. Université Grenoble Alpes, 2015.

[20] Chen, X. J.; Hwang, J. S.; Perillat-Merceroz, G.; Landis, S.; Martin, B.; Le Si Dang, D.; Eymery, J.; Durand, C. Wafer-Scale Selective Area Growth of GaN Hexagonal Prismatic Nanostructures on c-Sapphire Substrate. *J. Cryst. Growth* **2011**, *322*, 15–22. https://doi.org/10.1016/j.jcrysgro.2011.03.007.

[21] Hartmann, J.; Steib, F.; Zhou, H.; Ledig, J.; Fündling, S.; Albrecht, F.; Schimpke, T.; Avramescu, A.; Varghese, T.; Wehmann, H. H.; et al. High Aspect Ratio GaN Fin Microstructures with Nonpolar Sidewalls by Continuous Mode Metalorganic Vapor Phase Epitaxy. *Cryst. Growth Des.* **2016**, *16*, 1458–1462. https://doi.org/10.1021/acs.cgd.5b01598.

Chapter 3: Control of wavelength emission from *m*-plane InGaN/GaN radial QWs

This chapter presents different wavelength emission from *m*-plane core-shell InGaN/GaN wires by controlling the growth temperature of InGaN QWs. The section 3.1 will give an overview of already established blue emission by our group by highlighting the ease of reproducibility. After introducing the state of the art from laboratory, section 3.2 will focus on one of the main objective of this PhD thesis related to longer wavelength emission. A demonstration of green emission from *m*-plane core-shell InGaN/GaN wires is presented by combining optical, structural as well as electrical characterization. Once the blue and green emissions have been well managed, a study described in section 3.3 has been carried forward to target a dual color emission from the single core/shell InGaN/GaN heterostructures. A comprehensive investigation with similar characterization techniques used previously for green emission is presented for a detailed understanding of different wavelength emission from these core-shell wires.

3.1 State of the Art

The band gap engineering to target different wavelength emission from InGaN/GaN heterostructures is mostly governed by the indium composition present inside InGaN QWs.[1,2] For example, a low indium content in the range of (≈15-18%) is required to achieve blue emission (≈450 nm, ≈2.75 eV), while higher indium content (≥ 20%) is required to target green emission (≈520 nm, ≈2.38 eV). The In-composition of InGaN layers grown by the MOCVD technique is controlled by regulating the QW growth temperature for a given growth rate.[3,4] A decrease in growth temperature reduces the desorption of indium adatoms from the surface and thereby increases the indium incorporation.[5,6] The long wavelength emission from InGaN/GaN based heterostructures is possible when the QW growth temperature is enough reduced. However, the low temperature growth to target In-rich QW degrades the crystal quality of the alloy. The large lattice mismatch between GaN and InN results in an accumulation of strain in QWs, which can relax by defect formation. These intrinsic difficulties compromise the overall efficiency of LED devices. Therefore, unlike the well-established InGaN/GaN based blue LEDs grown by MOCVD, the longer wavelength emission remains a serious challenge. Further, it is more difficult for the core-shell InGaN/GaN wires to emit at higher wavelengths due to reduced In-incorporation on *m*-plane surfaces.[7,8] Therefore, this work is focused on the possibility to achieve long wavelength emissions based on core-shell *m*-plane InGaN QWs.

3.1.1 Blue emission: Previous work by the group

The early demonstration of blue emission from the core-shell wires has already been established by our group.[9,10,11,12] The work by *Koester et al.*[9] investigates a series of core-shell InGaN/GaN wires with five InGaN multiple quantum wells (MQWs) grown on sapphire by varying the QW growth temperature in the range (720-760 °C)[*] as well as the QW thickness (by varying the growth time between 20-120 s)[†]. The photoluminescence (PL) measurements performed at 5 K for the two series are shown in **Figure 3.1 (a)** and **Figure 3.1 (b)** respectively. The samples exhibit the PL emission in the range (396 - 425 nm) and are further characterized using High-angle annular dark-

---

[*] For a fixed growth duration of 80 s.
[†] For a fixed growth temperature at 750 °C.

field (HAADF) scanning transmission electron microscopy (STEM) to estimate their respective thicknesses as shown in **Figure 3.1 (c)**. Time-of-flight secondary ion mass spectrometry (ToF-SIMS) analyses performed for sample having InGaN QWs grown at 750 °C for 40 s reveals that the QWs having thickness around 2.5 nm contains an indium content of 16 (±2) % (see **Figure 3.1 (d)**). This evidences the PL emission around 406 nm and the electroluminescence (EL) emission measured near 400 nm on single wires at room temperature.
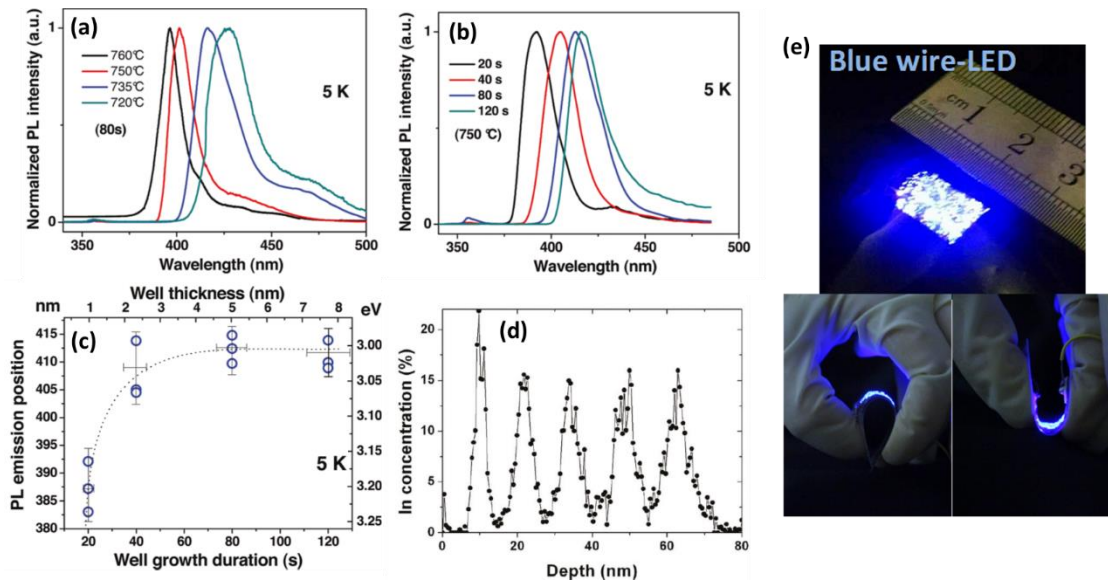
Figure 3.1: (a)-(d) Adapted from *Koester et al.* (*Ref. 9*): μ-photoluminescence (μ-PL) measurements of single core-shell InGaN/GaN MQWs wires for samples with 5x MQWs grown at different growth temperatures for 80 s in (a) and for several QW growth times (20 to 120 s) grown at 750 °C in (b), (c) Analysis of the μ-PL emission wavelength as a function of QW thickness. Symbols correspond to different wire measurements, (d) Estimation of the indium concentration as a function of the depth along the wire profile (QW growth time = 40 s) ; and (e) Taken from Dai *et al.* (*Ref. 11*): Photographs of the LED emitting blue light at curvature radii of ∞ (top), 3.5 mm (bottom left) and −2.5 mm (bottom right).

One advantage of wires is the possibility to grow defect-free GaN on different substrates, such as Si (111). This is reported by our group (*Salomon et al.*[13]) and in collaboration with CEA/LETI (*Bavencove et al.*[10]), where the GaN wires are grown on a 2-inch n-doped silicon substrates and are also covered radially by five InGaN/GaN QWs and finished with a p-type GaN:Mg shell. The core-shell wire-based LED produced blue EL at 450 nm recorded at room temperature. Another advantage of wires is the possibility to be used for flexible device fabrication. Further reports also from our group in collaboration with C2N laboratory (Univ. Paris Saclay) based on flexible LED

devices by *Dai et al.*[11] and *Guan et al.*[12] demonstrated blue emission at 437 nm for InGaN QWs grown at 720 °C separated by GaN barriers grown at 920 °C. The pictures for the flexible blue LED can be seen in **Figure 3.1 (e)**. This work has also been documented in the thesis of Agnes Messanvi[14] presenting a detailed understanding of the blue emission. In addition to the PL and EL measurements, the wires have also been measured based on low temperature cathodoluminescence (CL) to confirm the emission from wire sidewalls.[14] All these reports indicate the possibility to achieve well-controlled blue emission from core-shell InGaN/GaN wires grown by MOCVD. Therefore, the present Ph.D. work is initiated by first carrying forward the state of the art for blue LED device and to validate its reproducibility.

The self-assembled N-polar $\bar{c}$-GaN wires are grown on sapphire substrates with the similar growth parameters as described in chapter 2. Two different samples have been prepared with 7x InGaN QWs grown at 750 °C and 720 °C respectively using the same growth duration (80 s) under N_2 carrier gas. The QWs are separated by GaN barriers grown at 900 °C for 150 s. The MQWs growth is followed by the growth of p-GaN shell at 920 °C for 450 s to target a thickness around 150 nm. The as-grown wires having QWs grown at 720 °C can be seen in the scanning electron microscopy (SEM) image in **Figure 3.2 (a)**. The core-shell geometry is clearly visible in the single wire SEM image at the top-inset. The wire density remains similar for both samples and is estimated around 10^6 wires/cm^2. The dispersed wires on silicon substrates are characterized by PL measurements performed at low temperature as shown in **Figure 3.2 (b)**. A continuous wave doubled solid-state laser at 244 nm is used to excite the wires with a fixed excitation power of about 100 μW. The signals have been analyzed through a 46 cm focal length spectrometer equipped with a 600 grooves/cm grating, and detected with a liquid nitrogen cooled charge coupled device camera. The PL spectra of 750 °C sample shows a peak around 406 nm corresponding to the InGaN QW emission. A shoulder around 450 nm is also observed. Similarly, the spectra of 720 °C sample shows a peak at 446 nm with a presence of shoulder around 500 nm. The presence of two QW contributions in both samples is typically observed for core-shell InGaN/GaN wires corresponding to radial and axial QWs contributing to shorter and longer wavelengths, respectively.[‡] A redshift of about 40 nm for the QW emission grown at 720 °C is consistent with the lower growth

---

[‡] This will be discussed in detail later in Chapter 5 Section 5.2.3.

temperature favoring higher indium incorporation. The tunability from the violet emission achieved at 750 °C to the blue emission at 720 °C is consistent with the previous works and validates the state of the art developed in the laboratory. The GaN wires with core-shell InGaN/GaN MQWs grown at 750 °C have also been used in the fabrication of flexible LED devices. The fabrication process along with the EL measurements will be described in Chapter 5.

Additionally, a sample with 5x InGaN/GaN core-shell QWs is grown at 730 °C (without a p-GaN shell) keeping the remaining growth parameters similar as mentioned above. The as-grown wires are measured with PL in the same condition as mentioned above. The samples are cooled down in a helium flow cryostat allowing the temperature to go from 300 to 5 K (see **Figure 3.2 (c)**). The peak around 355 nm and a broad emission centered around 550-570 nm is attributed to the near band edge and yellow band emissions from GaN. A significant peak at 420 nm with full width at half maxima (FWHM) equal to 280 meV at low temperature arises from the InGaN QWs. A shoulder around 445 nm (see the inset of **Figure 3.2 (c)** showing the spectra in logarithm scale for the sake of clarity) is visible for all temperatures but more pronounced at low temperature. This
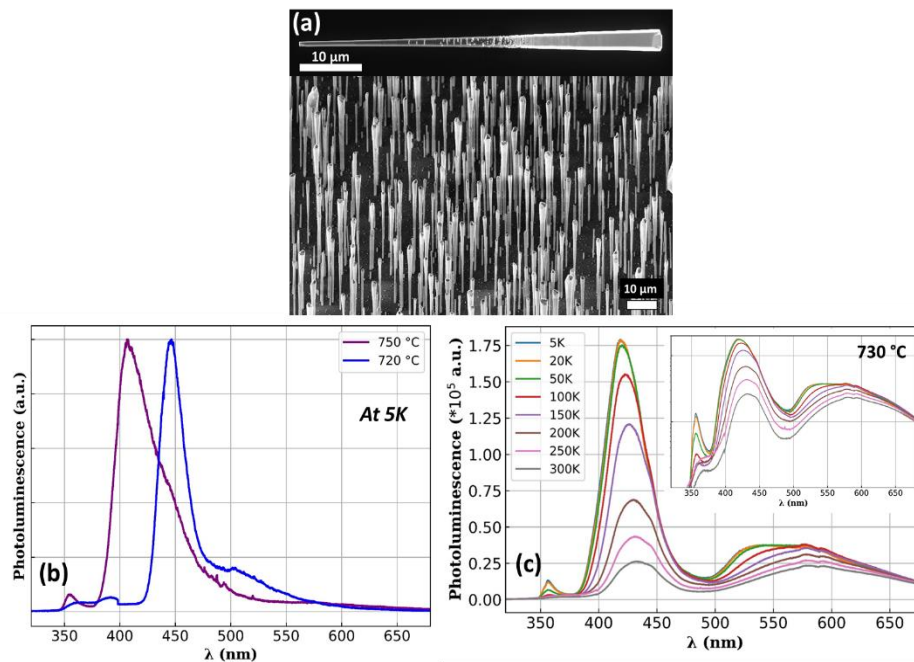
Figure 3.2: (a) SEM image of as-grown wires for sample with InGaN QWs grown at 720 °C with single wire SEM image at the top-inset (#T2610), (b) Low temperature photoluminescence (PL) spectra for samples with QWs grown at 720 °C and 750 °C (#T2400), (c) Temperature-dependent PL for additional sample with QW grown at 730 °C (#T2548).

shoulder observation is consistent with the emission from axial QWs, as already observed on the previous two samples. Assuming negligible non-radiative (NR) recombination at low temperature, the luminescence intensity at room temperature is normalized with the intensity at low temperature to provide an estimation of the upper bound of internal quantum efficiency (IQE).[15,16] An appreciable IQE of around 15% is estimated for the sample exhibiting blue emission.

3.2 Green emission

This section details the demonstration of the green luminescence from *m*-plane InGaN/GaN core-shell wires.[17] The growth explanation of InGaN QWs at different temperature is performed in section 3.2.1. The optical characterization of samples using both PL and CL is shown in section 3.2.2. The section 3.2.3 presents the structural observations of the wires by STEM using High Angle Annular Dark Field detector (HAADF). The estimation of In-content inside the QWs using energy-dispersive x-ray microscopy (EDX) combined with Atomic probe tomography (APT) is focused in section 3.2.4. A single wire device is also fabricated in collaboration with the C2N to study the electrical properties of the wire in section 3.2.5. Furthermore, a reproducibility control for the green emission is also discussed in section 3.2.6.

3.2.1 Growth of InGaN QWs as a function of QW growth temperature

Self-assembled N-polar $\bar{c}$-GaN wires with core-shell InGaN/GaN MQWs are grown on nitridated *c*-sapphire substrates, as depicted in **Figure 3.3 (a)**. The growth parameters for n-GaN wire core is similar to that explained in Chapter 2. It is followed by the radial growth of seven InGaN quantum wells (QWs) separated by GaN barriers around the GaN wires at 400 mbar. Four different samples are grown by varying only the growth temperature of the QWs (710, 685, 650, and 620 °C) keeping constant the barrier temperature at 885 °C. **Figure 3.3 (b)** illustrates the temperature evolution for InGaN/GaN QWs with the growth time. A decrease in the growth temperature of InGaN QWs is followed by a rapid increase to reach the constant growth temperature of GaN barriers. The last step corresponds to the growth of a thick p-doped GaN shell at 920 °C, followed by a dopant activation annealing at 700 °C during 20 min.
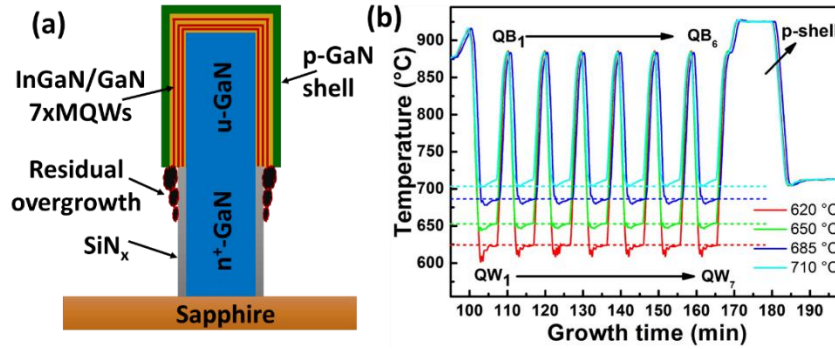
Figure 3.3: (a) Schematics of the core−shell MQWs grown on GaN wire sidewalls. (b) Growth temperature evolution as a function of growth time showing the decreasing temperature for InGaN quantum wells, keeping constant the growth temperature of the GaN barriers. (*Ref. 17*)
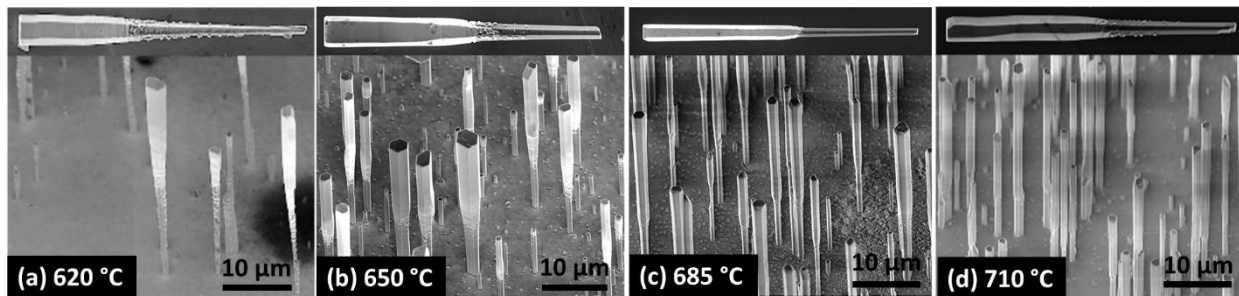
Figure 3.4: SEM images of as-grown wires with QWs grown at different temperatures: (a) 620, (b) 650, (c) 685 and (d) 710 °C. ((a) T2316, (b) T2313, (c) T2314, (d) T2315)) (*Ref. 17*)

Figure 3.4 shows SEM images of as-grown samples (with single wire image above) performed at various QW growth temperatures. The average wire density is 10^6 wire/cm^2, while the diameter and length of the wires are in the range of (0.65-1.2) μm and (28-33) μm, respectively. Interestingly, the core-shell geometry of InGaN/GaN MQWs is preserved for all samples, even for the sample synthesized at the lowest temperature. The main difference is the degradation of the SiN$_x$ selectivity on the bottom n$^+$-GaN part of the wires. Residual overgrowths are especially visible for the sample grown at 620 °C that can be attributed to a lower diffusion length of the species.

3.2.2 Optical characterization using Photoluminescence (PL) and cathodoluminescence (CL)

The PL experiment of all samples is performed on wire ensembles dispersed on silicon substrates in the similar experimental setup as used for the measurements of blue emission[§] but with a different laser excitation power of about 0.5 mW. **Figure 3.5 (a)** shows the behavior of normalized PL spectra at 5 K as a function of QW growth temperature. A red shift can be observed from 407 to 550 nm for QWs grown at temperatures from 710 to 620 °C, which can be attributed to an increase in the In incorporation associated with a lower growth temperature. The sample with QWs grown at 650 °C exhibits a significantly large emission peak centered at 510 nm indicating a green emission.
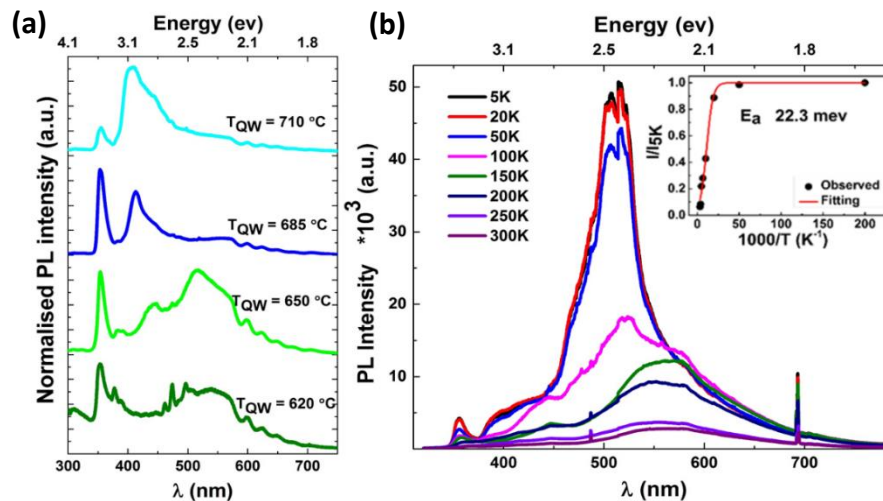
Figure 3.5: Photoluminescence (PL) measurement: (a) Normalized PL spectra at 5 K for all the samples with wires dispersed on silicon. (b) PL spectra of the sample with QWs grown at 650 °C as a function of temperature. The inset shows the experimental values and the fit of the integrated intensity vs. 1000/T. (*Ref. 17*).

It can also be noted that the maximum of intensity decreases accompanied by a peak broadening as the growth temperature decreases to 620 °C. Assuming a similar density of dispersed wires, the intensity decrease may correspond to the presence of structural defects in the QWs[18] and the large peak broadening (~300 meV) indicates strong inhomogeneity in In incorporation. The peak observed at 3.4 eV (352 nm) is attributed to the near band edge of highly n[+]-doped core GaN

[§] Refer to section 3.1.1.

segment present in all samples.[19] **Figure 3.5 (b)** shows temperature-dependence PL spectra for the sample with QWs grown at 650 °C. The measurement is performed on as-grown wires on sapphire using a laser power of 0.12 mW. The green emission dominates at low temperature with a FWHM of 272 meV, while two other contributions close to 400 and 550 nm are attributed to the blue residual emission and the yellow band defect emission, respectively. An upper limit of IQE is calculated by normalizing the PL intensities as 4%. The inset of **Figure 3.5 (b)** shows the Arrhenius plot of the integrated intensity as a function of 1000/T, which allows estimating an activation energy $E_a \approx 22$ meV. This value is consistent with the reported values for green emission *c*-plane MQWs,[20] which is related to localization effects.[21]
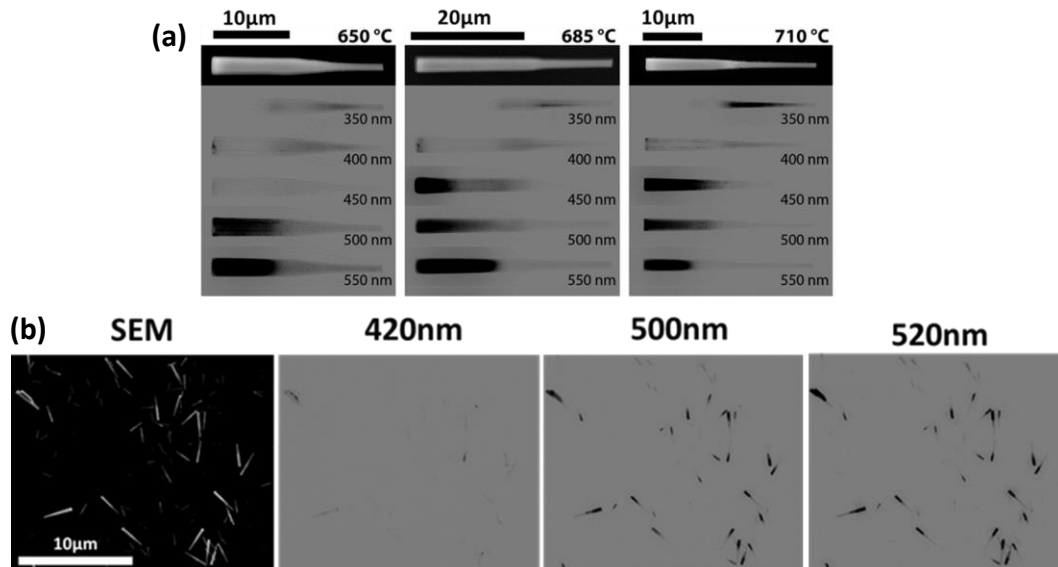
Figure 3.6: Cathodoluminescence (CL) measurement showing CL mappings with corresponding SEM images: (a) Typical single wires corresponding to QWs grown at 710, 685, and 650 ° measured at 350, 400, 450, 500 and 550 nm; (b) Wire-ensemble for QWs grown at 650 ° measured at 420, 500 and 520 nm. (*Ref. 17*)

In addition to PL measurements, CL mapping has been performed in order to understand the spatial emission of different spectral contributions of the luminescence. Typical electron beam voltage, current and size are 20 kV, <1 nA and 10 nm, respectively. The CL signal is collected by a parabolic mirror and analyzed with a grating monochromator equipped with a liquid-nitrogen-cooled CCD camera. **Figure 3.6 (a)** depicts spectrally filtered CL maps of single wires with QWs grown at 710, 685, and 650 °C (dark area corresponds to light emission). It can be clearly seen that

the near band edge emission of GaN (350 nm-CL maps) arises from the n$^+$-GaN wire base part. The emission for wavelengths above 400 nm mainly comes from the active regions of the wire corresponding to the QWs. The samples with QWs grown at 710 and 685 °C emit blue light as detected in the 450 nm-CL maps, contrary to the sample with QWs grown at 650 °C that emits only green light (visible in the 500 nm-CL maps). This emission at 500 nm is consistent with the above-described PL results, showing that the indium content is high enough to cause the green emission. The yellow band emission related to deep-defects centered at ~550 nm is visible in all samples and is attributed to the upper u-GaN part of wires, as previously reported.[19] For the QWs grown at 650 °C, the CL mapping at 500 nm highlights unambiguously that the green emission comes from the *m*-plane wire sidewalls. The measurement has also been extended to wire ensemble as shown in **Figure 3.6 (b)** to confirm that the green emission is consistent for other wires on the sample. A variation in intensity can be observed which is mainly related to the MQW area depending on wire size. Usually, the MQW growth also occurs at the wire top facets (*c*-plane and semi-polar planes at the junction between sidewall and flat top facets) with a higher In-content resulting in longer wavelength emission in the case of wire-blue LED.[22] The absence of light emission from axial/semi-polar InGaN MQWs for the present sample emitting green light can certainly be attributed to the defect generation related to the higher In content and to the low growth rate of $\bar{c}$-plane MQWs along the N-polar direction.[23,24]

3.2.3 Structural properties using STEM combined with EDX

Microstructural analyses of the 650 °C-QW sample have been carried out by STEM-HAADF to emphasize the chemical contrast (Z contrast) on the images. The experiments have been performed on a FEI OSIRIS microscope operated at 200 kV and equipped with four silicon drift detectors to record also Energy Dispersive X-ray (EDX) chemical maps. Thin slices of the wires have been cut perpendicular to the growth $\bar{c}$-axis by ultramicrotomy using a diamond blade.[25] **Figure 3.7** shows a part of one wire slice, where the 7 QWs appear in bright, whereas the GaN parts (barriers and p-GaN shell) are in dark. In the high resolution enlarged STEM image (**Figure 3.7 (b)**), the measured thicknesses of the QWs and barriers are 2.7 and 11 nm, respectively (except for the first QW, which is somewhat larger, we will come back to this point later), while that of the p-doped GaN shell is about 70 nm. Note that some faint white lines visible in **Figure 3.7 (a)** and **(b)**, originating from the interface between the GaN core and the first InGaN QW, propagate through the whole
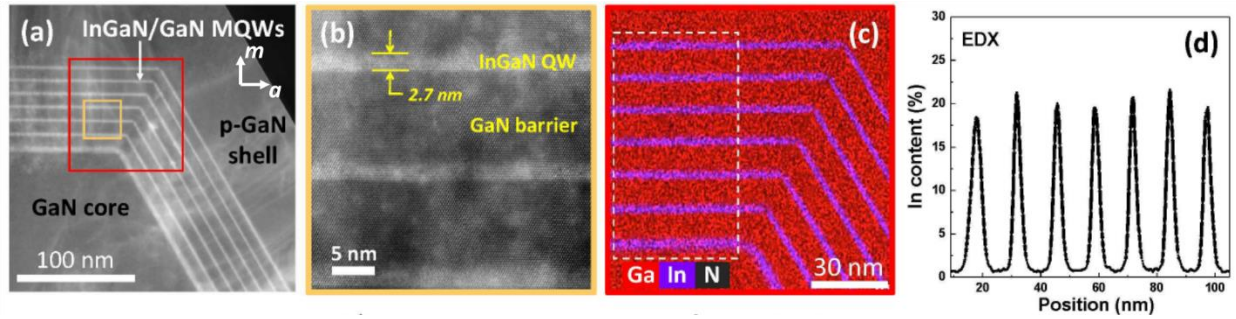
Figure 3.7: Structural characterization of the 650 °C QW sample. (a) Transversal cross-sectional STEM-HAADF images taken along the $\bar{c}$-zone axis depicting the seven quantum wells separating the core and p-GaN. (b) High resolution enlarged STEM-HAADF image showing distinctively the InGaN QWs and GaN barriers. (c) STEM-EDX elemental map for spatial distribution of Ga, In, and N in the core-shell heterostructures; and (d) Indium profile as a function of position from the 1st QW to 7th QW measured by EDX. (*Ref. 17*)

InGaN/GaN structure. Similar features have been already reported in MQWs core-shell structures and identified as stacking faults (SFs).[9,26] Detailed investigation of the SFs in the case of planar QWs on *m*-plane GaN systems reveals that these defects plastically relax the misfit strain accumulated during the growth process along the $\bar{c}$-direction.[27,28] **Figure 3.7 (c)** shows the spatial distribution of Ga, In, and N from EDX analyses measured inside the red rectangle shown in **Figure 3.7 (a)**. The In profile measured in the dash-line rectangle shown in the EDX mapping (**Figure 3.7 (c)**) has been depicted in **Figure 3.7 (d)** as a function of the position from the innermost QW to the last QW. Note that the uncertain values for the QW thicknesses obtained from the profile are due to the lack of enough spatial resolution in these maps. The average percentage of In content inside the 7x QWs obtained by EDX profile is in the order of 20% and stay almost constant in the range of ±2% whatever the QW. We consider that this value is underestimated due to the teardrop-shaped volume of the e-beam excitation along the slice width leading to overestimation of Ga content coming from the barriers. These maps do not have enough spatial resolution to detect any In-composition fluctuation that might exist at the atomic scale. These observations are therefore combined with Atom Probe Tomography (APT) experiment performed on the same sample and explained in the following section.

3.2.4 Estimation of indium content in QWs by Atom Probe Tomography (APT)

The APT experiment has been conducted at the Normandie University, INSA Rouen in the collaboration with Lorenzo Rigutti. The measurement is performed in a CAMECA laser assisted wide angle tomographic atom probe (LAWATAP) under conditions similar to those adopted for the analysis of InGaN/GaN *m*-plane QWs in the previous studies[**].[26,29] **Figure 3.8 (a)** shows the 2D cross-sectional view of the reconstructed positions of the In atoms within all 7x QWs. The similar cross-sectional and top view for a 2 nm thick slice of the innermost QW are shown in **Figure 3.8 (b)**, while the In-mapping to quantify the In-content within the QW volume is depicted in **Figure 3.8 (c)**. As can be seen, the In-content is non-uniformly distributed exhibiting a sequence of In-rich and In-poor bands aligned along the *a*-axis direction possibly related to the local perturbation induced by stacking faults.[9] Further, the mapping also reveals red zones with high In-content up to 30% related to strong inhomogeneous In-composition in the QW for an estimated average value of about 23%. However, the In-profile for a 25 nm × 25 nm cross section along the 7x QWs shown in **Figure 3.8 (d)** exhibits an In-composition around 25% with a variation of 2.5% from well-to-well. From this APT analysis, we can estimate an average In-content between 22±2 % and 27±2 % in the QWs, leading to an average value of around 24±4 %. Basically, the In-profile measured both by EDX and APT techniques reveals an In-content higher than 20% required for green emission originating from *m*-plane InGaN/GaN core-shell MQWs.
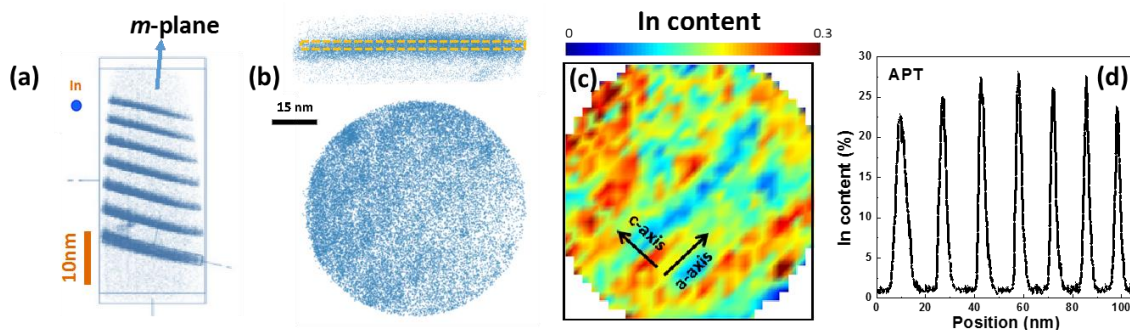
Figure 3.8: Atomic probe tomography (APT) observation: (a) APT reconstructed positions of In atoms in seven radial MQWs, (b) Focus on APT reconstructed In atoms along cross-sectional and top view of the innermost QW, (c) 2D map of In composition measured by APT extracted from the 1st QW and (d) In composition profile from the 1st QW to 7th QW measured by APT. (*Ref. 17*)

[**] The tip preparation perpendicular to the *m*-plane sidewall surfaces is performed by focused ion beam technique.

The crystal orientation is known to have a significant impact on the MQW growth (growth rate and In composition),[30] nevertheless no clear tendency about the In incorporation is reported in the literature on *m*-plane surfaces regarding the *c*-plane orientation[31] due to the strong dependence on growth techniques and conditions.[32] In the case of MOVPE, Horenburg *et al*. recently reported that In incorporation is strongly dependent on the strain state of the *m*-plane InGaN/GaN MQW systems by adding an InAlN buffer layer either lattice-matched along the *c*-axis or *a*-axis.[33] The higher In incorporation corresponds to the situation having the *c*-axis lattice matched and an elastic strain along the *a*-axis. It has been also shown that the high growth rate of InGaN can limit the In desorption resulting in a higher In-content inside the QWs.[34] Consequently, the In incorporation higher than 20% on *m*-plane sidewalls certainly results from a relatively high growth rate of the InGaN QWs (estimated at 0.7 Å/s) combined with a favorable strain state. Further, the thickness of the QWs measured to be 2.7 nm corresponds to a balance between the two following thermodynamic and kinetic factors. First, QW thickness is limited by the critical thickness (near 3 nm for 24% In-incorporation in planar growths)[35,36] to favor a pseudomorphic growth and limit the strain relaxation by defect generation. The critical thickness for core-shell geometry is comparable to planar growth due to the large GaN core diameter (about 1 μm) for a given In-content.[37] Second, as mentioned above, the QWs are grown at a relatively fast speed to prevent In desorption that leads to slightly thicker QWs facilitating high In incorporation in the QWs.

3.2.5 Electroluminescence of single wire device

The structural and optical measurements performed above are further combined with the electrical properties of the 650 °C QW sample. Single wire LED has been fabricated for optoelectronic characterizations following the procedure reported before.[22] This has been performed within the work of former Ph.D. student Nan Guan at C2N, Paris. **Figure 3.9 (a)** shows a SEM image of a single nanowire device. The Ni/Au and Ti/Al/Ti/Au metal contacts have been used for the shell p-contact and core n-contact respectively.[38] The current-voltage (I-V) curve of single nanowire devices is measured by a Keithley 2636 source meter at room temperature and shown in **Figure 3.9 (b)**. It has a rectifying behavior characteristic of an LED with a turn-on voltage of about 5 V. This relatively high turn-on voltage is due to the Schottky nature of the p-contact (no annealing of the Ni/Au contact was performed). The devices show a low leakage under reverse bias (at −20 V the reverse current is only 10 nA). This low reverse leakage demonstrates that the active region
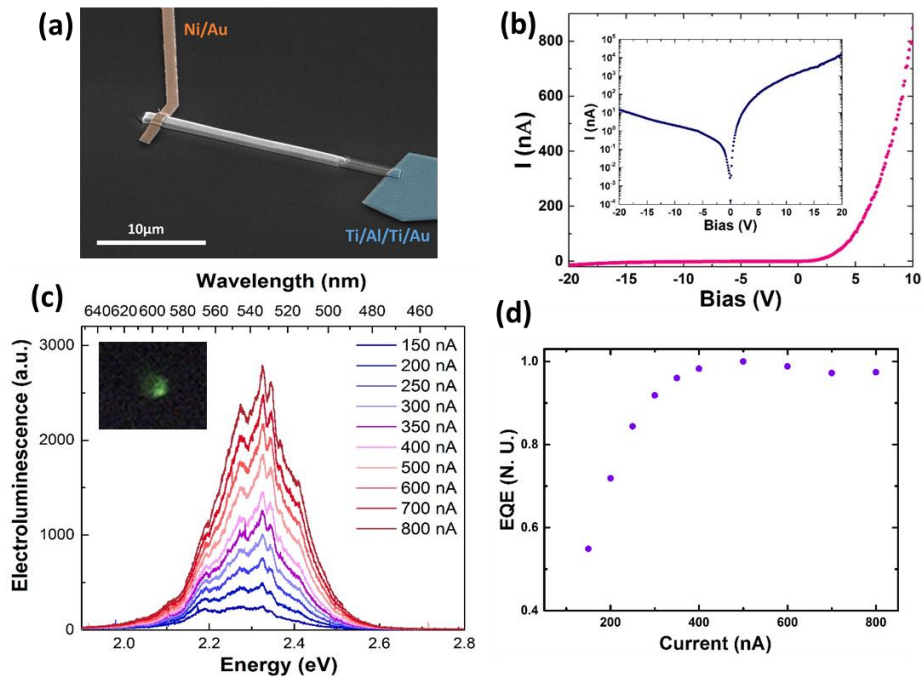
Figure 3.9: Wire-LED device based on the 650 °C-QW samples. (a) SEM image of a typical single wire-LED device with metal contacts, (b) Room temperature I-V curve of the single nanowire LED in linear scale, inset shows the I-V curve in logarithmic scale, (c) Room temperature EL spectra of the single nanowire LED under different injection currents from 150 to 800 nA (inset: optical image of the operating single nanowire LED) and (d) Room-temperature external quantum efficiency (EQE) of the single wire-LED as a function of injection current. (*Ref. 17*)

with QWs grown at 650 °C exhibits a good material quality. Room temperature electroluminescence (EL) spectra under different injection currents are shown in **Figure 3.9 (c)**. A measurable EL signal starts to appear around 100-150 nA. The spectra are peaked at 534 nm (2.32 eV) with an important broadening of 221 meV. The observed emission wavelength is consistent with the PL results. However the peak broadening is smaller than the one observed in PL (220 meV for EL vs. 300 meV for PL). This difference is attributed to the additional contribution of the yellow band emission tail to the broadening of the PL spectra, whereas the yellow band should not be excited in EL experiments. A small blue shift of the peak wavelength from 544 to 534 nm can be observed for small currents (from 150 to 200 nA) but peak wavelength and the spectral shape remain unchanged for currents above 200 nA. The observed stability of the EL wavelength with current is consistent with the attribution of this emission to the *m*-plane MQWs with unchanged distribution of current lines with applied bias.[39] The evolution of the external quantum efficiency (EQE) defined as the spectrally integrated EL intensity divided by the

injected electrical current with injected current is plotted in **Figure 3.9 (d)**. The EQE first increases following the saturation of non-radiative Shockley-Read-Hall recombination and reaches a maximum at 500 nA corresponding to a current density of 0.56 A/cm^{2}[††]. It then remains relatively stable in the analyzed current range. Apart from the single wire device fabricated with 650 °C-QW sample, additionally a flexible LED device using the wire-assembly has also been fabricated and measured with EL. This will be discussed in detail later in Chapter 5.

3.2.6 Challenges to achieve reproducibility in green emission

Although the green emission is achieved from *m*-plane InGaN/GaN core-shell wire geometry, the reproducibility control is another key challenge that needs to be addressed. A combination of optimum QW thickness, growth rate and a favorable strain state is required for green emission. Moreover, the temperature variations (and somehow a certain lack of control) in the MOCVD reactor make it even more sensitive to target the In-rich InGaN QWs. For example, the state of showerhead coating can induce a temperature variation of a few degrees (~ 5-7 °C) which can significantly influence the low temperature QW growth. Many growth experiments are performed one after the other and it is realized that the reproducibility control for green emission is indeed difficult to achieve.

Recently, some groups have reported the use of InGaN/AlGaN based MQW-heterostructures to target long wavelength emission.[40,41,42] The choice of AlGaN instead of GaN barriers can allow better carrier confinement inside the QWs due to larger band gap and can also allow strain-compensated InGaN/AlGaN QWs.[43] In addition, the presence of Al inside barriers has shown higher indium incorporation in QWs achieved for a relatively higher growth temperature.[40] An InGaN/GaN based MQWs structure grown by MOCVD with AlGaN interlayers (having 38% of Al-composition) between the InGaN QW and the GaN barrier has increased the radiative efficiency for emission in the range 530-590 nm.[40] Another study using a similar structure for a flip-chip small-size green LED device has shown PL emission at 530 nm. A high EQE of 38%, wall plug efficiency (WPE) of 32.1% and a low forward voltage of 2.8V at a current density of 20 A/cm^2 is reported.[42] A work on MBE grown core-shell InGaN/AlGaN nanowires has reported

---

[††] If the total surface of the six facets of the p-GaN shell is assumed to contribute to the current.

strong PL emission at 507 nm with a narrow spectral linewidth of 12 nm.[41] The study compares the results to a conventional InGaN nanowire array that shows a broader spectral linewidth of 35-50 nm. These reports indicate that using AlGaN layer in the InGaN/GaN based LEDs can provide an alternative structure to realize long wavelength emission. The QWs growth can be performed at a relatively higher temperature making them less prone to the temperature variations during the growth. Therefore, the growth experiments have been carried forward by investigating the influence of Al in barriers targeting green emission. Core-shell InGaN/AlGaN MQW heterostructures have been grown and studied by both optical and structural characterization.

The N-polar self-organized GaN wires are grown on sapphire with the typical growth parameters as reported in Chapter 2. The growth of n-GaN wire core is followed by the radial growth of 7x InGaN QWs at 680 °C for 75 s separated by AlGaN barriers grown at 855 °C for 80 s. It is worth mentioning that the growth of InGaN QW is followed by the typical growth of a GaN cap[‡‡] before growing AlGaN barriers. A low TMAl precursor flow of around 8 sccm diluted in 100 sccm of TEGa precursor flow has been used to grow AlGaN barriers. The reactor pressure is set to 400 mbar. The targeted Al composition in barriers is around 5%. The growth of InGaN/AlGaN QWs is then followed by the growth of a p-GaN shell at 920 °C. The SEM image in **Figure 3.10 (a)** of as-grown wires confirms the core-shell wire geometry with an average wire density of around 6.7×10^5 wires/cm^2. Low temperature CL mapping at 520 nm is performed in the similar conditions used earlier[§§] as shown in **Figure 3.10 (b)**. The green emission from the upper part of wire sidewall validates the growth of InGaN/AlGaN QWs on the non-polar *m*-plane wire-core. Strongly localized emission is observed indicating In-rich and poor regions present along the wire length. The as-grown wires are further measured by PL experiments performed by varying the temperature from 5 to 300 K. Note that when the wires are excited with a typical 244 nm laser, a yellow band usually appears between 500-600 nm originating from the GaN wire core.[19] This causes difficulty in distinguishing the green emission (if any) located around 520 nm. Therefore, a blue laser at 405 nm has been used to excite only the InGaN QWs with a laser power of 1 mW. The remaining

---

[‡‡] The GaN cap growth occurs at same temperature as InGaN QW for 30 s with a low TEGa precursor flow of 25 sccm.

[§§] Refer to section 3.2.2 explaining CL measurements for green emission.

experimental details are similar to that used before.*** **Figure 3.10 (c)** shows the temperature-dependent PL spectra. The QW emission is peaked at 520 nm with a FWHM of 298 meV at low temperature. The peak exhibits a redshift and becomes broader as the temperature increases. A shoulder located around 580 nm is also observed especially at low temperatures. The origin of this contribution is maybe related to residual axial QW growth, but this interpretation is not clear at this moment and requires further investigations, e.g. with photoluminescence measurements. The normalization of PL intensities provides an upper limit of IQE estimated as 6.3 %. The optical measurements are then followed by a detailed structural characterization by STEM-HAADF combined with EDX analyses.
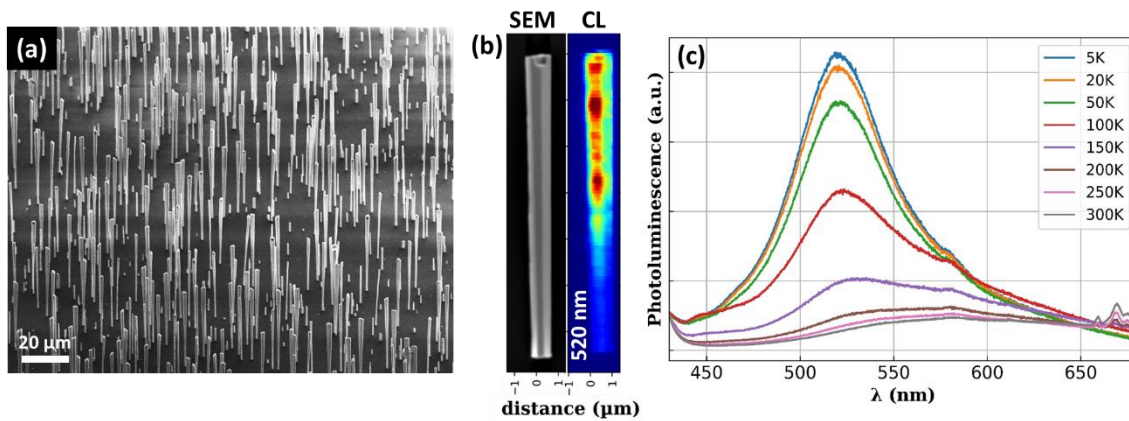
Figure 3.10: *m*-plane InGaN/AlGaN core-shell heterostructure: (a) 30° tilted SEM images of as-grown wires on sapphire, (b) CL mapping for single wire at 520 nm with SEM image on left; and (c) PL measurement performed on as-grown wires as a function of temperature from 5 to 300 K with an excitation laser at 405 nm. (Sample-T2581).

A thin wire slice is prepared by focused ion beam (FIB) using a STRATA 400S equipment††† in longitudinal mode, i.e. the cross-sectional view is parallel to the *c*-axis. The STEM images are acquired with a FEI TECNAI microscope operated at 200 kV using an HAADF detector. A large camera length is used to enhance the diffraction contrast related to the presence of defects with respect to chemical contrast. The high-resolution STEM image in **Figure 3.11 (a)** shows the 7x InGaN/AlGaN QWs. The presence of bright white lines originating at the first QW interface is similar to that observed for the previous green sample and can be attributed to stacking faults. The

---

*** Refer to section 3.1.1 explaining the PL measurements for blue emission.
††† The FIB preparation is performed by Vincent Grenier who is another Ph.D. student in our group.

STEM-HAADF image corresponding to the blue square in **Figure 3.11 (a)** is shown in **Figure 3.11 (b)**. The InGaN QWs appear in dark and have a thickness of 6.5 nm, while the AlGaN barriers look bright and have a thickness of 18.8 nm (including the GaN cap). Note that the first QW as well as barrier is somewhat thinner as compared to the successive QW/barriers. The lowering of temperature to grow the first QW after the high temperature growth of wire-core could induce instabilities in temperature during the first loop, leading to a low QW and barrier thicknesses.
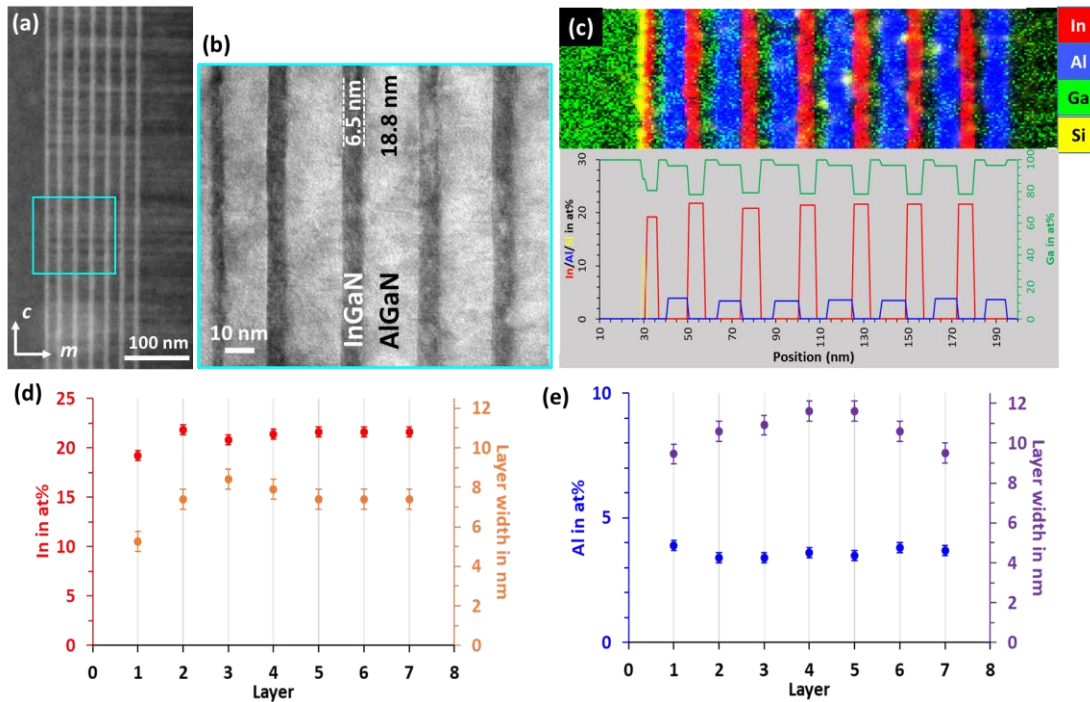
Figure 3.11: Structural characterization of wires presented in Figure 3.10 by STEM-HAADF and EDX of a longitudinal cross-section of wire slice taken perpendicular to $\bar{c}$-axis: (a) High resolution STEM image showing 7x InGaN/AlGaN QWs, (b) STEM-HAADF image depicting InGaN QW in dark separated by AlGaN barrier in light, (c) EDX-elemental mapping of Ga, Si, In and Al (on top) and their composition profile along the position (below), (d) In atomic % and QW thickness for the 7x QWs and (e) Al atomic % and QW thickness for the 7x barriers.

The EDX analysis is performed with a FEI THEMIS microscope equipped with super X detectors. The presence of In, Al, Ga and Si can be seen in the EDX elemental mapping in **Figure 3.11 (c)** on the top-inset and their corresponding composition profiles are shown in the bottom-inset. The EDX analysis shows that the InGaN wells and AlGaN barriers are separated by GaN caps. In addition, a thin layer of Si is also detected at the interface of wire core and the first InGaN QW.

The origin of this unintentional thin layer probably originates from the residual silane present in the MOCVD reactor[‡‡‡]. The composition profile of In and Al along with the corresponding QWs and barriers thicknesses have been summarized in **Figure 3.11 (d)** and **(e)**. The first QW thickness measured by EDX is around 5.3 (±0.5) nm contrary to 3.5 nm as measured by TEM. This is due to the presence of a Si-phase that gives a brighter contrast in the TEM images similar to Ga contrast. However, the overall thickness including InGaN QW, GaN cap, AlGaN barrier is comparable when measured by TEM (18.1 nm) and EDX 18.6 (±1.0) nm. Similarly, the total sum of successive layers is also consistent: 25.2 nm by TEM compared to 24.2 (±1.0) nm by EDX. An average In-content of around 22 (±1) % is revealed by the In-profile in **Figure 3.11 (d)** evidencing the PL emission at 520 nm. **Figure 3.11 (e)** shows the average Al-composition inside the barriers is around 3.5 (±1) %, which is close to the targeted composition (5%).

S.No.	Structure	QW Growth	QB Growth	TMIn flow (µmol/min)	TMAl flow (µmol/min)	FWHM (meV)	IQE
Standard design	InGaN/GaN (T2546)	650 °C for 40 s	880 °C for 75 s	13.51	-	521	9.8%
1st design with Al	InGaN/AlGaN (T2581)	680 °C for 80 s	855 °C for 75 s	8.11	1.96	298	6.3%
Comparing GaN and	InGaN/GaN (T2555)	660 °C for 40 s	880 °C for 75 s	13.51	-	493	9.9%
AlGaN barrier	InGaN/AlGaN (T2556)	660 °C for 40 s	880 °C for 75 s	13.51	1.96	307	10.0%

Table 3.1: Summarized growth parameters of (InGaN/GaN and InGaN/AlGaN) heterostructures exhibiting green emission peaked at 520 nm.

Overall, the detailed investigation of InGaN/AlGaN core-shell heterostructures has reproduced green emission by using Al in the barriers. A PL emission at 520 nm is observed from QWs grown at a higher temperature (680 °C) compared to the standard (650 °C). However a high defect density is observed in the structure which can explain the low estimated IQE. The study is further extended by comparing two different structures with GaN and AlGaN barriers, respectively. The growth parameters of these two additional samples along with the previously reported green structures have been summarized in **Table 3.1** for comparison. A change in estimated IQE is observed for the standard green InGaN/GaN structure from 9.8 % to previously reported value of 4 % (in section

---

[‡‡‡] This observation is further discussed in detail in chapter 4.

3.2.2). This is due to the difference in laser power density used for exciting the wires. Nevertheless, the comparison in this table is straightforward because the samples have been measured in identical conditions. The temperature-dependent PL spectra in **Figure 3.12 (a)** and **(b)**[§§§] show that both samples with different barriers but similar growth parameters exhibit green emission at 520 nm. As the temperature increases, a redshift in PL emission followed by the peak broadening is observed for both samples. A similar IQE of around 10% is calculated for both InGaN/GaN and InGaN/AlGaN structures, however the latter shows a narrow peak with FWHM of 307 meV as compared to 493 meV for the former.
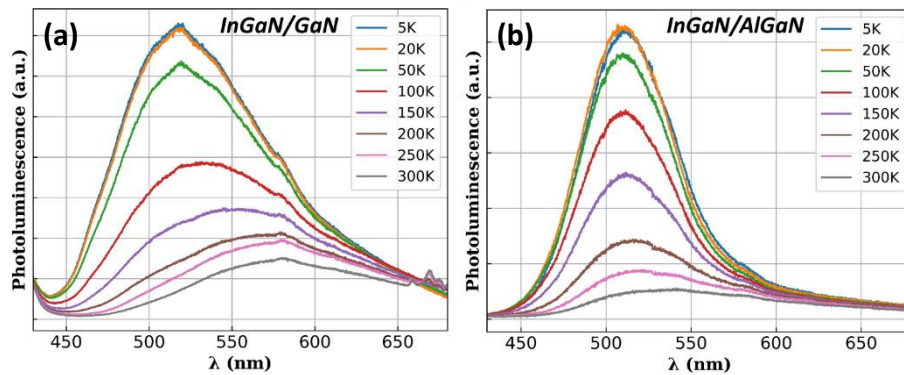
Figure 3.12: Temperature dependent PL spectra for (a) InGaN/GaN (#T2555) and (b) InGaN/AlGaN (#T2556) heterostructure showing green emission.

In conclusion, the present work using AlGaN barriers presents an alternative structure to achieve green emission and marks a beginning of some new experiments. Even if the structures exhibit low efficiency (and provide no real improvement with respect to the more standard design), the growth parameters to be able to control a given Al-composition and a narrow peak for green emission have been achieved in the present study. Additional growth experiments by varying the growth parameters or studying different Al-composition is needed to completely understand the behavior of Al for the long wavelength emissions.

[§§§] The PL experiment is performed in exactly similar conditions as used for the previous InGaN/AlGaN sample.

3.3 Dual color emission

The well-established blue emission and the ability to manage green emission from core-shell InGaN/GaN wires in the present thesis serve as a strong motivation to target a dual wavelength emission from single core-shell heterostructures. The demonstration of color mixing in MOCVD grown InGaN based LEDs has already been reported for different designs of 3D nanostructures. A recent work by *Cho et al.*[44] has reported orthogonally polarized dual-wavelength emission from site-controlled hexagonal Ga-polar InGaN/GaN core-shell microrod arrays. It is observed that the indium content in the *m*-plane facets is different compared to the edges between these facets and this leads to spatially separated blue-green emission. Another approach by creating a vertical stacking of axial QWs with two or three colors in a nanorod array by top-down approach has shown higher PL intensity as compared to the planar structure.[45] Although many groups have shown the color mixing by utilizing the variation of indium incorporation on different wire-facets[46,47,48] or using the methods explained above, no study has been reported by growing a lateral stack of InGaN active layers with different In-content in the case of core-shell wire-geometry to the best of our knowledge. The present work has been performed to target dual wavelength emission by growing InGaN/GaN core-shell heterostructures with two different sets of *m*-plane InGaN QWs having variable In-content. The wire growth has been presented in section 3.3.1 followed by the optical characterization using PL and CL in section 3.3.2. The wires have also been structurally investigated using STEM-HAADF combined with EDX analysis and will be described in section 3.3.3. The electrical properties of wires will be discussed later in the Chapter 5 based on fabrication and characterization of a flexible wire-LED.

3.3.1 MOCVD growth and structural observation

The growth of self-assembled $\bar{c}$-oriented GaN wires is performed on nitridated *c*-plane sapphire substrate with the similar growth parameters as mentioned in Chapter 2. A GaN-spacer is then radially grown around the wire-core at 900 °C for 100 s under N_2 to prevent the degradation of InGaN QWs from Si-contamination present at the wire sidewalls.[49,****] This is followed by the radial growth of three InGaN quantum wells (QWs) at 720 °C for 75 s separated by GaN barriers

---

[****] The detailed influence of GaN-spacer growth has been focused in Chapter 4.

grown at 900 °C for 150 s to target indium-content of about 15%. The growth of the third GaN barrier is then accompanied by the growth of seven InGaN QWs at 680 °C for 40 s separated by GaN barriers grown at 835 °C for 80 s to target higher indium content (~20%). The growth parameters of the two kinds of QWs have been summarized in **Table 3.2.**

Target In-content	QW number	QW temperature	QW growth time	QB temperature	QB growth time
15%	3	720 °C	75 s	900 °C	150 s
20%	7	680 °C	40 s	835 °C	80 s

Table 3.2: Growth parameters of two types of core-shell QWs targeting different indium-content.
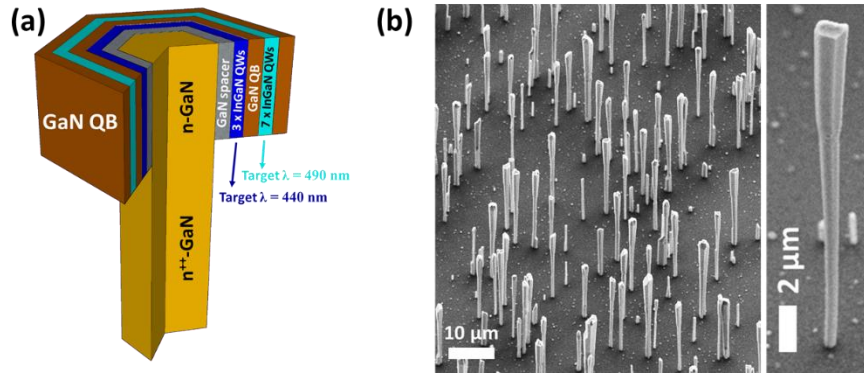
Figure 3.13: (a) Detailed schematics of *m*-plane InGaN/GaN heterostructure containing 3x InGaN QWs and 7x InGaN QWs with targeted emission at 440 and 490 nm, respectively; (b) 30°-tilted SEM images of the wires showing core-shell geometry (left) with an enlarged image of single wire (right). (Sample T2612).

The choice to firstly grow 3x QWs at higher temperature prior to the low temperature 7x QWs prevents the degradation of In-rich InGaN QWs with the lower growth temperature. Moreover, the QWs targeting lower indium content are positioned underneath the QWs with higher indium content in order to have less residual strain due to smaller lattice mismatch with lower In-content.[50] The larger number of green MQWs compared to the blue has been initially chosen to compensate a lower efficiency of the green emission with respect to the blue, and this point will be discussed later. **Figure 3.13 (a)** shows the schematics of the dual-color core-shell InGaN/GaN heterostructure. The SEM observation tilted at 30° of the as-grown wires on sapphire can be seen in **Figure 3.13 (b)** combined with an enlarged single wire image on the right. The wire average

density is in the order 10^6 wires/cm^2. The length of the wires is in the range of 35-40 μm, whereas the wire diameter at the top is around 1.0-1.5 μm.

3.3.2 Optical characterization

3.3.2.1 Temperature dependent PL (TDPL) and power dependent PL (PDPL)

The optical properties of the as-grown wires are investigated using PL measurements in the similar experimental setup used for the previous measurements for blue and green emission[††††]. **Figure 3.14 (a)** and **(c)** shows the temperature dependent PL (TDPL) spectra for a fixed laser power of 100 μW and a power dependent PL (PDPL) spectra for a fixed temperature at 5K respectively. A peak at 365 nm in both spectra corresponds to the near band edge of GaN. Two distinctive contributions can be observed at 435 and 485 nm in both spectra's arising from 3x InGaN QWs having low indium content and 7x InGaN QWs containing higher indium content respectively. A shoulder can also be observed in the TDPL spectra (see **Figure 3.14 (a)**) especially at low temperatures between 500-550 nm. It is probably related to a residual contribution arising from fluctuations in indium-rich area in QWs. Based on the PL intensity normalization at 300 K versus the intensity at 5 K (assuming 100% of QW efficiency at 5K), an upper limit of IQE is estimated to be 33.5% and 18% for the emission at 435 nm and 485 nm, respectively.[15] The lower value of IQE for longer wavelength emission is classically observed and is related to the local indium compositional fluctuations for QWs containing high indium content.[51] Further, the PL intensity of the longer wavelength emission dominates the short wavelength emission (almost doubles) at 5 K. As the low temperature PL spectra is mainly governed by the radiative recombination, the dominant behavior of the contribution at 485 nm can be directly associated with the increased number of QWs compared to the contribution at 435 nm. However, the non-radiative recombination becomes more and more significant as the temperature increases (especially for long wavelength emission) and consequently, the PL emission at 485 nm decreases and becomes comparable to the contribution at 435 nm, even if the QW number is higher. The comparable PL intensities at room temperature is also supported by the difference in the estimated IQE as mentioned above. Furthermore, an anomalous temperature dependence of the peak position is

---

[††††] Refer to Section 3.1.1
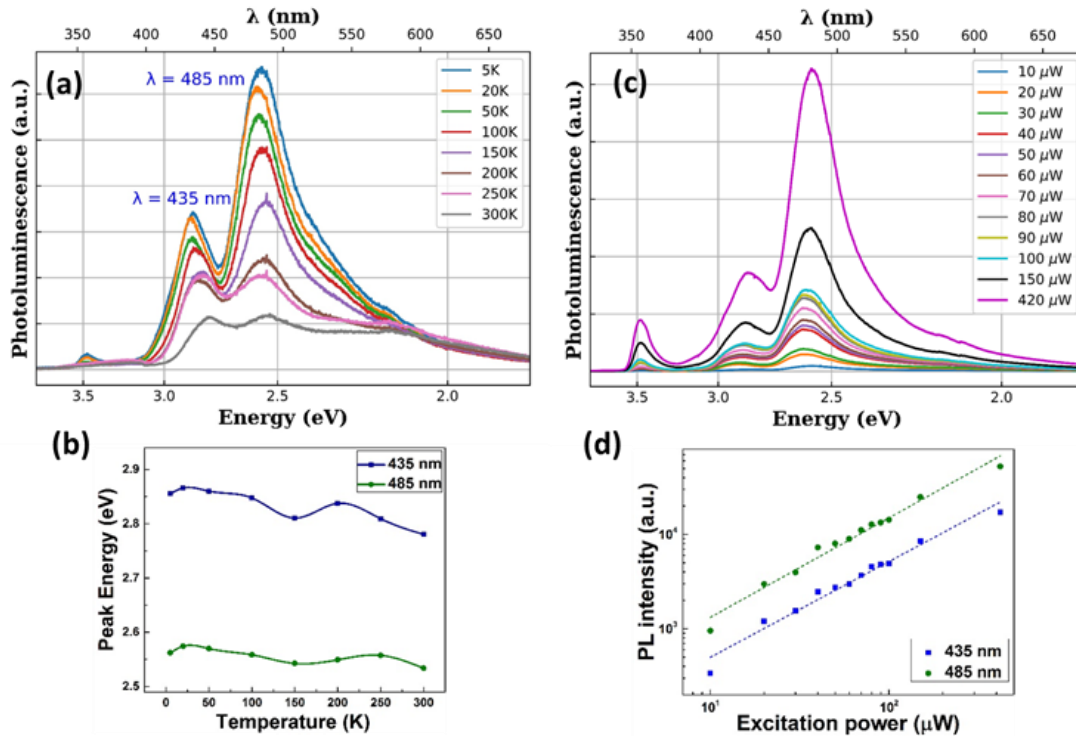
Figure 3.14: Photoluminescence (PL) measurement by exciting the wires with 244 nm laser: (a) temperature dependent PL (TDPL) spectra for a fixed laser power of 100 μW, (b) the temperature dependence of the PL peak positions for 435 and 485 nm contributions; (c) Excitation-power dependent PL (PDPL) spectra for a fixed temperature at 5 K, and (d) the power dependence of PL intensity for the two contributions.

observed for both contributions. The 'S-shape' behavior visible in the **Figure 3.14 (b)** indicates carrier localization in the two kinds of QWs. The mechanism behind this 'S-shape' can be explained as follows: when the temperature increases above 5 K, the created carriers are randomly distributed in the potential minima gain thermal energy. The thermally activated carriers relax into deepest localization states and recombine mainly from the lowest energy levels leading to a red-shift in the spectra.[52,53] As the temperature further increases, the carriers gain sufficient thermal energy to jump out of the potential minima and are randomly distributed again. They now occupy the highest energy states of the localized states and results in a blue shift of the spectra. Further increase in temperature leads to a red-shift of the spectra again as the recombination mechanism is now dominated by the temperature induced band gap shrinkage (Varshni's curve).[54,55]

In addition, the PDPL measurements at 5 K in **Figure 3.14 (c)** are performed for different laser excitation powers ranging from 10 to 420 μW. The screening of electric field in *c*-plane structures

usually occurs when excited with a high carrier density and causes a blue shift of the PL emission accompanied by peak narrowing.[56] In the present study, the stable luminescence for both 435 and 485 nm contributions with no clear shift evidences the origin of emission from *m*-plane QWs. Moreover, the evolution of the measured PL intensity 'I' with the laser excitation power 'P' obeys the relation: $I \propto P^{\alpha}$, where α defines the slope of the relation (see **Figure 3.14 (d)**). The derived values of α for both 435 and 485 nm contributions are 1.01 and 1.05 i.e. close to unity and evidence the dominance of radiative recombination at low temperature for non-polar QWs.[57]

3.3.2.2 Low temperature CL measurement

CL experiments have been performed to study the spatial emission of the two colors from wires dispersed on silicon substrates. The wires are excited with an electron beam having an acceleration voltage of 5 kV and a probe current of about 1 nA. A parabolic mirror is used to collect the resulting CL signal, which is then analyzed with a grating monochromator equipped with a Peltier cooled CCD camera (-60 °C). **Figure 3.15** represents the SEM image of a single wire with corresponding CL mappings integrated over a wavelength range of 10 nm. The near-band edge of GaN between 350-360 nm clearly arises from the bottom part of the wire, whereas both 430-440 and 480-490 nm contributions also observed in the PL measurements, emit from the core-shell active part located at the upper part of the wire. The 430-440 nm contribution seems to be non-uniformly distributed along the core-shell part. The emission with higher CL intensity is mainly located towards the top part of the wire and can also be seen between 440-450 nm. On the contrary, a relatively uniform emission is observed between 480-490 nm. Unlike PL spectra where the
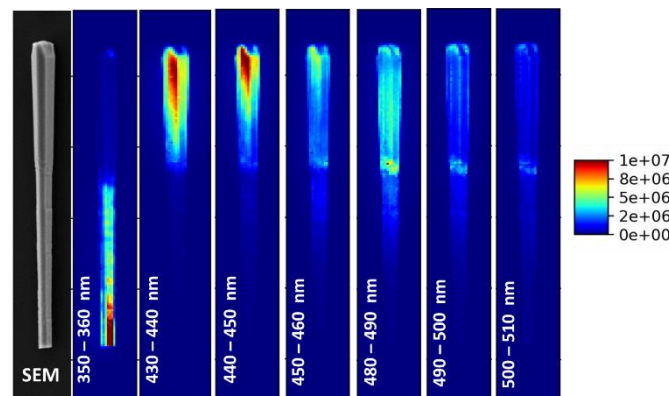
Figure 3.15: CL-mapping of single wire at 4 K for different wavelength emission with SEM image at extreme left.

emission intensity at 485 nm dominates the one at 435 nm, the reverse is revealed by CL mapping. This is probably explained by the different excitation processes: the PL probes a typical depth of 200 nm for nitrides considering the Lambert-Bert law, whereas the CL is more energetic process with a typical excitation depth at 5 kV around 300-400 nm. Consequently, the PL favors the emission of QWs close to the surface (here, the QW emitting at 480-490 nm), whereas the CL excites efficiently the deeper QWs emitting at 430-440 nm. Moreover, the wire-to-wire variations can be present on the sample and thus the direct comparison between the PL and CL measurements performed either on the wire ensemble or on single wires is not obvious. Regardless of the discrepancy in measured intensities, these CL measurements undoubtedly confirm the dual color emission from the non-polar *m*-plane wire sidewalls.

3.3.3 Structural characterization

The optical measurements are further correlated with structural properties of the wires. STEM observation combined with EDX analyses have been performed to confirm the presence of the two families of QWs having different indium content. The EDX measurements have been performed with the help of our collaborator Dr. Eric Robin (CEA/IRIG/MEM, LEMMA Laboratory).

3.3.3.1 STEM observation

The preparation of a thin wire slice and the details of STEM image acquisition are similar to that reported for InGaN/AlGaN heterostructures in section 3.2.6. The top part of the wire slice at low magnification can be seen on STEM images in **Figure 3.16 (a)** where the InGaN QWs appear in bright, while the GaN (wire core and barriers) appears dark. The presence of a flat top as well as a pyramidal tip shows a dual polarity for the wire corresponding to N- and Ga-polarity, respectively.[58] This is also confirmed by the existence of inversion domain boundary (IDB) distinguishing the two polarities (indicated by a white arrow).[59,60,61] Further, the *m*-plane radial InGaN QWs on the wire sidewall and the *c*-plane axial QWs on the wire top are visible for both polarities. **Figure 3.16 (b)** shows the high-resolution STEM image corresponding to the area indicated by the red square in **Figure 3.16 (a)**. Two families of QWs are clearly observed: one with 3x InGaN/GaN QWs that seem thicker as compared to the other 7x InGaN/GaN QWs. Some bright white lines are seen originating perpendicularly at the interface of the 1st QW of the second
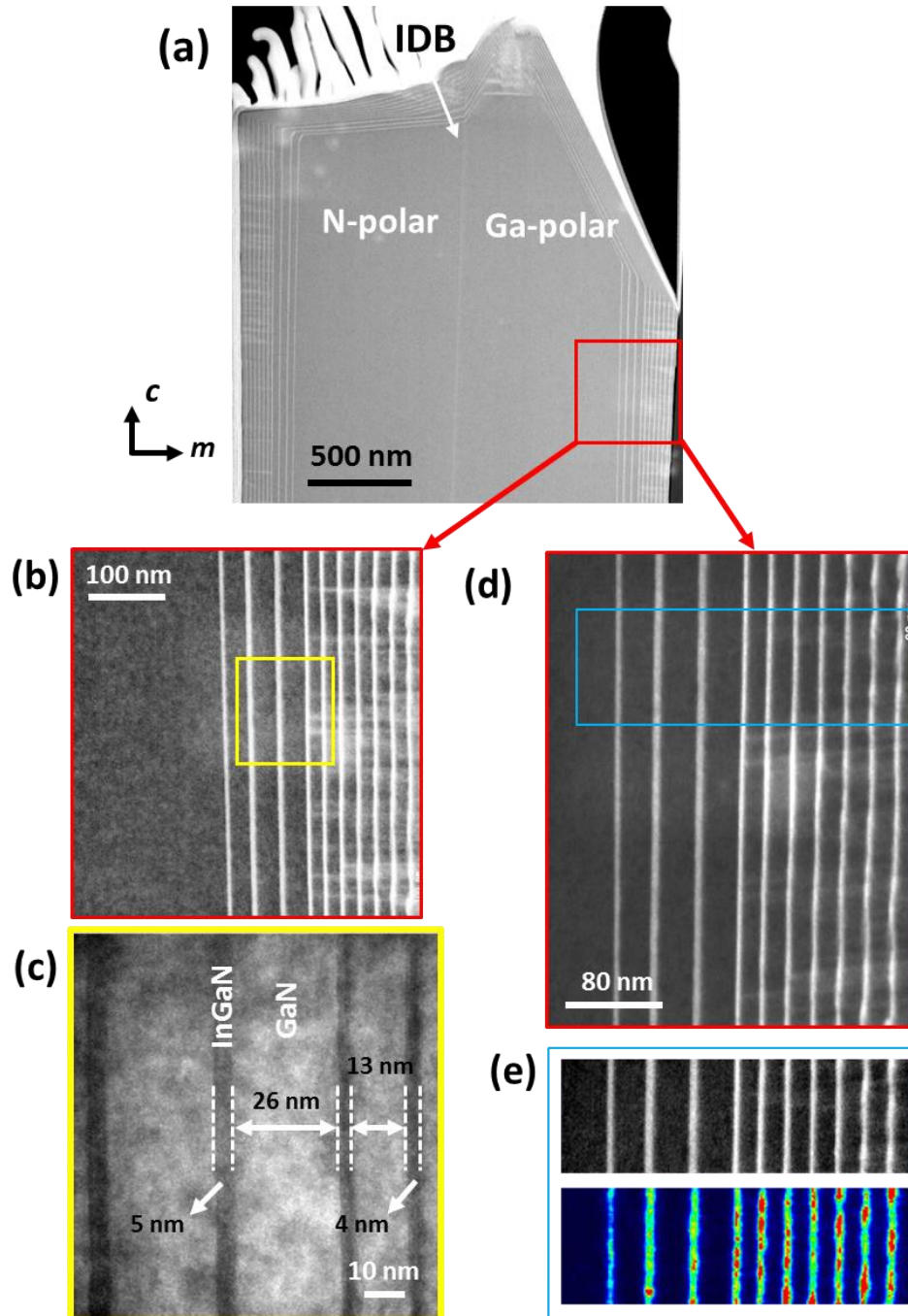
Figure 3.16: STEM-HAADF images of a longitudinal cross-section of wire taken perpendicular to $\bar{c}$-axis - (a) Top part of the wire slice showing dual polarity i.e. N- and Ga-polarity separated by Inversion domain boundary (IBD); (b&d) High resolution STEM image corresponding to the red square in (a) showing 3x InGaN/GaN QWs with higher thickness and 7x InGaN/GaN QWs with low thickness; (c) STEM-HAADF image with high resolution corresponding to yellow square in (b) revealing two distinctive families of QWs having different thicknesses; and (e) High resolution STEM image with corresponding EDX mapping representing area marked by blue square in (d).

family of 7x QWs and propagating across the structure. This contrast is similar to the structural observation for green QWs as described earlier and is attributed to extended defects such as the presence of stacking faults. The appearance of these defects only for the last 7x QWs and the absence (or much lower density) for the first 3x QWs is certainly related to the plastic strain relaxation due to higher indium composition present in the second family of QWs that induces a higher lattice mismatch.[27] The high resolution enlarged STEM-HAADF image corresponding to the area related to the yellow square in **Figure 3.16 (b)** is shown in **Figure 3.16 (c)**. The thickness of QW and barrier for first family containing 3x QWs is measured as 5 and 26 nm, while for the second family containing 7x QWs, the measured thicknesses are 4 and 13 nm for QWs and barriers, respectively. The STEM observation is further extended to EDX analysis performed on the same wire slice with the FEI THEMIS microscope equipped with super X detectors. A high-resolution STEM image in **Figure 3.16 (d)** shows similar features as **Figure 3.16 (b)**. The area marked by blue square is shown in **Figure 3.16 (e)** presenting the STEM image combined with the corresponding EDX mapping. An inhomogeneous indium distribution is visible for the last 7x QWs compared to first 3x QWs. In order to confirm this qualitative observation, a larger area of the slice has been measured to extract the indium composition inside the two sets of QWs as explained hereafter.

3.3.3.2 In-content profile by EDX analyses

The EDX elemental mapping for In with a higher resolution is shown in **Figure 3.17 (a**) but note that the color scale for first 3x QWs (layer 1-3) is different from that of last 7x QWs (layer 4-10). It can be seen that the indium distribution is relatively homogeneous in the first 3 QWs (while the composition is lower for layer 1), contrary to significant indium fluctuations observed for the last 7x QWs. Also, the last two QWs (layer 9&10) are not perfectly flat and exhibit a curvature at some places, which may be attributed to presence of defects that can perturb greatly the growth of last QWs. The In-content profile measured as a function of position from first to last QW integrated over the marked rectangle (corresponding to a width of 40 µm) is depicted in **Figure 3.17 (b)**. The red circles (connected by blue line) correspond to the experimental data. As previously explained for the EDX measurements, the teardrop shape of e-beam interaction can result in an over-estimation of Ga atoms from barriers. A correction considering an e-beam gaussian shape and sharp interfaces between QW/barrier reveals the calculated In-content profile (black dashed line)
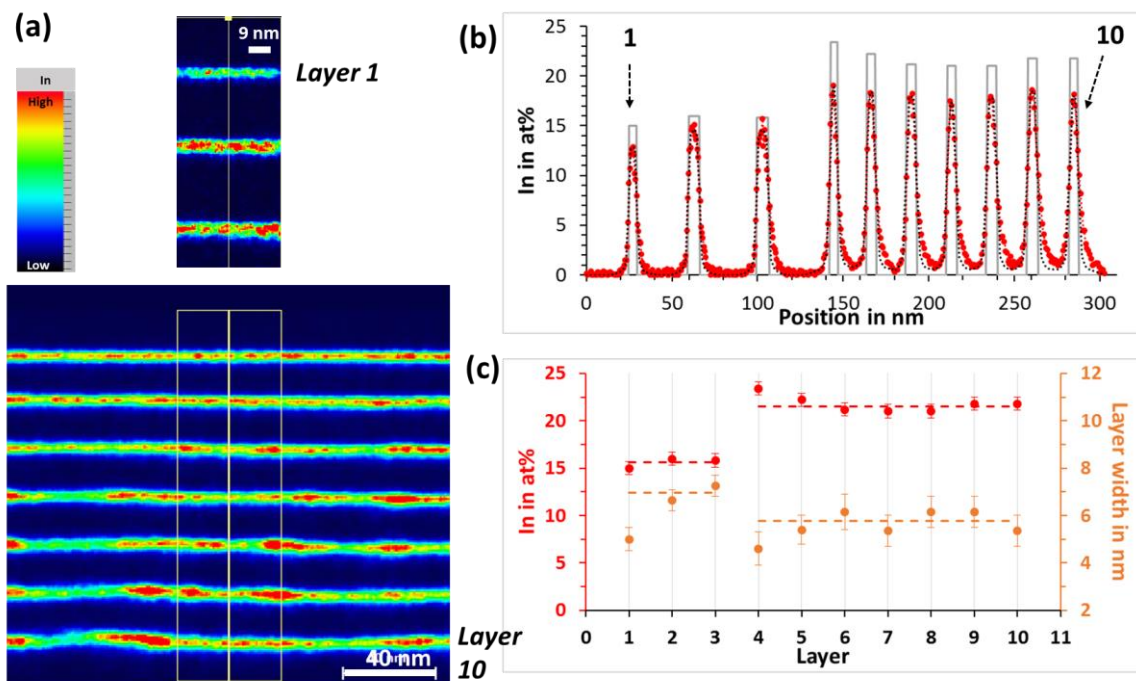
Figure 3.17: EDX measurements - (a) EDX elemental mapping of In for 3xQWs and 7xQWs with different color scale respectively, (b) In-profile as a function of position from first QW to last QW ; and (c) In-profile and QW thickness for first 3xQWs (layer 1-3) and last 7xQWs (layer 4-10).

close to the measured profile. The solid grey line shows the estimated true In-profile considering the corrections (e-beam shape and sharp interfaces). The two kinds of InGaN/GaN QWs are clearly visible and the estimated In-content as well as QW thickness are detailed in **Figure 3.17 (c)**. Note that the first well for both QW families has a lower thickness compared to the successive wells. This has also been observed in the STEM-HAADF images. The low thickness of the first QW (layer 1) can be attributed to a transition in growth temperature during the first loop of the growth. Similarly the transition in growth temperature from the 3rd barrier growth temperature at 900 °C to 4th QW growth temperature as 680 °C probably decreases the fourth QW (layer 4) thickness. An average indium content of around 15 ($\pm$1) % has been measured for the first 3x QWs (**see Figure 3.17 (c)**), which explains the optical emission around 435 nm.[9] Further, the measured thicknesses of the QWs with EDX show larger value $\approx$ 6.5 ($\pm$0.5) nm compared to the one already measured by STEM ($\approx$ 5.0 nm) (contradiction with STEM thickness is explained after). A variation in indium content and QW thickness is observed for 7x QWs, which can be explained by the large indium fluctuations revealed by the EDX mapping. Nevertheless, an average In-content for last 7x QWs is around 21.5 ($\pm$1) % and the average QW thickness is around 5.7 ($\pm$0.5) nm contrary to the

thickness measured by STEM (4.0 nm). This lack of agreement is observed for both sets of QWs and can be explained by the absence of sharp interfaces between the QWs and barriers as observed in STEM-HAADF images. A tail is also observed in the In-profile (red dots) measured by EDX for all QWs at both interfaces. Moreover, the change in QW shape for the last two layers could strongly impact their thickness estimation. However a relative difference of 1 nm is observed in the thickness of two sets of QWs by both STEM and EDX measurements. Hence, after considering these factors, the thickness for first 3x QWs and last 7x QWs can be assumed to be around 6 (±1) and 5 (±1) nm.

The combined optical and structural measurements have established the demonstration of dual color emission by growing two different kinds of InGaN QWs at different temperatures. The integration of lower (15%) and higher In-content (21%) in a single core-shell active region opens the possibility of multi-color emission from core-shell InGaN/GaN wires.

CONCLUSION

This chapter has provided an overview of our state of the art to target blue emission from *m*-plane InGaN/GaN core-shell heterostructures. The work is carried forward to target other wavelength emission from these core-shell structures. A comprehensive experimental analysis correlating structural, optical as well as electrical measurements presents the possibility of achieving green emission from core-shell *m*-plane InGaN/GaN MQWs. The In-content estimated to be equal to 24 (±4) % in the wire sidewalls leads to a green emission (500-520 nm) highlighting the potential of core-shell wire-based LEDs to emit long wavelength light. The reproducibility control for green emission is also discussed. Alternative structures based on InGaN/AlGaN MQWs have been explored and the influence of Al on emission properties of InGaN QWs has been studied. Unfortunately, this way does not provide an improvement of the emission efficiency. The work is then followed by the demonstration of color-mixing in the core-shell wires. A dual-color InGaN/GaN MQW structure has been grown and thoroughly studied by combining optical and structural measurements. The PL emission at 435 and 485 nm is explained by the estimated In-composition by EDX analysis around 15 and 21 %. Overall different wavelength emissions have been demonstrated by regulating the growth parameters of InGaN QWs and GaN barriers.

REFERENCES

[1] Feezell, D. F.; Schmidt, M. C.; DensBaars, S. P.; Shuji, N. Development of Nonpolar and Semipolar InGaN / GaN Visible Light-Emitting Diodes. *MRS Bull.* **2009**, 34, 318. https://doi.org/10.1557/mrs2009.93

[2] O'Donnell, K. P.; Mosselmans, J. F. W.; Martin, R. W.; Pereira, S.; White, M. E. Structural Analysis of InGaN Epilayers. *J. Phys. Condens. Matter* **2001**, *13*, 6977–6991. https://doi.org/10.1088/0953-8984/13/32/307.

[3] Akasaki, I.; Amano, H. Crystal Growth of Column III Nitrides and Their Applications to Short Wavelength Light Emitters. *J. Cryst. Growth* **1995**, *146* (1–4), 455–461. https://doi.org/10.1016/0022-0248(94)00501-X.

[4] Martin, R. W.; Edwards, P. R.; Pecharroman-Gallego, R.; Liu, C.; Deatcher, C. J.; Watson, I. M.; O'Donnell, K. P. Light Emission Ranging from Blue to Red from a Series of InGaN/GaN Single Quantum Wells. *J. Phys. D. Appl. Phys.* **2002**, *35*, 604–608. https://doi.org/10.1088/0022-3727/35/7/306.

[5] Matsuoka, T.; Yoshimoto, N.; Sasaki, T.; Katsui, A. Wide-Gap Semiconductor InGaN and InGaAln Grown by MOVPE. *J. Electron. Mater.* **1992**, *21* (2), 157–163. https://doi.org/10.1007/BF02655831.

[6] Keller, S.; Keller, B. P.; Kapolnek, D.; Mishra, U. K.; DenBaars, S. P.; Shmagin, I. K.; Kolbas, R. M.; Krishnankutty, S. Growth of Bulk InGaN Films and Quantum Wells by Atmospheric Pressure Metalorganic Chemical Vapour Deposition. *J. Cryst. Growth* **1997,** *170,* 349–352. https://doi.org/10.1016/S0022-0248(96)00553-2.

[7] Dühn, J.; Tessarek, C.; Schowalter, M.; Coenen, T.; Gerken, B.; Müller-Caspari, K.; Mehrtens, T.; Heilmann, M.; Christiansen, S.; Rosenauer, A.; et al. Spatially Resolved Luminescence Properties of Non- and Semi-Polar InGaN Quantum Wells on GaN Microrods. *J. Phys. D. Appl. Phys.* **2018***, 51,* 355102. https://doi.org/10.1088/1361-6463/aad4e6.

[8] Wernicke, T.; Schade, L.; Netzel, C.; Rass, J.; Hoffmann, V.; Ploch, S.; Knauer, A.; Weyers, M.; Schwarz, U.; Kneissl, M. Indium Incorporation and Emission Wavelength of Polar, Nonpolar and Semipolar InGaN Quantum Wells. *Semicond. Sci. Technol.* **2012**, *27*, 24014. https://doi.org/10.1088/0268-1242/27/2/024014.

[9] Koester, R.; Hwang, J.; Salomon, D.; Chen, X.; Bougerol, C.; Barnes, J.; Le Si Dang, D.; Rigutti, L.; Bugallo, A. D. L.; Jacopin, G.; et al. M-Plane Core-Shell InGaN/GaN Multiple-Quantum-Wells on GaN Wires for Electroluminescent Devices. *Nano Lett.* **2011**, *11*, 4839–4845. https://doi.org/10.1021/nl202686n.

[10] Bavencove, A. L.; Salomon, D.; Lafossas, M.; Martin, B.; Dussaigne, A.; Levy, F.; André, B.; Ferret, P.; Durand, C.; Eymery, J.; et al. Light Emitting Diodes Based on GaN Core/shell Wires Grown by MOVPE on N-Type Si Substrate. *Electron. Lett.* **2011**, *47* (13), 765–767. https://doi.org/10.1049/el.2011.1242.

[11] Dai, X.; Messanvi, A.; Zhang, H.; Durand, C.; Eymery, J.; Bougerol, C.; Julien, F. H.; Tchernycheva, M. Flexible Light-Emitting Diodes Based on Vertical Nitride Nanowires. *Nano Lett.* **2015**, *15*, 6958–6964. https://doi.org/10.1021/acs.nanolett.5b02900.

[12] Guan, N.; Dai, X.; Messanvi, A.; Zhang, H.; Yan, J.; Gautier, E.; Bougerol, C.; Julien, F. H.; Durand, C.; Eymery, J.; et al. Flexible White Light Emitting Diodes Based on Nitride Nanowires and Nanophosphors. *ACS Photonics* **2016**, *3*, 597–603. https://doi.org/10.1021/acsphotonics.5b00696.

[13] Salomon, D.; Dussaigne, A.; Lafossas, M.; Durand, C.; Bougerol, C.; Ferret, P.; Eymery, J. Metal Organic Vapour-Phase Epitaxy Growth of GaN Wires on Si (111) for Light-Emitting Diode Applications. *Nanoscale Res. Lett.* **2013**, *8* (61), 1–5. https://doi.org/10.1186/1556-276X-8-61.

[14] Messanvi, A. Composants Photoniques À Base de Fils de Nitrures D ' Élément S III : Du Fil Unique Aux Assemblées, *Universite Grenoble Alpes*, **2015**.

[15] Murotani, H.; Yamada, Y.; Tabata, T.; Honda, Y.; Yamaguchi, M.; Amano, H. Effects of Exciton Localization on Internal Quantum Efficiency of InGaN Nanowires. *J. Appl. Phys.* **2013**, *114*, 153506. https://doi.org/10.1063/1.4825124.

[16] Watanabe, S.; Yamada, N.; Nagashima, M.; Ueki, Y.; Sasaki, C.; Yamada, Y.; Taguchi, T.; Tadatomo, K.; Okagawa, H.; Kudo, H. Internal Quantum Efficiency of Highly-Efficient $In_xGa_{1-x}N$-Based near-Ultraviolet Light-Emitting Diodes. *Appl. Phys. Lett.* **2003**, *83*, 4906–4908. https://doi.org/10.1063/1.1633672.

[17] Kapoor, A.; Guan, N.; Vallo, M.; Messanvi, A.; Mancini, L.; Gautier, E.; Bougerol, C.; Gayral, B.; Julien, F. H.; Vurpillot, F.; et al. Green Electroluminescence from Radial M-Plane InGaN Quantum Wells Grown on GaN Wire Sidewalls by Metal-Organic Vapor Phase Epitaxy. *ACS Photonics* **2018**, *5*, 4330–4337. https://doi.org/10.1021/acsphotonics.8b00520.

[18] Yoshimoto, N.; Matsuoka, T.; Sasaki, T.; Katsui, A. Photoluminescence of InGaN Films Grown at High Temperature by Metalorganic Vapor Phase Epitaxy. *Appl. Phys. Lett.* **1991,** *59 (18)*, 2251–2253. https://doi.org/10.1063/1.106086.

[19] Koester, R.; Hwang, J. S.; Durand, C.; Dang, D. L. S.; Eymery, J. Self-Assembled Growth of Catalyst-Free GaN Wires by Metal-Organic Vapour Phase Epitaxy. *Nanotechnology* **2010**, *21*, 015602. https://doi.org/10.1088/0957-4484/21/1/015602.

[20] Lai, Y.-L.; Liu, C.-P.; Lin, Y.-H.; Hsueh, T.-H.; Lin, R.-M.; Lyu, D.-Y.; Peng, Z.-X.; Lin, T.-Y. Origins of Efficient Green Light Emission in Phase-Separated InGaN Quantum Wells. *Nanotechnology* **2006**, *17*, 3734−3739. https://doi.org/10.1088/0957-4484/17/15/020.

[21] Peng, H. Y.; McCluskey, M. D.; Gupta, Y. M.; Kneissl, M.; Johnson, N. M. Shock-Induced Band-Gap Shift in GaN: Anisotropy of the Deformation Potentials. *Phys. Rev. B* **2005**, *71,* 115207. https://doi.org/10.1103/PhysRevB.71.115207.

[22] Jacopin, G.; Bugallo, D. L. A.; Lavenus, P.; Rigutti, L.; Julien, F.H.; Zagonel, L. F.; Kociak, M.; Durand, C.; Salomon, D.; Chen, X. J.; Eymey, J.; Tchernycheva, M. Single-Wire Light-Emitting Diodes Based on GaN Wires Containing Both Polar and Nonpolar InGaN/GaN Quantum Wells. *Appl. Phys. Express* **2012,** *5*, 014101. https://doi.org/10.1143/APEX.5.014101.

[23] Keller, S.; Li, H.; Laurent, M.; Hu, Y.; Pfaff, N.; Lu, J.; Brown, D. F.; Fichtenbaum, N. A.; Speck, J. S.; Denbaars, S. P.; Mishra, U. K. Recent Progress in Metal-Organic Chemical Vapor Deposition of $(000\bar{1})$ N-Polar Group-III Nitrides. *Semicond. Sci. Technol.* **2014**, *29*, 113001. https://doi.org/10.1088/0268-1242/29/11/113001.

[24] Li, S.; Wang, X.; Fündling, S.; Erenburg, M.; Ledig, J.; Wei, J.; Wehmann, H. H.; Waag, A.; Bergbauer, W.; Mandl, M.; Strassburg, M.; Trampert, A.; Jahn, U.; Riechert, H.; Jönen, H.; Hangleiter, A. Nitrogen-

Polar Core-Shell GaN Light-Emitting Diodes Grown by Selective Area Metalorganic Vapor Phase Epitaxy. *Appl. Phys. Lett*. **2012**, *101*, 032103. https://doi.org/10.1063/1.4737395.

[25] Watson, D. C.; Martinez, R. V.; Fontana, Y.; Russo-Averchi, E.; Heiss, M.; Fontcuberta I Morral, A.; Whitesides, G. M.; Lončar, M. Nanoskiving Core-Shell Nanowires: A New Fabrication Method for Nano-Optics. *Nano Lett.* **2014**, *14,* 524−531. https://doi.org/10.1021/nl403552q.

[26] Mancini, L.; Lefebvre, W.; Houard, J.; Blum, I.; Vurpillot, F.; Eymery, J.; Durand, C.; Rigutti, L. Multi-Microscopy Study of the Influence of Stacking Faults and Three-Dimensional In Distribution on the Optical Properties of m-Plane InGaN Quantum Wells Grown on Microwire Sidewalls. *Appl. Phys. Lett.* **2016**, *108,* 042102. https://doi.org/10.1063/1.4940748.

[27] Fischer, A. M.; Wu, Z.; Sun, K.; Wei, Q.; Huang, Y.; Senda, R.; Iida, D.; Iwaya, M.; Amano, H.; Ponce, F. A. Misfit Strain Relaxation by Stacking Fault Generation in InGaN Quantum Wells Grown on M-Plane GaN. *Appl. Phys. Express* **2009**, *2*, 041002. https://doi.org/10.1143/APEX.2.041002.

[28] Krause, T.; Hanke, M.; Nicolai, L.; Cheng, Z.; Niehle, M.; Trampert, A. Structure and Composition of Isolated Core-Shell (In,Ga) N/GaN Rods Based on Nanofocus X-Ray Diffraction and Scanning Transmission Electron Microscopy. *Phys. Rev. Appl.* **2017**, *7*, 24033. https://doi.org/10.1103/PhysRevApplied.7.024033.

[29] Rigutti, L.; Blum, I.; Shinde, D.; Hernández-Maldonado, D.; Lefebvre, W.; Houard, J.; Vurpillot, F.; Vella, A.; Tchernycheva, M.; Durand, C.; Eymery, J.; Deconihout, B. Correlation of Microphotoluminescence Spectroscopy, Scanning Transmission Electron Microscopy, and Atom Probe Tomography on a Single Nano-Object Containing an InGaN/GaN Multi quantum Well System. *Nano Lett*. **2014**, *14*, 107−114. https://doi.org/10.1021/nl4034768.

[30] Ko, Y.-H.; Song, J.; Leung, B.; Han, J.; Cho, Y.-H. Multi-Color Broadband Visible Light Source via GaN Hexagonal Annular Structure. *Sci. Rep.* **2015,** *4*, 5514. https://doi.org/10.1038/srep05514.

[31] Damilano, B.; Gil, B. Yellow−Red Emission from (Ga,In)N Heterostructures. J. Phys. D: Appl. Phys. 2015, 48, 403001. https://doi.org/10.1088/0022-3727/48/40/403001.

[32] Browne, D. A.; Young, E. C.; Lang, J. R.; Hurni, C. A.; Speck, J. S. Indium and Impurity Incorporation in InGaN Films on Polar, Nonpolar, and Semipolar GaN Orientations Grown by Ammonia Molecular Beam Epitaxy. *J. Vac. Sci. Technol. A* **2012,** *30,* 041513. https://doi.org/10.1116/1.4727967.

[33] Horenburg, P.; Buß, E. R.; Rossow, U.; Bremers, H.; Ketzer, F. A.; Hangleiter, A. Strain Dependence of in Incorporation in m -Oriented GaInN/GaN Multi Quantum Well Structures. *Appl. Phys. Lett.* **2016,** *108,* 102105. https://doi.org/10.1063/1.4943232.

[34] Keller, S.; Keller, B. P.; Kapolnek, D.; Abare, A. C.; Masui, H.; Coldren, L. A.; Mishra, U. K.; Baars, S. P. Den. Growth and Characterization of Bulk InGaN Films and Quantum Wells. *Appl. Phys. Lett.* **1996,** *68,* 3147. https://doi.org/10.1016/j.jcrysgro.2005.01.075.

[35] Hsu, P. S.; Hardy, M. T.; Young, E. C.; Romanov, A. E.; Denbaars, S. P.; Nakamura, S.; Speck, J. S. Stress Relaxation and Critical Thickness for Misfit Dislocation Formation in (10−10) and (30−3−1) InGaN/GaN Heteroepitaxy. *Appl. Phys. Lett.* **2012,** *100,* 171917. https://doi.org/10.1063/1.4707160.

[36] Holec, D. Ã.; Costa, P. M. F. J.; Kappers, M. J.; Humphreys, C. J. Critical Thickness Calculations for InGaN/GaN. *J. Cryst. Growth* **2007**, *303,* 314−317. https://doi.org/10.1016/j.jcrysgro.2006.12.054.

[37] Raychaudhuri, S.; Yu, E. T. Critical Dimensions in Coherently Strained Coaxial Nanowire Heterostructures. *J. Appl. Phys.* **2006,** *99,* 114308. https://doi.org/10.1063/1.2202697.

[38] Guan, N. Nitride Nanowire Light-Emitting Diode, *Université Paris-Saclay*, **2018**.

[39] Ra, Y.-H.; Navamathavan, R.; Yoo, H.-I.; Lee, C.-R. Single Nanowire Light-Emitting Diodes Using Uniaxial and Coaxial InGaN/ GaN Multiple Quantum Wells Synthesized by Metalorganic Chemical Vapor Deposition. *Nano Lett.* **2014***, 14*, 1537−1545. https://doi.org/10.1021/nl404794v.

[40] Koleske, D. D.; Fischer, A. J.; Bryant, B. N.; Kotula, P. G.; Wierer, J. J. On the Increased Efficiency in InGaN-Based Multiple Quantum Wells Emitting at 530-590 Nm with AlGaN Interlayers. *J. Cryst. Growth* **2015**, *415*, 57–64. https://doi.org/10.1016/j.jcrysgro.2014.12.034.

[41] Mi, Z.; Ra, Y.; Rashid, R.; Liu, X. *US Pat. App. 16/044,337, July 24,* **2018***.

[42] Li, P.; Zhao, Y.; Li, H.; Li, Z.; Zhang, Y.; Kang, J.; Liang, M.; Liu, Z.; Yi, X.; Wang, G. Highly Efficient InGaN Green Mini-Size Flip-Chip Light-Emitting Diodes with AlGaN Insertion Layer. *Nanotechnology* **2019**, *30*, 95203. https://doi.org/10.1088/1361-6528/aaf656.

[43] Al Muyeed, S. A.; Sun, W.; Wei, X.; Song, R.; Koleske, D. D.; Tansu, N.; Wierer, J. J. Strain Compensation in InGaN-Based Multiple Quantum Wells Using AlGaN Interlayers. *AIP Adv.* **2017**, *7*, 105312. https://doi.org/10.1063/1.5000519.

[44] Choi, S.; Song, H. G.; Cho, S.; Cho, Y. Orthogonally Polarized, Dual-Wavelength Quantum Wire Network Emitters Embedded in Single Microrod. *Nano Lett.* **2019**. https://doi.org/10.1021/acs.nanolett.9b02731.

[45] Feng, L. Sen; Liu, Z.; Zhang, N.; Xue, B.; Wang, J. X.; Li, J. M. Effect of Nanorod Diameters on Optical Properties of GaN-Based Dual-Color Nanorod Arrays. *Chinese Phys. Lett.* **2019**, *36 (2),* 27802. https://doi.org/10.1088/0256-307X/36/2/027802.

[46] Funato, M.; Hayashi, K.; Ueda, M.; Kawakami, Y.; Narukawa, Y.; Mukai, T. Emission Color Tunable Light-Emitting Diodes Composed of InGaN Multifacet Quantum Wells. *Appl. Phys. Lett.* **2008**, *93*, 21126. https://doi.org/10.1063/1.2956404.

[47] Song, W.; Chen, H.; Luo, X.; Sun, Y.; Wang, X.; Wang, H.; Guo, D.; Qi, M.; Li, G.; Li, S. A Single InGaN/GaN Multiple Quantum Wells Microwire Light-Emitting Diode with High Efficiency Current Injection and Spreading. *J. Alloys Compd.* **2019**, *791*, 1241–1247. https://doi.org/10.1016/j.jallcom.2019.03.371.

[48] Schmidt, G.; Müller, M.; Veit, P.; Metzner, S.; Bertram, F.; Hartmann, J.; Zhou, H.; Wehmann, H. H.; Waag, A.; Christen, J. Direct Imaging of Indium-Rich Triangular Nanoprisms Self-Organized Formed at the Edges of InGaN/GaN Core-Shell Nanorods. *Sci. Rep.* **2018,** *8,* 16026. https://doi.org/10.1038/s41598-018-34382-y.

[49] Kapoor, A.; Finot, S.; Grenier, V.; Robin, E.; Bougerol, C.; Bleuse, J.; Jacopin, G.; Eymery, J.; Durand, C. Role of Underlayer for Efficient Core-Shell InGaN QWs Grown on m-Plane GaN Wire Sidewalls. *ACS Appl. Mater. Interfaces* **2020**, *12* (16), 19092–19101. https://doi.org/10.1021/acsami.9b19314.

[50] Zhu, J. H.; Wang, L. J.; Zhang, S. M.; Wang, H.; Zhao, D. G.; Zhu, J. J.; Liu, Z. S.; Jiang, D. S.; Qiu, Y. X.; Yang, H. The Investigation on Strain Relaxation and Double Peaks in Photoluminescence of InGaN/GaN MQW Layers. *J. Phys. D. Appl. Phys.* **2009**, *42*, 235104. https://doi.org/10.1088/0022-3727/42/23/235104.

[51] Yang, Y.; Cao, X. A.; Yan, C. Investigation of the Nonthermal Mechanism of Efficiency Rolloff in InGaN Light-Emitting Diodes. *IEEE Trans. Electron Devices* **2008**, *55 (7),* 1771–1775. https://doi.org/10.1109/TED.2008.923561.

[52] Mu, Q.; Xu, M.; Wang, X.; Wang, Q.; Lv, Y.; Feng, Z.; Xu, X.; Ji, Z. Influence of the InGaN/GaN Quasi-Superlattice Underlying Layer on Photoluminescence in InGaN/GaN Multiple Quantum Wells. *Phys. E* **2016**, *76*, 1–5. https://doi.org/10.1016/j.physe.2015.10.010.

[53] Liu, W.; Zhao, D. G.; Jiang, D. S.; Chen, P.; Liu, Z. S.; Zhu, J. J.; Shi, M.; Zhao, D. M.; Li, X.; Liu, J. P.; et al. Localization Effect in Green Light Emitting InGaN/GaN Multiple Quantum Wells with Varying Well Thickness. *J. Alloys Compd.* **2015**, *625*, 266–270. https://doi.org/10.1016/j.jallcom.2014.11.138.

[54] Varshni, Y. P. Temperature Dependence of the Energy Gap in Semiconductors. *Physica* **1967**, *34* (1), 149–154. https://doi.org/10.1016/0031-8914(67)90062-6.

[55] Shan, W.; Little, B. D.; Song, J. J.; Feng, Z. C.; Schurman, M.; Stall, R. A. Optical Transitions in InxGa1-xN Alloys Grown by Metalorganic Chemical Vapor Deposition. *Appl. Phys. Lett.* **1996**, *69*, 3315–3317. https://doi.org/10.1063/1.117291.

[56] Wang, T.; Nakagawa, D.; Wang, J.; Sugahara, T.; Sakai, S. Photoluminescence Investigation of InGaN/GaN Single Quantum Well and Multiple Quantum Wells. *Appl. Phys. Lett.* **1998**, *73*, 3571–3573. https://doi.org/10.1063/1.122810.

[57] Wang, H.; Ji, Z.; Qu, S.; Wang, G.; Jiang, Y.; Liu, B.; Xu, X.; Mino, H. Influences of Excitation Power and Temperature on Photoluminescence in InGaN/GaN Multiple Quantum Wells. *Opt. Express* **2012**, *20* (4), 3932–3940. https://doi.org/10.1088/1674-1056/24/2/024219.

[58] Chen, X. J.; Perillat-Merceroz, G.; Sam-Giao, D.; Durand, C.; Eymery, J. Homoepitaxial Growth of Catalyst-Free GaN Wires on N-Polar Substrates. *Appl. Phys. Lett.* **2010**, *97*, 151909. https://doi.org/10.1063/1.3497078.

[59] Chen, X. J.; Hwang, J. S.; Perillat-Merceroz, G.; Landis, S.; Martin, B.; Le Si Dang, D.; Eymery, J.; Durand, C. Wafer-Scale Selective Area Growth of gaN Hexagonal Prismatic Nanostructures on c-Sapphire Substrate. *J. Cryst. Growth* **2011**, *322*, 15–22. https://doi.org/10.1016/j.jcrysgro.2011.03.007.

[60] Labat, S.; Richard, M. I.; Dupraz, M.; Gailhanou, M.; Beutier, G.; Verdier, M.; Mastropietro, F.; Cornelius, T. W.; Schülli, T. U.; Eymery, J.; et al. Inversion Domain Boundaries in GaN Wires Revealed by Coherent Bragg Imaging. *ACS Nano* **2015**, *9* (9), 9210–9216. https://doi.org/10.1021/acsnano.5b03857.

[61] Lançon, F.; Genovese, L.; Eymery, J. Towards Simulation at Picometer-Scale Resolution: Revisiting Inversion Domain Boundaries in GaN. *Phys. Rev. B* **2018**, *98*, 165306. https://doi.org/10.1103/PhysRevB.98.165306.

Chapter 4: Improvement of light emission from core-shell InGaN/GaN wires

The previous chapter has reported different color emissions from m-plane core-shell InGaN/GaN wires using multiple quantum wells (MQWs) heterostructures. This chapter focusses on the improvement of internal quantum efficiency (IQE) of core-shell InGaN MQWs. For that, a single InGaN quantum well (SQW) heterostructure emitting blue light is chosen as a benchmark to study the emission properties. Two different kinds of core-shell underlayer are grown around GaN wires before the SQW in order to improve the light emission efficiency: 1) an InGaN underlayer (namely "InGaN UL") with low In-content and 2) a GaN underlayer (called "GaN spacer"). The properties of the m-plane core-shell InGaN/GaN SQW with the two types of underlayer have been investigated combining structural and optical measurements. PL and CL are performed at room temperature to study the spatial emission from wires, while time-resolved cathodoluminescence measurements provide insights of carriers' recombination along with an estimation of IQE variation. A detailed discussion including structural analyses by scanning transmission electron microscopy (STEM) as well as EDX analyses is proposed to understand the results.

4.1 State of the Art

Standard blue planar *c*-plane GaN light emitting diodes (LEDs) comprising several InGaN quantum wells (QWs) with indium content in the range of 15-18% can be achieved with an external quantum efficiency higher than 80%,[1,2] yet these conventional devices suffer adversely from the efficiency droop at high current injection. On the other hand, achieving high efficiency with wire-based LED remains a significant challenge till date to be able to compete against the present planar technology. For instance, an EQE of 3% has been reported for white wire-LED,[3] combining blue emission of InGaN/GaN core-shell microrod LED with yellow phosphors at a current density of 400 mA/mm^2 while 12.5% of EQE has been reported for flexible white wire-LED [4] having also core-shell InGaN/GaN wires at a current density of 140 mA/mm^2.

Presently, the *c*-planar LEDs exhibit enhanced efficiency by exploiting different types of buffer layers grown prior to the InGaN/GaN active well structures, such as short-period InGaN/GaN superlattices,[5,6] Si-doped (In)GaN prelayers[7] and InGaN underlayer (UL) with low In-content.[8,9,10,11] A recent investigation about the role of InGaN underlayer to increase the InGaN/GaN SQW efficiency reveals that an optimized thickness of 55 nm with around 3% indium content significantly improves the EQE by 3.5 times, while at room temperature the QW effective lifetime increases from 170 ps (no UL) to 20 ns (with UL) indicating a lower non-radiative (NR) recombination rate.[12] According to the proposed mechanism, the NR centers corresponds to the GaN surface point defects created by the high temperature growth of GaN template prior to QW grown at lower temperature. These point defects are then trapped by the InGaN UL allowing a later point defect-free QW growth.[12] Apart from utilizing InGaN UL as a buffer layer, some recent work also demonstrates that a GaN buffer layer grown at low temperature under nitrogen improves the PL emission (by 40%) by suppressing some QW chemical contaminations, as indicated by SIMS analysis.[13] In view of these remarkable improvements in the *c*-plane QW efficiency by inserting the buffer layers, we decided to extend this exploration to *m*-plane core-shell heterostructures by investigating the influence of different buffer layers on radial *m*-plane InGaN QWs in terms of luminescence efficiency.[14] Because the surface energy of GaN and growth mechanisms differs from *c*-plane to *m*-plane (especially in our case with the use of silane to favor the wire growth), a variation in the defect density for the InGaN QW grown on the two different

facets can be expected.

4.2 Investigating the role of GaN spacer and InGaN underlayer on *m*-plane InGaN SQW

The *m*-plane core-shell InGaN SQW heterostructures have been grown by MOCVD to target the blue light emission. The advantage to grow only one quantum well is to eliminate an average effect occurring in heterogeneous MQWs, e.g. with a superlattice effect, only the last QWs could emit efficiently. The samples are characterized by both PL and CL as shown in section 4.2.2. The results are further correlated with time-resolved (TRCL) measurement to determine the carriers' recombination life time, which can provide an estimation of IQE variation and shown in section 4.2.3.

4.2.1 MOCVD Growth and structural observation

Catalyst-free self-assembled GaN wires are grown along the $\bar{c}$-direction (i.e. N-polar) by MOVPE on nitridated *c*-plane sapphire substrates followed by a thin SiNx layer deposition to create a selective growth layer on the substrate surface.[15] The growth parameters are similar to those explained in Chapter 2. The heavily n^{++} doped GaN wire ($N_d \approx 10^{20}$ cm^{-3})[15,16,17] grown in the presence of silane is about 18 μm in length. The unintentionally doped part (but with quite strong residual n-type doping in the order of 10^{18} cm^{-3})[15,16] grown by switching off the silane is about 12 μm in length. Three different samples based on identical wire-geometry (see the schematics in **Figure 4.1**) are investigated for the present study.

The first sample is prepared by directly growing a radial InGaN SQW around the GaN core under N$_2$ at growth temperature of 750 °C for 80 s followed by the growth of a GaN barrier (sample #1 so-called "SQW", see **Figure 4.1 (a)**). The second sample (sample #2 so-called "GaN-spacer+SQW", see **Figure 4.1 (b)**) is grown under N$_2$ carrier gas by adding a core-shell GaN spacer at 900 °C for 100 s around the GaN core before the similar growth of InGaN SQW and GaN barrier as already performed for the sample #1. The third sample (sample #3 named as "GaN-spacer+UL+SQW") depicted in the **Figure 4.1 (c)** is prepared by growing a core-shell GaN spacer

(similar growth conditions as mentioned above) followed by the growth of an InGaN underlayer (UL) at 800 °C for 900 s to target an indium composition around 3-5% so as to be consistent with the work performed on *c*-plane planar based structures. The structure is completed by the growth of *m*-plane InGaN/GaN SQW and GaN barrier using the previous growth parameters. As already mentioned, the present study is only performed on single InGaN QW, because for the structures having two or more QWs, the first QW itself may act as a buffer layer, thereby altering the direct influence of a GaN spacer or an UL on the overall QW efficiency.

SEM images of the three tilted (30°) samples are shown in **Figure 4.1 (d), (e)** and **(f)** respectively. The core-shell geometry located in the upper part of wires is visible for all samples with wires having a diameter in the 0.7-1.2 µm range and length in the 25-30 µm range. The average wire density is around 10^6 wire/cm^2 for all samples. A residual sidewall overgrowth can be observed at the transition region located between the top and bottom part of the wires, which is attributed to a non-continuous passivating film of SiN$_x$ around the GaN core.[15,18]
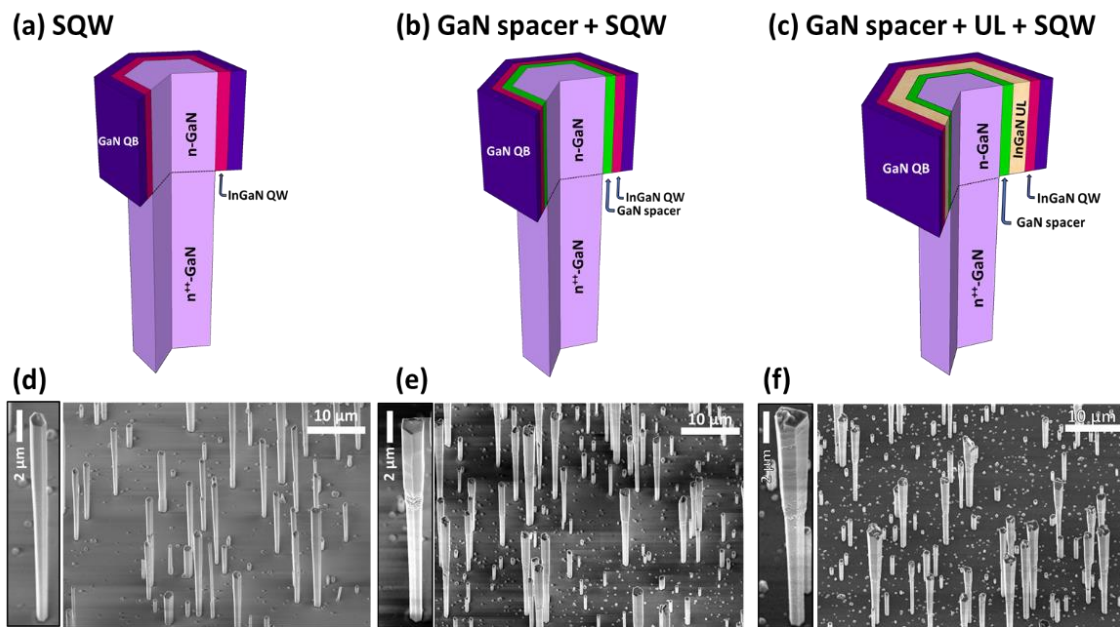
Figure 4.1: Schematics of the three core-shell heterostructures grown on $\bar{c}$-oriented GaN wires: (a) #1 InGaN single quantum well (SQW), (b) #2 with the addition of a GaN spacer prior to SQW, (c) #3 with the adding of an InGaN under-layer (UL) between the GaN spacer and the SQW. 30°-tilted SEM images of as-grown wires: (d), (e) and (f) corresponds to (a), (b) and (c) heterostructures respectively along with enlarged views on single wires. (#1: T2628, #2: T2594, #3: T2597)

4.2.2 Optical characterization using Photoluminescence and Cathodoluminescence

The influence of InGaN UL and GaN spacer on the SQW emission of the samples has been investigated using PL of as-grown wires on sapphire and CL of dispersed wires on silicon substrates. The PL experiment is carried out by using a continuous wave doubled solid-state laser to excite the wires at 244 nm with an excitation power density of 21 W/cm^2. The signals are analyzed through a 46 cm focal length spectrometer equipped with a 600 grooves/cm grating and detected with a liquid nitrogen cooled charge coupled device (CCD) camera. The CL measurements are performed at room temperature on single wires dispersed on silicon substrates. The experimental details are similar to that used for previous measurement performed on the dual-color LED in section 3.3.2.2.
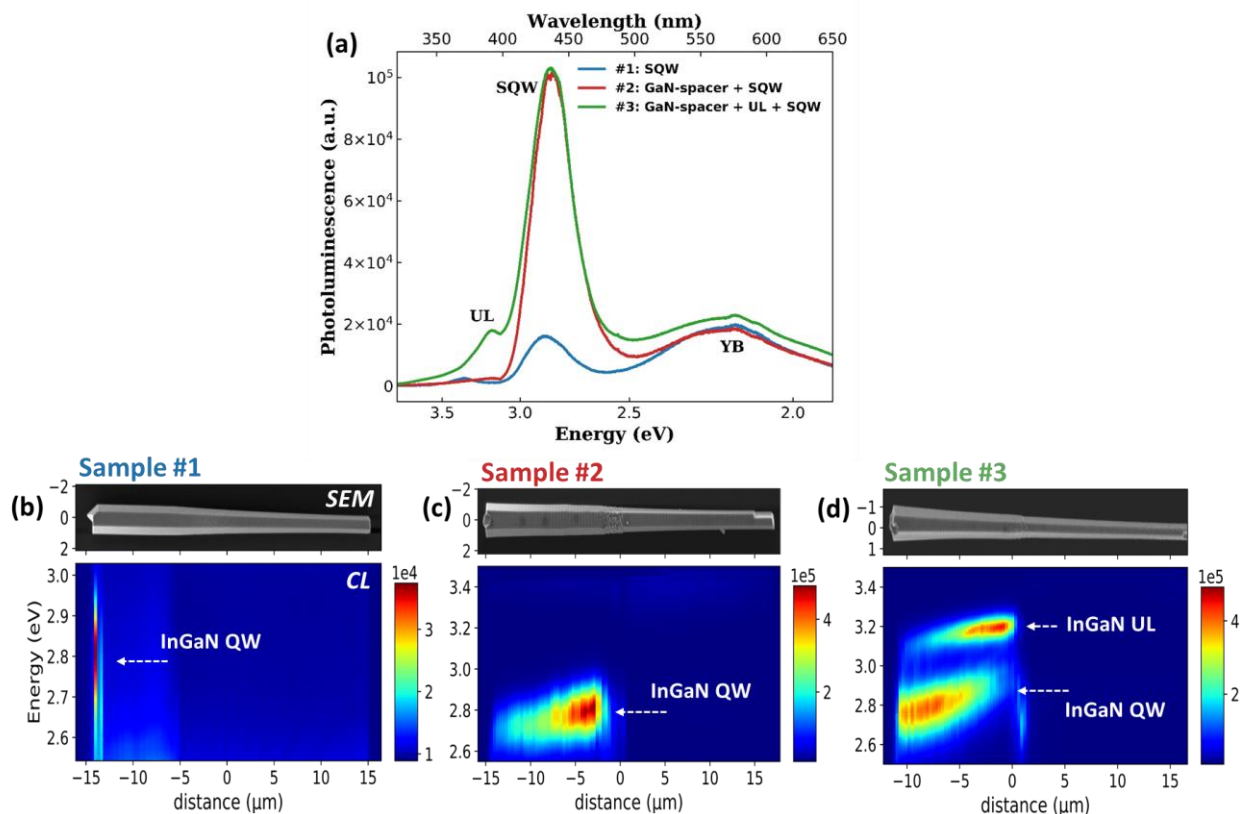
Figure 4.2: Optical measurements: (a) Photoluminescence (PL) spectra at 300 K by exciting the samples at 244 nm for the three as-grown wires heterostructures as presented in Fig. 4.1, (b)-(d) Room temperature cathodoluminescence (CL) hyperspectral analysis of the emission with the SEM image view of the measured wires for sample #1, #2 and #3 respectively.

The PL emission for the three samples recorded strictly in the same conditions at room temperature is shown in **Figure 4.2 (a)** and CL measurements in **Figure 4.2 (b)-(d)** represent the SEM images of the typical single wires for the three samples with their corresponding CL hyperspectral signals.

A PL emission around 431 nm can be seen from sample #1 with direct SQW growth in **Figure 4.2 (a)** with the full width at half maximum (FWHM) of 280 meV. However the CL mapping in **Figure 4.2 (b)** shows almost no emission from the *m*-plane sidewalls. Measurements on different single wires confirm that the overall *m*-plane emission from SQW sample is negligible and varies from wire-to-wire. Only the weak QW emission from the top facet can be observed for the present wire located around 2.8 eV (with a wire-to-wire variation down to 2.7 eV). Consequently, the PL emission observed for sample #1 is associated with QW located at the top facet and does not arise from the radial *m*-plane QW. The origin of light emission coming from the top facet can be attributed to the *c*-plane facets or also semipolar facets present at the junction between c-plane and m-plane surfaces. For sample #2 and #3, the PL emission of the InGaN QW positioned around 435nm is observed in **Figure 4.2 (a)** with the FWHM of 230 and 256 meV, respectively. Another contribution occurs at 3.2 eV (~390 nm) only for the sample #3 evidencing the presence of InGaN UL with a low indium content estimated at ~5% from the PL emission.[19] Further, the related CL measurements for wire containing GaN spacer without and with InGaN UL (sample #2 and #3) respectively clearly show an intense QW emission originating from the *m*-plane sidewalls (see **Figure 4.2 (c)** and (**d**)). This emission is located in the range of 2.7-2.9 eV, which is attributed to the indium fluctuations for a given target In composition.[20] We observe an overall redshift of the transition from the bottom to the top, as it is usually observed for such InGaN/GaN core-shell structures.[21,22] Also, **Figure 4.2 (d**) shows the emission from InGaN UL is localized around 3.2 eV all along the wire-sidewall without noticeable red-shift indicating much smaller indium fluctuations in agreement with the low-In content. This emission is present on full wire sidewalls and proves that the core-shell growth of low In-content InGaN UL is actually effective prior the QW growth on *m*-plane surfaces. The intensity decrease of InGaN UL contribution at 3.2 eV in the direction bottom-up (right to left) is attributed to the increase of shell thickness observed on SEM images allowing a reduced excitation of the InGaN UL by the e-beam.

From these CL analyses, a direct comparison of PL intensities of sample #2 and #3 with sample #1 is not straightforward because the origin of SQW luminescence is different: either related to top facets for sample #1 or related to *m*-plane facets for sample #2 and #3. We noticed that the emission from sample #1 in both PL and CL emission exhibits one order of magnitude lower intensity compared to other two samples, whereas a similar intensity for both PL and CL measurements is observed for sample #2 and #3.

The observation from PL spectra could also suggest that the thickness of UL chosen for the study was not optimized for the core-shell structure (the composition being fixed to the planar growth value). Therefore, a series of samples similar to sample #3 but with variable UL thickness (growth time varying from 300 to 1200 s) has been grown additionally and characterized by PL as shown in **Figure 4.3**.[*] These measurements evidenced no significant improvement in the QW emission as a function of the UL thickness.
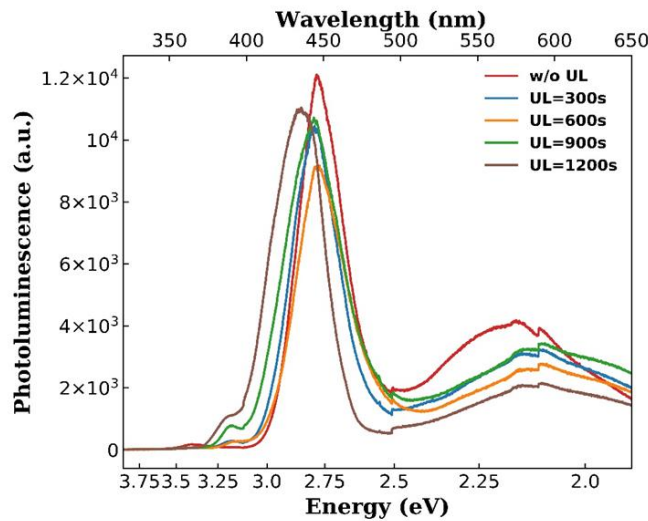
Figure 4.3: PL spectra for a series of samples similar to sample #3 but with varying thickness of InGaN UL by changing the growth time from 300 to 1200 s.

Further investigation for the three samples is performed using temperature dependent PL experiment to study the competition between the radiative and non-radiative (NR) recombination as shown in **Figure 4.4**. For samples #2 and #3 containing GaN spacer - without and with UL (see

---

[*] This series of samples has been measured separately compared to the samples measured in Figure 4.2 (a). Therefore, considering a variation in the measurement setup, a change in the resulting PL intensity can be expected even though the wire density remains similar for all the samples.

Figure 4.4 (b) and **(c)**), the IQE of SQW is estimated to be 15.3% and 14.9% respectively corresponding to *m*-plane QWs. The high IQE in both cases is clearly linked to the presence of GaN spacer, since the presence of UL does not strongly change the IQE, pointing out the dominance of the 'spacer effect' over the 'UL effect'. It is observed from the above PL and CL measurements that indeed the presence GaN spacer grown prior to the InGaN SQW significantly improves the QW emission efficiency in the case of *m*-plane InGaN/GaN core-shell wires.
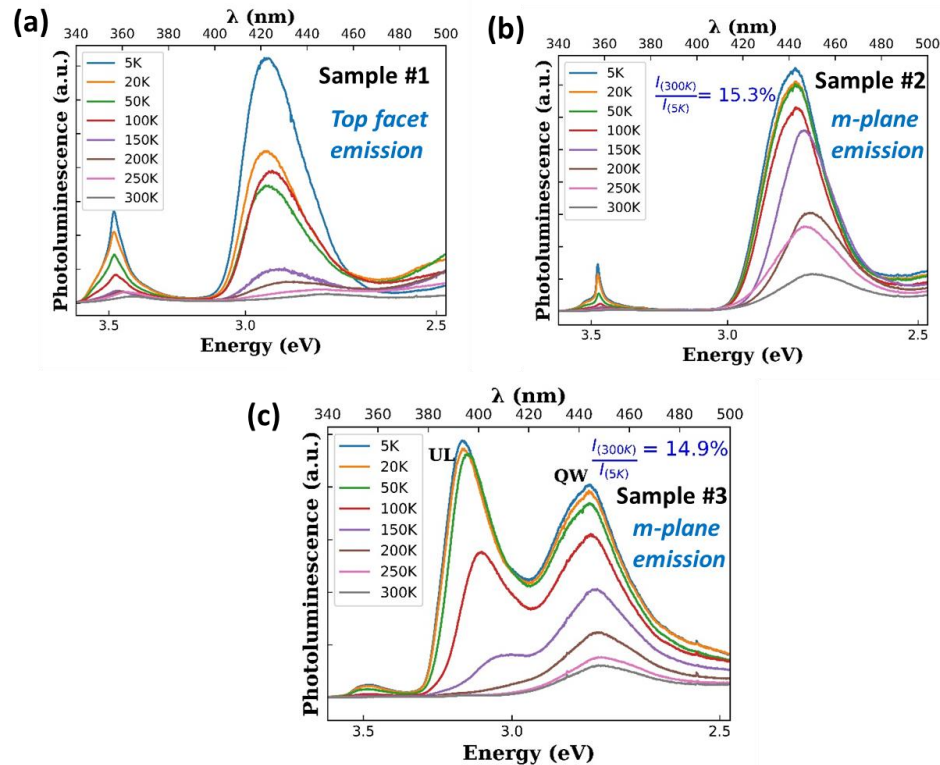
Figure 4.4: Temperature dependent PL spectra for the three as-grown samples as presented in Fig. 4.1.

4.2.3 Estimating carrier lifetime using time resolved CL measurements

Considering now that the results obtained in PL can be influenced by the emission of $\bar{c}$-plane surface (as seen in **Figure 4.2 (a)**) and that the PL and CL intensity is not a reliable parameter for comparing different samples (since it can be affected by the difference in extraction efficiency), a time-resolved CL (TRCL) analysis is carried out to estimate the light emission efficiency.[†] In

---

[†] Both CL and TRCL measurements have been performed with the help of Sylvain Finot and Gwénolé Jacopin at Institute Néel, Grenoble.

addition to the CL setup described above, a beam blanker has been used to generate short electron pulses and the recombination rate is measured using a fast photodetector. Details of the experimental setup can be found elsewhere.[23] Considering the size of the wires (about 1.5 µm in diameter) and the rise time of the pulse generator, the temporal resolution is limited by the detector and estimated to be around 50 ps. The CL decay lifetime is calculated by fitting the experimental data with a mono-exponential decay:

$$I(t) = I_0 \exp\left(-\frac{t}{\tau}\right) \qquad\qquad \ldots\ldots \text{ (Eq. 4.1)}$$

$$\frac{1}{\tau} = \frac{1}{\tau_r} + \frac{1}{\tau_{nr}} \qquad\qquad \ldots\ldots \text{ (Eq. 4.2)}$$

where τ is the effective lifetime considering both radiative (τ_r) and non-radiative (τ_{nr}) processes. The internal quantum efficiency is then defined as IQE = τ/τ_r.

Assuming that the radiative lifetime is the same for all samples, we can compare the relative change of IQE between the different samples by simply probing the effective lifetime at room temperature.[12] Firstly, the measurements at different temperatures are performed on a single wire from sample #2 having GaN spacer as shown in **Figure 4.5 (a)**. The decrease in effective lifetime with increasing temperature shown in **Figure 4.5 (b)** is attributed to the activation of non-radiative processes – Shockley Read Hall (SRH) mechanism. Further, a comparison of the relative IQE of sample #2 (without UL) and sample #3 (with UL) is made to study the influence of the UL. To do so, the effective lifetime for more than five wires has been measured for each sample at room temperature (see the **Figure 4.5 (c)**). No significant difference is recorded in the measured values remaining in the 100-200 ps range (see averaged values indicated by dotted lines).

Therefore, the overall optical measurements do not show any IQE improvement by adding an UL to the *m*-plane QW indicating that the presence of GaN spacer layer is sufficient to significantly improve the QW efficiency.
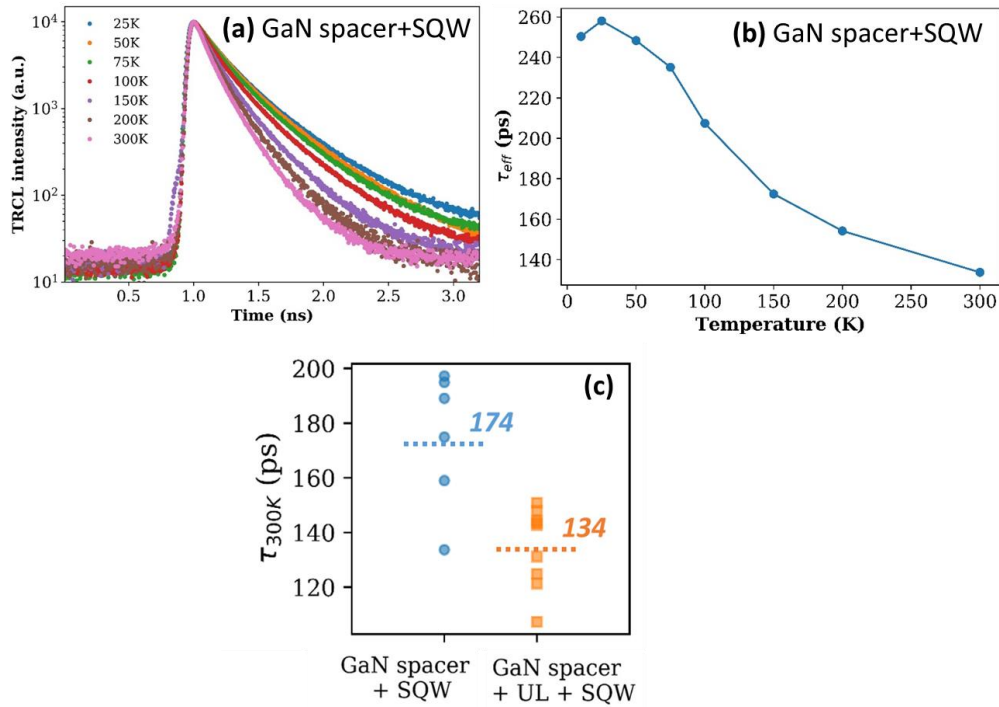
Figure 4.5: TRCL measurements: For sample #2 GaN spacer+SQW - (a) Intensity decay curves as a function of temperature, (b) effective lifetime (τ_{eff}) as a function of temperature; and (c) Comparison of τ_{eff} at 300 K of sample #2 with sample #3 GaN spacer+UL+SQW.

4.3 Understanding the influence of GaN spacer on InGaN QW growth by STEM and EDX analyses

To further understand the influence of GaN spacer on the growth of InGaN QW and to correlate with the improved light emission, two additional typical core-shell InGaN samples without and with GaN spacer have been studied by STEM. Note that unlike the samples characterized above which contain single QW, additional samples studied by STEM have multiple QWs so as to easily observe the presence of structural defects (if any). Thin cross-section slices of the wires either in longitudinal or in transversal mode (cutting along and perpendicular to the *c*-axis, respectively) are prepared by focused ion beam (FIB) using a STRATA 400S equipment.

First STEM analyses (see **Figures 4.6 (a)** and **(d)**) at low magnification are performed with the similar experimental setup as used for the dual-color emission in section 3.3.3. A rather large camera length has been used to enhance the diffraction contrast related to the presence of defects with respect to the chemical contrast. The core-shell InGaN QWs in these STEM images appear bright and the GaN barriers look dark. **Figure 4.6 (a)** reveals a significant number of bright lines corresponding to extended defects originating from the first QW, when the QWs are directly grown on wire sidewalls, whereas no defect is visible in the case of GaN spacer growth (**Figure 4.6 (d)**). InGaN/GaN core-shell wires usually exhibit stacking faults (SFs) showing contrast perpendicular to the QWs.[15,24] Detailed investigation of the SFs in the case of planar QWs on *m*-plane GaN systems reveals that these defects plastically relax the misfit strain accumulated during the growth process along the $\bar{c}$-direction.[25,26] The pronounced difference between the defect densities in the two images is clearly related to the growth of GaN spacer. It demonstrates that the presence of GaN spacer grown at lower temperature prevents the formation of extended defects which cause the degradation of the QWs' properties.

To understand the origin of defect formation, STEM-HAADF images at high magnification combined with energy dispersive X-ray (EDX) spectra are acquired using a FEI THEMIS operated at 200 kV and equipped with super X detectors. The STEM images along with EDX mapping including Si (yellow), In (red) and Ga (green) elements and an EDX profile for the two samples having InGaN/GaN QWs without and with GaN spacer are shown in **Figure 4.6 ((b)&(c))** and **Figure 4.6 ((e)&(f))** respectively. In **Figure 4.6 (e)**, the presence of a GaN spacer having a thickness of ~150 nm is clearly visible separating the GaN core from the first QW as indicated by a narrow dark line pointed by a yellow arrow. EDX mapping reveals the presence of Si inside this dark line. In the high-resolution STEM image (left part), the thickness of this residual layer is about 1 nm. Further investigation by EDX profile in **Figure 4.6 (f)** confirms the presence of Si-content with around 7% composition located far away from the first QW while the average In-content in the wells is around 14%.[‡] Since the presence of Ga and N atoms with a considerably high composition is expected during the growth, this ultra-thin Si-enriched layer probably corresponds to $SiGa_xN_y$. Such a layer seems to be spontaneously formed on GaN wire

---

[‡] A variation in the indium content compared to the first and next two QWs can be related to the change in thickness of QWs as can be seen in Figure 4.6 (e).
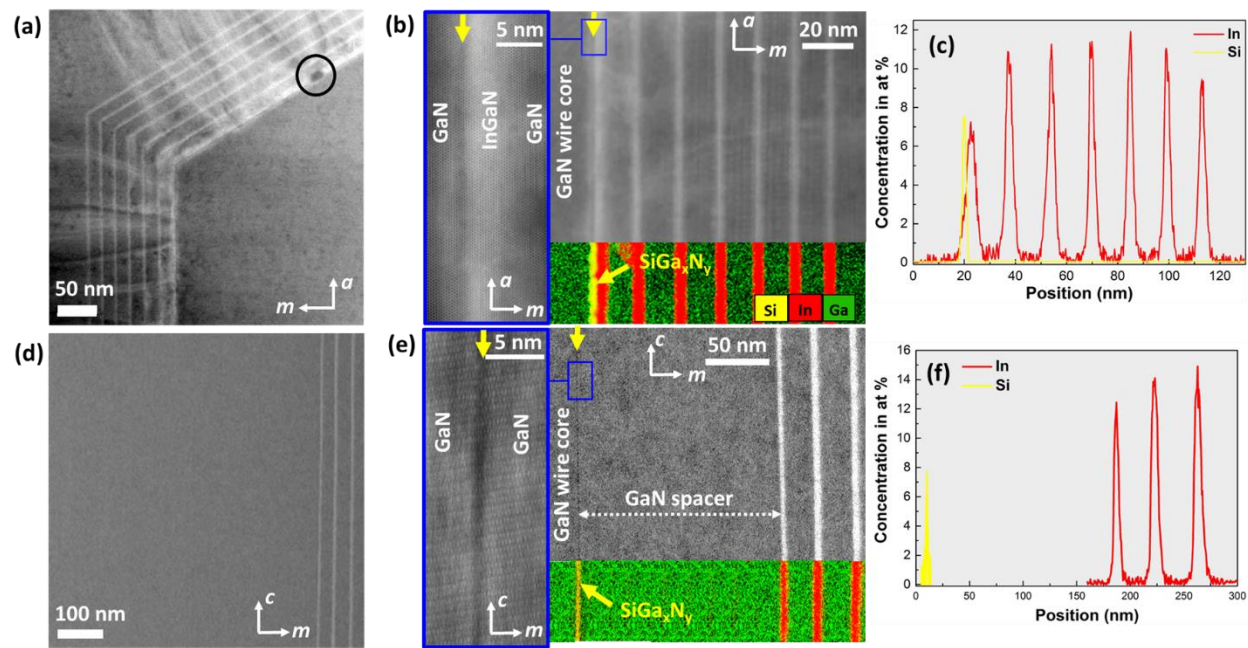
Figure 4.6: STEM-HAADF images at low ((a)&(d)) and high magnification ((b)&(e)) for samples without and with GaN spacer (150 nm thick) respectively. EDX maps and EDX profile ((c)&(f)) complete the high magnification observation. ((a)&(b)): Transversal cross-sectional STEM-HAADF images taken along the [0001] zone axis. The enlarged image (left image in (b)) corresponding to the blue square of the right image shows the presence of a dark line at the interface between the GaN core (yellow arrow) and the first QW, STEM-EDX elemental map of Ga (green), In (red) and Si (yellow) (bottom image in (b)) indicates that the dark line is a Si-enriched layer. EDX profile in (c) confirms the Si presence with around 7% composition; ((d)&(e)) Longitudinal cross-sectional STEM-HAADF images taken along the [10$\bar{1}$0] zone axis. The enlarged image (left image in (e)) and STEM-EDX elemental map (bottom image in (e)) show that the Si-enriched layer (dark line) is located at the interface between the GaN core and the GaN spacer, far away from the first InGaN QW with around 7% composition as evidenced in the EDX profile (shown in (f)). (w/o spacer: T2255 and with spacer: T2612)

sidewalls during the wire growth (even if silane is stopped) or when the wire growth is stopped to reach the MQW growth conditions. Ultra-thin layer in core-shell MQW wires has also been previously reported[27,28] and related to Si-enrichment as shown by EDX measurements.[18,29] This contaminated layer formation is attributed to some residual silane that may be still present in the reactor, because of the high flux silane injection used to passivate the lateral surface[30] around the wire-stem during the first stage of the GaN wire growth. When the silane flux is stopped, 'a memory effect' can lead to an unintentional thin SiGa$_x$N$_y$ deposition and eventually to a Si surface

segregation. Indeed, the EDX mapping (bottom image in **Figure 4.6 (b)**) highlights the presence of an ultra-thin layer containing Si at the interface between the GaN wire sidewalls and the first InGaN QW. The presence of this unintentional layer having a thickness of about 1 nm (as revealed by HR-STEM image on the left side of **Figure 4.6 (b)**) is detrimental for the first QW grown immediately after the GaN core, exhibiting rough interfaces, a large thickness gradient and the nucleation of a high-density of extended defects. This is also evidenced by the EDX profile in **Figure 4.6 (c)** where a relative difference of around 4% in the In incorporation is observed by comparing the In-content in the first QW ($\approx$ 7%) to the average In-content in the successive QWs ($\approx$ 11%). The growth of GaN spacer allows burying the unintentional $SiGa_xN_y$ layer in order to prevent the defect formation inside InGaN MQW stacks. This observation is consistent with the previous optical characterization confirming that GaN spacer growth provides performance improvement.[31]

The SiN_x layer is known to act as a passivation layer in selective area growth and prevents growth of (In)GaN. Therefore, it can be suspected that this residual $SiGa_xN_y$ layer highly perturbs the InGaN QW growth.[§] In **Figure 4.6 (a)**, a small hole is even visible (see the black circle) on the first QW related to an effect of selective area growth of InGaN on the $SiGa_xN_y$ layer. In fact as shown in **Figure 4.7**, the structural characterization of core-shell wires in older works[32,33,34,35] has already demonstrated the existence of such holes and thin dark lines. The zoomed images of MQWs in **Figure 4.7 (a), (b)** and **(c)** show a dark line located either away from the first QW or present on the QW as indicated by yellow arrows. The absence of defects in **Figure 4.7 (a)** can be clearly linked to the presence of GaN spacer before the first QW. The presence of holes at different positions in the MQW shell with varying sizes can also be observed in **Figure 4.7 (c)** and **(d)** highlighted in dotted yellow circles. The work by A. Messanvi *et al.*[34] in **Figure 4.7 (d)** compares a thick InGaN shell (60 nm) (top image) to a 30xInGaN MQW shell (image below).

[§] Si-doping effects have also been studied for MBE grown wires. A report on Si-doped GaN wires has shown an average Si concentration of 2.5×10^{20} at/cm^3 inside the wire core while the outer part has a higher concentration of around 6.5×10^{20} at/cm^3 *(Z. Fang et al. Nano Lett. **2015**, 15, 6794–6801).* Another work based on Si-doping effects on (In,Ga)N wires have shown a reduction in wire coalescence with increased Si doping level with an improved morphology even at a lowest substrate temperature of 500 °C (*J. Kamimura et al. J. Appl. Phys. **2014**, 116, 244310).*
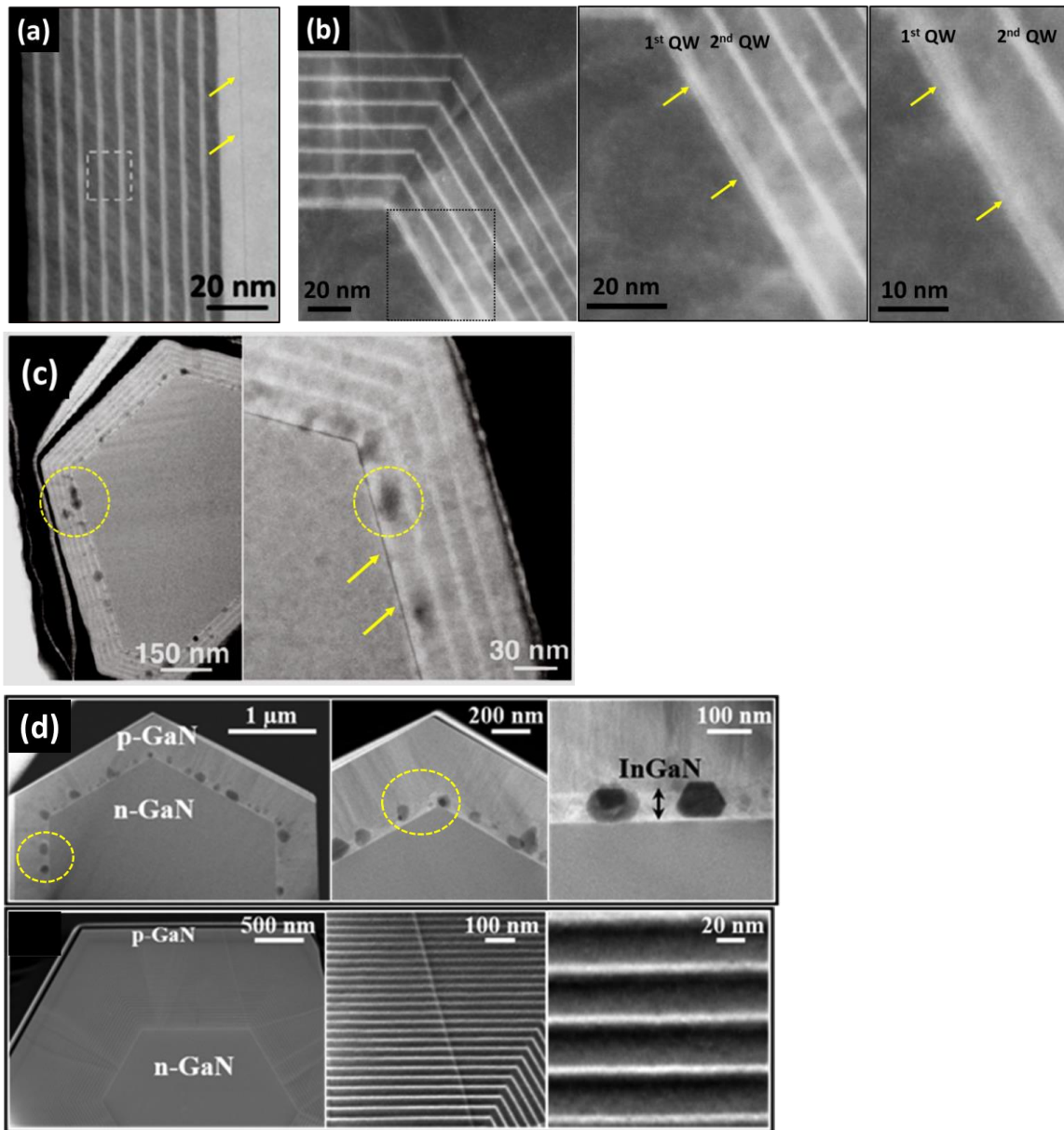
Figure 4.7: Previous results on structural characterization using STEM-HAADF images- (a) Adapted from *Ref. 32*: Longitudinal cross-sectional view taken along [11−20] zone-axis with MQWs on the wire sidewalls; (b) Adapted from *Ref. 35*: Transversal cross-sectional images taken along the *c*-zone axis depicting the 7x QWs separating the core and p-GaN (left image) with corresponding zoomed images of the first two QWs (right images); (c) Adapted from *Ref. 33:* Similar orientation of wire slice as (b) but without p-GaN; and (d) Adapted from *Ref. 34*: Cross sectional images of a wire with 60 nm $In_{0.1}Ga_{0.9}N$ shell (top image) and a wire with $30\times In_{0.18}Ga_{0.82}N$/GaN MQWs shell (image below).

The density of holes is quite pronounced in the thick InGaN shell but absent in MQW shell probably as they get covered by GaN barrier in the latter case. In the thick layer case, a gain of energy is obtained by the development of internal facets that is not possible in the thinner layers.

Apart from the beneficial role of GaN spacer, another important finding from these results is that the introduction of an UL does not improve the IQE of the active region in the core-shell region[14] in stark contrast to *c*-plane QWs.[12] Such a drastic change when moving from *c*-plane QW to *m*-plane QW might be linked to the strong increase of residual doping observed in *m*-plane QWs compared to *c*-plane QWs, which may lead to an apparent increase of IQE.[36] However, similar experiments have been performed on n-GaN core/active region/p-GaN shell, in order to place the active region in the center of the space charge region to reduce the effect of the residual doping. These experiments lead to similar conclusions, *i.e.* the UL does not improve *m*-plane QW IQE. One may wonder if the surface punctual defect density is lower in the samples due to the intrinsic role of the *m*-plane surface or to the growth conditions (with Si-incorporation). It has been shown on *c*-plane QWs that punctual surface defects are created only when the GaN buffer is grown at high temperature (> 850°C) associated with a thermal activation energy of 3.6 eV close to the decomposition activation of *c*-plane GaN.[12] In addition, it has been observed that the deep level density is drastically reduced for N type *m*-plane GaN compared to the *c*-plane GaN.[37]

CONCLUSION

In conclusion, a detailed analysis correlating optical and structural characterization has been performed on wires with *m*-plane core-shell InGaN/GaN QWs to study the influence of GaN spacer and low In-content InGaN UL on the InGaN SQW emission efficiency. The PL and CL measurements reveal that for sample with direct growth of SQW, almost no *m*-plane emission is measured whereas it is observed for sample having GaN spacer with and without InGaN UL exhibiting an IQE of 15.3 and 14.9 % respectively. A dominance of GaN spacer effect over InGaN UL effect is observed. The effective lifetime (τ_{eff}) of the charge carriers estimated by TRCL for single wire in sample containing GaN spacer decreases from 260 ps at 5 K to only 130 ps at 300 K. This demonstrates a quite appreciable efficiency of the SQW. The enhancement in the optical properties of SQW is explained by the structural observations obtained by STEM since the

presence of 150 nm-thick GaN spacer prevents the degradation of InGaN QWs induced by an unintended ultra-thin $SiGa_xN_y$ layer present around the GaN core. On the contrary, the presence of low In-content InGaN UL does not further improve the SQW efficiency, whereas such UL has been proposed to explain the strong enhancement of the emission efficiency for standard planar *c*-plane InGaN/GaN MQWs. If the explanations proposed for the planar structures are assumed ruling out the importance of extended defects for QW emission efficiency, the density of point defects in these wires would be considered less significant to act as NR centers and a single GaN spacer is definitely sufficient to prevent the QW efficiency degradation. The surface formation energy of the point defects such as vacancy is certainly different for *c*-plane GaN to *m*-plane GaN. Additional *ab-initio* calculations and growth experiments on planar *m*-plane LED containing UL are required to extend this effect on all types of *m*-plane surfaces.

REFERENCES

[1] Damilano, B.; Gil, B. Yellow–red Emission from (Ga,In)N Heterostructures. *J. Phys. D. Appl. Phys.* **2015**, *48* (40), 403001. https://doi.org/10.1088/0022-3727/48/40/403001.

[2] Narukawa, Y.; Ichikawa, M.; Sanga, D.; Sano, M.; Takashi, M. White Light Emitting Diodes with Super-High Luminous Efficacy. *J. Phys. D. Appl. Phys.* **2010**, *43*, 354002. https://doi.org/10.1088/0022-3727/43/35/354002.

[3] Schimpke, T.; Mandl, M.; Stoll, I.; Pohl-Klein, B.; Bichler, D.; Zwaschka, F.; Strube-Knyrim, J.; Huckenbeck, B.; Max, B.; Müller, M.; Veit, P.; Bertram, F.; Christen, J.; Hartmann, J.; Waag, A.; Lugauer, H. J.; Strassburg, M. Phosphor-Converted White Light from Blue-Emitting InGaN Microrod LEDs. *Phys. Status Solidi Appl. Mater. Sci.* **2016**, *213* (6), 1577–1584. https://doi.org/10.1002/pssa.201532904.

[4] Guan, N.; Dai, X.; Messanvi, A.; Zhang, H.; Yan, J.; Gautier, E.; Bougerol, C.; Julien, F. H.; Durand, C.; Eymery, J.; Tchernycheva, M. Flexible White Light Emitting Diodes Based on Nitride Nanowires and Nanophosphors. *ACS Photonics* **2016**, *3*, 597–603. https://doi.org/10.1021/acsphotonics.5b00696.

[5] Sugimoto, K.; Denpo, Y.; Okada, N.; Tadatomo, K. Effect of Superlattice on Light Output Power of InGaN-Based Light-Emitting Diodes Fabricated on Underlying GaN Substrates with Different Dislocation Densities. *Phys. Status Solidi (C).* **2016**, *13* (5–6), 270–273. https://doi.org/10.1002/pssc.201510203.

[6] Mu, Q.; Xu, M.; Wang, X.; Wang, Q.; Lv, Y.; Feng, Z.; Xu, X.; Ji, Z. Influence of the InGaN/GaN Quasi-Superlattice Underlying Layer on Photoluminescence in InGaN/GaN Multiple Quantum Wells. *Phys. E* **2016**, *76*, 1–5. https://doi.org/10.1016/j.physe.2015.10.010.

[7] Davies, M. J.; Dawson, P.; Massabuau, F. C. P.; Fol, A. Le; Oliver, R. A.; Kappers, M. J.; Humphreys, C. J. A Study of the Inclusion of Prelayers in InGaN/GaN Single- and Multiple-Quantum-Well Structures. *Phys. Status Solidi (B)* **2015**, *252* (5), 866–872. https://doi.org/10.1002/pssb.201451535.

[8] Akasaka, T.; Gotoh, H.; Saito, T.; Makimoto, T. High Luminescent Efficiency of InGaN Multiple Quantum Wells Grown on InGaN Underlying Layers. *Appl. Phys. Lett.* **2004**, *85*, 3089–3091. https://doi.org/10.1063/1.1804607.

[9] Otsuji, N.; Fujiwara, K.; Sheu, J. K. Electroluminescence Efficiency of Blue InGaN/GaN Quantum-Well Diodes with and without an N-InGaN Electron Reservoir Layer. *J. Appl. Phys.* **2006**, *100*, 113105. https://doi.org/10.1063/1.2398690.

[10] Armstrong, A. M.; Bryant, B. N.; Crawford, M. H.; Koleske, D. D.; Lee, S. R.; Wierer, J. J. Defect-Reduction Mechanism for Improving Radiative Efficiency in InGaN/GaN Light-Emitting Diodes Using InGaN Underlayers. *J. Appl. Phys.* **2015**, *117*, 134501. https://doi.org/10.1063/1.4916727.

[11] Haller, C.; Carlin, J. F.; Jacopin, G.; Martin, D.; Butté, R.; Grandjean, N. Burying Non-Radiative Defects in InGaN Underlayer to Increase InGaN/GaN Quantum Well Efficiency. *Appl. Phys. Lett.* **2017**, *111*, 262101. https://doi.org/10.1063/1.5007616.

[12] Haller, C.; Carlin, J.-F.; Jacopin, G.; Liu, W.; Martin, D.; Butté, R.; Grandjean, N. GaN Surface as the Source of Non-Radiative Defects in InGaN/GaN Quantum Wells. *Appl. Phys. Lett.* **2018**, *113*, 111106. https://doi.org/10.1063/1.5048010.

[13] Dominec, F.; Hospodková, A.; Hubáček, T.; Zíková, M.; Pangrác, J.; Kuldová, K.; Vetushka, A.; Hulicius, E. Influence of GaN Buffer Layer under InGaN/GaN MQWs on Luminescent Properties. *J. Cryst. Growth* **2019**, *507*, 246–250. https://doi.org/10.1016/j.jcrysgro.2018.11.025.

[14] Kapoor, A.; Finot, S.; Grenier, V.; Robin, E.; Bougerol, C.; Bleuse, J.; Jacopin, G.; Eymery, J.; Durand, C. Role of Underlayer for Efficient Core-Shell InGaN QWs Grown on m-Plane GaN Wire Sidewalls. *ACS Appl. Mater. Interfaces* **2020**, *12* (16), 19092–19101. https://doi.org/10.1021/acsami.9b19314.

[15] Koester, R.; Hwang, J. S.; Durand, C.; Dang, D. L. S.; Eymery, J. Self-Assembled Growth of Catalyst-Free GaN Wires by Metal-Organic Vapour Phase Epitaxy. *Nanotechnology* **2010**, *21*, 015602. https://doi.org/10.1088/0957-4484/21/1/015602.

[16] Tchoulfian, P.; Donatini, F.; Levy, F.; Dussaigne, A.; Ferret, P.; Pernot, J. Direct Imaging of P-N Junction in Core-Shell GaN Wires. *Nano Lett.* **2014**, *14*, 3491–3498. https://doi.org/10.1021/nl5010493.

[17] Tchoulfian, P.; Donatini, F.; Levy, F.; Amstatt, B.; Ferret, P.; Pernot, J. High Conductivity in Si-Doped GaN Wires. *Appl. Phys. Lett.* **2013**, *102*, 122116. https://doi.org/10.1063/1.4799167.

[18] Tessarek, C.; Heilmann, M.; Butzen, E.; Haab, A.; Hardtdegen, H.; Dieker, C.; Spiecker, E.; Christiansen, S. The Role of Si during the Growth of Gan Micro- and Nanorods. *Cryst. Growth Des.* **2014**, *14*, 1486–1492. https://doi.org/10.1021/cg500054w.

[19] Pelá, R. R.; Caetano, C.; Marques, M.; Ferreira, L. G.; Furthmüller, J.; Teles, L. K. Accurate Band Gaps of AlGaN, InGaN, and AlInN Alloys Calculations Based on LDA-1/2 Approach. *Appl. Phys. Lett.* **2011**, *98*, 151907. https://doi.org/10.1063/1.3576570.

[20] Auf Der Maur, M.; Pecchia, A.; Penazzi, G.; Rodrigues, W.; Di Carlo, A. Efficiency Drop in Green InGaN/GaN Light Emitting Diodes: The Role of Random Alloy Fluctuations. *Phys. Rev. Lett.* **2016**, *116*, 27401. https://doi.org/10.1103/PhysRevLett.116.027401.

[21] Shahmohammadi, M.; Ganière, J. D.; Zhang, H.; Ciechonski, R.; Vescovi, G.; Kryliouk, O.;

Tchernycheva, M.; Jacopin, G. Excitonic Diffusion in InGaN/GaN Core-Shell Nanowires. *Nano Lett.* **2016**, *16*, 243–249. https://doi.org/10.1021/acs.nanolett.5b03611.

[22] Liu, W.; Mounir, C.; Rossbach, G.; Schimpke, T.; Avramescu, A.; Lugauer, H. J.; Strassburg, M.; Schwarz, U.; Deveaud, B.; Jacopin, G. Spatially Dependent Carrier Dynamics in Single InGaN/GaN Core-Shell Microrod by Time-Resolved Cathodoluminescence. *Appl. Phys. Lett.* **2018**, *112*, 52106. https://doi.org/10.1063/1.5009728.

[23] Donatini, F.; Pernot, J. Exciton Diffusion Coefficient Measurement in ZnO Nanowires under Electron Beam Irradiation. *Nanotechnology* **2018**, *29*, 105703. https://doi.org/10.1088/1361-6528/aaa638.

[24] Mancini, L.; Hernández-Maldonado, D.; Lefebvre, W.; Houard, J.; Blum, I.; Vurpillot, F.; Eymery, J.; Durand, C.; Tchernycheva, M.; Rigutti, L. Multi-Microscopy Study of the Influence of Stacking Faults and Three-Dimensional In Distribution on the Optical Properties of M-Plane InGaN Quantum Wells Grown on Microwire Sidewalls. *Appl. Phys. Lett.* **2016**, *108*, 042102. https://doi.org/10.1063/1.4940748.

[25] Fischer, A. M.; Wu, Z.; Sun, K.; Wei, Q.; Huang, Y.; Senda, R.; Iida, D.; Iwaya, M.; Amano, H.; Ponce, F. A. Misfit Strain Relaxation by Stacking Fault Generation in InGaN Quantum Wells Grown on M-Plane GaN. *Appl. Phys. Express* **2009**, *2*, 041002. https://doi.org/10.1143/APEX.2.041002.

[26] Krause, T.; Hanke, M.; Nicolai, L.; Cheng, Z.; Niehle, M.; Trampert, A. Structure and Composition of Isolated Core-Shell (In,Ga) N/GaN Rods Based on Nanofocus X-Ray Diffraction and Scanning Transmission Electron Microscopy. *Phys. Rev. Appl.* **2017**, *7*, 24033. https://doi.org/10.1103/PhysRevApplied.7.024033.

[27] Mandl, M.; Wang, X.; Schimpke, T.; Kölper, C.; Binder, M.; Ledig, J.; Waag, A.; Kong, X.; Trampert, A.; Bertram, F.; et al. Group III Nitride Core-Shell Nano- and Microrods for Optoelectronic Applications. *Phys. Status Solidi - Rapid Res. Lett.* **2013**, *7* (10), 800–814. https://doi.org/10.1002/pssr.201307250.

[28] Yi, W.; Uzuhashi, J.; Chen, J.; Kimura, T.; Kamiyama, S.; Takeuchi, T.; Ohkubo, T.; Sekiguchi, T.; Hono, K. Cathodoluminescence and Scanning Transmission Electron Microscopy Study of InGaN/GaN Quantum Wells in Core-Shell GaN Nanowires. *Appl. Phys. Express* **2019**, *12*, 85003. https://doi.org/https://doi.org/10.7567/1882-0786/ab2e37.

[29] Ren, C. X.; Tang, F.; Oliver, R. A.; Zhu, T. Nanoscopic Insights into the Effect of Silicon on Core-Shell InGaN/GaN Nanorods: Luminescence, Composition, and Structure. *J. Appl. Phys.* **2018**, *123*, 45103. https://doi.org/10.1063/1.5008363.

[30] Markurt, T.; Lymperakis, L.; Neugebauer, J.; Drechsel, P.; Stauss, P.; Schulz, T.; Remmele, T.; Grillo, V.; Rotunno, E.; Albrecht, M. Blocking Growth by an Electrically Active Subsurface Layer: The Effect of Si as an Antisurfactant in the Growth of GaN. *Phys. Rev. Lett.* **2013**, *110*, 36103. https://doi.org/10.1103/PhysRevLett.110.036103.

[31] Gilet, P.; Dussaigne, A.; Salomon, D.; Eymery, J.; Durand, C. Optoelectronic Device Comprising Three-Dimensional Semiconductors Elements, and Method for Manufacturing Said Device. *US Pat. App. 15/745,429, July 26,* **2018**.

[32] Durand, C.; Bougerol, C.; Carlin, J. F.; Rossbach, G.; Godel, F.; Eymery, J.; Jouneau, P. H.; Mukhtarova, A.; Butté, R.; Grandjean, N. M-Plane GaN/InAlN Multiple Quantum Wells in Core-Shell Wire Structure for UV Emission. *ACS Photonics* **2014**, *1*, 38–46. https://doi.org/10.1021/ph400031x.

[33] Koester, R.; Hwang, J.; Salomon, D.; Chen, X.; Bougerol, C.; Barnes, J.; Le Si Dang, D.; Rigutti, L.; Bugallo, A. D. L.; Jacopin, G.; et al. M-Plane Core-Shell InGaN/GaN Multiple-Quantum-Wells on GaN Wires for Electroluminescent Devices. *Nano Lett.* **2011**, *11*, 4839–4845. https://doi.org/10.1021/nl202686n.

[34] Messanvi, A.; Zhang, H.; Neplokh, V.; Julien, F. H.; Bayle, F.; Foldyna, M.; Bougerol, C.; Gautier, E.; Babichev, A.; Durand, C.; et al. Investigation of Photovoltaic Properties of Single Core-Shell GaN/InGaN Wires. *ACS Appl. Mater. Interfaces* **2015**, *7*, 21898–21906. https://doi.org/10.1021/acsami.5b06473.

[35] Kapoor, A.; Guan, N.; Vallo, M.; Messanvi, A.; Mancini, L.; Gautier, E.; Bougerol, C.; Gayral, B.; Julien, F. H.; Vurpillot, F.; et al. Green Electroluminescence from Radial M-Plane InGaN Quantum Wells Grown on GaN Wire Sidewalls by Metal-Organic Vapor Phase Epitaxy. *ACS Photonics* **2018**, *5*, 4330–4337. https://doi.org/10.1021/acsphotonics.8b00520.

[36] Liu, W.; Butté, R.; Dussaigne, A.; Grandjean, N.; Deveaud, B.; Jacopin, G. Carrier-Density-Dependent Recombination Dynamics of Excitons and Electron-Hole Plasma in *m*-plane InGaN/GaN Quantum Wells. *Phys. Rev. B* **2016**, *94*, 195411. https://doi.org/10.1103/PhysRevB.94.195411.

[37] Henry, T. A.; Armstrong, A.; Kelchner, K. M.; Nakamura, S.; Denbaars, S. P.; Speck, J. S. Assessment of Deep Level Defects in M-Plane GaN Grown by Metalorganic Chemical Vapor Deposition. *Appl. Phys. Lett.* **2012**, *100*, 82103. https://doi.org/10.1063/1.3687700.

Chapter 5: Integrating wires in flexible LED devices

This chapter presents a direct encapsulation of self-assembled core-shell *m*-plane InGaN/GaN microwires in flexible polymer matrix gaining flexibility while maintaining high brilliance in nitride wire-based LEDs. The as-grown microwires on sapphire are embedded into a PDMS layer and mechanically lifted from their growth substrate to preserve their vertical orientation. The detailed technology involved in device fabrication including electrical flexible contacts will be explained. Different flexible wire-LED devices luminescing blue (450 nm), green (520 nm) and also dual-color emission will be fabricated and characterized at room temperature. The difficulties to achieve uniform emission from the devices are discussed. Finally, a color management by phosphors will be presented based on the well-established blue LEDs to target white light emission. The color-control in wire-based LEDs using phosphors as wavelength converters to achieve highly efficient and uniform emission serves as a future perspective that requires additional work.

5.1 Fabrication of flexible LED devices

The InGaN/GaN core-shell wires with p-GaN (on top) and n-GaN (at the bottom) grown by MOCVD are used to fabricate flexible LED devices. The diameter of the wires is in the range of 1 (±0.2) µm while different lengths of the wires are used ranging from 25 (±5) µm to 85 (±5) µm. The average wire density is around 10^6 wire/cm^2. The step by step processing will be described and various difficulties encountered during the device preparation will be discussed in this section.

5.1.1 Ni/Au deposition for ohmic contact

In GaN-based LEDs, Ni/Au thin metallic bilayers are commonly used as an ohmic contact on *p*-type GaN top layer. They exhibit a specific contact resistance of 4.0 x 10^{-6} Ω cm^2 after an annealing temperature of 450 °C as revealed by circular transmission line measurements.[1,2,*] Considering the wire geometry in the present case, it is necessary to protect the bottom part of the wire corresponding to the n-type GaN in order to deposit the Ni/Au layer only on the *p*-type GaN top part. The as-grown wires are spin coated with a thick photoresist named as 'AZ4562' and flood exposed with ultra-violet (UV) light in order to bury only the wire-bottom part in the photoresist. However, this step is challenging due to the inhomogeneous length as well the density of the microwires that leads to an uncontrolled thickness of the resist after deposition. Several tests have been made by changing parameters such as the spin speed of the photoresist, the spin duration, as well the UV exposure time. It is observed that a very high spin speed (> 4000 rpm) results in wire falling from the host substrate, whereas a low spin speed (< 500 rpm) leads to a thick resist making difficult the lift-off later. The optimization of the parameters becomes more difficult with the increasing lengths of wires. For example, the spin coating of 25 (±5) µm and 45 (±5) µm long wires is less challenging due to an intermediate resist thickness and wires are less prone to fall as shown in **Figure 5.1 (a)** and **Figure 5.1 (b)** respectively. The corresponding optimized parameters are

---

[*] Even if the circular line transmission measurements are typically used to measure the specific contact resistances (ρ_c), there are some limitations for the values of $\rho_c < 10^{-4}$ Ω cm^2. This is due to a small contribution of contact resistance to the overall resistance. In such cases, the estimated ρ_c becomes sensitive to the uncertainities in the measured contact radii and resistances *(L Lewis et al.* **Semicond. Sci. Technol.** *2006, 21, 1738).*

summarized in **Table 1.** In the case of long wires 85 (±5) μm, it is difficult to prevent the wires from coalescing for almost all the tests as can be seen in **Figure 5.1 (c)**.[†]

After protecting the *n*-GaN wire-bottom with the photoresist, the samples are treated with a dilute HCl solution (HCl:H$_2$O = 1:4) for 1 minute to remove any contamination or surface oxides from GaN wires. A thin layer of Ni/Au (3 nm/3 nm) is deposited on the wires using a MEB550 PLASSYS evaporator. Then, the photoresist is lifted-off using acetone. The wires standing on their native substrate are annealed at 400°C in atmosphere for 10 min to enhance the conductivity of the Ni/Au and thus improve the p-contact.[3,4]
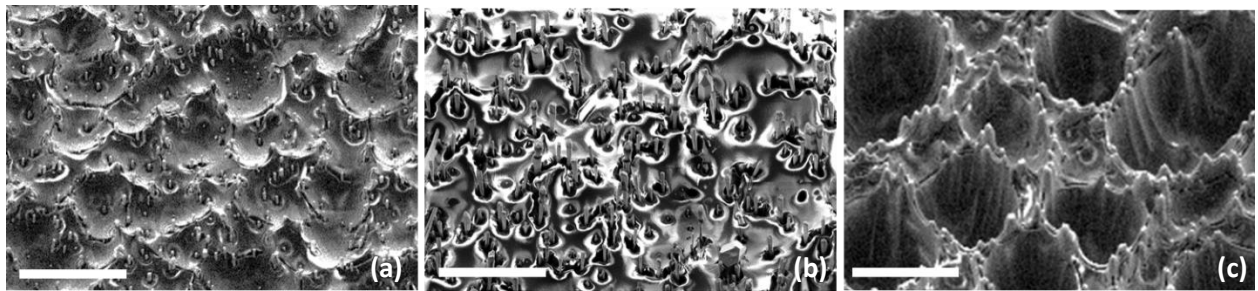
Figure 5.1: SEM images tilted at 30° illustrating the top part of the wires protruding out of the photoresist for wires having length: (a) 25 (±5) μm, (b) 45 (±5) μm and (c) 85 (±5) μm respectively. Scale bar in the SEM image corresponds to 50 μm.

Length (μm)	25 (±5)	45 (±5)
Spin coating of resist	2000 rpm @ 1000 rpm for 60 s	1500 rpm @ 700 rpm for 60 s
UV exposure time (s)	80	70
Development time (s)	150	150

Table 5.1: Details about spin coating the photoresist 'AZ4562' on wires having different length.

5.1.2 Wire encapsulation in PDMS matrix

Following the ohmic contact on *p*-GaN by Ni/Au deposition, the microwires are encapsulated in a silicone-based polymer named as polydimethylsiloxane (PDMS) and peeled off mechanically from their host substrate with the help of a scalpel and tweezers onto an arbitrary substrate. This

---

[†] SEM observation after lifting off the resist has shown existence of broken wires.

technique has already been well managed for the fabrication of flexible piezoelectric sensors using ultra long GaN wires in capacitive structures as documented in the thesis of Amine EL Kacimi.[5] In this work, the GaN wires with length L > 100 µm are buried inside the PDMS with a thickness of about 1.5*L to be successfully peeled off to study their contribution in piezoelectric signals.[6] PDMS is an optically transparent, electrically insulating and a mechanically flexible material, which is also non-toxic with a high chemical inertness.[7,8] These properties make it an ideal candidate to be used in flexible LED devices. A 'Dow Corning Sylgard 184 Silicone Elastomer Kit' is used to prepare the PDMS liquid. The base polymer and curing agent are mixed in a ratio 10:1 (by weight) and the mixture is whisked at a high speed with a spatula to ensure a thorough mixing of the two products. The rigidity of the PDMS can easily be tuned by changing the mixing ratio (by increasing the amount of curing agent).[9] In the present case, the ratio is chosen to be (10:1) after considering the optimum mechanical flexibility of the PDMS. A fast mixing of the base polymer and the curing agent creates a lot of air bubbles in the mixture, which should be removed before spin coating them onto the wires. The mixture is allowed to rest at room temperature for 1 hour to release the bubbles from the surface[‡], and then spin coated onto the wires to achieve a given thickness.

The standard spin-thickness curve for PDMS[10,11][§] cannot be followed in the present work as the thickness will depend on the penetration of PDMS between the wires with a given viscosity, the wire density and length.[12] **Figure 5.2 (a)** shows the thickness curve with spin speed of the PDMS when mixed with different length of the wires. Each point in the curve has been measured for a given length of wire *L* targeting a PDMS thickness to be similar to L. This can be clearly observed in the images taken by optical microscope in **Figure 5.2 (b)** and **(c)** where the PDMS thickness directly corresponds to the wire length. In addition, the spinning time of the PDMS is also critical in the case of self-assembled wires due to the high possibility of the creation of air pockets between the wires at small pitches. A necessity to compete against the PDMS viscosity to achieve a homogenous layer has to be considered. This issue is overcome by spinning for a longer duration

---

[‡] This method provides good results for small quantity of PDMS. An efficient release of air bubbles from large amounts can be obtained by vacuum pumping the mixture for a given time depending on the quantity.

[§]Theoretically derived relationship by Emslie et al.: $h = \frac{h_o}{(1+c\omega^2 h_o^2 t)^{0.5}}$, where *t* is spin time, ω is angular velocity, *h* is thickness and h_o and *c* are experimentally derived to be 180 µm and 2.86 x 10^{-10} rpm[-2]µm^{-2}s[-1].

of time to allow efficient penetration of mixture between the wires, and thus the spinning time is fixed at 300 s for all experiments.
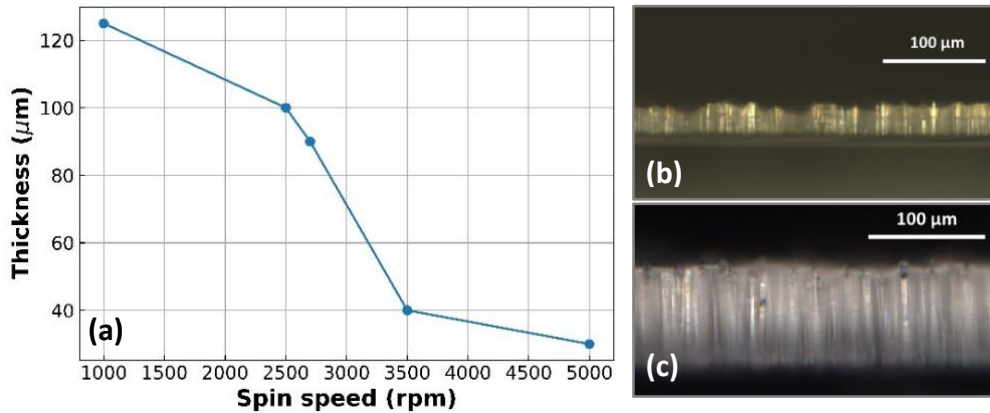

Figure 5.2: (a) PDMS thickness curve for a rotation time of 5 min; Images captured with an optical microscope for GaN wires embedded in PDMS having length: (b) 50 μm & (c) 100 μm.
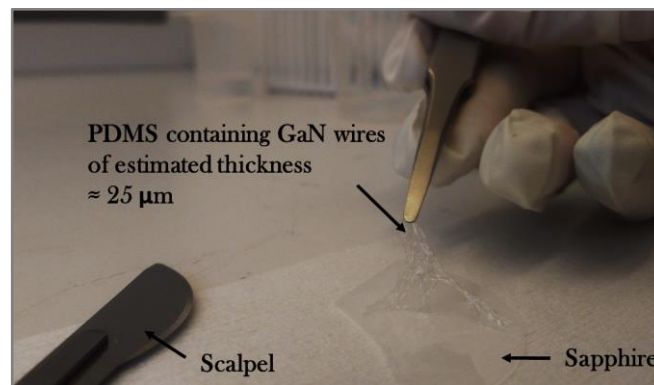
Figure 5.3: Tearing of PDMS captured during the peeling off from sapphire substrate.

The first test is made with 25 (±5) μm long wires. The PDMS is spin coated at an optimized spin speed of 5000 rpm for 300 s and cured at 80 °C for 1 hour. Note that the amount of mixture poured onto the sample is related to the surface area of the sample as well as the desired thickness. A volume of approximately 15 ml is used for a sample with 2 cm^2 of surface area. The polymer layer encapsulating the wires is carefully peeled off from the host substrate (sapphire) with the help of scalpel and tweezers. This step is far from being straightforward and is one of the most challenging steps involved in the fabrication, because the wires to be peeled off mechanically are very short (L ≈ 25 μm). The sharp edges of the scalpel introduces holes in the polymer layer and sometimes also leads to tearing of the layer completely as illustrated in **Figure 5.3**. This difficulty has not been

observed in the work of A. El Kacimi as it involved the peeling of ultra-long wires (L>100 μm) with thicker PDMS layers, as mentioned before.

Different methods have been approached to address the peeling issue. One of the common techniques is to use a TRS 'REVALPHA' tape (thermal release sheet) which behaves like a normal adhesive tape at room temperature. It is widely used in electronic industrial applications as a sacrificial and supporting layer during reversal soft UV nanoimprint.[13] It adheres strongly to the substrate (having the 'layer' to be peeled off) at room temperature and is peeled off easily without damaging the surface. It can be released by giving a heat treatment at 80 °C for a few minutes and the 'layer' is mounted on an arbitrary substrate. When this tape is tested to peel the thin PDMS layer from sapphire substrate, it is observed that the PDMS is very strongly bonded to the sapphire substrate and the adhesion between the PDMS and the tape is too weak to facilitate the peeling of tape along with the PDMS. Many tests are made by applying large mechanical pressure onto the tape to achieve better adhesion, however the bonding between the PDMS and substrate remains strong in all cases. Thus, the REVALPHA tape could not be used to solve the difficulty of PDMS peeling. Another approach is to use a commercially produced organic chemical called 'Cyclododecane' (CDD) which melts at 58 °C, dissolves in many non-polar solvents and sublimates at room temperature. This volatile binder is extensively used as a temporary masking material for paintings, textiles and architectural conservation.[14] It is anticipated that it can temporarily bind to the PDMS layer and increase the overall thickness to be peeled off. After peeling, CDD can be allowed to evaporate at room temperature leaving behind the PDMS layer only. A test is made by mixing the CDD with toluene at 100 °C to prepare a saturated solution which is poured onto the PDMS layer. Due to the fast sublimation of CDD, a non-uniform crystal-like layer is formed as soon as it is poured, showing a poor flexibility which makes the peeling even more difficult and it also partially damages the PDMS underneath.

Following different solutions, we realized that peeling the thin PDMS layer is a serious challenge. The more straightforward approach is simply to increase the polymer thickness. The minimum thickness of the PDMS, which could be easily peeled off, is found to be around 40 μm. Therefore, the length of the wires used to make the devices is targeted to be 45 (±5) μm. Note that using longer wires having length 85 (±5) μm could further facilitate the ease of peeling, however it is difficult

to coat the top-part of the wires with Ni/Au in the first step as already described in the previous section. The cured PDMS layer is carefully peeled off using a scalpel and a pair of tweezers. Firstly, a sharp cut is made at one edge of the substrate and the PDMS layer is very slowly peeled off. The layer coming out is held by the tweezers with a delicate force and the peeling is continued until the entire layer comes out. This process is time consuming but can be efficiently performed with some experience of the manipulator. A typical duration to peel off the PDMS from a full 2-inch wafer is around one hour.[**] During the process, there are instances when the PDMS layer may stick back to the sapphire substrate after being peeled off. In such cases, a few drops of isopropanol (IPA) is poured onto the substrate which acts as a lubricant and helps to glide the already peeled off PDMS. The layer is delicately pulled away from the substrate with the help of tweezers and the peeling is continued further. **Figure 5.4 (a)** shows a SEM image of the surface of sapphire substrate after peeling off indicating that the wires ave been removed efficiently with few residues left behind.
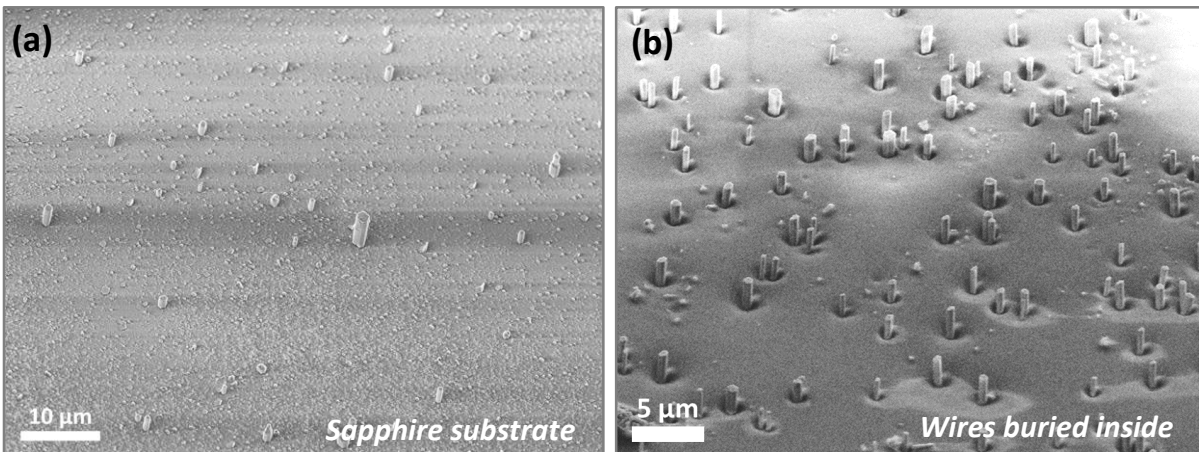
Figure 5.4: SEM images after PDMS peeling off: (a) titled at 30° showing the surface of sapphire substrate and (b) tilted at 45° showing n-GaN wire bottoms protruding out of the PDMS layer after RIE etching.

The polymer layer with embedded wires is then flipped and mounted onto a kapton plastic sheet that has a high thermal tolerance (~300 °C). Also, the corners are temporarily secured with a kapton tape. The layer flipping is done to upside-down the wires so as to manipulate the bottom segment of the wires (i.e. the n-GaN side). A reactive ion-etching (RIE) is performed to etch a small thickness of the PDMS, since the wires are buried inside the polymer. A mixture of 45 sccm of CF_4 and 20 sccm of O_2 gas under a pressure of 50 mTorr with 150 W of radio frequency power and 200

[**] Further improvements have to be developed in the future to speed up the process.

W of ion-coupled plasma power allows to etch the PDMS with an etch rate of 500 nm/min. The PDMS surface etched for 4 min can be seen in the **Figure 5.4 (b)** depicting 1-2 µm long wire segments protruding out of the PDMS.

5.1.3 Ti/Al/Ti/Au deposition for n-GaN contact

A composite metal layer Ti/Al/Ti/Au is used as an ohmic contact for the *n*-GaN side. Ti provides good adhesion as well as mechanical stability to the GaN surface. Moreover, upon annealing the contact at high temperature, solid phase reactions between Ti and GaN can take place forming TiN on the surface and thus creating N vacancies. These N vacancies on the GaN surface act as donor sites making this interfacial region heavily doped.[15] Although Ti/Al metallization provides a low contact resistance, there is a risk of oxidation for both metals, which can degrade the contact quality with time. This issue is overcome by a second bilayer of Ti/Au, as Au is resistant to oxidation.

In practice, after etching of the PDMS based on the process described above, a layer of Ti/Al/Ti/Au (10nm/20nm/10nm/200nm) is deposited onto the n-GaN part of wires using a MEB550 PLASSYS Evaporator. The PDMS membrane is once again flipped and stuck to a conductive copper adhesive tape to achieve a back contact with n-GaN wires and the corners of the membrane are secured using a kapton tape. The top part of the PDMS is also etched with reactive ions with the similar parameters as mentioned above in order to access the p-GaN part located on the wire top. **Figure 5.5** shows the p-GaN wire tops protruding out of the PDMS after an etching for 2 min. Different lengths of the wire-tops are observed which is directly related to the length inhomogeneity occurred during the self-assembled wire growth.
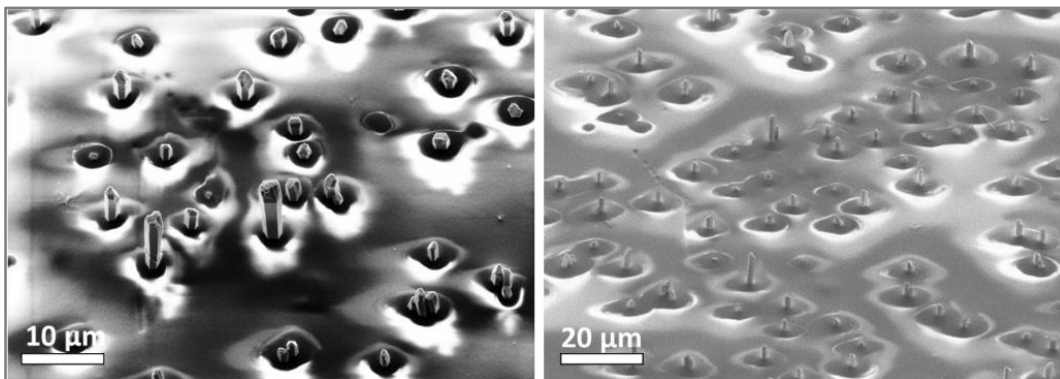

Figure 5.5: SEM images tilted at 30° showing the p-GaN wire tops protruding out of the PDMS layer.

5.1.4 Dispersing silver nanowires for p-GaN contact

The final step is the dispersion of Ag nanowires (NWs) on the p-GaN wires protruding out of the PDMS surface to provide a Schottky contact. In addition to being highly bendable, the Ag NWs offers a very low sheet resistance (11.7 Ω/sq) with a high optical transmittance in the visible spectrum.[16] The Ag NWs dispersed in IPA have been commercially bought with different lengths like 12, 40 and 120 μm[††]. Note that both short and long wires are chosen so as to efficiently contact the GaN wires located at random pitches.

The edges of the PDMS membrane is carefully covered with a kapton tape to avoid any penetration of the Ag NWs to the copper tape (back contact) to avoid any short-circuiting. The Ag NWs are spin coated onto the PDMS layer at 1000 rpm for 25 s successively with different lengths (longer wires are spin coated first followed by the short wires) to achieve a uniform density contacting the GaN wires. The samples are annealed at 200 °C for 20 min under air to decompose the chemical solvents and promote the fusion of Ag NWs thus increasing their conductivity.[17] **Figure 5.6** shows a mesh of Ag NWs dispersed on the PDMS membrane contacting the tops of GaN wires. The inset depicts a single GaN wire-top well covered with Ag NWs. The contacts using such a network of Ag NWs can facilitate a uniform current spreading thanks to the thin shell of Ni/Au (3 nm/3 nm) covering the p-GaN part at the wire-top.
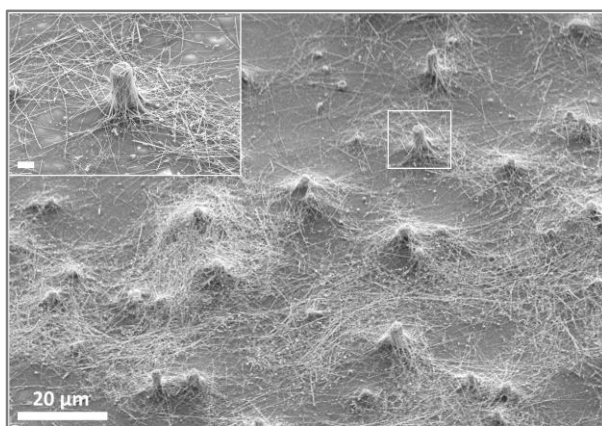

Figure 5.6: SEM image titled at 45° showing Ag NWs contacting one GaN wire to the other. The scale bar in the inset corresponds to 2 μm.

[††] The wires with length 12 μm and 40 μm are supplied by Sigma Aldrich while 120 μm long wires have been supplied by ACS Materials.

All processing steps involved from the as-grown InGaN/GaN wires on native substrate to the fabrication of flexible LED device explained in this section is summarized in **Figure 5.7.**
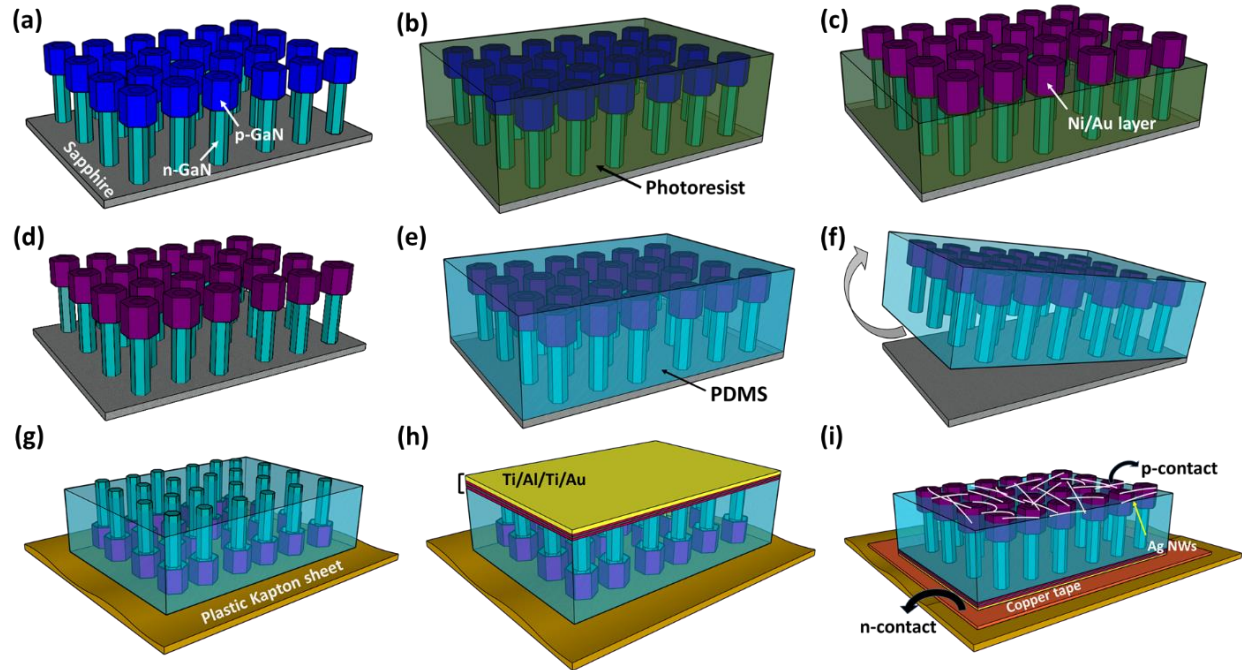
Figure 5.7: (a) As-grown InGaN/GaN wires standing on sapphire substrate, (b) Wires spin-coated with photo-resist 'AZ4562', (c) Flood exposed with UV and Ni/Au (3 nm/3 nm) is deposited on the top p-GaN part, (d) Resist is lifted-off with acetone, (e) PDMS is spin coated onto the wires, (f) Peeling-off the PDMS membrane, (g) The PDMS layer is flipped and mounted on a kapton plastic sheet and etched from the top to access the wire-bottom, (h) Ti/Al/Ti/Au (10nm/20nm/10nm/200nm) is deposited to contact the n-GaN and (i) PDMS layer is flipped again and etched to contact the wire-top by Ag NWs as a Schottky p-contact.

5.2 Electroluminescence from LED device based on wire-assembly

The electroluminescence (EL) spectroscopy is a standard technique that allows to study the radiative recombination in a LED device by applying a potential and measuring the photons generated from the electron-hole recombination. It also helps to understand various aspects about the final device such as electrical properties of the active layer combined with the optical emission and the injection efficiency of electrical contacts, contrary to the photoluminescence (PL) and

cathodoluminescence (CL) techniques that mainly provide information only about the basic optical properties of the LED structure. A shift in luminescence spectra recorded with PL and EL is usually observed,[18,19] which is attributed to several reasons such as different mode of carrier excitation (injection with photons and electrons in case of PL and EL respectively), heat generation (via carrier relaxation in PL and via joule heating in EL) and compositional fluctuations in alloy etc. In this part, we will focus only on the EL characterization and the understanding of EL spectrum evolution with increasing voltage bias will be discussed.

5.2.1 Demonstration of blue, green, dual color and multicolor emission

The realization of flexible LEDs based on the method described in section 5.1 has been firstly demonstrated in the Ph.D. thesis of Agnes Messanvi[4] and an appreciable conductivity with a resistance of about 8.16 x 10^3 and 7.17 x 10^5 Ω for the wire core and p-GaN shell respectively has been reported.[22] A bending radius of 3.5 mm positive curvature and -2.5mm negative curvature during the mechanical tests of the device does not degrade the electroluminescence performances of the device and thus validates the strategy involved in the device fabrication. This work aims to extend this approach to deduce further understanding of flexible devices as well as to manage the emission of longer wavelength such as the green emission.

Flexible LED devices targeting different wavelength emission have been fabricated and characterized by EL measurements performed at room temperature. The growth of core-shell InGaN/GaN wires, which will be integrated in flexible LED devices has already been fully described along with their structural and optical characterization in the section 3.1, 3.2 and 3.3 corresponding to blue, green and multicolor emission respectively. The EL measurements for the device emitting blue luminescence has been performed at CEA-Grenoble, while for the devices showing green and multicolor emission has been performed within the framework of former Ph.D. student Nan Guan at C2N, Paris.[20,23]

The current in the blue LED is injected using a Keithley 2450 source and the emitted light is collected by an optical fiber located on the top of the sample and measured by combining a HR460 spectrometer and a CCD camera. Two different positions namely Position-I and Position-II on the sample have been measured, as shown in **Figure 5.8** and **Figure 5.9** respectively. It is important to
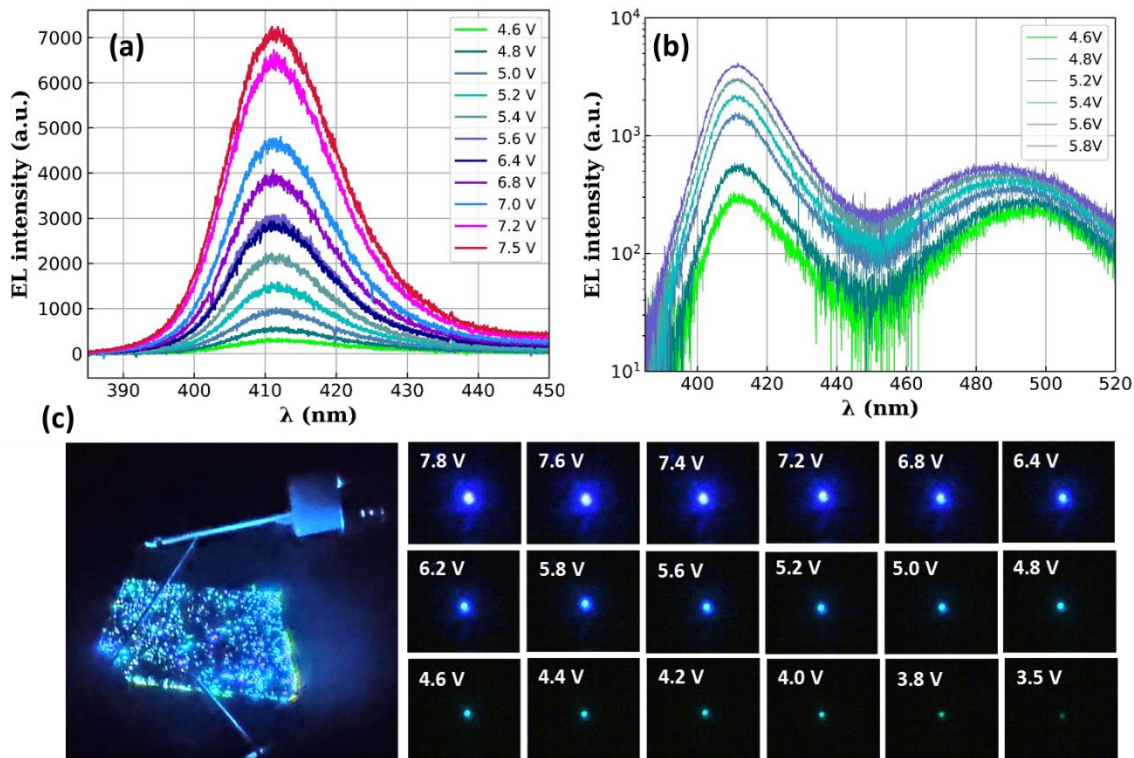
Figure 5.8: Voltage-dependent EL spectra for Position-1 on Blue LED in the wavelength range: (a) (380-450) nm, (b) (380-520) nm; (c) Photographs captured during the light emission at different bias voltage.

mention that the EL spectra is represented as a function of applied bias contrary to the injection current. It is because a variation in injection current is observed for a similar applied bias at different locations on the LED device. This could indicate different current spreading paths on the flexible surfaces and also a current leakage through the electrical contacts.

Figure 5.8 (a) presents the EL spectra showing a peak around 412 nm with a narrow broadening of full width at half maxima (FWHM) as 140 meV. The turn-on voltage is recorded to be 3.5 V, whereas, a measurable signal starts to appear only at 4.6 V. No color change and no shift in the emission wavelength are observed when the voltage bias increases. This observation indicates that the luminescence originates from the radial non-polar *m*-plane QWs.[21,35] In the logarithmic scale, it is noticed that another small contribution is measured around 484 nm (see **Figure 5.8(b)**) when the applied voltage is below 6.0 V. This peak is no longer visible for voltage higher than 6.0 V[‡‡].

[‡‡] Not shown in Figure 5.8 (a) due to limited range of wavelength window ($\approx$ 80 nm) in the measurement setup. The spectra in Figure 5.8 (b) has been presented by concatenating two different spectra measured under identical condition.

This contribution is attributed to axial MQWs located in the wire-top part, since the peak exhibits a blue-shift from 494 nm to 484 nm when the applied bias increases from 4.6 V to 5.8 V. Such a distinctive trace of radial and axial contributions from the InGaN/GaN QWs has also been reported before.[22,23,24] A detailed investigation of a single core-shell wire based LED injected by graphene based contacts reveals that a contribution at 415 nm dominates the EL spectra during high current injection (10 µA), while at low injection ($\approx$ 0.16 µA) another peak at 494 nm is recorded.[22] Similar results have been observed for flexible blue LED device injected at different bias voltage.[23] A comparison of the two contributions 412 nm and 484 nm at an applied bias of 5.8 V reveals that the former is 8 times more intense than the latter, while the intensities becomes almost comparable as the voltage decreases to 4.6 V. This is also evidenced by the captured images of the light emission taken at different bias voltages, as can be seen in **Figure 5.8 (c)**[§§]. The blue color emission perceptibly dominates within the voltage range (5.0 V – 7.8 V), however it is dominated by a turquoise color as the voltage decreases below 5.0 V. The presence of two wavelength contributions at varying bias is attributed to different current paths along the nanowire geometry and will be discussed further in section 5.2.2.

The EL spectra for Position-II in **Figure 5.9 (a)** reveals an emission peaked around 472 nm and exhibits no significant shift as the applied bias increases to 7.2 V. A higher FWHM value is measured (225 meV) compared to that measured previously for emission at 412 nm (= 140 meV). This FWHM increase is simply related to the increasing indium fluctuations typically observed for longer wavelength emission.[25] An enlargement of the EL spectra is presented in **Figure 5.9 (b)** for bias voltage in the range (4.8 - 5.6 V). A second contribution around 490 nm is visible and almost dominates the EL spectra at low injection current. Although the main blue emission is shifted, the same behavior of EL spectrum is observed between the position I and II with the presence of a second emission around 490 nm at low current injection. The optical pictures of the emission in **Figure 5.9 (c)** shows a gradual transition from blue emission at 7.5 V to red emission at 3.8 V, pointing out once again a strong difference in the current injection path in the wires. Similar full visible-color range emission controlled by adjusting the bias voltage has already been reported for GaN nanorod based LEDs.[26] In this former work, Ga-polar GaN nanorod array with InGaN QWs

---

[§§] To check colour rendering, the image at the left for the full LED device is taken by a mobile camera while the images on the right at different bias voltage are captured by a visualization camera.
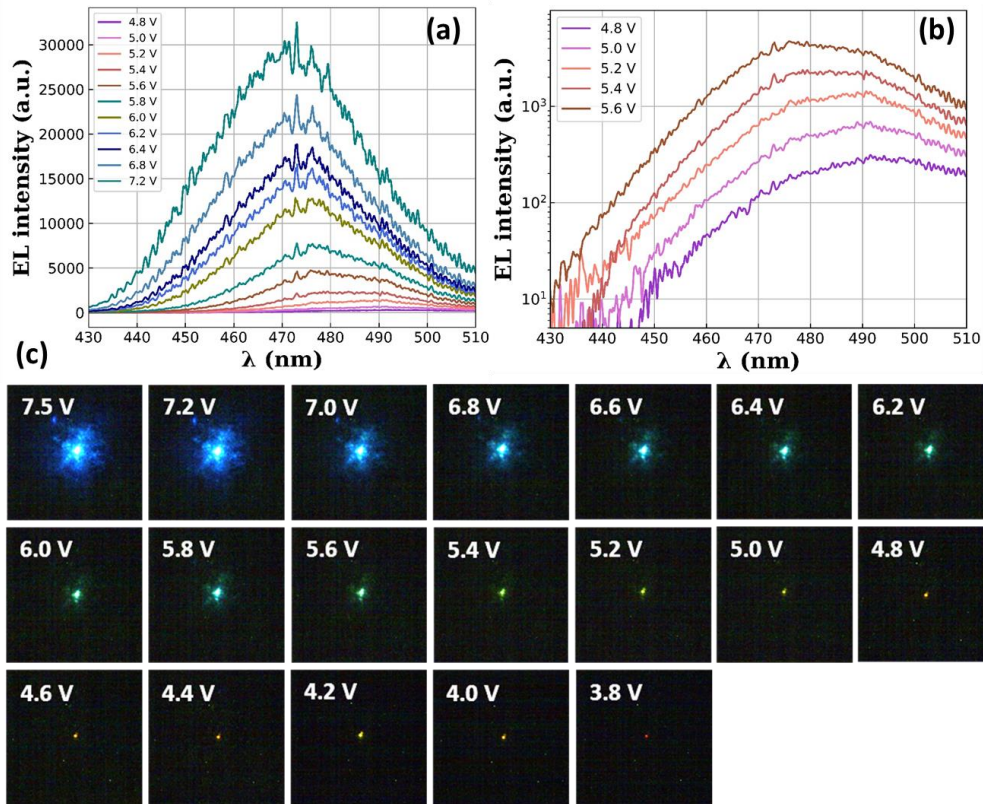
Figure 5.9. Voltage-dependent EL spectra for Position-2 on Blue LED in (a) linear and (b) log scale; and (c) Photographs captured during the light emission at different bias voltage.

on the tip and the sidewalls having length around 0.5µm were grown on n^+-GaN/Al$_2$O$_3$ (0001) substrates and employed to fabricate rigid LED devices.[26] Overall, the trend in change of wavelength emission as a function of voltage is consistent for different positions on the blue LED. Note that the signals corresponding to long wavelengths like red and yellow emission are unfortunately too low to be collected by the optical fiber.

The device targeting green emission has been characterized using a Keithley 2636 source meter, a HR460 spectrometer and a CCD camera. The EL characteristics displayed in **Figure 5.10 (a)** exhibits a weak peak around 580 nm at low bias voltage, whereas a second peak at short wavelength (540-550 nm) appears and becomes dominant for highest voltage, corresponding to high current injection. The emission at high injection exhibits a broad peak with FWHM equal to 350 meV. Once again, this value is significantly higher than the blue emission (140 meV) due to the large indium fluctuations for indium-rich green QWs.[25,27] The room temperature I-V curve in **Figure 5.10 (c)** shows a rectifying behaviour with a turn-off voltage equal to 3.5 V. The photographs of

the LED under operation can be seen in **Figure 5.10 (d)** without bending (left), for a moderate outward bending (center) and for an extremely outward bending (right) with a radius of curvature around 3 mm. The device has shown no degradation in the EL intensity and I-V characteristics after several bending cycles (>10) indicating the electrical reliability of the meshed Ag nanowires networks under deformation. The device storage in ambient conditions for more than 30 days has
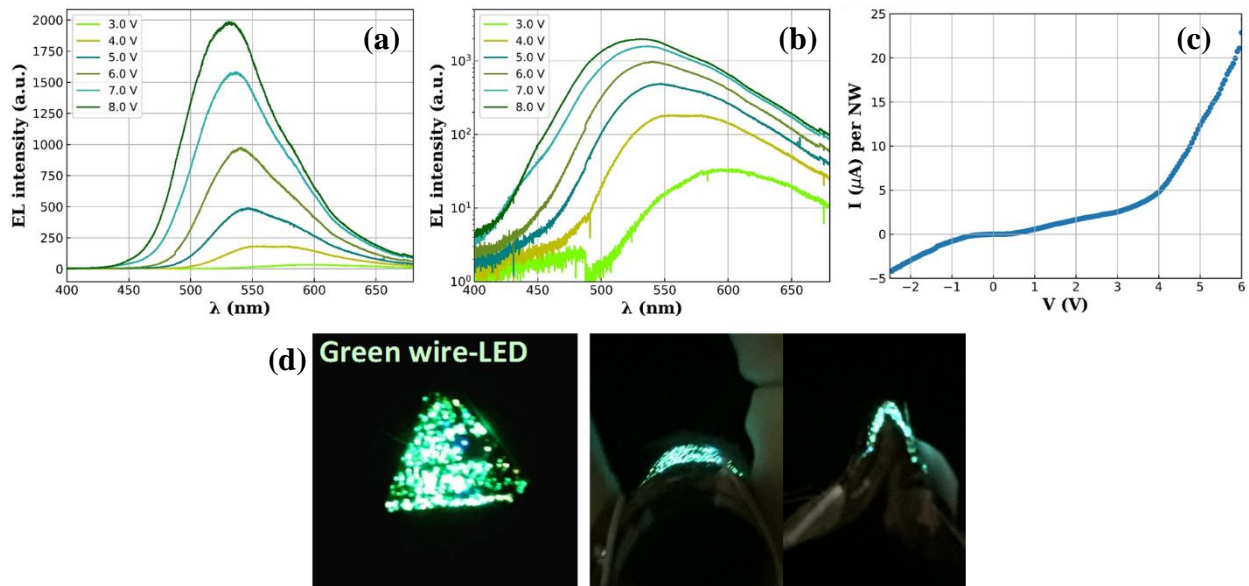
Figure 5.10: Room-temperature EL spectra at various applied biases from 3 V to 8 V in (a) linear and (b) log scale; (c) I-V curve and (d) Photographs of the flexible green LED in top view (left), moderate outward bending (center), extremely outward bending (right).
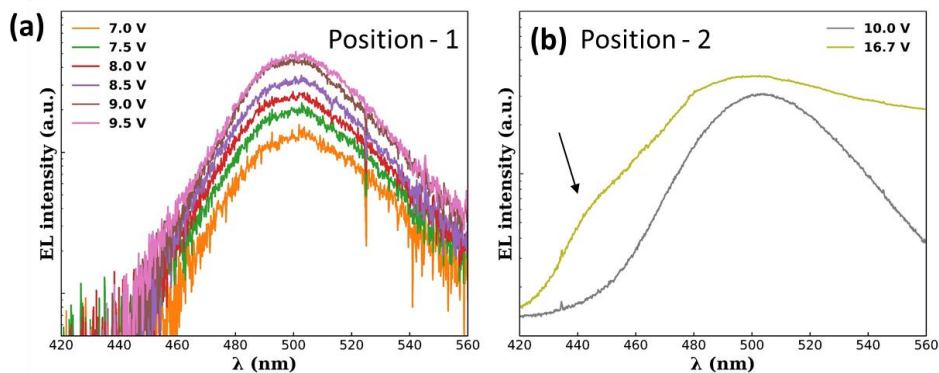
Figure 5.11: EL spectra of the dual-color LED for (a) position-1 when the applied bias changes from 7.0 to 9.5 V, (b) position-2 measured at 10 and 16.7 V.

shown no impact on the LED performance evidencing that flexibility, reliability and stability of the fabricated wire-based LED devices.

The wires exhibiting dual-color emission is also used to fabricate a flexible device. The measured EL spectra at two different positions namely 1 and 2 are shown in **Figure 5.11 (a)** and **(b)** respectively. As described in Chapter 3, this core-shell heterostructure consists of 3 QWs with low indium composition followed by 7 QWs with high indium composition located close to the p-shell. The contribution for long wavelength emission around 500 nm is clearly visible in both the spectra whereas the signature for short wavelength emission around 445 nm is only visible at high voltage. The poor hole mobility probably limits the transportation of holes from one family of QWs into the other. This prevents the emission for the short wavelength and only the long wavelength emission is measured in the EL measurement. An improvement in the structure design can be performed in the future by reducing overall the number of QWs, e.g. from (3,7) to (1,3) so as to facilitate an efficient transportation of charge carriers across the whole active region.
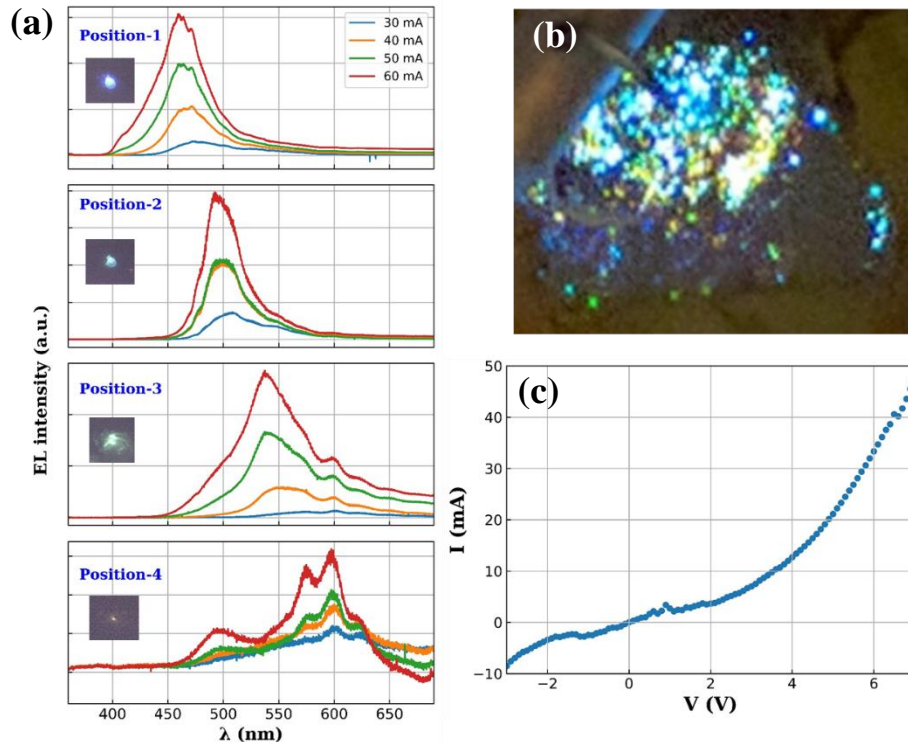
Figure 5.12: (a) Multi-color emission captured during the device operation, (b) EL spectra (top to bottom) at different positions on the sample corresponding to blue, green, yellow and red emission respectively and (c) I-V curve.

Another demonstration of flexible device from core-shell InGaN/GaN wires is presented in **Figure 5.12**. This new device exhibits a multi-color light emission. The EL spectra in **Figure 5.12 (a)** at different positions on the sample show different wavelength emission peaked around 450 nm

(blue), 500 nm (green), 540 nm (yellow) and 600 nm (red) respectively that increases with the current injection. It is noticed that nearly all the emission peaks are broad and several contributions appear for the yellow emission and become more pronounced for the red emission i.e. the fluctuations increases for long wavelength emission probably corresponding to indium rich QWs or quasi quantum dots (QDs). Another possible origin of these fluctuations could be the varying indium content in different crystallographic facets such from the polar QWs located on the tip of the wire or the junction between polar and semi-polar facets. Further, the I-V curve in **Figure 5.12 (c)** shows a rectifying behavior of the device with a turn-off voltage to be around 3V. But note that a significant leakage current is recorded at reverse bias, probably arising due to high contact resistances. These results highlights the possibility to get a multi-color emission covering the entire visible spectrum from core-shell InGaN/GaN MQWs in GaN wire-based LEDs that opens the route for monolithic white flexible LED without phosphors. However intensive efforts will be required to achieve a well-controlled and reproducible growth targeting indium rich InGaN QWs.

5.2.2 Discussion about current injection

The flexible LED devices exhibiting different wavelength emission has been well established as described above. However, the emission is not uniform with the presence of numerous spotlights. Additionally, twinkling of light is recorded with changing applied bias. These instabilities can be attributed to the following two reasons:

1. Bunching of wires during fabrication of the device: As illustrated by SEM image in **Figure 5.13** corresponding to the as-grown wires with Ni/Au deposition after lifting off the photoresist using acetone (explained in section 5.1.1), some wires' top can be glued together. The crowding of these tilted wires is clearly visible at different positions on the samples and can be responsible for bright spots. V. Kaganer *et al.* has also reported bundling of GaN nanowires grown by MBE.[28] They show that such bundling of wire having maximum length of about 2.5 μm becomes favorable when the total surface energy of the wire exceeds the elastic energy of bending at a certain critical wire length. However, further studies are required to apply this approach to MOCVD wires considering the surface charges, lower wire density and high aspect ratio. Therefore, we believe that the wire

coalescence occurs during the device fabrication process.[***] Perhaps, the high flow of acetone, which is necessary to remove the photoresist, applies a pressure onto the wires making these local wire coalescences. Further optimization in the lift off step may help to overcome this problem. Another reason could be the electrostatic attractions between the wires caused due to electron exposure during microscopic observations.
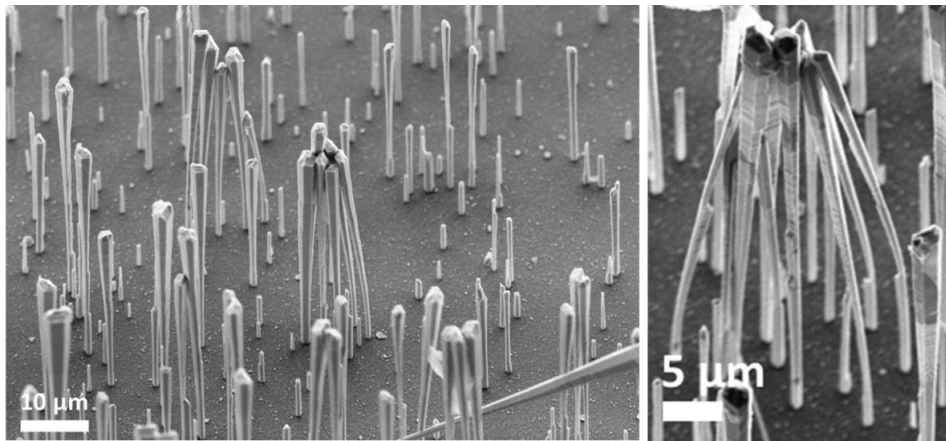
Figure 5.13: SEM images titled at 30° showing the as-grown wires with wire-tops covered with Ni/Au.

2. Poor spreading of current during electrical injection: the non-uniform current spreading is one of the challenging issues in realizing a uniform emission from the wire-based devices that becomes even more perplexing in the case of flexible devices. The origins of non-uniform current spreading are mainly due to inefficient contacts on n and p-sides, as well as the existence of several paths for the electrical transport arising from intra-wire injection inhomogeneities.[†††] The back contact for n-GaN side had been a matter of concern. Since the beginning of the device fabrication, it was difficult to find a highly conductive material, which can also act as an adhesive at the same time to be able to stick correctly the PDMS membrane. Although some materials are commercially available, they cannot withstand the high temperature annealing at 200 °C, which is required during the final step of device fabrication to improve the Ag NW conductivity. Following many efforts, a slight

---

[***] No coalescing of wires has been observed after the PDMS deposition as can be seen in Figure 5.5 and 5.6.

[†††] Due to finite core and shell resistance, different current paths exist inside the wire such as wire-facets, junctions at the facets, core, shell etc. In addition, the percolation of conduction paths in Ag NWs is also plays an important role.

modification is introduced in the device preparation. The Ag NWs are dispersed by mounting the PDMS on a temporary substrate[‡‡‡] and the annealing step is performed prior to making the n-contact. Once annealed, the PDMS is stuck onto a copper tape with some silver paint that acts as a 'conductive glue' for n-contact. Significant improvement in the light emission has been observed following this technique thanks to the conductive silver paint that helps to make a good electrical contact between the copper tape and the wire bottom. However, the use of silver paint cannot be considered as an ideal solution as it comes at the cost of flexibility. Further tests with other flexible adhesives are required to definitely improve the n-contact. Apart from the back contact, it is also important to inject uniformly in the p-GaN wire tops, taking into account the length fluctuations that occurs during the self-assembled wire growth. The etching of the PDMS to contact the GaN wire top (as explained in section 5.1.3) is performed by considering the maximum length of the wires. To avoid a short circuit in the final device, the shorter wires get compromised and will not be active because they are fully buried inside the PDMS. Further, the wires with an intermediate length can barely protrude out of the PDMS leading to a shorter part of the wire to be contacted by the Ag NWs. On the contrary the longer wires can benefit from the good contact by Ag NWs covering efficiently the sidewalls. The variation in wire contacting may induce fluctuating emission. Such a non-uniformity in the wires' length limits the final number of emitters and also affects the current spreading in the wire-LED device. This issue can be addressed by using SAG wires that show better length homogeneity[29] and has already been employed for LED fabrication.[30] Although this solution has the potential to increase the number of active wires in the device, the usual difficulty of carrier injection in the wires still remains.[31] Moreover, the reproducibility control for the SAG growth (as described in Chapter 2) makes this approach far from being straightforward coming at a high cost of fabrication due to substrate patterning. In order to reduce the inhomogeneities in the luminescence especially the spot-like emission, one of the key solutions is to combine the wire-LED with phosphors. This allows better color mixing facilitating a homogenous emission from the wire-based LED due to diffusion with phosphor. This approach will be presented in section 5.3.

[‡‡‡] Any non-adhesive flexible substrate with a good thermal tolerance such as a kapton sheet (serial no 300 HN supplied by RS PRO company that can withstand a maximum temperature of 300 °C).

5.2.3 Origin of wavelength variation in wire-based LED

Apart from the technological issues related to inhomogeneous current injection, a uniform wavelength emission is another key challenge that needs to be addressed in a wire-based LED. A variation in the color of emitted light has been observed as a function of applied voltage bias in the EL spectra as described above. The significant shift from blue color (at high injection) to red color (at low injection) in the case of blue-LED as shown in **Figure 5.9 (c)** and the presence of different colors for multi-color LED shown in **Figure 5.12 (a)** indicates strong compositional inhomogeneities introduced during the growth of the wire-LED structures.

It has been well documented in the literature that the indium content in the InGaN QWs varies for different crystallographic planes covering the multi-faceted GaN wires.[22,26,32,33,34,31] As can be seen in **Figure 5.14**, Y. J. Hong *et al.*[26] report that the polar QWs grown along *c*-plane present in the Ga-polar nanorod top contain higher indium content as compared to the non-polar *m*-plane QWs covering the sidewalls. They have demonstrated a full visible-color range from red to blue color from InGaN/GaN nanorod-embedded LEDs by adjusting the forward voltage bias. Similarly, Robin *et al.*[32] (see **Figure 5.15**) explain the flow of current from the tip of GaN rod to the sidewalls results in a successive non-uniform excitation of different regions. This leads to different contributions in the EL spectra at 380 nm, 450 nm, 505 nm and 590 nm as a function of injection current. These findings are further supported by a detailed investigation of an InGaN/GaN single wire-based LED by Maria *et al.*,[22] where the color emission is directly related to the position of metal contacts (see **Figure 5.16**). They found that the blue emission originates from the non-polar *m*-plane QWs, whereas the green emission comes from the contact #2 positioned at the junction between *m*-plane and semi-polar QWs. While these reports are mainly based on Ga-polar InGaN/GaN nanostructures, a study by J. Dühn *et al.*[33] has been performed for an InGaN/GaN microrod with mixed polarity. **Figure 5.17** shows HAADF-STEM images of the microrod along with the In concentration EDX map, where the Ga-polar domains form pyramidal top facets, while N-polar domains form flat top facets. The spatially integrated PL and CL spectra of a microrod from the top facet in **Figure 5.17 (d)** evidences strongly localized emissions with lower energy from the semi-polar QWs compared to the *m*-plane non-polar QWs emitting at higher energy.
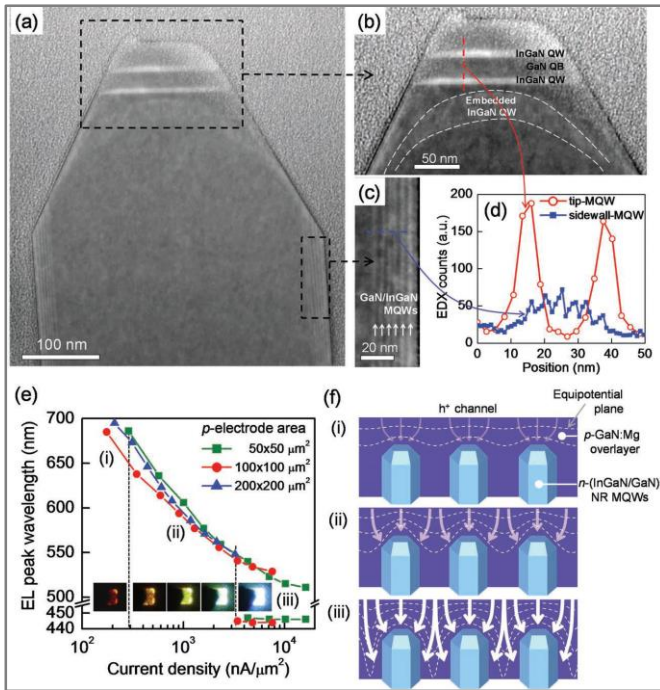
Figure 5.14: (a) Low-magnification STEM image of InGaN/GaN nanorod (NR). High-magnification scanning TEM images of the MQWs formed on: (b) topmost and (c) upright sidewall of NRs. (d) EDX line profiles of the indium. (e) Plots of the EL peak wavelength of nanostructured LEDs with different p-electrode areas as a function of current density. (f) Schematic illustrations of the change of equipotential planes (white dotted lines) in the p-GaN overlayer of the nanostructured LEDs and paths of hole carriers - i) under a low electric field near the turn-on voltage, ii) with increasing applied voltage, and iii) at very high bias voltage. Taken from *Ref. 26*.
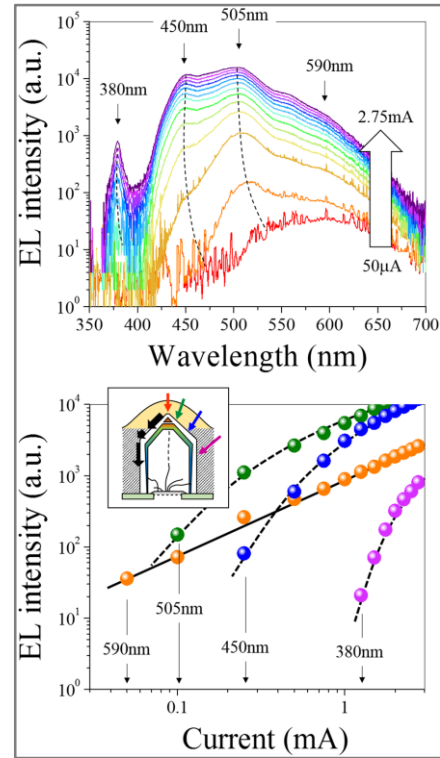
Figure 5.15: RT-EL spectra recorded at different injection currents (top). Current dependencies of emission intensities at different wavelengths (down). The inset illustrates the electrical pumping. Taken from *Ref. 32*.
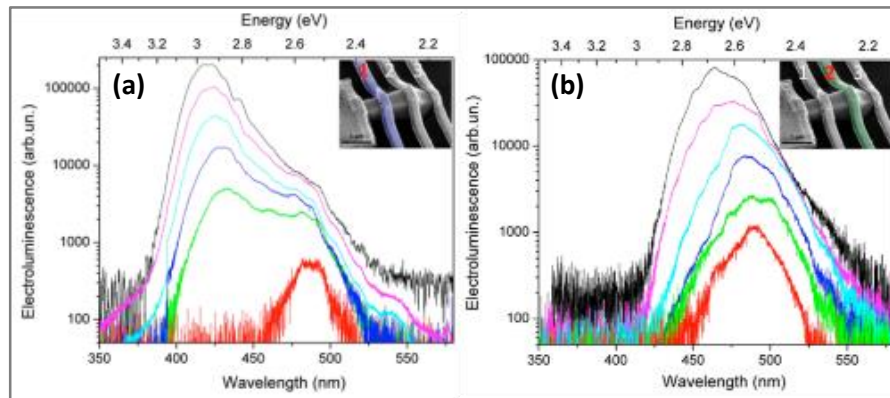
Figure 5.16: Room temperature EL spectra for increasing injection current of a single wire LED (a) with a metal contact at the middle of the lateral facet; (b) with a metal contact at the *m*-plane and semi-polar plane junction. The inset to figure (a) and (b) shows the SEM image of the multi-contact reference LED. Adapted from *Ref. 22*.
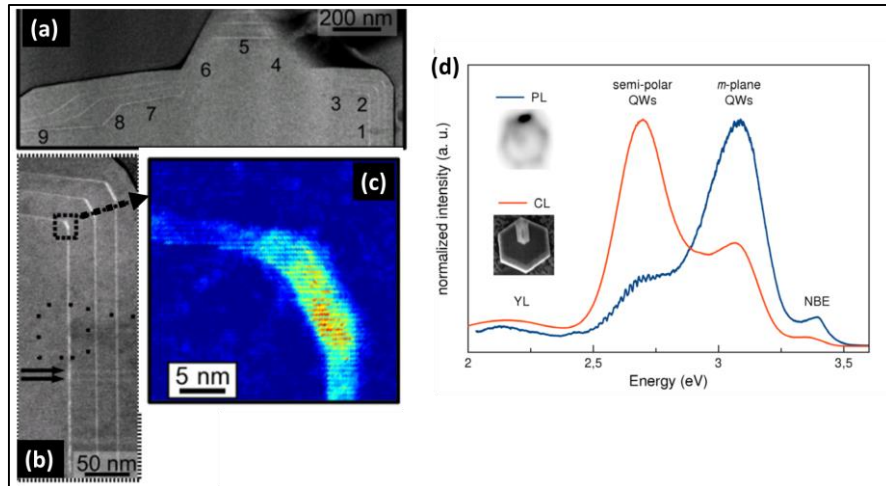
Figure 5.17: (a) HAADF-STEM image of a microrod with the top sidewall facet shown in (b), (c) In concentration map of the innermost InGaN layer and (d) Spatially integrated PL and CL of the top facet of a free standing MR. Adapted from *Ref. 33*.

The color variations observed in the EL spectra as a function of applied voltage bias in the present work seems consistent with the above reports indicating varying indium incorporation depending on the wire facets. As already described in Chapter 2, wires of mixed polarity have also been observed during the growths. Therefore different families of indium rich and indium poor QWs
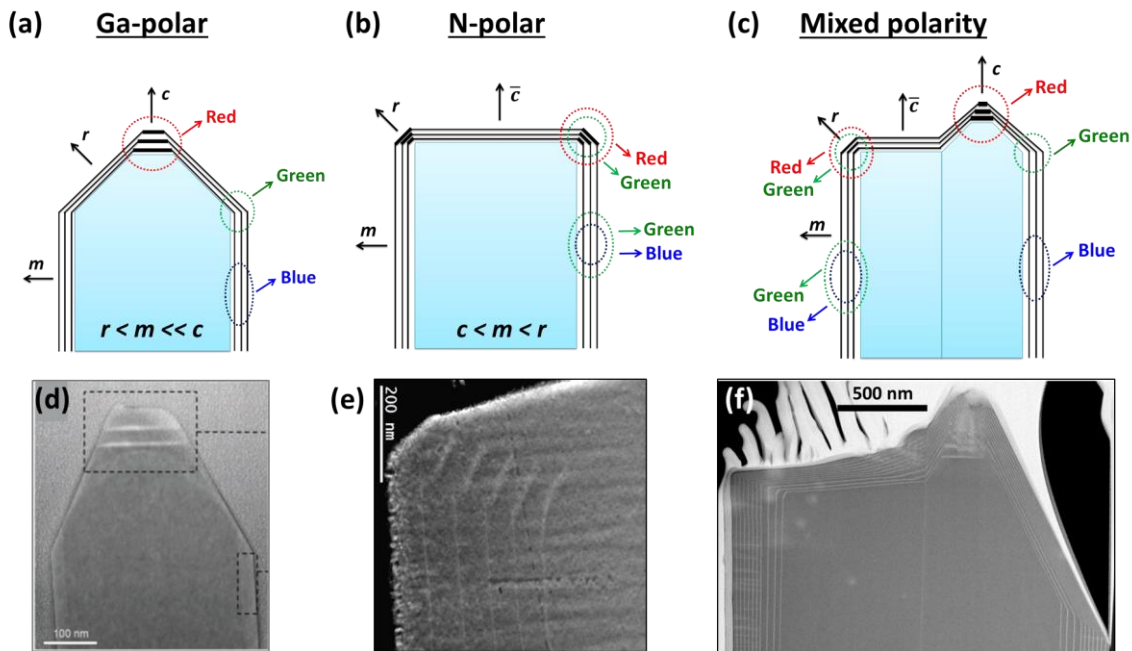
Figure 5.18: Schematics of wires having different polarity with their corresponding TEM image: (a&d) → Ga-polar wires, (b&e) → N-polar wire; and (c&f) → Mixed Polarity. TEM images in (d) and (e) are adapted from *Ref. 26* and *Ref. 23* respectively.

can be present in the wires depending on their polarity giving rise to a variation in the color emission. A schematic of the three cases of wire-polarity with corresponding TEM image is presented **Figure 5.18** to summarize the variation of color emissions from polar *c*-plane QWs, semi-polar *r*-plane QWs and non-polar *m*-plane QWs. The Ga-polar wires in **Figure 5.18 (a)** with TEM image in **Figure 5.18 (c)**[26] have thicker *c*-plane QWs at the top containing higher indium content as compared to the *m*-plane QWs at the sidewalls with indium rich regions located also at the junction between *r*-plane and *m*-plane QWs. Thus, the long wavelength emission such as red and green are expected to arise from the wire-top and the junction of *r*-plane and *m*-plane QWs respectively, while the blue emission originates from the *m*-plane QWs. The wire with N-polarity in **Figure 5.18 (b)** and TEM image in **Figure 5.18 (d)**[23] has higher indium incorporation in the *r*-plane QWs leading to longer wavelength emission as compared to the *c*-plane and *m*-plane QWs. The wire with mixed polarity can be seen in **Figure 5.18 (c)**. The long wavelength emission is expected either from the *r*-plane for the N-polarity part or the wire-top and junctions of *r*-plane and *m*-plane QWs for the Ga-polar part i.e. the green and red emission arise mainly from the top. The short wavelength emission is expected from the *m*-plane QWs regardless of the polarity.

Due to the strong variation in the indium incorporation between the wire top and the sidewalls explained above, the current flow within the GaN-wire plays a key role in the activation of In-rich and poor regions. As already described in the section 5.1.4, the carrier injection in the p-doped GaN shell occurs via the mesh of Ag NWs spread across the top surface of the device. The favorable condition to achieve the contribution from the non-polar QWs is to inject the charge carriers into the GaN-wire sidewalls. This is illustrated using an SEM image in **Figure 5.19 (a)** where the Ag NWs can be seen covering the GaN wire sidewall (highlighted by blue circle). A magnified view can be seen in **Figure 5.19 (b)**. It can be thus expected to measure the *m*-plane sidewall emission from these wires that will exhibit no shift as a function of applied bias. However, due to the non-uniform length of the GaN wires, only the longer wires are efficiently covered from the sidewalls by the Ag NWs, whereas the shorter wires are only covered from the top or at the junction of top and sidewalls because they are barely protruding out of the PDMS (see the wire marked by red circle in **Figure 5.19 (a)** and higher magnified image in **Figure 5.19 (c)**). Therefore, at low current injection, the contribution from the short wires is mainly related to the polar or semi-polar QWs located at the wire-top containing higher indium content. This explains the long wavelength

emission observed at the low applied bias voltage in the EL spectra. When the applied bias is increased, the current is injected through the wire sidewalls due to the increased density of charge carriers. This leads to a redistribution of current across the device and the short wavelength contribution from the non-polar QWs begins to dominate. Hence, blue shift in the emission as a function of bias voltage is recorded.
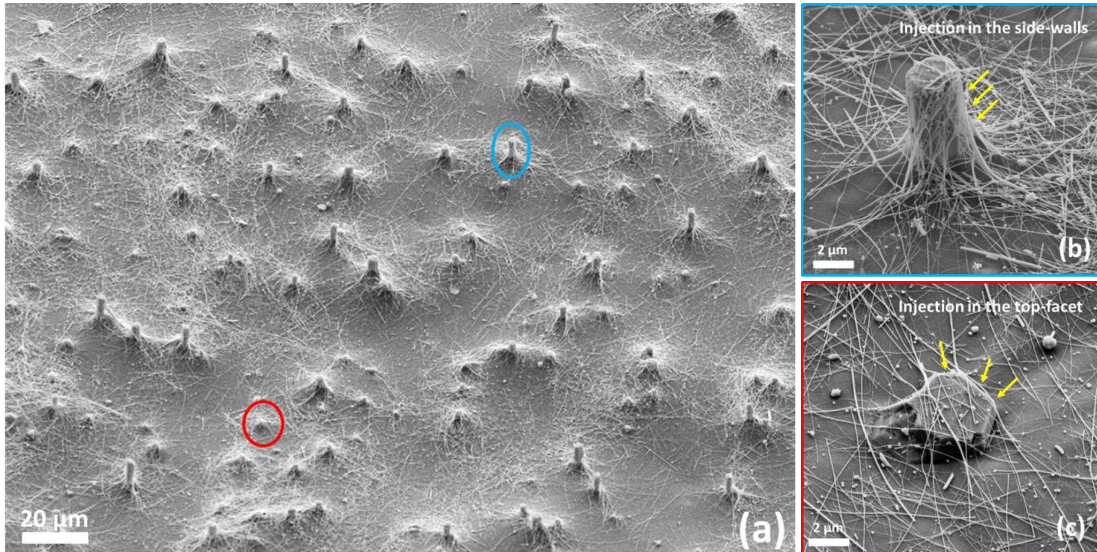
Figure 5.19: (a) SEM image illustrating Ag NWs contacting the GaN wires of different lengths, (b) Sufficiently etched wire with Ag NWs covering the sidewall; and (c) Barely protruding wire with Ag NWs covering mainly the top.

5.3 The color control in LED using phosphor down conversion

5.3.1 Investigating yellow phosphors dispersed in PDMS

The first demonstration of dispersing the YAG:Ce^{+3} phosphors in between the blue InGaN/GaN core-shell wires to achieve white light has already been performed in our group.[35] Further work is also performed by investigating different colors of phosphors (yellow, orange and green) having different grain size combined with core-shell wire LED. An improvement in CRI value from 54 to 86 is observed when a single layer of yellow phosphor covers the wire LED from top.[36] In continuation of this work, it is important to optimize various aspects of the yellow phosphor film

such as thickness and composition. Two different series of samples namely S1 and S2 are prepared by mixing YAG:Ce^{+3} yellow phosphors in a PDMS mixture and curing at high temperature (80 °C) to make polymer slabs encapsulating the phosphors. Series S1 includes samples of different thickness: 45 μm, 90 μm, 182 μm and 310 μm while the mass ratio of YAG:PDMS remains similar as 1:18. Series S2 includes samples having different mass ratio as 1:18 and 1:36 but similar thickness as 182 μm.
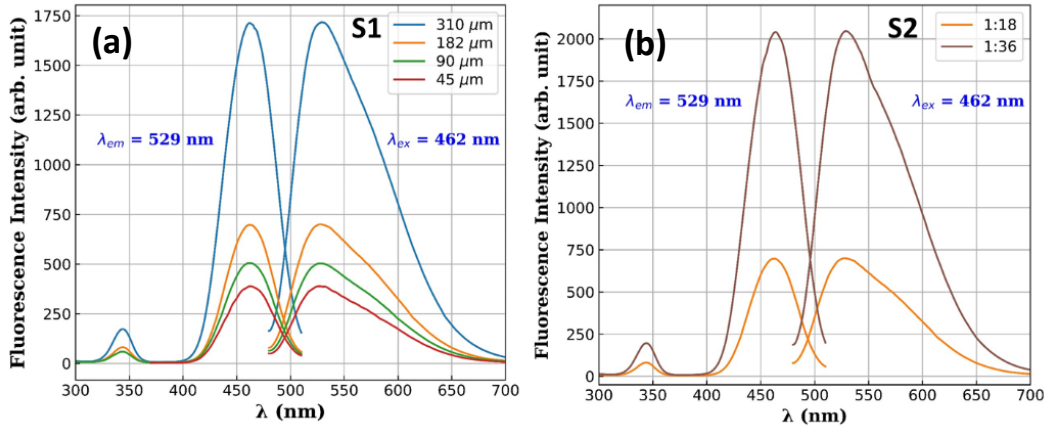
Figure 5.20: Excitation-Emission spectra of phosphors dispersed in PDMS mixture: (a) series S1 with mixing ratio 1:18 and varying thickness; (b) series S2 with thickness 182 μm and varying mixing ratio.

Figure 5.20 (a) and **(b)** presents the excitation and emission (EE) for series S1 and S2 respectively that has been measured with a scan speed of 1200 nm/min using an Hitachi F-4500 fluorescence spectrophotometer equipped with a Xe lamp. The excitation spectra are recorded at an emitting wavelength (λ_{em}) of 529 nm, while the emission spectra are recorded at an excitation wavelength (λ_{ex}) of 462 nm. The electronic configuration of Ce^{+3} ion in its ground state has one electron in the $4f$ orbital that has two allowed states $^2F_{7/2}$ and $^2F_{5/2}$. The electron after excitation enters in $5d$ orbital that splits in two energy states via spin-orbit coupling into $^2D_{5/2}$ and $^2D_{3/2}$. The two distinctive excitation peaks at 343 nm and 462 nm corresponds to the transition from $^2F_{5/2 \text{ or } 7/2}$ to $^2D_{5/2}$ and $^2F_{5/2 \text{ or } 7/2}$ to $^2D_{3/2}$ respectively.[37] The emission peak at 529 nm arises from the electron jumping back from $^2D_{3/2}$ to $^2F_{5/2}$, while the transition of electron from $^2D_{3/2}$ to $^2F_{7/2}$ give rise to a second contribution that is visible as a shoulder between 550-600 nm.[38] This is more pronounced for the sample with mass ratio 1:36 in **Figure 5.20 (b)**. The upper $5d$ states are strongly affected by the crystal field and so the resulting 343 nm peak is less intense as compared to the strong peak at 462 nm, which occurs from the lowest lying $5d$ states.[37] The excitation component peaked at 462 nm

falls in the blue wavelength band (440-470 nm) of the visible spectrum and thus these phosphors can be efficiently excited by a blue LED. The FWHM of the emission peak is similar for all the samples and calculated to be 0.4eV indicating an efficient coverage of the long wavelength band in the visible spectrum. Further, the intensity emitted by phosphors clearly increases with increasing thickness of the polymer slabs as well as with the mass ratio although the increase is non-linear. This can be due to scattering of light as well as re-absorption by the neighboring phosphor particles, which becomes more significant for thicker phosphor films or higher composition.[39]
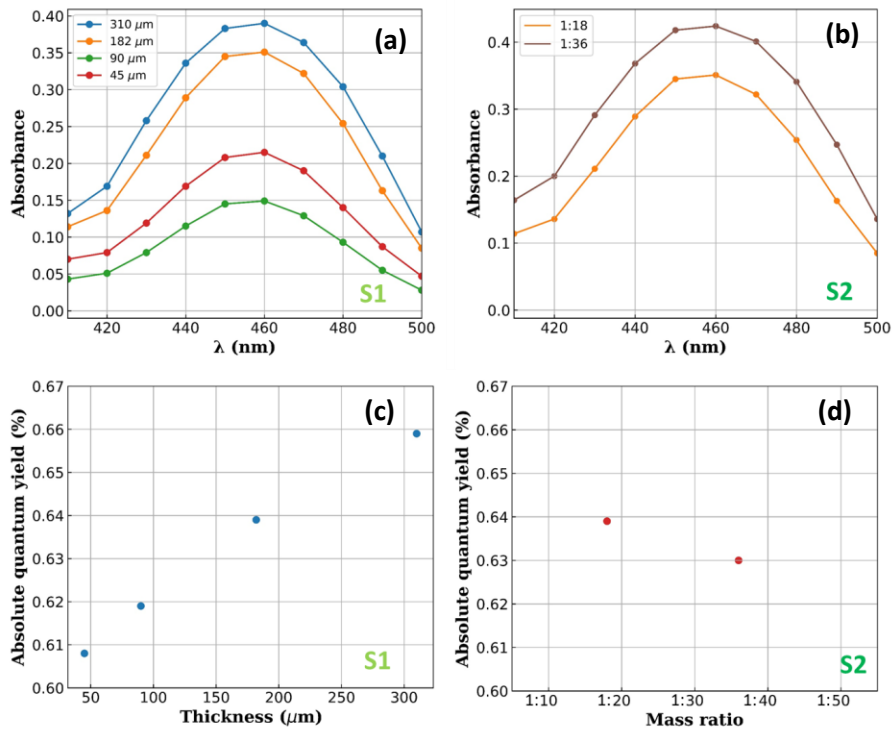
Figure 5.21: Absorbance curves for (a) series S1 & (b) series S2; Absolute quantum yield at $\lambda_{ex} = 460$ nm for (c) Series S1 and (d) Series S2.

The samples are further characterized by comparing their absorbance and quantum yield (QY). Unlike the excitation spectra which is measured at a fixed emission wavelength, the absorbance is recorded by an integrating sphere to measure all the wavelengths absorbed by the sample. The PL QY (Φ_{PL}) is defined as the ratio of photons emitted by the sample to those absorbed by the sample. A 'Quantaurus-QY' Absolute PL Quantum yield spectrometer (C11347 series) specialized in measuring absolute QY by PL method has been used for the measurements with a multichannel

detector and an integration sphere.[§§§] The absorbance curves of series S1 and S2 are depicted in **Figure 5.21 (a)** and **(b)** respectively. Clearly the samples absorb maximum intensity at 460 nm and the increase in absorbance is observed with increasing thickness as well as the mass-ratio of the sample (although the trend is non-linear similar to the intensity in **Figure 5.20** above). Further, it is noticed that the sample with thickness 310 μm and mass ratio 1:18 shows an absorbance of 39% while the sample 182 μm thick and mass ratio 1:36 shows an absorbance of 42.4%. The comparable values in the two cases indicate that the similar absorbance can be achieved by a relatively thicker phosphor film with lower composition rather than a thinner film with higher composition that can save the amount of phosphor material used in the final device. This is also consistent with the QY measurements presented in **Figure 5.21 (c)** and **(d)** for series S1 and S2 respectively. The maximum Φ_{PL} of 66% has been recorded for sample with mass ratio 1:18 and thickness 310 μm while the Φ_{PL} for sample with mass ratio 1:36 and 182 μm thick is estimated to be 63%.

5.3.2 Study of the fluorescence from phosphors excited by a blue LED

The characterization of different yellow phosphor samples is then performed by their excitation with a blue LED to study the electroluminescence spectra of the resulting white light emission. Note that a commercial blue LED emitting at 460 nm has been used for this experiment.[****] **Figure 5.22 (c)** shows the schematic of the experimental setup in which a standard blue LED (source) is positioned at the bottom with an optical fiber (collector) located at the top. The phosphors slabs have been measured one by one by keeping the source and the collector fixed.

The electroluminescence spectra for series S1 and S2 are represented in **Figure 5.22 (a)** and **(b)** respectively where the arrows indicate the increase or decrease of intensity. It is observed in **Figure 5.22 (a)** that with the increasing thickness, more and more blue light gets absorbed by the samples to be converted to longer wavelengths thereby resulting in a broad spectra. The sample having

---

[§§§] The measurements are performed with the help of Gille Le Blevennec at CEA Leti's Optics and Photonics Division (DOPT).

[****] The spotty emission observed from the fabricated home-made LED as described in section 5.2 leads to inhomogeneous excitation of the phosphors. Therefore, a commercial LED has been used to excite the phosphors uniformly. A 4-pin super flux device made up of InGaN on sapphire was acquired from RS company with reported luminous intensity of about 1500 mcd and a forward voltage of 3.5 V.

thickness 310 µm shows a better coverage for the entire visible spectrum among series S1 and the intensity of the blue emission almost decreases by two orders of magnitude compared to the blue source LED. Similarly in **Figure 5.22 (b)**, the sample with mass ratio 1:36 shows a broader spectrum as compared to the sample with mass ratio 1:18 showing a better conversion of the blue light. A decrease in intensity for blue emission by two orders of magnitude and a corresponding increase in the long wavelength emission is visible for both the samples. In addition, for both series S1 and S2, a lack in the wavelength emission can be seen between 650 – 700 nm. This is also evidenced by a very low contribution for the long wavelengths above 650 nm in the emission spectra as described in **Figure 5.20**.[††††] This issue can in principle be addressed by using additional orange/red phosphors to cover the longer wavelengths and thus requires further experiments.
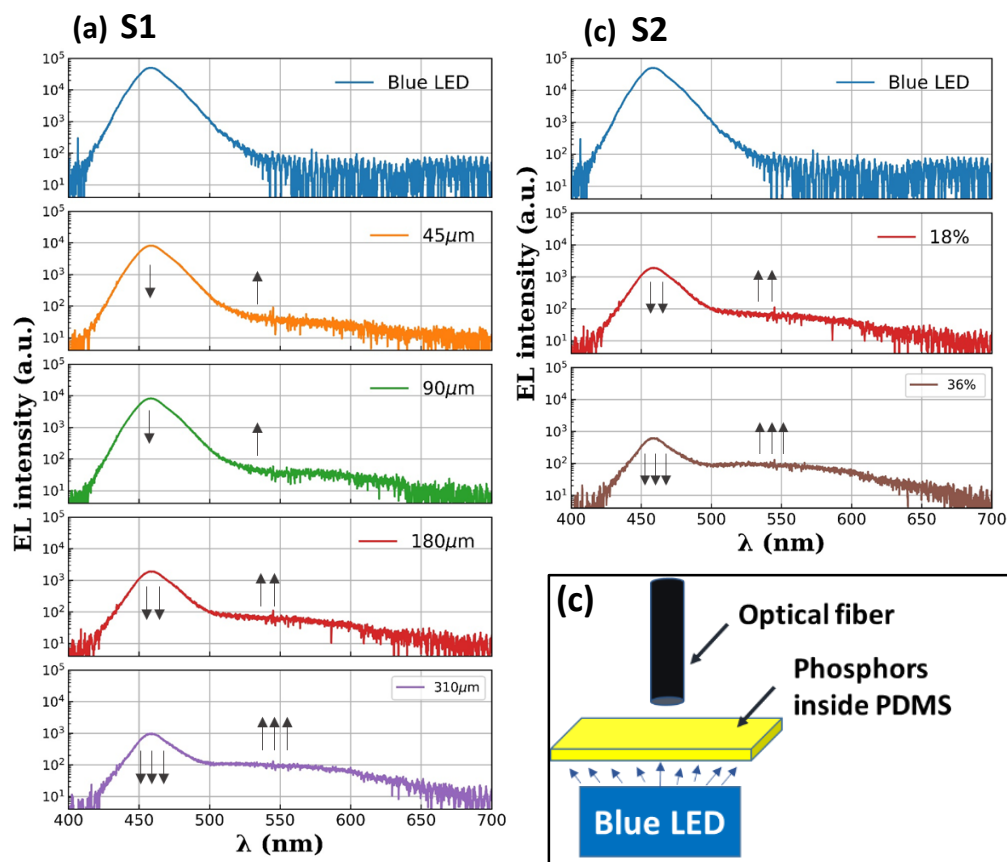

Figure 5.22: Electroluminescence (EL) spectra for blue LED shown in blue curve, for series S1 in (a), for series S2 in (b) and schematics of the experiment in (c).

[††††] This contribution is almost negligible for the samples with low thicknesses.

The two samples called #1 for thickness 310 μm and mass ratio 1:18 and #2 for thickness 180 μm and mass ratio 1:36 have similar EL spectra showing coverage of the visible spectrum. Both samples also have a comparable absorbance (39% for #1 and 41% for #2) and quantum yield (66% for #1 and 63% for #2) as mentioned before. These results indicate that a better coupling between the blue LED and yellow phosphor to target white light emission can be achieved by a relatively thicker phosphor film with low composition rather than a thin film with higher composition thus saving the amount of phosphor material used in the final device.

CONCLUSION

This chapter has explained the detailed technology involved in fabrication of flexible LED devices incorporating core-shell InGaN/GaN wires. Different devices emitting blue, green and multicolor emission have been successfully fabricated and studied with electroluminescence experiments. The investigation of device electrical properties has allowed a thorough understanding of the current injection in the wire based LED. Because the electrical injection is occurring also at the top of the wire, different current paths may lead to emission arising from different wire facets having inhomogeneous indium incorporation and it can be difficult to excite only the *m*-plane MQWs to fully benefit from the wire geometry. This results in a variation in the color of the emitted light with changing applied bias voltage. Novel methods able to only inject current in the non-polar *m*-plane sidewalls by avoiding the semi-polar and polar QWs located the wire top need to be developed to address this issue.

This work is further extended to demonstrate the color management using phosphors to target white light emission. An optimization of different phosphor/PDMS samples in terms of thickness and composition has shown that phosphor slabs with increased thickness (310 μm) and low composition (1:18) show better covering of the visible spectrum when excited by a standard blue LED. Considering the wire-based LED in the present work, it could also be interesting to study resulting white light emission by investigating different designs of coupling the phosphors with the blue LED. A comparison can be made by dispersing the phosphor particles between the wires emitting blue light to the typical design of covering the wires by a phosphor slab from the top. Additional samples have already been prepared by dispersing the phosphors (mixed with PDMS) between the wires. The fabrication of LED devices using these sample therefore requires further

experiments and can be beneficial in improving the overall efficiency of the already established flexible white LED.

REFERENCES

[1] Ho, J. K.; Jong, C. S.; Chiu, C. C.; Huang, C. N.; Shih, K. K.; Chen, L. C.; Chen, F. R.; Kai, J. J. Low-Resistance Ohmic Contacts to P-Type GaN Achieved by the Oxidation of Ni/Au Films. *J. Appl. Phys.* **1999**, *86,* 4491–4497. https://doi.org/10.1063/1.371392.

[2] Ho, J.-K.; Jong, C.-S.; Chiu, C. C.; Huang, C.-N.; Chen, C.-Y.; Shih, K.-K. Low-Resistance Ohmic Contacts to P-Type GaN. *Appl. Phys. Lett* **1999**, *74,* 1275. https://doi.org/10.1063/1.123546.

[3] Lavenus, P.; Messanvi, A.; Rigutti, L.; De Luna Bugallo, A.; Zhang, H.; Bayle, F.; Julien, F. H.; Eymery, J.; Durand, C.; Tchernycheva, M. Experimental and Theoretical Analysis of Transport Properties of Core-Shell Wire Light Emitting Diodes Probed by Electron Beam Induced Current Microscopy. *Nanotechnology* **2014**, *25*, 255201. https://doi.org/10.1088/0957-4484/25/25/255201.

[4] Messanvi, A. Composants Photoniques À Base de Fils de Nitrures D ' Élément S III : Du Fil Unique Aux Assemblées, *Universite Grenoble Alpes,* **2015**. https://tel.archives-ouvertes.fr/tel-01311168/document.

[5] El Kacimi, A. Capteurs Piézoélectriques Souples À Base de Microfils de GaN En Structure Capacitive, *Universite Grenoble Alpes,* **2018.** https://tel.archives-ouvertes.fr/tel-01311168/document.

[6] El Kacimi, A.; Pauliac-Vaujour, E.; Eymery, J. Flexible Capacitive Piezoelectric Sensor with Vertically Aligned Ultralong GaN Wires. *ACS Appl. Mater. Interfaces* **2018**, *10,* 4794–4800. https://doi.org/10.1021/acsami.7b15649.

[7] Fuard, D.; Tzvetkova-Chevolleau, T.; Decossas, S.; Tracqui, P.; Schiavone, P. Optimization of Poly-Di-Methyl-Siloxane (PDMS) Substrates for Studying Cellular Adhesion and Motility. *Microelectron. Eng*. **2008**, *85*, 1289–1293. https://doi.org/10.1016/j.mee.2008.02.004.

[8] Schneider, F.; Draheim, J.; Kamberger, R.; Wallrabe, U. Process and Material Properties of Polydimethylsiloxane (PDMS) for Optical MEMS. *Sensors Actuators, A* **2009**, *151*, 95–99. https://doi.org/10.1016/j.sna.2009.01.026.

[9] Mata, A.; Fleischman, A. J.; Roy, S. Characterization of Polydimethylsiloxane (PDMS) Properties for Biomedical Micro/Nanosystems. *Biomed. Microdevices* **2005**, *7* (4), 281–293. https://doi.org/10.18226/35353535.v5.2016.108.

[10] Koschwanez, J. H.; Carlson, R. H.; Meldrum, D. R. Thin PDMS Films Using Long Spin Times or Tert-Butyl Alcohol as a Solvent. *PLoS One* **2009**, *4* (2), 4572. https://doi.org/10.1371/journal.pone.0004572.g001.

[11] Emslie, A. G.; Bonner, F. T.; Peck, L. G. Flow of a Viscous Liquid on a Rotating Disk. *J. Appl. Phys.* **1958**, *29,* 858–862. https://doi.org/10.1063/1.1723300.

[12] Standing, A. J.; Assali, S.; Haverkort, J. E. M.; Bakkers, E. P. A. M. High Yield Transfer of Ordered Nanowire Arrays into Transparent Flexible Polymer Films. *Nanotechnology* **2012**, *23*, 495305. https://doi.org/10.1088/0957-4484/23/49/495305.

[13] Ge, L.; Wang, X.; Chen, H.; Qiu, K.; Fu, S. Flexible Subwavelength Gratings Fabricated by Reversal Soft UV Nanoimprint. *Chinese Opt. Lett.* **2012**, *10*, 090502. https://doi.org/10.3788/COL201210.090502.

[14] Stein, R.; Kimmel, J.; Marincola, M.; Klemm, F. Observations on Cyclododecane as a Temporary Consolidant for Stone. *J. Am. Inst. Conserv.* **2000**, *39* (3), 355–369. https://doi.org/10.2307/3179979.

[15] Motayed, A.; Bathe, R.; Wood, M. C.; Diouf, O. S.; Vispute, R. D.; Noor Mohammad, S. Electrical, Thermal, and Microstructural Characteristics of Ti/Al/Ti/Au Multilayer Ohmic Contacts to N-Type GaN. *J. Appl. Phys.* **2003**, *93*, 1087–1094. https://doi.org/10.1063/1.1528294.

[16] Oh, M.; Jin, W. Y.; Jun Jeong, H.; Jeong, M. S.; Kang, J. W.; Kim, H. Silver Nanowire Transparent Conductive Electrodes for High-Efficiency III-Nitride Light-Emitting Diodes. *Sci. Rep.* **2015**, *5*, 13483. https://doi.org/10.1038/srep13483.

[17] Lee, J. Y.; Connor, S. T.; Cui, Y.; Peumans, P. Solution-Processed Metal Nanowire Mesh Transparent Electrodes. *Nano Lett.* **2008**, *8* (2), 689–692. https://doi.org/10.1021/nl073296g.

[18] Masui, H.; Sonoda, J.; Pfaff, N.; Koslow, I.; Nakamura, S.; DenBaars, S. P. Quantum-Confined Stark Effect on Photoluminescence and Electroluminescence Characteristics of InGaN-Based Light-Emitting Diodes. *J. Phys. D. Appl. Phys.* **2008**, *41*, 165105. https://doi.org/10.1088/0022-3727/41/16/165105.

[19] Masui, H.; Nakamura, S.; Denbaars, S. P. Experimental Technique to Correlate Optical Excitation Intensities with Electrical Excitation Intensities for Semiconductor Optoelectronic Device Characterization. *Semicond. Sci. Technol.* **2008**, *23*, 85018. https://doi.org/10.1088/0268-1242/23/8/085018.

[20] Guan, N. Nitride Nanowire Light-Emitting Diode, *Université Paris-Saclay,* **2018**. https://tel.archives-ouvertes.fr/tel-01915009/document.

[21] Ra, Y.-H.; Navamathavan, R.; Yoo, H.-I.; Lee, C.-R. Single Nanowire Light-Emitting Diodes Using Uniaxial and Coaxial InGaN/GaN Multiple Quantum Wells Synthesized by Metalorganic Chemical Vapor Deposition. *Nano Lett.* **2014**, *14*, 1537–1545. https://doi.org/10.1021/nl404794v.

[22] Tchernycheva, M.; Lavenus, P.; Zhang, H.; Babichev, A. V.; Jacopin, G.; Shahmohammadi, M.; Julien, F. H.; Ciechonski, R.; Vescovi, G.; Kryliouk, O. InGaN/GaN Core − Shell Single Nanowire Light Emitting Diodes with Graphene-Based P - Contact. *Nano Lett.* **2014**, *14*, 2456–2465. https://doi.org/10.1021/nl5001295.

[23] Dai, X.; Messanvi, A.; Zhang, H.; Durand, C.; Eymery, J.; Bougerol, C.; Julien, F. H.; Tchernycheva, M. Flexible Light-Emitting Diodes Based on Vertical Nitride Nanowires. *Nano Lett.* **2015**, *15*, 6958–6964. https://doi.org/10.1021/acs.nanolett.5b02900.

[24] Jacopin, G.; Bugallo, A. D. L.; Lavenus, P.; Rigutti, L.; Julien, F. H.; Zagonel, L. F.; Kociak, M.; Durand, C.; Salomon, D.; Chen, X. J.; et al. Single-Wire Light-Emitting Diodes Based on GaN Wires Containing Both Polar and Nonpolar InGaN/GaN Quantum Wells. *Appl. Phys. Express* **2012**, *5*, 014101. https://doi.org/10.1143/APEX.5.014101.

[25] Lin, Y. S.; Ma, K. J.; Hsu, C.; Feng, S. W.; Cheng, Y. C.; Liao, C. C.; Yang, C. C.; Chou, C. C.; Lee, C. M.; Chyi, J. I. Dependence of Composition Fluctuation on Indium Content in InGaN/GaN Multiple Quantum Wells. *Appl. Phys. Lett.* **2000**, *77*, 2988–2990. https://doi.org/10.1063/1.1323542.

[26] Hong, Y. J.; Lee, C.; Yoon, A.; Kim, M.; Seong, H.; Chung, H. J.; Sone, C.; Park, Y. J.; Yi, G. Visible-Color-Tunable Light-Emitting Diodes. *Adv. Mater.* **2011**, *23*, 3284–3288. https://doi.org/10.1002/adma.201100806.

[27] Karpov, S. Y. Carrier Localization in InGaN by Composition Fluctuations: Implication to the "green Gap." *Photonics Res.* **2017**, *5* (2), A7. https://doi.org/10.1364/prj.5.0000a7.

[28] Kaganer, V. M.; Fernández-Garrido, S.; Dogan, P.; Sabelfeld, K. K.; Brandt, O. Nucleation, Growth, and Bundling of GaN Nanowires in Molecular Beam Epitaxy: Disentangling the Origin of Nanowire Coalescence. *Nano Lett.* **2016**, *16*, 3717–3725. https://doi.org/10.1021/acs.nanolett.6b01044.

[29] Lin, Y. T.; Yeh, T. W.; Nakajima, Y.; Dapkus, P. D. Catalyst-Free GaN Nanorods Synthesized by Selective Area Growth. *Adv. Funct. Mater.* **2014**, *24*, 3162–3171. https://doi.org/10.1002/adfm.201303671.

[30] Chen, H.-S.; Yao, Y.-F.; Liao, C.-H.; Tu, C.-G.; Su, C.-Y.; Chang, W.-M.; Kiang, Y.-W.; Yang, C. C. Light-Emitting Device with Regularly Patterned Growth of an InGaN/GaN Quantum-Well Nanorod Light-Emitting Diode Array. *Opt. Lett.* **2013**, *38* (17), 3370. https://doi.org/10.1364/ol.38.003370.

[31] Schimpke, T.; Martin, M.; Stoll, I.; Pohl-Klein, B.; Bichler, D.; Franz, Z.; Strube-knyrim, J.; Huckenbeck, B.; Max, B.; Marcus, M.; et al. Phosphor-Converted White Light from Blue-Emitting InGaN Microrod LEDs. *Phys. stat. sol.* **2016**, *213 (6),* 1577–1584. https://doi.org/10.1002/pssa.201532904.

[32] Robin, Y.; Bae, S. Y.; Shubina, T. V; Pristovsek, M.; Evropeitsev, E. A.; Kirilenko, D. A.; Davydov, V. Y.; Smirnnov, A. N.; Toropov, A. A.; Jmerik, V. N.; et al. Insight into the Performance of Multi-Color InGaN / GaN Nanorod Light Emitting Diodes. *Sci. Rep*. **2018**, *8*, 7311. https://doi.org/10.1038/s41598-018-25473-x.

[33] Dühn, J.; Tessarek, C.; Schowalter, M.; Coenen, T.; Gerken, B.; Müller-Caspari, K.; Mehrtens, T.; Heilmann, M.; Christiansen, S.; Rosenauer, A.; et al. Spatially Resolved Luminescence Properties of Non- and Semi-Polar InGaN Quantum Wells on GaN Microrods. *J. Phys. D. Appl. Phys.* **2018**, *51*, 355102. https://doi.org/10.1088/1361-6463/aad4e6.

[34] Wernicke, T.; Schade, L.; Netzel, C.; Rass, J.; Hoffmann, V.; Ploch, S.; Knauer, A.; Weyers, M.; Schwarz, U.; Kneissl, M. Indium Incorporation and Emission Wavelength of Polar, Nonpolar and Semipolar InGaN Quantum Wells. *Semicond. Sci. Technol.* **2012**, *27*, 24014. https://doi.org/10.1088/0268-1242/27/2/024014.

[35] Guan, N.; Dai, X.; Messanvi, A.; Zhang, H.; Yan, J.; Gautier, E.; Bougerol, C.; Julien, F. H.; Durand, C.; Eymery, J.; et al. Flexible White Light Emitting Diodes Based on Nitride Nanowires and Nanophosphors. *ACS Photonics* **2016**, *3,* 597–603. https://doi.org/10.1021/acsphotonics.5b00696

[36] Guan, N.; Amador-Mendez, N.; Wang, J.; Das, S.; Kapoor, A.; Julien, F. H.; Gogneau, N.; Foldyna, M.; Som, S.; Eymery, J.; et al. Colour Optimization of Phosphor-Converted Flexible Nitride Nanowire White Light Emitting Diodes. *J. Phys. Photonics* **2019**, *1*, 35003. https://doi.org/10.1088/2515-7647/ab2c84.

[37] Haranath, D.; Chander, H.; Sharma, P.; Singh, S. Enhanced Luminescence of Y3Al5O12: Ce 3+ Nanophosphor for White Light-Emitting Diodes. *Appl. Phys. Lett.* **2006**, *89*, 1–4. https://doi.org/10.1063/1.2367657.

[38] Dong, Y.; Zhou, G.; Jun, X.; Zhao, G.; Su, F.; Su, L.; Zhang, G.; Zhang, D.; Li, H.; Si, J. L. Luminescence Studies of Ce:YAG Using Vacuum Ultraviolet Synchrotron Radiation. *Mater. Res. Bull.* **2006**, *41*, 1959–1963. https://doi.org/10.1016/j.materresbull.2006.02.035.

[39] Tran, N. T.; You, J. P.; Shi, F. G. Effect of Phosphor Particle Size on Luminous Efficacy of Phosphor-Converted White LED. *J. Light. Technol*. **2009**, *27 (22),* 5145–5150. https://doi.org/10.1109/JLT.2009.2028087.

Conclusions & Perspectives

❖ Conclusions

This Ph.D. work has been dedicated to the realization and understanding of *m*-plane core-shell InGaN/GaN wire based visible-LEDs. A complete study has been presented beginning from the wire growth to their integration in working devices on flexible substrates.

Firstly, the technology to produce flexible LEDs has been well adapted from the expertise of C2N laboratory (Univ. Paris-Saclay) and has enabled to perform such fabrication at CEA, IRIG, Grenoble. Flexible devices exhibiting different wavelength emission have been successfully fabricated with their electrical characterization. Several challenges have been faced in device fabrication and have been carefully analyzed. The major difficulty in PDMS peeling is also realized in this work, which remains challenging till date despite the use of different possible solutions. Presently, this is overcome by using longer wires (40 μm) to increase the related PDMS thickness. Other issues in the wire-based LED such as the spot-like emission and the color shifting in EL spectra with the changing bias have been observed. This color shift is attributed to an inhomogeneous carrier injection in different wire facets and also the compositional variations and fluctuations within active QWs. The selective area growth (SAG) has also been performed on sapphire substrates to try to reduce the spotty emission. Even if SAG can help to increase the number of active wires incorporated in the device, the reproducibility control is a challenge in itself. Many experiments have been conducted in this Ph.D. work so as to improve the organized growth. We realize that the growth is highly sensitive to both surface preparation of the SiN mask and the growth conditions, and so the use of self-assembled wires remains promising for the moment.

Another important outcome of this work has been the demonstration of improved efficiency for an InGaN/GaN SQW emitting blue light thanks to the insertion of a GaN-spacer between GaN wire core and the QW. The beneficial role of GaN-spacer has been understood in detail by correlating

the optical and structural properties of the heterostructure. It is observed that the spacer helps to prevent the degradation of QW coming from an unintentional ultra-thin layer of SiGa$_x$N$_y$ created around the surface of wire core due to high residual silane present in the reactor required to favour the wire growth. This finding has also helped to understand the older results of our group. Furthermore, it is revealed that the presence of an additional InGaN underlayer (UL), which is known to strongly improve the efficiency of *c*-plane planar QWs by removing GaN point defects, does not influence the performance of radial QWs in our wires. This result proves that the InGaN UL is ineffective in the case of our core-shell m-plane QWs structure suggesting the different impact of InGaN UL with point defect on m-plane surfaces. Further experiments directly on m-GaN substrates can be performed to validate this assumption. On the other hand, the GaN-spacer is highly effective on GaN wire grown by silane-assisted mode to improve the light emission efficiency. Consequently, this result allows us to work with SQW for device application, unlike the typical MQW structure (having at least five QWs) used earlier.

One of the key-objectives of this Ph.D. has been to target longer emission wavelength from core-shell wires. A comprehensive study correlating the structural, optical and electrical properties is presented to demonstrate green emission (around 520 nm) from the *m*-plane radial InGaN QWs. An average In-content of about 24 (±4) % using EDX and APT measurements is revealed in the QWs having thickness of 2.7 nm grown at 650 °C. A single wire device has also been produced, which demonstrates the green electroluminescence from radial *m*-plane QWs. This work has been carried further to achieve a dual-color emission by growing two different families of QWs within a single core-shell InGaN/GaN heterostructure. The optical measurements reveal two distinctive wavelength emission at 435 and 485 nm corresponding to an estimated indium content of about 15 (±1) and 21 (±1) % by EDX measurements respectively. A flexible LED device has also been fabricated using wire ensembles. The luminescence is dominated by the longer wavelength emission, which is explained by the low hole mobility of p-GaN and only the QWs with higher indium content located close to the p-GaN side are able to emit efficiently.

In addition, further optimizations of phosphor have been performed to be combined with the blue LED in terms of phosphor size and composition. The results obtained by combining the yellow

phosphors (YAG:Ce^{+3}) with a commercial blue LED have shown that a higher quantum yield (QY) and absorbance can be obtained by using thicker phosphors slab with lower composition. In the present study, a phosphors slab with thickness 310 μm and mixing ratio of 1:18 has shown the highest QY of 66%. This study is also extended to home-made wire-LEDs. Different samples have already been prepared by dispersing the phosphors particles in between the wires. Final device fabrication with these samples is still under progress.

❖   Perspectives

The results obtained in this thesis have marked the beginning of some new experiments that can be conveyed forward both in case of wire growth and device technology. Likewise some strategies to target long wavelength emission and to achieve large flexible LEDs are additionally proposed.

The <u>long wavelength emission</u> from *m*-plane InGaN/GaN core-shell wires is demonstrated in this present work reporting green emission, although it requires an excellent reproducibility control. Other than green, wavelength emission such as yellow and red still remains a challenge for this core-shell geometry. The following ways are proposed to address this issue:

1. The AlGaN barriers can be used in place of standard GaN barriers, since it is predicted that Al prevents the In-desorption from QWs. In addition, the growth of InGaN QWs can be performed at a relatively higher temperature to target the similar In-content. This reduces the degradation of crystal quality and influence of temperature variations on InGaN QWs. This thesis has experimented the InGaN/AlGaN heterostructures using a low Al-content (3%) inside the barriers to demonstrate green emission with a narrow peak at 520 nm. Further works can be performed by exploring different heterostructures varying the Al-content in the barriers to fully explore the role of Al for the InGaN QW emission. This approach has to carefully consider the critical thickness to be under plastic strain relaxation.

2. The group of L. Samuelson at Lund University (Sweden) has reported the strategy of ordered platelets producing relaxed InGaN templates to grow c-plane InGaN QWs for long wavelength emission.[*] These templates are InGaN pyramids grown by selective area MOVPE that are thermally etched to form InGaN platelets. The emission peak for InGaN QW grown on InGaN platelet was shifted from 2.17 eV (yellow) on the $In_{0.09}Ga_{0.91}N$ platelet to 1.95 eV (red) on the $In_{0.18}Ga_{0.82}N$ platelet. They attribute the red shift to higher thickness of QW (5.8 nm) and reduced indium pulling effect when grown on platelet with higher In-content. Similar approach can be used for core-shell InGaN/GaN heterostructures. The top-down etching of thick InGaN layers can be performed to achieve InGaN wires allowing the growth of radial MQW growth on the wire surface that can be expected to contain higher indium content. However, thick relaxed InGaN layers with high quality and low defect density by MOCVD still remain an issue. This point can be addressed by using InGaNOS substrates to grow a thicker relaxed InGaN layer.[†]

3. The use of phosphors is gaining high visibility day by day for planar GaN based LEDs and is also an attractive choice to be integrated with core-shell wires. The blue emission with InGaN/GaN core shell wires is now well established and can be coupled with different phosphors such as europium-doped compounds, $Sr[LiAl_3N_4]:Eu^{2+}$ to achieve red emission. Note that the efficiency of red phosphors is low but is currently focused in the industries for further improvements.

The <u>color mixing</u> in InGaN/GaN core shell wires is also interesting in view of producing phosphor free white light LED. A dual-color LED has been studied in this Ph.D., which emits at 435 and 485 nm. But the EL spectrum is dominated by 485 nm emission due to a poor hole mobility as described above. Perhaps, an improvement in the design structure can be performed in the future by reducing the number of QWs from (3x blue, 7x green) to (1x blue, 3x green). This can allow an efficient transport of carriers across the entire active region leading to an improved dual-color LED that emits

---

[*] Bi, Z.; Lenrick et al. InGaN Platelets: Synthesis and Applications toward Green and Red Light-Emitting Diodes. *Nano Lett.* **2019**, *19*, 2832–2839.
[†] Even, A. et al. Enhanced in Incorporation in Full InGaN Heterostructure Grown on Relaxed InGaN Pseudo-Substrate. *Appl. Phys. Lett.* **2017**, *110*, 262103.

distinctively when excited electrically. In addition, it is also important to grow QWs by carefully tuning the growth temperature to target the blue (450 nm) and green (520 nm) emission from core-shell wire based LED. Fortunately, if the future studies are able to realize yellow emission from the core-shell wires, it can be combined with the blue emission to target white light. Nevertheless, the broadening of the yellow MQW emission will play a key-role to be able to achieve full white color emission with controlled CRI value.

Further experiments are also required to optimize the <u>white light LED using phosphors</u>. The work in collaboration with C2N has reported an increase in CRI to 86 when a single layer of yellow phosphor covers the wire-LED (having a dual EL emission at 439 and 485 nm) compared to 54 when the phosphors are dispersed both inside the wires and cover the top.[‡] This thesis further provides an optimized thickness and composition of the phosphor slabs that are excited by a commercial blue LED, but additional experiments have to be performed with these results to combine with blue wire-based LEDs.

The <u>flexibility</u> in LED devices is an additional functionality that has been focused in this thesis. The route to prepare flexible devices is explained by mechanical lift off of the wire encapsulated in the PDMS polymer. However, the PDMS peeling issue is one of the major concerns and can be overcome by using an alternative method, which has already been reported earlier for GaN/ZnO coaxial LEDs.[§] The growth of InGaN/GaN core-shell wires can be performed on graphene-covered SiO_2/Si (001) substrates and then encapsulated in the PDMS polymer. A solution of buffered HF can help to remove the Si/SiO_2 substrate, while the encapsulated wires on graphene floating in the solution can be mounted on an arbitrary flexible substrate. Alternatively, the growth of wires on Si (111) substrates that has been previously reported in our group[**] can also be extended to perform the

[‡] Guan, N. Colour Optimization of Phosphor-Converted Flexible Nitride Nanowire White Light Emitting Diodes. *J. Phys. Photonics* **2019**, *1*, 35003.

[§] Chung, K. et al. Growth and Characterizations of GaN Micro-Rods on Graphene Films for Flexible Light Emitting Diodes. *APL Mater.* **2014**, *2*, 92512.

[**] Salomon, D. et al. Metal Organic Vapour-Phase Epitaxy Growth of GaN Wires on Si (111) for Light-Emitting Diode Applications. *Nanoscale Res. Lett.* **2013**, *8* (61), 1–5.

growth on SOI (111) substrates. This approach does not involve any PDMS peeling and opens the possibility to produce flexible devices with shorter wires (<20 μm).

****

ABSTRACT

The InGaN/GaN-based planar heterostructures are now widely used to produce light emitting diodes (LEDs). The blue LEDs and phosphor-converted white LEDs are already commercialized with high efficiencies. But further scope to reach long wavelength emission with improved efficiencies and mitigating issues likes efficiency droop and poor light extraction still remains. This Ph.D. thesis presents the use of core-shell InGaN/GaN wires as an attractive choice for visible LEDs thanks to their smaller footprint, high aspect ratio and low defect density. The bendable wires also allow fabricating LEDs with flexibility in view of rapidly growing demands for rollable displays, wearable devices, flexible biomedical instruments, etc. This work focuses on a complete study, beginning from the self-assembled growth of m-plane core-shell InGaN/GaN wires by metal organic vapor phase epitaxy to their integration in working devices on flexible substrates, especially on original green-emitting heterostructures. The influence of an InGaN under layer (UL) and GaN-spacer is investigated to improve the efficiency of a blue single quantum well. It is found that the presence of a GaN spacer is required to achieve efficient m-plane emission from core-shell wires, while no internal quantum efficiency change is observed by adding an InGaN UL. Further, flexible LEDs with different wavelengths such as blue, green and dual-color emission have been realized by tuning the indium content inside InGaN/GaN multiple quantum well heterostructures followed by a comprehensive study correlating structural, optical and electrical properties. The use of selective area growth is also approached to address the issues encountered in device emission and remaining challenges in the reproducibility control are discussed. To target white light emission, an optimization study of yellow phosphors combined with the well-established blue LED has also been performed.

Keywords: InGaN/GaN, green emission, flexible devices, phosphors.

Les hétérostructures planaires à base de puits quantiques InGaN/GaN sont désormais largement utilisées dans les diodes électroluminescentes (LED). Les LED bleues et les LED blanches à phosphores sont largement commercialisées avec des rendements d'émission de lumière très élevés. Néanmoins, il reste encore des problèmes à résoudre avec ce type de dispositifs : l'émission à plus grande longueur d'onde (rouge) avec de bonnes efficacités, le problème du la chute du rendement à forte puissance (« *droop efficiency* ») et l'amélioration de l'extraction de la lumière. Ce travail de thèse présente l'utilisation de fils GaN ayant une hétérostructure radiale InGaN/GaN qui peut s'avérer un choix intéressant pour le développement de nouvelles LED visibles grâce à plusieurs avantages-clés : un encombrement réduit, un rapport d'aspect élevé et une grande qualité cristalline avec de faible densité de défauts. Les fils permettent également de fabriquer des LED flexibles intéressantes pour de nouvelles applications comme les écrans enroulables, les dispositifs médicaux de petite taille et flexibles, etc. Ce travail est consacré à une étude complète qui part de la croissance auto-assemblée de fils à hétérostructures InGaN/GaN radiale plan-m par la méthode d'épitaxie en phase vapeur d'organiques métalliques, jusqu'à l'intégration des fils dans des dispositifs flexibles, en étudiant en particulier des hétérostructures émettant dans le vert. L'influence d'une sous-couche InGaN et d'un espaceur GaN est spécifiquement étudiée pour améliorer l'efficacité d'émission d'un puits quantique (PQ) unique émettant dans le bleu. On constate que la présence de l'espaceur GaN est nécessaire pour obtenir une émission efficace du PQ dans le plan-m des fils de GaN, alors qu'aucun changement n'est observé en ajoutant une sous-couche d'InGaN. De plus, des LED flexibles avec différentes longueurs d'onde telles que l'émission bleue, verte et bicolore ont été réalisées en ajustant la teneur en indium à l'intérieur des hétérostructures à puits quantiques InGaN/GaN. Cette étude approfondie corrèlent les propriétés structurelles, optiques et électriques. L'utilisation de la croissance sélective est également abordée pour essayer d'améliorer les performances des LED flexibles à nanofils mais la maitrise de la reproductibilité reste difficile à contrôler. Pour obtenir un dispositif LED flexible émettant une lumière blanche, une étude d'optimisation des phosphores combinés à la LED bleue a également été réalisée.